UCTEA Turkish Chamber of Civil Engineers

Teknik Dergi

Technical Journal

Volume 30 Issue 6 November 2019

TEKNİK DERGİ PUBLICATION PRINCIPLES

Teknik Dergi is a scientific and technical journal indexed by the Science Citation Index Expanded. Annually six issues are published, three in Turkish in the months of January, May and September, three in English in March, July and November. Its main principles of publication are summarized below:

1. Articles reporting original scientific research and those reflecting interesting engineering applications are accepted for publication. To be classified as original, the work should either produce new scientific knowledge or add a genuinely new dimension to the existing knowledge or develop a totally new method or substantially improve an existing method.
2. Articles reporting preliminary results of scientific studies and those which do not qualify as full articles but provide useful information for the reader can be considered for publication as technical notes.
3. Discussions received from the readers of the published articles within three months from publication are reviewed by the Editorial Board and then published together with the closing remarks of the author.
4. Manuscripts submitted for publication are evaluated by two or three reviewers unknown to the authors. In the light of their reports, final decision to accept or decline is taken by the Editorial Board. General policy of the Board is to get the insufficient manuscripts improved in line with the reviewers' proposals. Articles that fail to reach the desired level are declined. Reasons behind decisions are not declared.
5. A signed statement is taken from the authors, declaring that the article has not been published as a "journal article or book chapter". In case the Editorial Board is in the opinion that the article has already been published elsewhere with minor changes or suspects plagiarism or a similar violation of ethics, then not only that article, but none of the articles of the same authors are published.
6. Papers reporting works presented as conference papers and developed further may be considered for publication. The conference it was presented to is given as a footnote in the first page.
7. Additionally, a document signed by all authors, transferring the copyright to UCTEA Chamber of Civil Engineers is submitted together with the manuscript.

UCTEA Turkish Chamber of Civil Engineers

Teknik Dergi

Technical Journal

Volume 30 Issue 6 November 2019

UCTEA *(TMMOB)*
Turkish Chamber of Civil Engineers *(İnşaat Mühendisleri Odası)*
Necatibey St. No: 57, Kızılay 06440 Ankara, Turkey
Tel: +90.312.294 30 00 - Faks: +90.312.294 30 88
E-mail: imo@imo.org.tr - www.imo.org.tr

Publisher *(Sahibi)*:
Cemal GÖKÇE
On behalf of UCTEA Turkish Chamber of Civil Engineers

Administrative Officer *(Yazı İşleri Müdürü)*:
Bahaettin SARI

Volume 30 - Issue 6 - November 2019 *(Cilt 30 - Sayı 6 - Kasım 2019)*

Published bi-monthly. Local periodical. *(İki ayda bir yayınlanır, yerel süreli yayın)*

Date of Print: 01 November 2019 *(Baskı Tarihi: 1 Kasım 2019)*

Number of copies: 1.000 *(1.000 adet basılmıştır)*

ISSN: 1300-3453

Printed by *(Baskı)*:
Başak Matbaacılık ve Tanıtım Hiz. Ltd. Şti.
Anadolu Blv. Meka Plaza No:5/15 Gimat - Yenimahalle /Ankara - Tel: 0.312.397 16 17

UCTEA Turkish Chamber of Civil Engineers

Teknik Dergi

Teknik Dergi is indexed by

- Science Citation Index Expanded
- Scopus
- Journal Citation Reports / Science Edition
- Engineering Index
- Concrete Abstracts (American Concrete Institute)
- National Technical Information Service (US NTIS)
- CITIS
- Ulrich's International Periodical's Directory
- TÜBİTAK / ULAKBİM

Teknik Dergi is a peer reviewed open access periodical publishing papers of original research and interesting practice cases. It addresses both the research community and the practicing engineers.

Reviewers:

This list is renewed each year and includes reviewers who served in the last two years of publication.

Ayda Şafak AĞAR ÖZBEK
Ragıp AKBAŞ
Sami Oğuzhan AKBAŞ
Rıfat AKBIYIKLI
Özge AKBOĞA KALE
Burcu AKÇAY ALDANMAZ
Cihan Taylan AKDAĞ
Cem AKGÜNER
M. Vefa AKPINAR
Atakan AKSOY
Zuhal AKYÜREK
Fatih ALEMDAR
Pelin ALPKÖKİN
Sinan ALTIN
Hilmi Doğan ALTINBİLEK
Adlen ALTUNBAŞ
Fuat ARAS
Davit ARDITI
Deniz ARTAN İLTER
Hakan Nuri ATAHAN
Shady ATTIA
Mustafa Tamer AYVAZ
Lale BALAS
Selim BARADAN
Bekir Oğuz BARTIN
Bilge BAŞ
Zeynep BAŞARAN BUNDUR
Cüneyt BAYKAL
Zerrin BAYRAKDAR
İdris BEDİRHANOĞLU
Serkan BEKİROĞLU
Mehmet BERİLGEN
Saadet Arzu BERİLGEN
Niyazi Özgür BEZGİN
Selçuk BİLDİK
Senem BİLİR MAHÇİÇEK
Barış BİNİCİ
İlknur BOZBEY
Zafer BOZKUŞ
Burcu BURAK BAKIR
Erdem CANBAY
Zekai CELEP
Cihan CENGİZ
Halim CEYLAN
Ömer CİVALEK
Mustafa CÖMERT
Ali Fırat ÇABALAR
Barlas Özden ÇAĞLAYAN
Özgür ÇAKIR
Gülben ÇALIŞ
Necati ÇATBAŞ
Erkan ÇELEBİ
Kutay ÇELEBİOĞLU
Ahmet Ozan ÇELİK
Oğuz Cem ÇELİK
Osman Nuri ÇELİK
Hilmi Berk ÇELİKOĞLU
Kemal Önder ÇETİN
Mecit ÇETİN
Reha ÇETİNKAYA
Safiye Feyza ÇİNİCİOĞLU
Erdal ÇOKÇA
Kutlu DARILMAZ
Cem DEMİR
Ender DEMİREL
Mehmet Cüneyd DEMİREL
Fatih DİKBAŞ
Seyyit Ümit DİKMEN
İrem DİKMEN TOKER
Ahmet Anıl DİNDAR
Emrah DOĞAN
Nurhan ECEMİŞ ZEREN
Özgür EKİNCİOĞLU
Alper ELÇİ
Şebnem ELÇİ
Nilay ELGİNÖZ KANAT
Murat Altuğ ERBERİK
E. Mete ERDEMGİL
Saffet ERDOĞAN
Esin ERGEN PEHLEVAN
Ayşen ERGİN
Gökmen ERGÜN
Esra Ece ESELLER BAYAT
Tuğba ESKİŞAR TEFÇİ
Güngör EVREN
Antonio FORMISANO
Nuray GEDİK
Ergun GEDİZLİOĞLU
Haluk GERÇEK
Ilgın GÖKAŞAR
Çağlar GÖKSU
Burcu GÜLDÜR ERKAL
Fazlı Erol GÜLER
Zeynep GÜLERCE
Taylan GÜNAY
Necmettin GÜNDÜZ
Abdurrahman GÜNER
Ülker GÜNER BACANLI
Aslı Pelin GÜRGÜN
İpek GÜRSEL DİNO
Gürşans GÜVEN IŞIN
Soner HALDENBİLEN
Murat HAMDERİ
Zeki HASGÜR
Abdul HAYIR
Nejan HUVAJ SARIHAN
Zeynep IŞIK
Sabriye Banu İKİZLER
Eren İNCİ
Pınar İNCİ
Erdal İRTEM
Recep İYİSAN
Nihat KABAY
M. Rifat KAHYAOĞLU
Volkan KALPAKÇI
Erhan KARAESMEN
Halil KARAHAN
Himmet KARAMAN
Mustafa KARAŞAHİN
İlker KAZAZ
Cevza Melek KAZEZYILMAZ ALHAN
Mustafa Kubilay KELEŞOĞLU
Elçin KENTEL
Havvanur KILIÇ
Ufuk KIRBAŞ
Veysel Şadan Özgür KIRCA
Gökhan KİRKİL
Niyazi Uğur KOÇKAL
Önder KOÇYİĞİT
Mete KÖKEN
Ali Ümran KÖMÜŞÇÜ
Özgür KURÇ
Akif KUTLU
Semih KÜÇÜKARSLAN
Hilmi LUŞ
Kasım MERMERTAŞ
Mehmet Murat MONKUL
Yetiş Şazi MURAT
Elif OĞUZ
Mehmet Hakkı OMURTAG
Sema ONURLU
Engin ORAKDÖĞEN
Şeref ORUÇ
Okan ÖNAL
Akın ÖNALP
Aybike ÖNGEL
Bihrat ÖNÖZ
Ali Hakan ÖREN
Murat ÖZEN
Pelin ÖZENER
Abdullah Tolga ÖZER
Eren Arman ÖZGÜVEN
Hakkı Oral ÖZHAN
Zeynep Huri ÖZKUL BİRGÖREN
Beliz ÖZORHON ORAKÇAL
Sadık ÖZTOPRAK
Turan ÖZTURAN
Baki ÖZTÜRK
Mustafa ÖZUYSAL
Tolga Yılmaz ÖZÜDOĞRU
Nilüfer ÖZYURT ZİHNİOĞLU
Bekir Yılmaz PEKMEZCİ
Şamil Şeref POLAT
Gül POLAT TATAR
Selim PUL
Selman SAĞLAM
Mehmet SALTAN
Altuğ SAYGILI
Hasan SAYGIN
Neslihan SEÇKİN
Serdar SELAMET
Serdar SOYÖZ
Ayşe Filiz SUNAR
Erol ŞADOĞLU
Burak ŞENGÖZ
Aykut ŞENOL
Ali Ünal ŞORMAN
Özcan TAN
Ali Hamza TANRIKULU
Serhan TANYEL
Ergin TARI
Taha TAŞKIRAN
Gökmen TAYFUR
Berrak TEYMUR
H. Onur TEZCAN
Mesut TIĞDEMİR
Şahnaz TİĞREK
Vedat TOĞAN
Onur Behzat TOKDEMİR
Nabi Kartal TOKER
Mustafa TOKYAY
Ali TOPAL
Cem TOPKAYA
Ahmet TORTUM
Gökçe TÖNÜK
Nursu TUNALIOĞLU
Eda TURAN
Ahmet TÜRER
Kaan TÜRKER
Handan TÜRKOĞLU
Cüneyt TÜZÜN
Eren UÇKAN
Berna UNUTMAZ
Mehmet UTKU
Volkan Emre UZ
Deniz ÜLGEN
Aslı ÜLKE KESKİN
Alper ÜNLÜ
Ahmet YAKUT
İsmail Özgür YAMAN
A. Melih YANMAZ
Mert Yücel YARDIMCI
Ufuk YAZGAN
Anıl YAZICI
Emine Beyhan YEĞEN
İrem Zeynep YILDIRIM
Koray Kamil YILMAZ
M. Tuğrul YILMAZ
Mehmet YILMAZ
İsmail YÜCEL
Yeliz YÜKSELEN AKSOY
Nabi YÜZER
Ahmet Şahin ZAİMOĞLU

UCTEA Turkish Chamber of Civil Engineers

Teknik Dergi

Volume: 30 Issue: 6 November 2019

CONTENTS

Teknik Dergi, 2019 9533-9559, Paper 555

Modeling the Effects of Hydrated Lime Additives on Asphalt Mixtures by Fuzzy Logic and ANN

Mustafa Sinan YARDIM[1]
Betül DEĞER ŞİTİLBAY[2]
Selim DÜNDAR[3]

ABSTRACT

In this study, Marshall design test parameters of hot mix asphalt samples with various rates of Hydrated Lime (HL) content were modelled using Fuzzy Logic (FL) and Artificial Neural Networks (ANN). HL was used as an additive material in asphalt mixtures and it affects the properties of the mixture. The effect of this material varies depending on the rate of use and the asphalt content of the mixtures. With the Marshall Stability test, optimal Asphalt Content (AC) ratios in the mixtures were obtained. The effect of the HL additive, which was introduced precisely in the mixtures in a wide range, on the Marshall parameters and depending also on the asphalt content was investigated. For this purpose, 15 Marshall design sets were prepared by decreasing the ratio of the mineral filler in the mixture starting from 6.8% by weight, by 0.5% intervals, and replacing it with the same ratio of HL. In addition, 45 control samples were produced for soft-computation. Marshall test results showed that the use of HL additive with lower amounts in the mixtures yields better results compared to higher rates in terms of the material properties. The Marshall test results were used to develop the FL and ANN models. The models which were developed produced acceptable estimations of the mixture parameters.

Keywords: Hot mix asphalt, hydrated lime, Marshall mix design, fuzzy logic, artificial neural networks.

1. INTRODUCTION

Deformations in flexible pavements are amongst the most important problems encountered in highway construction and operation. The main reasons for the deformations are excessive

Note:
- This paper has been received on March 07, 2018 and accepted for publication by the Editorial Board on January 28, 2019.
- Discussions on this paper will be accepted by January 31, 2020.
- https://dx.doi.org/10.18400/tekderg.402816

1 Yıldız Technical University, Department of Civil Engineering, İstanbul, Turkey - yardim@yildiz.edu.tr https://orcid.org/0000-0003-0799-9294

2 Yıldız Technical University, Department of Civil Engineering, İstanbul, Turkey - bdeger@yildiz.edu.tr https://orcid.org/0000-0003-0723-9789

3 İstanbul Okan University, Dep. of Civil Engineering, İstanbul, Turkey - selim.dundar@okan.edu.tr - https://orcid.org/0000-0003-4433-1998

traffic loads and environmental conditions such as the temperature change or exposure to water. These factors shorten the service life of the highways which is undesirable for both the users and administrators of the highways. Several methods have been implemented in order to prevent and control various deformations in flexible pavements. One method is to modify the bituminous mixtures used in the pavements. Various additives can be used for the modification process. Either the aggregate or the bitumen in the mixture can be modified according to the deformation problem encountered.

The use of hydrated lime (HL) in the modification of hot mix asphalt has an important place in the solution of problems encountered in pavements. There are many studies in the literature to determine the positive and negative effects of HL in mixtures [1, 2]. Not only the type, but also the amount of the additive, has an effect on the mixture. In this study, the filler amount has been gradually decreased in the mixture by substituting it with HL. In order to see the gradual effect of the HL, the changes are made in small percentage intervals. The Marshall Stability Test was applied to the samples which were prepared in accordance with standards [3]. Optimal Asphalt Content (AC) and the parameters that define the properties of the mixture (unit weight or practical specific weight (Dp), void filled with asphalt (VFA), Marshall Stability (MS), air voids (Va), voids in mineral aggregate (VMA), flow rate (F) and Marshall Quotient (MQ)) for each HL content have been obtained as a result of the tests. Practically speaking, estimation of the mixture parameters from the AC and HL percentages using soft computing methods is useful to obtain fast and realistic results to aid the decision making processes. In this study, FL and ANN models have been developed to estimate the mixture parameters from the AC and HL percentages introduced.

2. BACKGROUND

Bitumen mixtures have to provide the desired performance during their service life. The main physical and mechanical properties of bitumen mixtures are stability, durability, flexibility, resistance to fatigue and creep, impermeability and workability [4]. Many studies have been carried out to improve these properties. One of these methods is the usage of HL as an additive. Lime, which decreases both the moisture sensitivity and stripping, has been used as an additive in the US since 1910. Although HL has been recognized for its antistripping feature, recently other benefits have also been discovered. Resistance to wheel track formation, resistance to enlarging of low temperature cracks, increasing the rigidity, altering the oxidation properties of the binder, decreasing the aging stiffening, adjusting the moisture and increasing the stability by modifying the clay grains can be listed amongst them [1]. The main problems of hot mix asphalt pavements that are affected by the rheological properties of asphalt are stripping, deterioration and cracking [5]. Especially, some aggregate types have a tendency to strip. Temperature, heavy rainfall, freeze-thaw cycle and traffic loads have a great impact on the stripping feature. HL is the most effective stripping-preventive additive and is widely used for this purpose [1, 6, 7]. HL decreases the failure risk of the asphalt-aggregate bond mechanically and has a positive effect on this problem even with lack of water in the environment [1, 6]. HL increases the tensile strength of the pavements [8, 9] by increasing the elasticity modulus of the mixture [10, 11]. It especially increases the strength by helping dispersion of the strains caused by traffic loads [12]. [13-20] remark on the significant effect of HL on the decrement of permanent deformations. This effect helps to improve the stiffening properties and to resist wheel track formations [15, 21-22]. HL alters

the oxidation properties of the binder [23], decreases ageing stiffening [15, 16, 24-26] and increases ageing performance [27-32]. As moisture damage decreases the effective life period of the pavement by damaging its integrity, usage of HL increases the pavement life [33] up to 38% [34]. Various benefits of HL usage on hot mix asphalt have been reported under specific conditions (the type, origin and gradation of the aggregate used; the type, properties and amount of the binder; the type, amount, property and usage type of other additives; climate and temperature changes, project service life; and pavement load conditions, etc.); in this context, HL is defined as a multi-functional additive [1, 26, 35].

In this study, FL and ANN models that estimate the Marshall test results from given AC and HL ratios have been developed. Soft computing methods are widely used in the literature on modeling hot mix asphalt properties. [36] used the Fuzzy Logic (FL) approach on investigating the fatigue behavior of asphalt concrete pavements. Fatigue life has been estimated by a fuzzy algorithm taking deformation measurements into account. [37] modeled the deflection behavior of flexible pavements under dynamic loading using FL. FL provided better modeling performance than linear elastic theory and finite element methods. [38] developed an ANN that uses experimental results and finite element method outputs to model the behavior of the free material in the sub-base layer of flexible pavements. The proposed approach was considered suitable for realistic solutions of back-calculation problems. [39] used ANN on modeling emulsified asphalt mixtures. Curing time, cement addition level, and residual asphalt content were used as the input, and the flexibility modulus was used as the output parameters of the model. The development of a 3-layered back propagating ANN provided good results on estimating the flexibility modulus. [40] modeled the Marshall Stability of hot mix asphalt samples exposed to various temperatures under various times. [41] developed an ANN to model the long term aging of the bitumen binder. ANN had better performance and easier usage than the regression models. [42] used artificial intelligence methods to analyze permanent deformations of asphalt mixtures and to investigate the wheel track potential of dense asphalt-aggregate mixtures. Multi Expression Programming (MEP)-based straightforward formulas have been developed which are easy tools to use in various engineering applications. ANN have also been used to estimate the results of repeated creep tests [43] and Marshall Stability, flow rate and Marshall Quotient [44] for Polypropylene (PP) modified asphalt mixtures. The physical properties of the asphalt mixture, such as the PP type, PP ratio, AC, sample height, unit weight, VMA, VFA and air voids have been used. [45] used ANN to estimate the rigidity behavior of reclaimed asphalt pavements having rubberized asphalt concrete. ANN performed better than the regression model to estimate the fatigue life of the modified mixtures. ANN are also used to determine the complex modulus of Styrene Butadiene Styrene (SBS) modified bitumen. The bitumen heat, frequency and SBS content [46] and mixing heat, rate, time, experiment temperature and frequency [47] were used as the inputs of the ANN model to determine the complex modulus of SBS modified bitumen. [48] developed two genetic algorithms (GA) to determine the damping ratio and shear modulus of sand-mica mixtures. The mica content and effective stress and strain values were used to determine the damping ratio and shear modulus. A good correlation (R^2=0.95) was established between the developed model and the test results. [49] developed a heuristic k Nearest Neighbor (k-NN) estimator based on genetic programming to model Marshall Stability test data of asphalt mixtures. The model estimated the Marshall parameters with high accuracy. [50] developed an Adaptive Neuro-Fuzzy Inference System (ANFIS) to determine the wheel track of Polyethylene Terephthalate (PET) modified asphalt mixtures.

PET content, strain levels and test temperatures were used as the input parameters. Comparison with test results proved that ANFIS can be an effective estimation method. [51] simulated the elasticity modulus of hot mix asphalts containing Recycled Concrete Aggregates (RCA) and stone mastic asphalt mixtures using ANFIS. RCA content and test temperatures were used as the input parameters. ANFIS supplied the best results for mixed RCA while the most erroneous results were obtained for coarse RCA when compared with the test results.

3. EXPERIMENTAL STUDY

3.1. Material Properties

In this study, the aggregates used were provided from İsfalt A. Ş. Ümraniye Asphalt Plant. The source of this material is the limestone quarries of Ömerli, Istanbul, located in the northwestern part of Turkey. CaO, of 52.9% content, comprises the main oxide element of the limestone of this region and 75% of the mineralogical composition is calcite. The limestone used for the production has a grey to dark grey color [52]. No. 2, No. 1 and stone powder aggregates were washed, dried and sifted on 3/4", 1/2", 3/8", No. 4, No. 10, No. 40, No. 80 and No. 200 sieves of the shaking machine in accordance with the standards [53]. Weight of the material passing from each sieve was calculated and its distribution was determined according to the Wearing Course Type-1 mixture ratios of the Highway Technical Specifications of the General Directorate of Turkish Highways (Karayolları Genel Müdürlüğü – KGM) [54]. In this study, aggregate No. 2 was taken at 15%, No. 1 at 40% and the stone powder at 45%. The coarse and fine aggregates and mineral filler material had ratios of 51.3%, 41.9% and 6.8%, respectively in the mixture. This aggregate mixture was dense, in other words it was well-graded. The properties of the aggregate are given in Table 1 while the gradation curve of the aggregate mixture is given in Figure 1.

Table 1 - Physical properties of aggregates

Aggregate Type	Apparent Specific Gravity (g/cm^3)	Bulk Specific Gravity (g/cm^3)	Water Absorption (%)
Coarse Aggregate	2.729	2.698	0.42
Fine Aggregate	2.754	2.693	0.82
Mineral Filler	2.735	-	-
Aggregate Mixture	2.740	2.699	-

50/70 penetration bitumen provided from İzmit Oil Refinery (Tüpraş) was used as the asphalt cement. The properties and criteria of this binder were obtained using the tests applied as shown in Table 2. Optimum AC was determined for different HL content using the Marshall method. For this reason, 3 samples were prepared for each AC, varying between 4.0% and 6.5%, with 0.5% intervals, comprising a total of 18 sample sets.

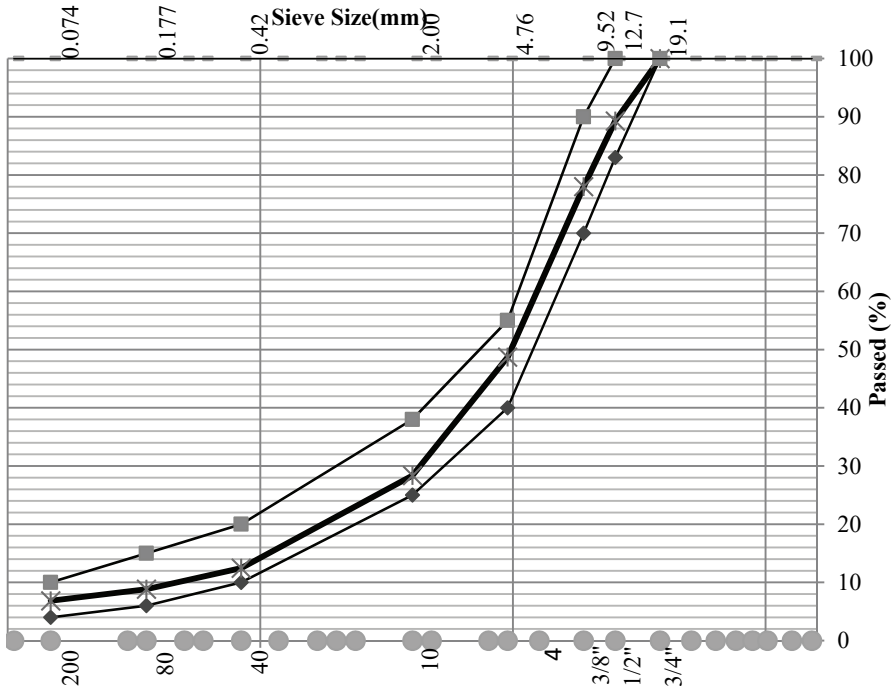

Figure 1 - Aggregate gradation curve

Table 2 - Physical properties of the bitumen

Properties	Standards	Test Value	Specification
Specific gravity (g/cm^3), at 25 ºC	ASTM D 70	1.009	-
Flash point (Cleveland) (ºC)	ASTM D 92	345	>230
Penetration (0.1 mm), at 25 ºC, 100 g, 5 sec	ASTM D 5	59.80	50-70
Ductility (cm), at 25 ºC, 5 cm/min	ASTM D 113	>100	>100
Thin film heating loss (%), at163 ºC, 5 hr	ASTM D 1754	11	<80
Penetration percentage after heating loss (%)	ASTM D 5	65.90	>54
Ductility after heating loss (cm)	ASTM D 113	65.40	>50
Softening point (ºC)	ASTM D 36	48.50	45-55

In this study, the mineral filler material percentage of the aggregate mixture with a determined gradation was decreased gradually, and replaced with the same amount of HL. The additive used in the experiment was the powdered calcium lime, produced with the code S-KK 80-T at the

Bartın Lime Factory which is located in northern Turkey. The properties of this material which also has one of the lowest densities in the Turkish market, are given in Table 3.

Table 3 - Properties of hydrated lime

Properties	Standards	Test Value	Specification
Chemical Properties			
Total CaO (%)	TS EN 459-1 TS 32 EN 459-2	85.78	> 80
MgO (%)	TS EN 459-1 TS 32 EN 459-2	3.52	< 5
Total CaO+MgO (%)	TS EN 459-1	89.30	>80
Loss on Ignition (%)	TS 32 EN 459-2	22.51	
SO_3 (%)	TS EN 459-1 TS 32 EN 459-2	1.47	< 2.00
CO_2 (%)	TS EN 459-1 TS 32 EN 459-2	3.89	< 7.00
Physical Properties			
Fineness over 90 microns (%)	TS EN 459-1 TS 32 EN 459-2	6.00	< 9.00
Density (kg/m^3)	TS 32 EN 459-2	472	< 600

3.2. Preparation of the Mixtures and the Marshall Test

In this study, to determine the effect of each HL ratio, the mineral filler material content of the mixture was decreased with intervals of 0.5%, and replaced with the HL, in order to prepare various designs. In other words, a different design, in line with the Marshall Method [55, 56], was prepared for each HL ratio, to determine the optimum AC ratio. Three samples for each of the 6 AC values (2x50 strokes were applied on two sides) were produced for each of the 15 different HL ratios and properties of each sample were determined [57].

15 different HL ratios were used in the developed model. In order to determine the optimum amount of AC for each different HL ratio, Marshall designs were prepared using 6 different ACs. (In traditional Marshall design methods, curves with 3rd degree equations produce high precision levels. Thus, the relation between the Marshall parameters and the AC were defined as 3rd degree curves). Three samples were prepared for each HL-AC pair and the arithmetic mean of the results obtained from the analyses was used in the model. For this reason, 90 data were obtained from the 270 samples in the model. The samples produced were used to develop, train, validate and test the FL and ANN models as will be seen in the following sections. The Marshall designs for different amounts of HL, the optimum AC obtained, and the associated parameters are summarized in Table 4. Also, the apparent specific gravity values of the sum of the mineral filler and HL (Gsa) are added into the third column of the table.

Table 4 - Marshall Test results for different HL content

Design No.	**HL Cont.**	Gsa	**Opt. AC**	Dp	VFA	MS	Va	F	VMA	MQ (MS/F)
	(%)	(g/cm^3)	(%)	(g/cm^3)	(%)	(kN)	(%)	mm	(%)	
1	**0.0**	2.806	**5.20**	2.409	73.0	11.6	4.10	4.4	15.27	2.64
2	**0.5**	2.776	**5.28**	2.398	71.6	11.64	4.45	4.85	15.70	2.40
3	**1.0**	2.760	**5.25**	2.400	72.0	11.60	4.40	4.75	15.58	2.44
4	**1.5**	2.702	**5.47**	2.371	68.9	8.58	5.18	4.13	16.63	2.08
5	**2.0**	2.519	**5.35**	2.387	72.9	9.81	4.09	4.20	15.55	2.34
6	**2.5**	2.588	**5.59**	2.372	71.6	8.41	4.62	4.40	16.29	1.91
7	**3.0**	2.609	**5.38**	2.377	70.05	9.25	4.80	6.05	16.20	1.53
8	**3.5**	2.586	**5.60**	2.374	72.0	8.75	4.50	4.27	16.26	2.05
9	**4.0**	2.571	**5.39**	2.371	70.03	10.24	4.84	4.55	16.25	2.25
10	**4.5**	2.505	**5.54**	2.355	69.0	8.70	5.18	4.10	16.65	2.12
11	**5.0**	2.448	**6.16**	2.342	73.0	8.41	4.80	5.10	17.32	1.65
12	**5.5**	2.544	**6.33**	2.358	76.5	8.05	4.20	5.40	17.44	1.49
13	**6.0**	2.501	**6.23**	2.366	77.0	8.30	3.80	6.52	16.78	1.27
14	**6.5**	2.488	**5.74**	2.324	66.0	8.12	6.10	4.11	17.94	1.98
15	**6.8**	2.419	**6.10**	2.350	74.0	8.70	4.42	4.60	17.04	1.89

Table 5 - Marshall Test results for control production samples (CPS)

Design No.	**HL Cont.**	**Opt. AC**	Dp	VFA	MS	Va	F	VMA	MQ (MS/F)
	(%)	(%)	(g/cm^3)	(%)	(kN)	(%)	mm	(%)	
1	**0.0**	**5.20**	2.403	71.72	11.35	4.38	6.57	15.50	1.73
2	**0.5**	**5.28**	2.369	66.64	9.79	5.57	4.73	16.70	2.07
3	**1.0**	**5.25**	2.365	65.77	8.89	5.75	4.55	16.79	1.96
4	**1.5**	**5.47**	2.356	66.78	8.33	5.70	3.99	17.17	2.09
5	**2.0**	**5.35**	2.370	69.93	9.56	4.85	4.28	16.14	2.23
6	**2.5**	**5.59**	2.367	70.94	8.63	4.82	3.84	16.60	2.24
7	**3.0**	**5.38**	2.348	65.47	8.69	5.93	3.86	17.17	2.25
8	**3.5**	**5.60**	2.340	66.35	7.43	5.91	4.03	17.57	1.84
9	**4.0**	**5.39**	2.357	67.43	10.08	5.46	4.08	16.77	2.47

Table 5 - Marshall Test results for control production samples (CPS) (continued)

Design No.	**HL Cont.**	**Opt. AC**	Dp	VFA	MS	Va	F	VMA	MQ (MS/F)
	(%)	(%)	(g/cm^3)	(%)	(kN)	(%)	mm	(%)	
10	**4.5**	**5.54**	2.352	68.51	9.76	5.33	5.28	16.92	1.85
11	**5.0**	**6.16**	2.354	75.06	8.73	4.29	5.83	17.18	1.50
12	**5.5**	**6.33**	2.362	76.99	8.17	3.97	4.54	17.27	1.80
13	**6.0**	**6.23**	2.368	77.77	8.67	3.75	4.61	16.87	1.88
14	**6.5**	**5.74**	2.319	65.08	8.12	6.36	3.88	18.20	2.09
15	**6.8**	**6.10**	2.338	71.94	8.52	4.95	4.20	17.63	2.03

In addition, three different samples with optimum AC for each of the 15 different HL ratios were produced, consisting of a total of 45 new samples. The Dp values of these Control Production Samples (CPS) were obtained during the sample preparation stage while MS and F values were obtained by testing of the Marshall device (Table 5). The values of the other parameters, namely Va, VMA and VFA were obtained as a result of the calculations used in the Marshall design method [55, 56].

The results of this sample set were used in re-testing the validity of the FL and ANN models. Also, the Dp, MS, Va, VFA, VMA, F and MQ values for each optimum AC were obtained from their respective 3rd degree curves and defined as the mathematical model results.

4. FL MODEL

In this study, each of the input parameters (AC and HL) and the output parameters (Dp, VFA, MS, Va, VMA, F and MQ) of the FL model are defined with 3 membership functions as "low", "medium" and "high". It was considered that the input parameters might not have the same impact on each of the 7 properties of the asphalt samples. In other words, for example, when estimating the MS of the sample, the values of the HL between 3 and 5 can be considered as medium, but when estimating the flow rate the limits of a medium set can be between 2 and 4.5. Therefore, instead of developing a single FL model to estimate the value of the 7 output parameters, 7 separate FL models were developed to estimate each one. Thus, the values of each parameter were estimated with higher precision. The following steps were carried out while developing the FL models:

(a) Fuzzification: First of all, the input and output parameters of each model were fuzzified. In order to develop the simplest models, input and output parameters were divided into 3 fuzzy sets as "low", "medium" and "high" and the triangular membership functions seen in Figure 2 were used to define them. Also, the usage of 3 fuzzy sets defines the rule base with the minimum number of rules. The triangular membership functions are defined with 3 critical points, namely the start (a), the peak (b) and the end (c) points. Points a and c correspond to the membership function value of 0, while b corresponds to the value of 1.

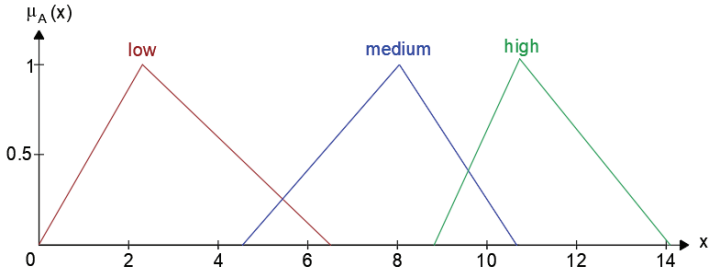

Figure 2 - Membership functions

(b) Generation of the Rule Base: In order to generate the initial rule base, 3D graphics were drawn which show the change of the output values according to the change in input values (Figures 3-9). By using the graphics, rules formed from 2 inputs and a single output parameter were generated. The rules defining the relation between input and output parameters are defined as:

$$R_1: IF\ AC\ is\ A(1)\ AND\ SK\ is\ B(1)\ THEN\ output\ is\ C(1)$$

$$R_2: IF\ AC\ is\ A(2)\ AND\ SK\ is\ B(1)\ THEN\ output\ is\ C(2) \quad (1)$$

$$Also$$

$$R_N: IF\ AC\ is\ A(n)\ AND\ SK\ is\ B(n)\ THEN\ output\ is\ C(n)$$

Here n = 3, N = 3 x 3 = 9, A(1), A(2), A(3) and B(1), B(2), B(3) represent the fuzzy sets of input parameters while C(1), C(2), C(3) represent the fuzzy sets of the output parameters.

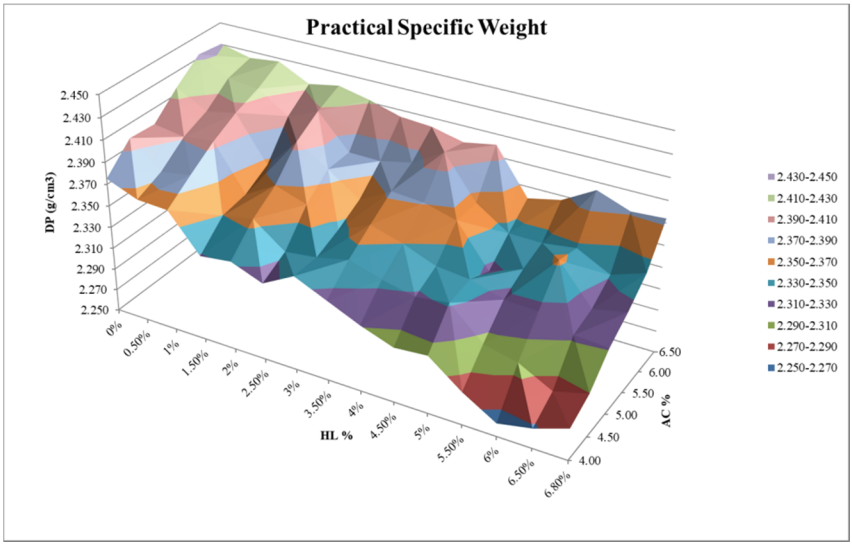

Figure 3 - Change of unit weight according to the change in HL and AC

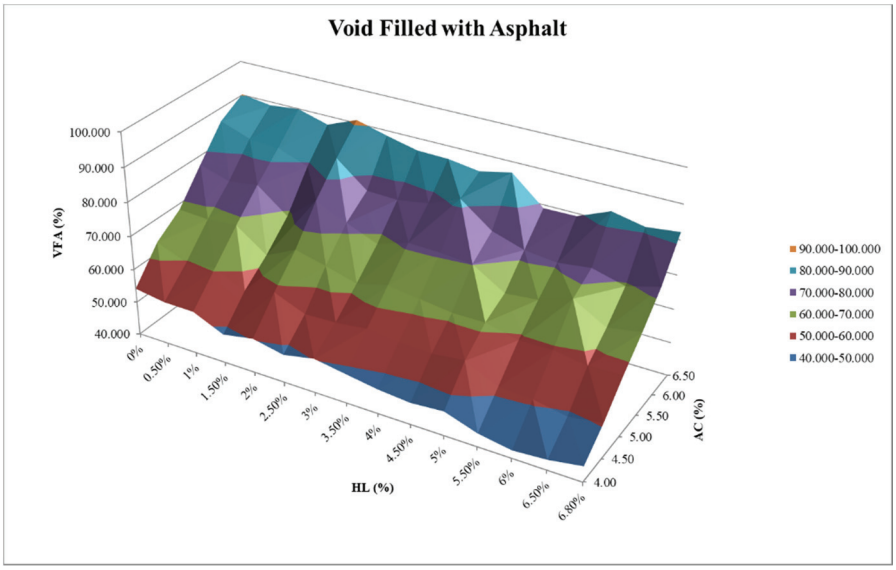

Figure 4 - Change of VFA according to the change in HL and AC

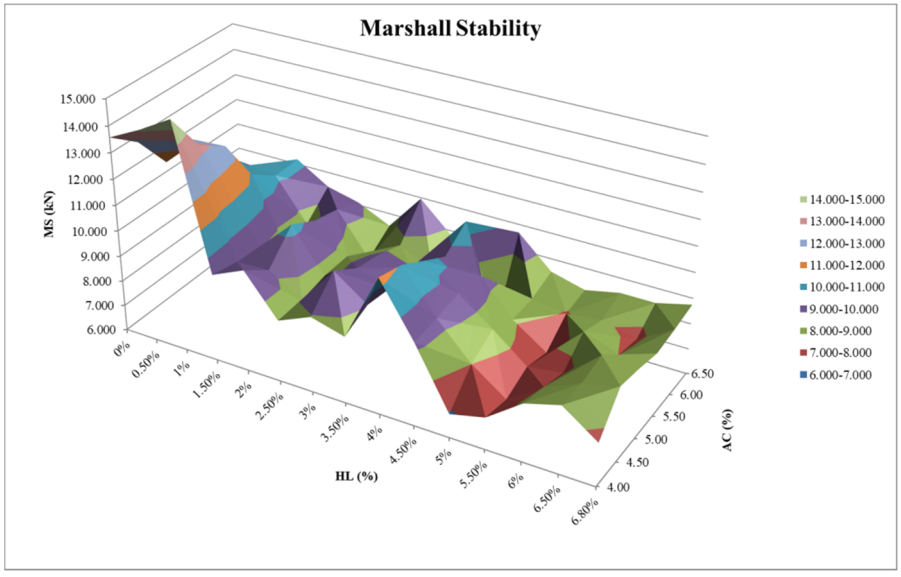

Figure 5 - Change of Marshall stability according to the change in HL and AC

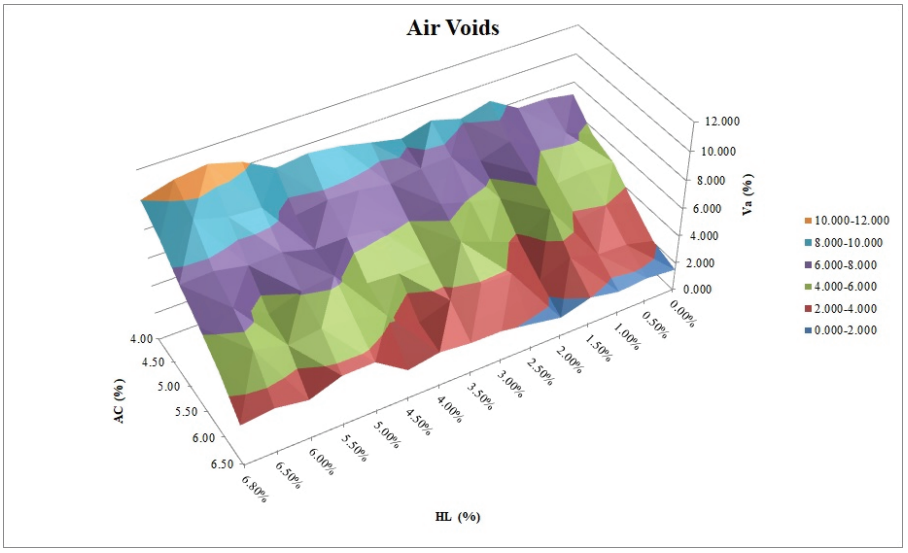

Figure 6 - Change of air voids according to the change in HL and AC

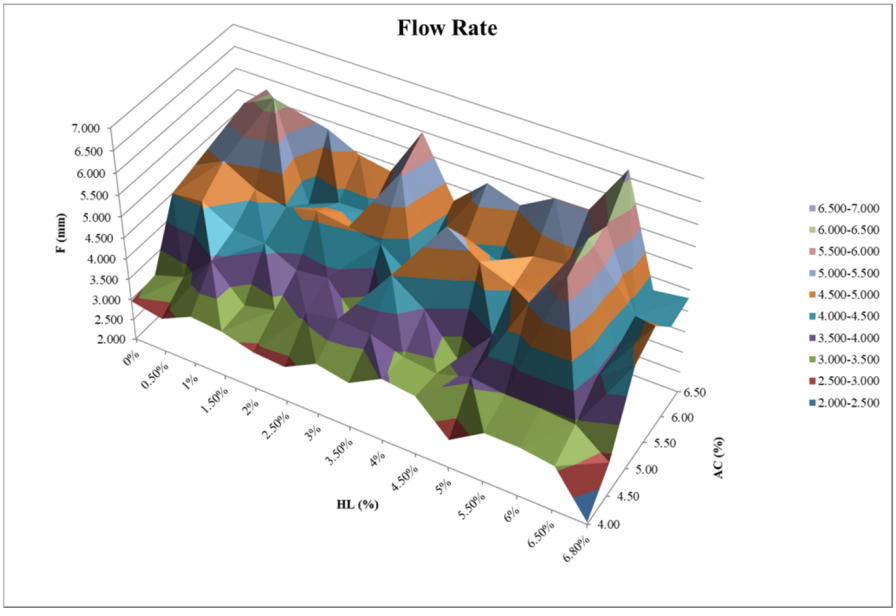

Figure 7 - Change of flow rate according to the change in HL and AC

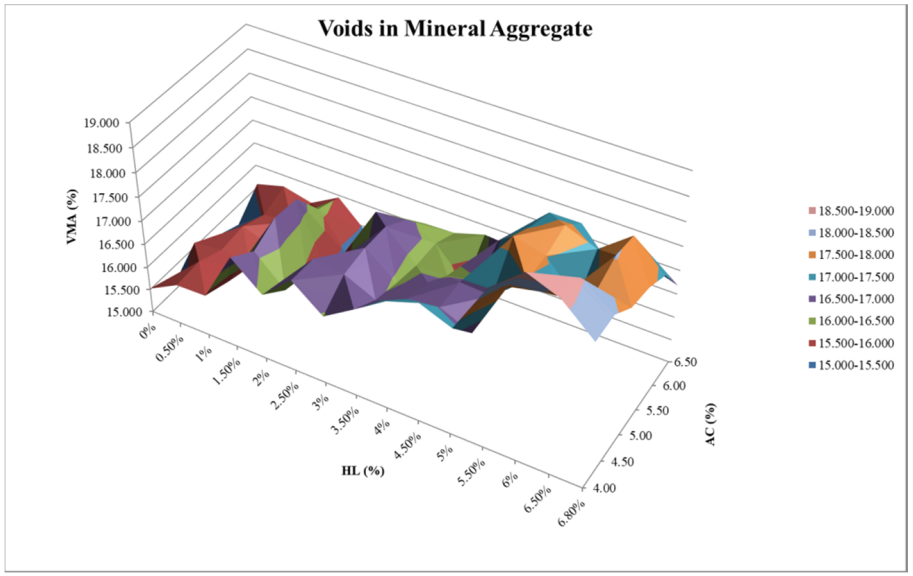

Figure 8 - Change of voids in mineral aggregate according to the change in HL and AC

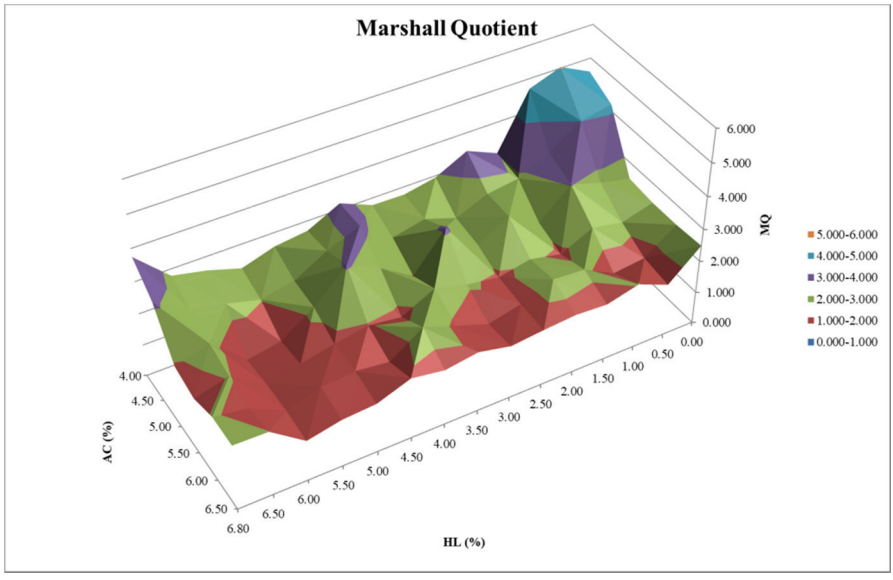

Figure 9 - Change of Marshall quotient according to the change in HL and AC

(c) Defuzzification: Each input and output value activates one or more of the rules of the rule base. Various membership function graphics are obtained by the superposition of the activated output functions. In the defuzzification process, a single value is extracted from the graphics obtained. A number of methods can be used in defuzzification. In this study, the center of gravity method was preferred due to its simplicity. In this method, the abscissa of the center of gravity of the obtained figure is taken as the output value. [58] defines this value as:

$$\bar{x}_0(A) = \frac{\int_a^c x\mu_A(x)dx}{\int_a^c \mu_A(x)dx} \tag{2}$$

Here, $\bar{x}_0(A)$ represents the projection of the figure on the horizontal axis, a and c represent the abscissa of the start and end points of the figure, respectively and μ_A represents the membership function of A.

(d) Calibration: In this study, a GA optimizes the rule base as well as the membership functions, avoiding the risk of using incorrectly defined rules.

Each chromosome that represents the individuals of the GA is comprised of 36 genes as seen in Figure 10. Genes 1-9, 10-18 and 19-27 are values that represent the critical points of the fuzzy sets of the AC, HL and output parameter, respectively. The first 3 critical points represent the "low", the second 3 represent the "medium" and the last 3 represent the "high" for the start, peak and end points of the set of each parameter. Genes 28-36 represent the 9 rules located in the rule base and take the values of 1, 2 or 3 representing "low", "medium" and "high", respectively.

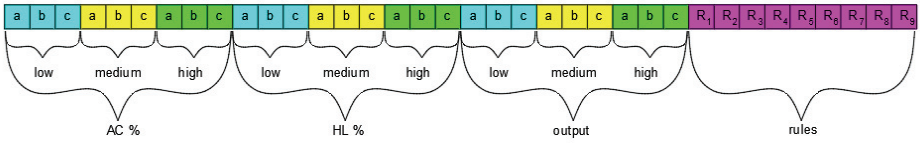

Figure 10 - Chromosome model used in the genetic algorithm

Each generation of the GA is comprised of 200 individuals. Root mean square error (RMSE) between the experiment results and the FL is used as the fitness function:

$$RMSE = \sqrt{\frac{1}{n}\sum_{i=1}^{n}(y_i - o_i)^2} \tag{3}$$

Here, n represents the number of data (individuals), y_i represents the experiment result and o_i represents the outputs of the FL model. Selection of individuals is made by the fitness proportionate selection method. In order to use fitness proportionate selection, solutions having a lower RMSE value should provide a higher fitness value. For this

reason, the fitness value of each chromosome is updated by subtracting it from the highest fitness value of the relevant generation. Afterwards, cumulative fitness values are obtained by adding the fitness value of every previous individual onto the value of the current one. The cumulative fitness values are scaled between 0 and 1 by dividing each cumulative fitness value by the sum of all fitness values. Afterwards, the algorithm generates a random value between 0 and 1 and the first individual that has a greater cumulative fitness value than the random value generated is selected as a parent individual. The selection process is completed after selecting 198 parent individuals. Any individual can be selected more than once in this method.

Once the selection phase is completed, cross-over is applied to each parent individual with the probability of P(C) = 1. This means that each parent mates and crosses over with another (or sometimes the same) individual. In the cross-over process, each mating parent individual is cut from a random point and the values at the right hand side of the cutting point is swapped. Thus, two new individuals are formed. In order not to produce individuals having infeasible solutions, the condition a<b<c is checked, each representing the start, peak and end points of the triangular membership function as seen in Figure 2. If this condition is not fulfilled, b is changed randomly between the values of a and c.

Mutation is applied on each gene of the 198 new individuals with the probability of P(M) = 0.001 upon completion of the cross-over phase. If the random value between 0 and 1, generated for each gene by the algorithm, is smaller than 0.001, then the value of the gene is changed randomly. The a<b<c condition is checked again if the mutation is applied. Afterwards, the 2 best individuals of the previous generation, which have the best fitness values, are copied into the relevant generation in an elitist way to complete a step of the GA. The aforementioned steps are repeated 1000 times before termination of the algorithm.

Upon termination of the GA, a local search method that looks for better solutions (individuals) around the best solution obtained, is applied. In this method, the value of each gene of the best individual is changed with small margins to check whether the fitness function provides a better solution or not. If a lower RMSE value is obtained, the search continues, or else the value of the next gene is changed. If none of the 36 genes provides a better solution, the local search is finalized.

The performance of the GA is affected by the initial values that are generated randomly, as well as the selected parameters. For this reason, each GA developed was run 10 times and the best values obtained were used as the triangular membership functions and rule base of the FL model. Flowchart of the FL model is given in Figure 11.

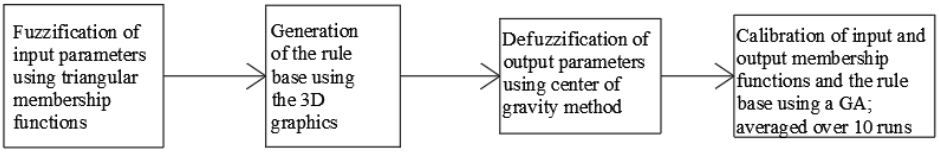

Figure 11 - Flowchart of the fuzzy logic model

5. ANN MODEL

Contrary to FL models, ANN is a single network structure, using AC and HL values as input parameters to estimate Dp, VMA, MS, Va, F, VMA and MQ. The number of hidden layers and the number of neurons in each hidden layer were determined using the trial-error method. The best network performance was obtained using 20 neurons in a single hidden layer. The ANN model used is shown in Figure 12. In order to increase the performance of the ANN model, all input and output parameters were scaled between 0.1 and 0.9 as seen in Eq. 4.

$$x_n = \frac{(x_n - x_{min}) * 0.8}{(x_{max} - x_{min})} + 0.1 \quad (4)$$

Here, x_n represents the input or output value to be scaled, and x_{min} and x_{max} represent the minimum and the maximum values of this parameter in the data set, respectively. Sigmoid function (Eq. 5) is used as the activation function of both the hidden and the output layers. Thus, the output layer of each neuron was scaled between 0 and 1.

$$F(x) = \frac{1}{1+e^{-x}} \quad (5)$$

Of the data with 90 varying AC from the Marshall design with 15 different HL content, 70% were randomly assigned to the training set, 15% to the validation set and 15% to the test set. Gradient descent with momentum method was used in the training of the ANN model developed. Since the ANN model contains 7 different output parameters, the sum of the RMSE of each parameter was selected as the function to be minimized. In this way, all output parameters were optimized simultaneously. The flowchart of the ANN model is given in Figure 13.

The performance of both the FL and ANN models was also tested using the test results of 45 samples having optimum AC. Both FL and ANN models were developed using MATLAB R2017b ® software and Fuzzy Logic and Neural Network toolboxes.

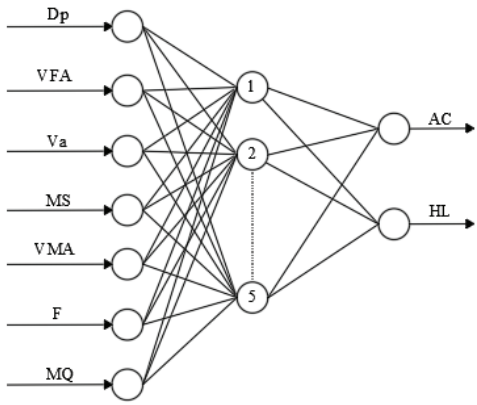

Figure 12 - Proposed ANN model

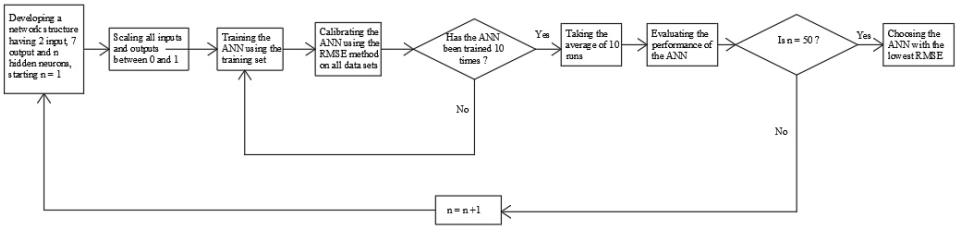

Figure 13 - Flowchart of the ANN model

6. RESULTS AND DISCUSSIONS

In this study, the change of hot mix asphalt properties obtained by the addition of HL into the mixture in a wide and precise range was investigated. In this context, 15 Marshall designs were prepared with HL content varying between 0.5% and 6.8% including a sample without any HL additive. In addition to the 270 samples in these designs, 45 control product samples were produced. Marshall test results, performed within the scope of the study, showed that the change of HL and AC content in the mixtures affects the Marshall design parameters. These effects can be summarized as follows:

When the relation between AC-HL ratios and Dp or VFA is examined, Dp and VFA decrease as the HL ratio increases and Dp and VFA increase as the AC ratio increases. In other words, while the ratio of HL is high and the rate of AC is low, Dp and VFA are low and vice versa.

The specific gravity of the HL is lower than that of the mineral filler, thus reducing the specific gravity of the total filler (Mineral filler + HL) in the mixture and also the practical specific gravity of the mixture (Table 4, Figure 14). Thus, as the amount of HL increases, the mixture gains a structure with more voids (Table 4, Figure 15). Although the aggregate mixture in the study is dense, in other words well-graded, this condition continues to be observed due to the low density of the HL.

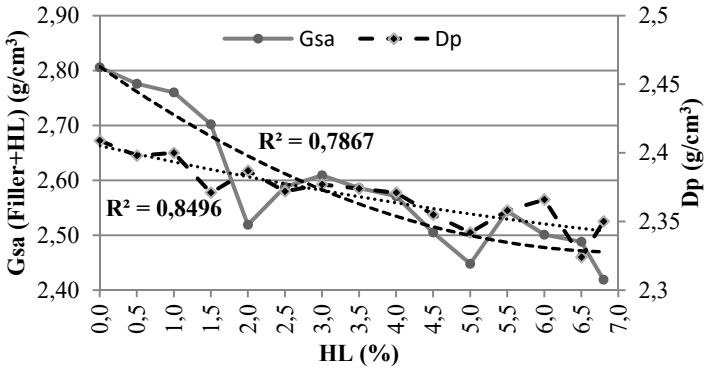

Figure 14 - Reduction effect of HL on specific gravity of filler mix and Dp

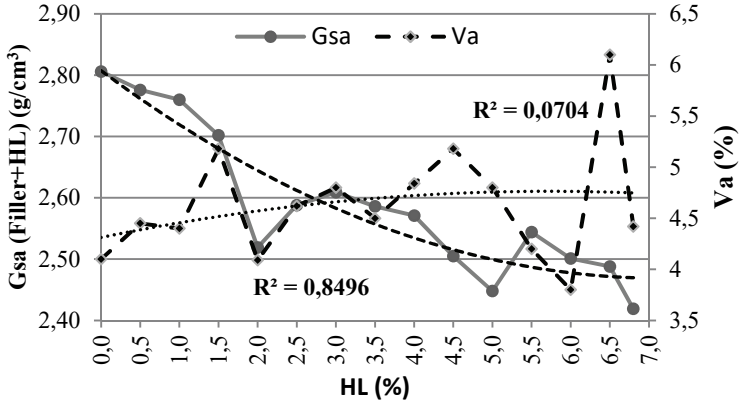

Figure 15 - Effect of HL on air voids and specific gravity of filler mix

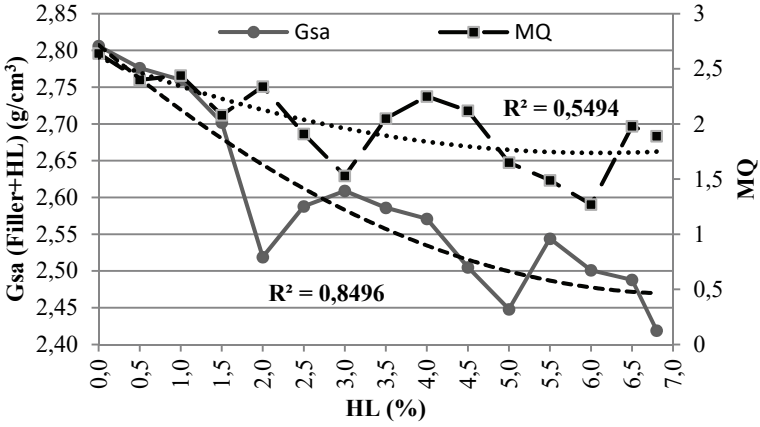

Figure 16 - Effect of HL on MQ and specific gravity of filler mix

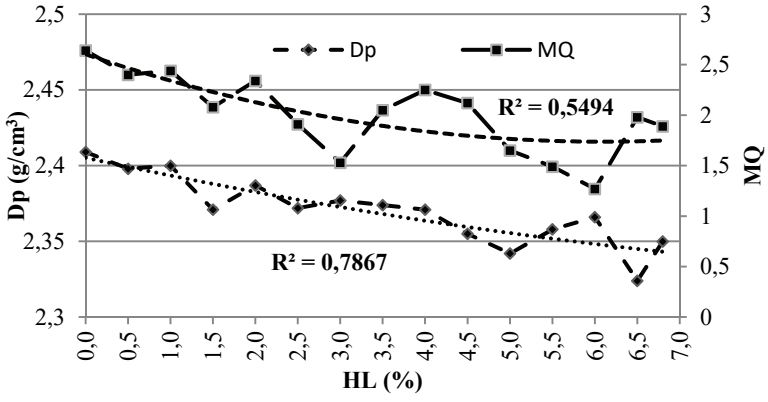

Figure 17 - Effect of HL on MQ and practical specific weight of specimen

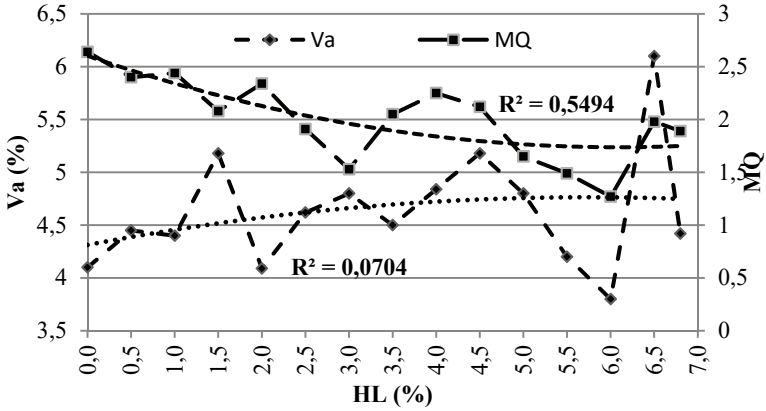

Figure 18 - Effect of HL on MQ and air voids

As is well-known, MQ is used as a measure of the rigidity of the mixture and its resistance to deformation. MQ helps to evaluate the deformation strength of the asphalt specimens produced and shows the fractural strengths of the mixtures during displacement. In this respect, it can be said that mixtures with higher MQ cause less displacement at the time of fracture. When the HL ratio increases in the mixtures, Gsa and Dp are reduced. In parallel, MQ also has a tendency to decrease in this context (Table 4, Figure 17). Similarly, in parallel with the increase in HL ratio, the decrease in MQ is observed when the air voids in the mixtures increase (Table 4, Figure 18).

When the relationship between AC-HL ratio and Va or VMA is examined, Va and VMA increase as the ratio of HL increases, and Va and VMA decrease as the AC ratio increases. That is, while the HL ratio is high and the AC ratio is low, Va and VMA are high and vice versa. When the HL is almost the same size as the mineral filler material and is a material with a high void ratio, then as the amount of HL in the mixture increases, the aggregate gradation is also affected and the total amount of voids increases. This increase causes a decrease in the MQ.

The HL ratio in the mixture can be evaluated differently from the other parameters for MS and F. The highest MS values were obtained in the mixture where HL was used at 1%. The increase in AC ratio decreases the MS value.

Testing of the results found by conventional methods using the models established with the help of soft computation methods guides the decisions in systematic control of the obtained data. This contributes to making the decision making processes more reliable and faster. Findings of the model comparisons obtained within the scope of the study can be summarized as follows:

In order to measure and compare the performances of the developed models, the determination coefficient (R^2), mean, and minimum and maximum error values were calculated for the model and test results. Table 6 shows the comparison between each model developed with the test results for 90 samples having various bitumen contents. Table 7 shows comparison of the results of each model developed with the test results for 15 samples having optimum bitumen content.

Table 6 - Performance values of models for 90 samples having various bitumen contents

Parameter	Performance criteria	Mathematical Model	FL	ANN
Dp	**R^2**	**0.9650**	0.8842	0.9435
	Mean Error (%)	**0.2563**	0.4700	0.3168
	Maximum Error (%)	**0.8515**	1.3709	1.2787
	Minimum Error (%)	0.0053	**0.0027**	0.0079
VFA	**R^2**	**0.9945**	0.9401	0.9799
	Mean Error (%)	**1.0369**	4.3433	2.0885
	Maximum Error (%)	**6.1400**	14.3738	8.5664
	Minimum Error (%)	**0.0058**	0.0309	0.0480
MS	**R^2**	**0.9345**	0.6611	0.7533
	Mean Error (%)	**3.0333**	7.3677	6.2303
	Maximum Error (%)	**26.1047**	26.3525	27.7899
	Minimum Error (%)	**0.0005**	0.1015	0.0850
Va	**R^2**	**0.9914**	0.8837	0.9699
	Mean Error (%)	**3.1172**	17.9592	7.5526
	Maximum Error (%)	**18.2326**	122.8118	46.8119
	Minimum Error (%)	**0.0098**	0.1519	0.0389
F	**R^2**	**0.7607**	0.6297	0.7121
	Mean Error (%)	**7.6361**	10.0912	8.7926
	Maximum Error (%)	88.7000	41.7493	**37.8947**
	Minimum Error (%)	0.1232	0.3837	**0.0147**
VMA	**R^2**	**0.9226**	0.8519	0.8205
	Mean Error (%)	**1.1078**	1.6149	1.7953
	Maximum Error (%)	**4.7083**	5.5784	8.8705
	Minimum Error (%)	**0.0000**	0.0002	0.0031
MQ	**R^2**	**0.8845**	0.6694	0.8534
	Mean Error (%)	**7.3088**	13.7737	9.8347
	Maximum Error (%)	45.3700	63.4532	**32.6505**
	Minimum Error (%)	**0.0518**	0.1131	0.0565

Table 7 - Performance values of models for 15 samples having optimum bitumen content

Parameter	Performance criteria	Mathematical Model	FL	ANN
Dp	**R^2**	0.6063	0.6198	**0.8162**
	Mean Error (%)	0.6281	0.6273	**0.2500**
	Maximum Error (%)	1.4799	1.9223	**0.6804**
	Minimum Error (%)	0.0845	0.0387	**0.0047**
VFA	**R^2**	0.6832	0.7175	**0.8545**
	Mean Error (%)	3.7188	5.0791	**1.6780**
	Maximum Error (%)	9.4724	11.2696	**4.8664**
	Minimum Error (%)	0.6364	0.8322	**0.1908**
MS	**R^2**	0.4855	0.2590	**0.6292**
	Mean Error (%)	7.1947	7.0599	**5.8861**
	Maximum Error (%)	30.4837	**18.9283**	20.2716
	Minimum Error (%)	0.0000	0.3913	**0.0036**
Va	**R^2**	0.4642	0.2519	**0.7688**
	Mean Error (%)	11.3209	14.8203	**5.2815**
	Maximum Error (%)	23.8579	35.9588	**17.3608**
	Minimum Error (%)	1.3333	3.0521	**0.0173**
F	**R^2**	0.0001	0.0324	**0.5499**
	Mean Error (%)	16.3220	14.8838	**7.6077**
	Maximum Error (%)	56.7358	33.0518	**18.2677**
	Minimum Error (%)	1.8692	1.8841	**0.7264**
VMA	**R^2**	0.6465	0.5000	**0.7164**
	Mean Error (%)	3.2171	3.0526	**1.4261**
	Maximum Error (%)	7.4559	6.9994	**4.6335**
	Minimum Error (%)	0.5335	0.6796	**0.0101**
MQ	**R^2**	0.0308	0.0260	**0.2753**
	Mean Error (%)	16.7765	11.8207	**9.7571**
	Maximum Error (%)	52.3910	27.5497	**25.1477**
	Minimum Error (%)	0.5990	0.7054	**0.2724**

According to Table 6, it is seen that ANN provides better results in estimating the Marshall design parameters than the FL and ANN models. This is an expected outcome since the mathematical model was developed to give the best result for the provided samples. According to Table 7, the performance of the mathematical model is the lowest compared to the FL and ANN models in terms of R^2 and error values. This shows that the mathematical model performs well only for its own data set and is not suitable for generalization. It can be seen that the FL model, like the mathematical model, is not very successful in predicting the values of the samples having optimum bitumen content. The generalization performance of the ANN model is the best amongst the three models developed.

The low generalization performance of the mathematical model indicates that the superstructure designs made using this calculation method cannot show the expected performance and may encounter different types of deformations before the end of their desired service life. The FL model also fails to provide satisfactory performance in estimating the Marshall design parameters. The main reason for this low performance may be that the developed model is kept as simple as possible. For example, expressing each input and output value with more than 3 classes could significantly increase the model performance.

However, the identification of too many classes will cause the model to become unnecessarily complicated and may reduce the ability to generalize. It is seen that the ANN model can estimate the Dp, VFA and Va of the samples more accurately than the remaining parameters. Nevertheless, the overall performance of the ANN model is lower when compared with similar studies [40, 43, 44, 47, 59] in the literature. In this study, for the MS values of 90 samples with AC and 15 samples with optimum AC, the correlation coefficients between the test results and ANN model results were 0.7533 and 0.6292, respectively, while [40] obtained these results as 0.969 and 0.933. In [44], the coefficients of correlation between the test results of polypropylene-modified Marshall samples and the ANN model were 0.97, 0.81 and 0.87 for MS, F and MQ, respectively; in this study, the coefficients for 90 samples were 0.7533, 0.7121 and 0.8534 and for the 15 samples were 0.6292, 0.5499 and 0.2753, respectively. The test data were obtained from the re-creep test results applied on the polypropylene modified Marshall samples in [43]; on the SBS modified bitumen in [47]; and from the test results of permanent deformations on asphalt-concrete mixtures modified with nano additives in [59]. All 3 studies obtained high correlation coefficients ($R^2 > 0.90$) between the test and ANN model results. In this study, such high coefficients were obtained only for the Dp, VFA and Va values of the 90 samples with different AC.

Between the two different models developed within the scope of the study, the ANN model provides better results. However, the R^2 values obtained with the estimations made by this model gave lower predictive values for some parameters (MS, F) while providing better estimates for the remaining parameters compared to [60] on the estimation of the Marshall parameters of bituminous mixtures using artificial intelligence techniques. One of the reasons for this performance is the attempt to estimate seven different parameters using only two input values, AC and HL. There may be different factors that affect each of these seven parameters. Determination of these factors and incorporation of them into the model could lead to much better performance values. Another reason is the possibility of measurement errors in the samples in the laboratory tests. When looking at the data in this light, then for example, a flow rate of 6.52 mm (Table 4) appears to be an extremely high value. When these measurement errors are eliminated, the performance of the models can also increase

significantly. In addition, the presence of only limited samples with the optimum bitumen content is another reason why the performance, especially the R^2 value, is low. Also, more samples having optimum bitumen content for different HL contents can be developed and tested in order to improve the performance of the models. It shall be noted that the prediction performance of the models is valid only for the given data set. As the data set increases with experiments carried out using different materials, the superiority of one model over another may also change.

7. CONCLUSIONS

In this study, the effect of the use of HL as an additive in asphalt mixtures on the Marshall parameters was investigated and it was observed that the use of additive materials changes the properties of the mixture and also depends on the AC ratio. In general, it is possible to say that Dp and VFA values decrease and Va and VMA values increase due to an increase in HL ratio. When the relationship between HL and AC is evaluated, it is possible to say that due to the porous structure of the HL, as its usage rate in the mixtures increases, the AC ratio that has to be used in the mixtures also increase. In addition, the highest MS values from the experimental results were found to be obtained for 1% HL usage rate, also depending on the AC content, and the yield values in the relevant ratio were found to be acceptable.

Estimating the properties of asphalt samples with HL additive by using artificial intelligence methods is a rather simple, fast and inexpensive solution compared to making laboratory tests on each sample. This study shows that a model developed using preliminary test results can be used to estimate the Marshall design parameters such as Dp, VMA, Va, MS, VFA, F and MQ of asphalt samples. Naturally, since the developed models have been calibrated for certain materials, they will work well for mixtures prepared by using the materials obtained from the same source and having the same material properties. If the material properties change, a re-calibration process will be required. Once this calibration is done, the models will be able to produce effective results for every mixture of materials having the same feature. Various specifications indicate the upper and lower limit values for the Marshall design parameters of the asphalt samples. Using advanced artificial intelligence methods, designs with different AC and HL values can be checked as to whether they meet the specified limits or not, without further need for laboratory tests. In addition, the models can be further developed to determine the asphalt mixture having the lowest cost that will meet the required ranges in the specifications.

Symbols

a : Start point of a membership function

b : Midpoint of a membership function

c : Endpoint of a membership function

Dp : Unit weight (practical specific weight) (g/cm^3)

F : Flow rate (mm)

F(x) : Sigmoid activation function

Gsa : Apparent specific gravity of mineral filler and HL mixture (g/cm^3)

MS : Marshall Stability (kN)

MQ : Marshall Quotient (MS/F)

n : Number of values in the data set

o_i : Output values of the FL model

P(C) : Cross-over probability

P(M) : Mutation probability

R : Rules defined in the rule base of the FL model

Va : Air voids (%)

VFA : Void filled with asphalt (%)

VMA : Voids in mineral aggregate (%)

x_{max} : Maximum value of parameter x

x_{min} : Minimum value of parameter x

x_n : Input or output parameter x

$\bar{x}_o$: Projection of the membership function on the horizontal axis

μ_A : Membership function of A

Acknowledgments

The authors would like to thank YTU BAP Coordination Unit for their support for the Research Project with ID 29-05-01-KAP01 and also Isfalt A.Ş. for their support with the experiments.

References

[1] NLA, Hydrated Lime – A Solution for High Performance Hot Mix Asphalt. Retrieved January 8, 2016, from http://www.lime.org/documents/publications/free_downloads/fact-asphalt.pdf

[2] Lesueur, D., Hydrated Lime: a Proven Additive for Durable Asphalt Pavements – Critical Literature Review, European Lime Association (EuLA) Ed., 2010, Brussels, Belgium, 2010.

[3] TSE, Turkish Standard 3720: Bituminous mixtures - Asphalt concrete - Mix design - Marshall method, 2010.

[4] Asphalt Institute, The Asphalt Handbook (MS-4), 7th. ed., Asphalt Institute: Lexington, 2007.

[5] Witczak, M., Bari, J., Development of a master curve (E*) database for lime modified asphaltic mixtures. *Arizona State University Research Report, Tempe (Arizona, USA): Arizona State University*, (July) 2004.

[6] Lesueur, D., Little, D., Effect of Hydrated Lime on Rheology, Fracture, and Aging of Bitumen. *Transportation Research Record: Journal of the Transportation Research Board*, *1661*(-1), 93–105, 1999.

[7] Petersen, J. C., Plancher, H., Harnsberger, P. M., Lime Treatment of Asphalt to Reduce Age Hardening and Improve Flow Properties. *Association of Asphalt Paving Technologists*, *56-87*, 632–653, 1987.

[8] Cross, S., Experimental Cold In-Place Recycling with Hydrated Lime. *Transportation Research Record*, *1684*(1), 186–193, 1999.

[9] Sebaaly, P., Hitti, E., Weitzel, D., Effectiveness of Lime in Hot-Mix Asphalt Pavements. *Transportation Research Record*, *1832*(1), 34–41, 2003.

[10] Lee, S., Seo, Y., Kim, Y. R., Effect of hydrated lime on dynamic modulus of asphalt-aggregate mixtures in the state of North Carolina. *KSCE Journal of Civil Engineering*, *14*(6), 829–837, 2010.

[11] Niazi, Y., Jalili, M., Effect of Portland cement and lime additives on properties of cold in-place recycled mixtures with asphalt emulsion. *Construction and Building Materials*, *23*(3), 1338–1343, 2009.

[12] Rogge, D. F., Leahy, R. B., Blair, R., Cold-In-Place (CIP) Recycling with Lime. *Transportation Research Report,* 95-17, 1995.

[13] Al-Suhaibani, A. R., Al-Mudaiheem, J., Al-Fozan, F., Effect of Filler Type and Content on Properties of Asphalt Concrete Mixes. In *Effects of Aggregates and Mineral Fillers on Asphalt Mixtures Performance*, 107–130, 1992.

[14] Niazi, Y., Jalili, M., Effect of Portland cement and lime additives on properties of cold in-place recycled mixtures with asphalt emulsion. *In Construction and Building Materials* 23(3):1338-1343, 2009.

[15] Lesueur, D., Little, D., Hydrated Lime as an Active Filler in Bitumen. Paper Presented at the Annual Meeting of the TRB, Washington, D.C., January 1999.

[16] Mohammad, L., Abadie, C., Gokmen, R., Puppala, A., Mechanistic Evaluation of Hydrated Lime in Hot-Mix Asphalt Mixtures. *Transportation Research Record*, *1723*(1), 26–36, 2000.

[17] Kennedy, T. W., Ping, W. V., An Evaluation Of Effectiveness Of Antistripping Additives In Protecting Asphalt Mixtures From Moisture Damage (With Discussion) (pp. 230–263). Washington: Association of Asphalt Paving Technologists, 1991.

[18] Si, Z., Little, D. N., Asce, F., Lytton, R. L. (2002). Effects of Inorganic and Polymer Filler on Tertiary Damage Development in Asphalt Mixtures, (April), 164–172.

[19] Huang, S.-C., Claine Petersen, J., Robertson, R., Branthaver, J., Effect of Hydrated Lime on Long-Term Oxidative Aging Characteristics of Asphalt. *Transportation Research Record*, *1810*(307), 17–24, 2002.

[20] Radenberg, M., Effect of Hydrated Lime Addition on the Deformation of Hot Mix Asphalt in the Wheel Tracking Test. In *Lhoist HMA Symposium*. Düsseldorf, 1998.

[21] Rogge, D. F., Leahy, R. B. and Blair, R., Cold In-Place (CIP) Recycling with Lime. Transportation Research Instit., OR State Univ, Corvallis, OR, July 1995.

[22] Şengül, C. E., Asfalt Kaplamalarda Tekerlek İzinde Oturma ve Su Hasarı Problemlerinin Azaltılması İçin Sönmüş Kireç Kullanımı. Karadeniz Technical University, 2006.

[23] Verhasselt, A. F., Choquet, F. S., Comparing Field And Laboratory Aging Of Bitumens On A Kinetic Basis. *Transportation Research Record*, 30–38, 1993.

[24] Hicks, R. G., *Moisture Damage in Asphalt Concrete*. Washington: NCHRP Transportation Research Board, 1991.

[25] Kennedy, T. W., Ping, W. V., Evaluation of Effectiveness of Antistripping Additives in Protecting Asphalt Mixtures from Moisture Damage. Journal of the Association of Asphalt Paving Technologists, from the Proceedings of Technical Sessions, Vol. 60, March 1991.

[26] Little, D. N., Epps, J. A., *The Benefits of Hydrated Lime in Hot Mix Asphalt*. Arlington, 2001.

[27] Petersen, J.C., Plancher, H., and Harnsberger, P.M., *Lime Treatment of Asphalt to Reduce Age Hardening and Improve Flow Properties*. AAPT, Volume 56, 1987.

[28] Sebaaly, P.E., Tohme, P., Hitti, E., Stansburry, K., Epps, J., *Asphalt Concrete Antistripping Techniques*, Pierre, 2003.

[29] Rogge, D. F., Leahy, R. B. and Blair, R., Cold In-Place (CIP) Recycling with Lime, Transportation Research Instit., OR State Univ, Corvallis, OR, July 1995.

[30] Jones, G. M., *The Effect of Hydrated Lime on Asphalt in Bituminous Pavements*. NLA Meeting, Utah DOT, May 22, 1997.

[31] Kim, Y. R., Little, D. N., Song, I., Effect of Mineral Fillers on Fatigue Resistance and Fundamental Material Characteristics. *Transportation Research Record*, (1832), 1–8, 2003.

[32] Recasens, R. M., Martinez, A., Jimenez, F. P., Bianchetto, H., Effect of Filler on the Aging Potential of Asphalt Mixtures. *Transportation Research Board*, (1901), 10–17, 2005.

[33] Cheng, D. X., Little, D. N., Lytton, R. L., Holste, J. C., Moisture Damage Evaluation of Asphalt Mixture by Considering Both Moisture Diffusion and Repeated Load Conditions. *Transportation Research Board*, (1832), 42–49, 2003.

[34] Hicks, R. G., Todd, V. S., Life Cycle Costs for Lime in Hot Mix Asphalt, 2001. Retrieved January 11, 2016, from https://lime.org/documents/publications/free_downloads/lcca_vol-2.pdf

[35] Yardım, M. S., Balcı, U., The Effect of Hydrated Lime on the Marshall Stability for a Specific Amount of Asphalt Content in the Hot Mix Asphalt, Proceedings of the 9th International Fracture Conference, 9th International Fracture Conference, pp. 571-580. Yıldız Technical University, Istanbul, 2011.

[36] Tigdemir, M., Karasahin, M., Sen, Z., Investigation of fatigue behaviour of asphalt concrete pavements with fuzzy-logic approach. *International Journal of Fatigue*, *24*(8), 903–910, 2002.

[37] Saltan, M., Saltan, S., Şahiner, A., Fuzzy logic modeling of deflection behavior against dynamic loading in flexible pavements. *Construction and Building Materials*, *21*(7), 1406–1414, 2007.

[38] Saltan, M. Sezgin, H., Hybrid neural network and finite element modeling of sub-base layer material properties in flexible pavements. *Materials and Design, 28*, 1725–1730, 2007.

[39] Ozsahin, T.H., Oruc, S., Neural network model for resilient modulus of emulsified asphalt mixtures. *Construction and Building Materials, 22*, 1436–1445, 2008.

[40] Ozgan, E., Artificial neural network based modelling of the Marshall Stability of asphalt concrete. *Expert Systems with Applications*, *38*(5), 6025–6030, 2011.

[41] Xiao, F., Amirkhanian, S. N., Juang, C. H., Hu, S., Shen, J., Model developments of long-term aged asphalt binders. *Construction and Building Materials*, *37*, 248–256, 2012.

[42] Mirzahosseini, M. R., Aghaeifar, A., Alavi, A. H., Gandomi, A. H., Seyednour, R., Permanent deformation analysis of asphalt mixtures using soft computing techniques. *Expert Systems with Applications*, *38*(5), 6081–6100, 2011.

[43] Tapkin, S., Çevik, A., Uşar, Ü., Accumulated strain prediction of polypropylene modified marshall specimens in repeated creep test using artificial neural networks. *Expert Systems with Applications*, *36*, 11186-11197, 2009.

[44] Tapkin, S., Çevik, A., Uşar, Ü., Prediction of Marshall test results for polypropylene modified dense bituminous mixtures using neural networks. *Expert Systems with Applications*, *37*, 4660–4670, 2010.

[45] Xiao, F., Amirkhanian, S. N., Artificial Neural Network Approach to Estimating Stiffness Behavior of Rubberized Asphalt Concrete Containing Reclaimed Asphalt Pavement. *Journal of Transportation Engineering*, *135*(8), 580–589, 2009.

[46] Kok, B.V., Yilmaz, M., Sengoz, B., Sengur, A., Avci, E., Investigation of complex modulus of base and SBS modified bitumen with artificial neural networks. *Expert Systems with Applications, 37,* 7775–7780, 2010.

[47] Kok, B.V., Yilmaz, M., Cakiroglu, M., Kuloglu, N. Sengur, A., Neural network modeling of SBS modified bitumen produced with different methods*. Fuel, 106,* 265–270, 2013.

[48] Cevik, A., Cabalar, A.F., Modelling damping ratio and shear modulus of sand–mica mixtures using genetic programming. *Expert Systems with Applications, 36*, 7749–7757, 2009.

[49] Aksoy, A., Iskender, E., Kahraman, H.T., Application of the intuitive k-NN Estimator for prediction of the Marshall Test (ASTM D1559) results for asphalt mixtures. *Construction and Building Materials, 34,* 561–569, 2012.

[50] Moghaddam, T.B., Shamshirband, S., Soltani, M., Petkovic, D., Karim, M.R. Baaj, H., Estimation of the rutting performance of Polyethylene Terephthalate modified asphalt mixtures by adaptive neuro-fuzzy methodology. *Construction and Building Materials, 96,* 550–555, 2015.

[51] Pourtahmasb, M. S., Karim, M.R. Shamshirband, S. Resilient modulus prediction of asphalt mixtures containing Recycled Concrete Aggregate using an adaptive neuro-fuzzy methodology. *Construction and Building Materials, 82*, 257–263, 2015.

[52] Kavak, A., Lime Stabilization in Turkey. In *The Seminar of Lime in Asphalt*. İstanbul: İsfalt, 2011.

[53] Denayer, C., Lime Stabilization. In *The Seminar of Lime in Asphalt*. İstanbul: İsfalt, 2011.

[54] Highway Technical Specifications, General Directorate of Highways, Item No. 170/2, Ankara, Turkey, 2006.

[55] ASTM D 6927-15, Standard Test Method for Marshall Stability and Flow of Bituminous Mixtures, 1–7, 2010.

[56] KGM, *Karayolu Teknik Şartnamesi*. Ankara: Karayolları Genel Müdürlüğü, 2006.

[57] Yardım, M. S., Gürsoy, M, Balcı, U., The Effect of Hydrated Lime Content Amount on Low Temperature Cracking Strength of Flexible Pavements for Various Temperature Values (in Turkish), YTÜ BAP Research Project, No. 29-05-01-KAP01, İstanbul, 2014.

[58] Wang, W.J., Luoh, L., Simple Computation of the Defuzzifications of Center of Sum and Center of Gravity," Journal of Intelligent and Fuzzy Systems (9) 1-2, pp. 53-59, 2000.

[59] Shafabakhsh, G.H., Jafari Ani, O., Talebsafa, M., Artificial neural network modeling (ANN) for predicting rutting performance of nano-modified hot-mix asphalt mixtures containing steel slag aggregates. Construction and Building Materials, 85, 136-143, 2015.

[60] Khuntia, S., Das, A.K., Mohanty M., Panda, M., Prediction of Marshall Parameters of Modified Bituminous Mixtures Using Artificial Intelligence Techniques. *International Journal of Transportation Science and Technology,* 3, 211-228, 2014.

Teknik Dergi, 2019 9561-9580, Paper 556

Time-Cost Trade-Off Optimization with a New Initial Population Approach

Vedat TOĞAN[1]
Mohammad Azim EIRGASH[2]

ABSTRACT

Completion of a project on time is crucial for its stakeholders when the competitive environment in all industries is considered. This favorable target is achieved by finding the optimal set of time-cost alternatives, which is known as time-cost trade-off problem (TCTP) in the literature. In this study, a new initial population approach is presented to improve the quality of the optimal set of time-cost alternatives. It employs a predefined number of solutions to the single objective TCTP into the initial population of teaching learning-based algorithm, which is an optimizer for the multi-objective optimization of TCTP. Hence, it is aimed at descending randomness on the initial population and decreasing searching effort to catch the optimal set of time-cost alternatives in the search space. The proposed methodology is tested on a series of benchmark problems and the solutions obtained are compared with those available in the technical literature. Results show that the present method can produce favorable solutions as effective as other techniques applied for simultaneous optimization of TCTPs.

Keywords: Construction project, **t**ime-cost trade-off problem, multi-objective optimization, metaheuristic algorithm.

1. INTRODUCTION

From the construction management point of view, both the client and the contractor look for the best economical scheduling subject to different parameters such as time, cost and other operational resources in a construction project. Each activity in a construction project has a normal duration and a crashed duration. Completing an activity in its forced (crashed) duration involves more direct cost and resources. On the other hand, it leads to decrease project's total duration and indirect costs (i.e. site utilities, supervisors, head-office expenses and so on). The balancing between time and cost of a project is known as the time cost trade-

Note:
- This paper has been received on March 29, 2018 and accepted for publication by the Editorial Board on December 24, 2018.
- Discussions on this paper will be accepted by January 31, 2020.

• https://dx.doi.org/10.18400/tekderg.410934

1 Karadeniz Technical University, Department of Civil Engineering, Trabzon, Turkey - togan@ktu.edu.tr https://orcid.org/0000-0001-8734-6300

2 Karadeniz Technical University, Department of Civil Engineering, Trabzon, Turkey - azim.eirgash@gmail.com - https://orcid.org/0000-0001-5399-115X

off problem (TCTP) in the literature and solving of this problem requires application of an optimization method.

The first optimization methods employed to solve TCTPs are based on mathematical solutions including the linear programming, the integer programming and the dynamic programming methods [1-5]. These were employed on relatively small test cases. On the other hand, they assume continuous relations between the all design variables of the evaluated problem. However, in practice, the execution of an activity needs operational resources such as time, cost, workmanship etc. having several options, which are discrete. Due to this feature, optimization methods based on the mathematical theory are not appropriate for problems having discrete time-cost relationships [6]. Besides, the integer programming and the dynamic programming require numerous computational efforts for solving more complex project networks or for solving projects with many different activities.

Other common methods for the solution of TCTPs are based on the heuristic algorithms [7, 8]. They apply simple rules unlike the exact algorithms as in the mathematics-based (theory based) methods. Owing to this necessity, the heuristic algorithms can be used easily for the complex problem with less effort. However, globality of the obtained solution is always questionable since they generally find the local-global solutions or the near-global ones for these algorithms. Nevertheless, the metaheuristic algorithms based on natural events were introduced as the last alternative for solving TCTPs in order to overcome the shortcomings of first two methods aforementioned.

In recent decades, various modern metaheuristic optimization methods including genetic algorithms [6, 9, 10], simulated annealing [10, 11], particle swarm optimization [10, 12-15], ant colony optimization [16-19], and shuffled frog leaping optimization [20] have been applied for solving TCTPs. In addition to these methods, differential evolution algorithm [21], Electimize algorithm [22] and Branch and Bound algorithm [23] were also utilized for optimizing the TCTPs. These algorithms numerically represent the natural events. Since the meta-heuristic algorithms improve the quality of the obtained solution iteratively, they might not stick to the local optimum due to their stochastic natures. This latter feature improves the detection chance of global optimum solution searched by the metaheuristic algorithms. As mentioned above, the algorithms into this type of optimization methods simulate the evolutionary computation and swarm intelligence. They are very useful solvers for problems that the global solutions are very difficult to obtain, as they find the near-optimal solutions instead of global ones.

To take advantage of some prominent features of each metaheuristic algorithm, some of them were hybridized to enhance the computational effort required to reach the optimal solution of the problem, and also to improve the optimality of those solutions [10, 14, 15]. All metaheuristics addressed above are the population-based algorithms, except simulated annealing. To start the iterative process of the algorithm, they need a set of possible solutions, which are randomly generated within the problem boundaries. These solutions are collected in a matrix known as the initial population. Then, they are improved through the executed subsequent iterations until reaching the predefined termination criteria. Therefore, the candidate solutions in the initial population affect the performance of the utilized optimization algorithms. Based on this observation, Aminbakhsh [14] developed a new initial population formation phase for particle swarm optimization (PSO). A certain portion of the initial population was produced by means of Siemens algorithm, and fed into the model to

accelerate the searching process. Some changes were made to the original Siemens method, which is suitable for continuous problems to solve the discrete TCTPs.

In this study, a new initial population approach is proposed to enhance the convergence capability and performance of the teaching learning-based optimization (TLBO) used for the multi-objective optimization of TCTPs. The proposed approach combines the certain solutions obtained from implementing the minimum of the minimum (min-min) approach with the remaining solutions being generated randomly to compose the initial population. The min-min approach is an optimization algorithm utilized to find the acceptable solutions for the simple single objective version of TCTP. Either minimization of the project duration or the cost can be adopted as the objective function for the optimization of TCTPs having the single objective. However, for a given project cost, a single project duration can be identified in the solution space of TCTP, whereas there might be plenty of project cost values for the certain project duration. This conclusion can be observed easily from the reported results in the technical literature related to the optimization of TCTPs and also from the investigation of the solution space of the handled TCTP. Therefore, in the present study, project cost is considered as the single objective function in the optimization of TCTP by the min-min approach.

The rest of the study is organized as follows: Firstly, basic formulations for the TCTP optimization is presented and then the proposed initial population approach is detailed along with characteristics of the multi-objective teaching learning-based algorithm (MTLBO) to solve the TCTPs for construction projects. MTLBO is also integrated with the non-dominating sorting approach (NS) in order to evaluate the fitness of the possible solutions. Effect of the partial random initial population in NS-MTLBO model is exhibited by numerical simulations of benchmark TCTPs and conclusions are presented in the last section of the study.

2. TIME-COST TRADE-OFF PROBLEM (TCTP)

TCTP is a bi-objective problem, and is a balanced relationship between time and cost. During planning or in case of a delay, the project manager needs to balance the time and cost of a project to improve the overall efficiency. Therefore, TCTP is adapted to identify the set of time–cost alternatives that will provide the optimal schedule. The time of a project T can be calculated according to the following equation:

$$T = \sum_{i=1}^{k} t_i^k \, x_i^k \tag{1}$$

where k is the number of total activities of a project, t_i^k is the duration of activity i when performing the kth option, x_i^k is index variable of activity i when performing the kth option:

$$x_i^k = \begin{cases} 1 & \text{when activity } i \text{ performs the } k\text{th option} \\ 0 & \text{else} \end{cases} \tag{2}$$

where $\sum_{i=1}^{k} x_i^k = 1$. The project duration T is calculated by using the critical path method depending on the defined activity relationships for that project. The total cost of a project consists of two parts: direct and indirect costs. The first one is determined by the sum of

direct costs of all activities within a project network. The last one depends heavily upon the project duration, i.e., the longer the duration, the higher the indirect cost. The total cost of a project can be calculated by

$$C = \sum_{i=1}^{k} DC_i^k \, x_i^k + t_i ic_i^k \tag{3}$$

where C is the total cost of a project, DC_i^k is the direct cost of activity i when performing the kth option, x_i^k is index variable of activity i when performing the kth option, t_i is the duration of activity i, and ic_i^k is the indirect cost rate of a project.

3. INITIAL POPULATION APPROACH

In the past few decades, many attempts have been made for solving construction optimization problems those utilizing the various modern metaheuristic optimization methods including genetic algorithms, simulated annealing, particle swarm optimization, ant colony optimization, and shuffled frog leaping optimization. Thereby, in this study, a relatively young metaheuristic algorithm called teaching learning-based optimization (TLBO) is applied as an alternative to solving TCTPs.

It is observed that the utilized basic non-dominating sorting multi-objective teaching learning-based optimization (NS-MTLBO) algorithm is not able to achieve the optimum solutions as good as hybridized algorithms for the large scale TCTPs [24]. Therefore, in the present study, to enhance the prediction capacity of NS-MTLBO algorithm, a new approach is proposed to generate the initial population in NS-MTLBO. Apart from the simulated annealing, a set of possible solutions which are randomly generated within the problem boundaries are needed to start the iterative search process for the metaheuristic algorithms. After that, they are enhanced through the executed subsequent iterations until reaching the predefined termination criteria. Based on the numerical simulation process conducted for the solution of the optimization problem, it might be stated that the candidate solutions in the initial population affect the efficiency of the optimization algorithms used. A modified version of the Siemens method is added into the Discrete Particle Swarm Optimization (DPSO) to improve the quality of the initial swarm for improving the optimization results and for accelerating the optimization process [14].

In this study, to improve the quality of the solutions obtained at the end of the optimization process conducted with NS-MTLBO and to accelerate the search carried out within the solution space, a new initial population creation concept is proposed. The main principle behind this concept is based on the separation of the candidate solutions of the initial population as pre-known and randomly generated. A specific number of solutions for the initial population named as pre-known are picked up automatically among those obtained from the solution of optimization problem with single objective by TLBO method. The proposed model takes advantages of the min-min approach which is based on performing the straightforward single objective optimization. The min-min approach is available in the optimization engines placing in some software. For example, MATLAB offers an optimization library including mathematical and metaheuristic algorithms. Use of this library does not requires knowledge of coding in implementing the algorithms proposed. In the min-min approach, all the possible set of solutions are ordered according to the quality of the

objective functions of time and cost within a small computational effort. The aim is to find the solution that gives the least total project cost subjected to the least project duration. The objective functions are either minimization of the project duration or cost. For performing this approach, in the present study, the project cost is initially considered as the objective function. However, there are plenty of solutions in the solution pool, which indicate the same project duration with different cost. The minimum duration for the particular minimum cost is taken as the optimum solution in each iteration and stored in an external archive. This process continues until the stopping criteria is met, and is called min-min approach. Then, the predefined number of solutions are picked up among those that are kept in the external archive, and thus pre-known solutions are defined for the initial population. The remaining possible solutions to be needed to complete the initial population are generated randomly to preserve diversity. The graphical demonstration of the proposed new initial population concept denoted as partial random initial population is illustrated in Fig. 1.

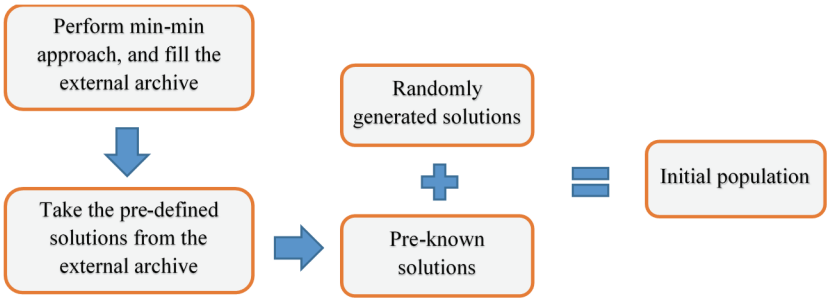

Fig. 1 - Partial random initial population in NDS-MTLBO model

Table 1 - Alternative percentages of pre-known and randomly generated solutions for the initial population

Indices	Percentage of pre-known solutions in the initial population	Percentage of randomly generated solutions in the initial population
O_1	60	40
O_2	40	60
O_3	30	70
O_4	50	50

To determine the proper percentages of pre-known and randomly generated solutions in the initial population, a set of percentage alternatives are defined in Table 1. Each of these alternatives is tested to further verify the effect of partial random initial population on the NS-MTLBO algorithm. For simplicity, an index is identified for each combination considered in Table 1. For example, in the case of the population size being 100, the initial population consist of 60 (100×60%) pre-known solutions and 40 (100×40%) randomly generated solutions, for index of O_1.

4. NON-DOMINATED SORTING TLBO ALGORITHM FOR MULTI-OBJECTIVE OPTIMIZATION

Minimization of time and total cost of the project at the same time requires the implementation of multi-objective optimization, and in contrast to optimization with the single objective, there is no unique global optimum solution for the multi-objective optimization. Instead, a set of solutions known as Pareto optimal is identified at the end of the multi-objective optimization process. Any solution in Pareto optimal is not preferred to another. The multi-objective optimization models developed for the solutions of TCTPs are generally based on the modified adaptive weight approach (MAWA) and non-dominating sorting (NS) approach. However, instead of MAWA approach, NS as a superior approach along with the mechanism of crowding distance computation has been broadly utilized in solving the mentioned TCTP problems, recently.

NS-MTLBO algorithm proposed in the current work comprises remarkable features of NS approach and TLBO algorithm to solve multi-objective optimization problems and to find out a bunch of diverse solutions. NS approach and crowding distance computation mechanism proposed by Deb et al. [25] are responsible for handling the objectives effectively and efficiently in NS-MTLBO model. Besides, the teacher and learner phases of TLBO guarantee the exploration and exploitation of the solution space searched.

The initial population including predefined P number of students is arranged with the non-dominance concept. Application of NS approach assigns a rank value to the solution. The higher rank implies higher superiority in accordance with the non-dominance concept. However, it cannot be said anything about the dominance of the solutions which are in the same rank. To describe the superiority of these solutions, the crowding distance metric is utilized. Ultimately, all solutions are kept up in the external archive.

Teaching learning-based optimization (TLBO)

TLBO algorithm proposed by Rao et al. [26] simulates the teacher and students of a classroom. This algorithm proceeds with two basic phases; (i) teacher phase and (ii) learner phase. In the former phase, the class learns through the teacher. However, in the latter, learning is carried out with interaction among the students in the class. Analogously, all students (learners) represent the population for an optimization algorithm; the subjects taught are considered as the design variables of the optimization problem; the exam result of the learners gives the 'fitness' value for the corresponding subject taught. TLBO has emerged as one of the simple and efficient techniques for solving single-objective benchmark and real-life application problems, in which it has been empirically shown to perform well on many optimization problems [27-30].

In NS-MTLBO model, the learner with the highest value of rank and the crowding distance is adopted as the teacher of the class. Once the teacher is chosen, the process continues according to the teacher phase of the TLBO algorithm. At the end of the teacher phase process of TLBO, P updated solutions are created. Combining these updated solutions with P solutions in the external produces 2P solutions. To continue the learning phase of TLBO, P numbers of the best learners are chosen from the 2P solutions according to the non-dominating sorting concept and the crowding distance metric. Then, these learners are further

updated depending on the learner phase of the TLBO algorithm. These steps are continuously repeated until satisfying a pre-defined criterion.

Optimum solution of TCTP via NS-MTLBO algorithm

The solution of TCTP employing NS-MTLBO process including the partial random initial population newly proposed in this study is summarized as follows:

Step I: Perform an optimization process through the min-min approach detailed above and collect the solutions which have the minimum project cost corresponding to the minimum project duration into an external archive. In that process, the total cost of the project is taken as a sole objective function, and is used TLBO algorithm.

Step II: Convey a pre-defined number of solutions from the external archive into the initial population and fill the initial population with the randomly generated solutions. It (initial population; CL) contains *pn* (student or population size) number of solution vectors and *dn* number of randomly generated design variables (X_i) between the upper (X_i^{max}) and lower (X_i^{min}) limit of the solution range. In addition, to initialize the TLBO algorithm, define the maximum number of iterations (stopping criteria).

Thus, initial matrix (CL) can be written as:

$$CL = \begin{bmatrix} X_{1,1} & \cdots & X_{1,dn} \\ \vdots & \ddots & \vdots \\ X_{pn,1} & \cdots & X_{pn,dn} \end{bmatrix} \tag{4}$$

Evaluate the matrix and determine the corresponding two objective function values associated with the project duration ($f_t(\mathbf{X})$) and the total project cost ($f_c(\mathbf{X})$) by

$$f(\mathbf{X}) = \begin{bmatrix} f_t(\mathbf{X}_1), f_c(\mathbf{X}_1) \\ \vdots \\ f_t(\mathbf{X}_{pn}), f_c(\mathbf{X}_{pn}) \end{bmatrix} \tag{5}$$

Perform a non-dominated sorting concept on the solutions. Then, calculate the crowded distance values of solutions in the front(s) and sort them. Keep the sorted solutions in an external archive.

Step III: Apply "teaching phase (t_p)" of the TLBO algorithm. Due to the fact that teacher has the best knowledge, the best learner in the class is assigned as a teacher ($\mathbf{X}_{\text{teacher}}$) of the class based on non-dominated sorting and crowding distance metric.

$$\mathbf{X}_{teacher} = \mathbf{X}_i | \text{ in front 1 and having max. crowded distance} \tag{6}$$

Afterwards, knowledge of the teacher is used to increase the capacity of whole class. The main aim is to increase the mean ($\mathbf{X}_{\text{mean}}$) of the class. For that reason, the equation of new students is found according to the teacher and the mean of the class as in the following:

$$\mathbf{X}_{new,i}^{tp} = \mathbf{X}_{old,i} + rand(0,1)\ (\mathbf{X}_{teacher} - T_F\ \mathbf{X}_{mean}) \tag{7}$$

where T_F represents teaching factor defined as

$$T_F = round\ [1 + rand(0,1)] \rightarrow \{1, 2\} \tag{8}$$

and it takes a value 1 or 2 based on the uniformly distributed random numbers within the range [0, 1]. If the new solution ($\mathbf{X}_{new,i}^{tp}$) is better than the old one, the new solution is accepted.

After employing the teaching phase, combine the current population with the archived one. Perform a non-dominated sorting concept on the combined population. Then calculate the crowded distance values of solutions in the front(s) and sort them. Select P individual from it.

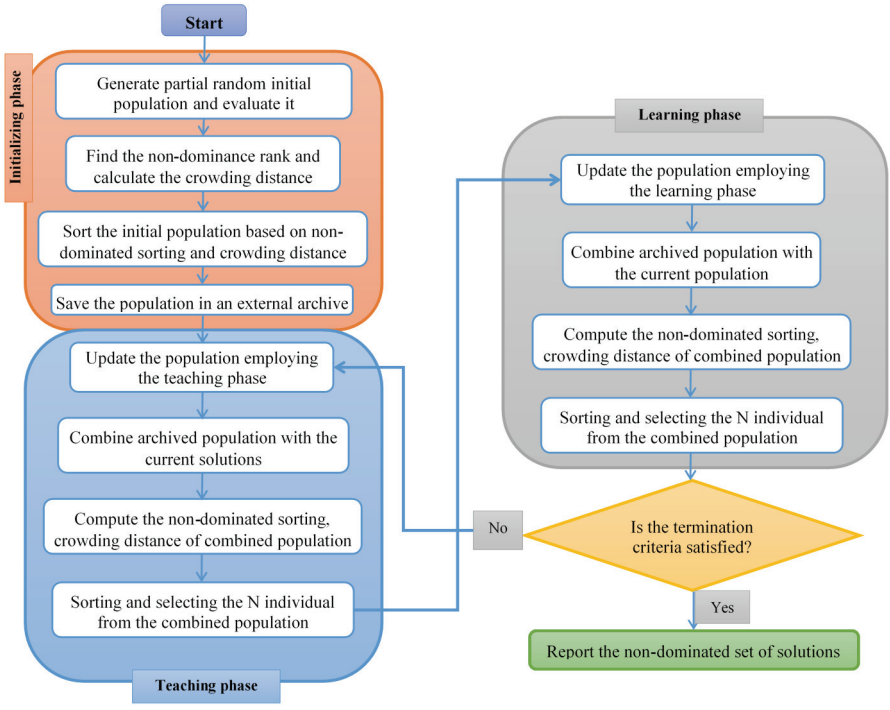

Fig. 2 - Flowchart of the NS-MTLBO algorithm for the solution of TCTP

Step IV: Proceed with the "learning phase (l_p)" of the TLBO algorithm. As stated above, students also have an important role in the learning process by communication, interaction, investigation, etc. This interaction can be expressed as follows:

$$\mathbf{X}_{new,i}^{lp} = \begin{cases} \mathbf{X}_{old,i} + rand(0,1)\left(\mathbf{X}_i - \mathbf{X}_j\right) \rightarrow \text{if } \mathbf{X}_i \text{ lies on a better non-dominated front than } \mathbf{X}_j \\ \mathbf{X}_{old,i} + rand(0,1)\left(\mathbf{X}_j - \mathbf{X}_i\right) \rightarrow \text{if } \mathbf{X}_j \text{ lies on a better non-dominated front than } \mathbf{X}_i \end{cases} \quad (9)$$

where $\mathbf{X}_i$ and $\mathbf{X}_j$ are randomly selected learners that are different from each other. If the new solution ($\mathbf{X}_{new,i}^{lp}$) is better, it is replaced with the old one.

Combine the current population with that used at the starting of the phase. Perform a non-dominated sorting on the combined population. Then calculate the crowded distance values of solutions in the front(s) and sort them. Select *P* individual from it.

Step V: Check the stopping criterion. This criterion is usually defined as the maximum iteration number. If the stopping criterion is satisfied, the optimization process is terminated, otherwise, the iteration process continues from the Step III. The flowchart of the process can be seen in Fig. 2.

5. NUMERICAL EXAMPLES

For performance evaluation of the NS-MTLBO method, a medium-scale problem and a large-scale problem are evaluated. The algorithm is implemented in MATLAB (R2015a), and runs are executed on a personal computer having Intel (R) Core (TM) i3 CPU 2.40 GHz and 3GB RAM. Total number of objective function evaluations is adopted as terminating criteria for the multi-objective optimization process. Due to stochastic nature of TLBO, 10 consecutive experimental runs are conducted for the entire instances.

Medium-scale test problem

A medium-scale project with 63 activities taken from Bettemir [31] is examined as the first test project to exhibit the performance of the proposed NS-TLBO. The activity-on-node diagram for the project is presented in Fig. 3. The project involves two activities with three modes, 15 activities with four modes, and 46 activities with five modes. The number of total possible time–cost alternatives for the project is 1.4E+42. The project is tested over two cases. The indirect cost is taken to be \$2300/day in the first case (63a), whereas \$3500/day in the second case (63b).

Ten consecutive experimental runs are conducted with the proposed initial population concept in NS-MTLBO for this project. Experimental runs are repeated for each predefined percentage alternatives given in Table 1. Pareto front solutions obtained from these investigations for both cases are illustrated in Tables 2 to 5, respectively.

In Tables 2-5, it can be observed that the proposed algorithm works well with the O_2 index (40% pre-defined solutions +60% randomly generated solutions). Therefore, Pareto front solutions obtained with O_2 index are used to compare the results with the others to clearly demonstrate the performance of the proposed new initial population approach in NS-MTLBO algorithm. Tables 6 and 7 compare the best results of obtained in the present study and the other studies for Case 1 and Case 2 with corresponding average percent deviations (%APD) from the optima. The optimal solutions obtained using the integer programming for both cases were reported in Bettemir [31] as 630 days with \$5.421.120 for 63a (Case 1) and 621

days with \$6.176.170 for 63b (Case 2). In addition, Table 8 shows %APD comparison of Case 1 and Case 2 for the proposed model and previous ones.

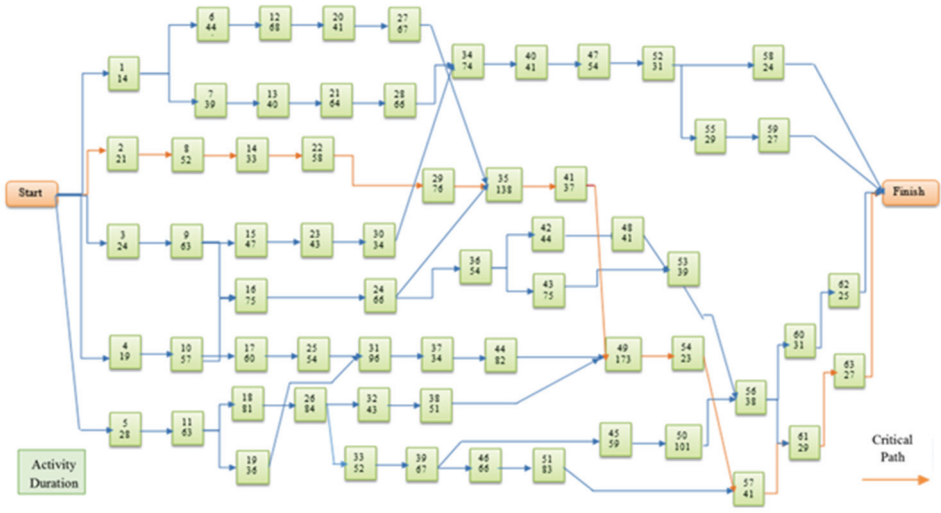

Fig. 3 - Network representation of the 63 activities project

Table 2 - Pareto front solutions of 63-activity project with O_1 *index for both cases*

Partial Random Initial population-based NS- MTLBO			
Case 1 (ic=2300 \$/day)		Case 2 (ic=3500 \$/day)	
Duration (days)	Total cost (\$)	Duration (days)	Total cost (\$)
633	5427920	621	6179720
634	5448920	622	6183820
635	5430670	623	6188920
636	5438370	624	6184220
637	5428220	625	6181020
638	5432270	626	6186070
639	5431570	627	6193420
640	5441670	628	6197070
641	5430070	629	6192260
642	5436520	630	6198570
NFE	50000	50000	

ic: indirect cost, NFE: number of objective function evaluations with 100 population size and 250 number of iteration

Table 3 - Pareto front solutions of 63-activity project with O_2 *index for both cases*

Partial Random Initial population based NS- MTLBO			
Case 1 (ic=2300 $/day)		Case 2 (ic=3500 $/day)	
Duration (days)	Total cost ($)	Duration (days)	Total cost ($)
633	5427920	621	6180020
628	5428170	621	6179720
637	5428220	621	6181820
630	5427770	621	6182640
633	5427920	622	6179470
630	5427770	625	6180070
628	5428170	621	6179720
630	5428870	618	6182020
630	5427770	621	6182640
630	5428120	623	6182070
NFE	50000	50000	

Table 4 - Pareto front solutions of 63-activity project with O_3 *index for both cases*

Partial Random Initial population based NS- MTLBO			
Case 1 (ic=2300 $/day)		Case 2 (ic=3500 $/day)	
Duration (days)	Total cost ($)	Duration (days)	Total cost ($)
630	5428170	626	6186070
631	5433170	629	6192260
634	5428220	627	6193420
637	5436520	621	6179720
638	5428970	612	6192270
639	5429920	623	6191170
640	5434770	620	6196270
641	5431420	622	6183820
644	5438220	625	6181020
645	5438720	624	6184220
NFE	50000	50000	

Table 5 - Pareto front solutions of 63-activity project with O_4 *index for both cases*

Partial Random Initial population based NS- MTLBO			
Case 1 (ic=2300 $/day)		Case 2 (ic=3500 $/day)	
Duration (days)	Total cost ($)	Duration (days)	Total cost ($)
630	5427770	621	6180020
639	5429920	625	6190070
634	5428070	627	6189770
642	5436520	624	6188170
633	5427920	628	6197070
631	5433170	631	6210010
638	5428970	630	6198570
635	5442370	629	6188670
637	5428220	626	6186070
640	5430570	632	6212020
NFE	50000	50000	

*Table 6 - The best results for 63-Activity project (*Case 1*: daily indirect cost of* $*2300)*

Run no	Sönmez and Bettemir [10]		Aminbakhsh [14]		This study		%PD
	GASA		DPSO		TLBO		
	Dur. (days)	Cost ($)	Dur. (days)	Cost ($)	Dur. (days)	Cost ($)	
1	633	5421320	630	5421120	633	5427920	0.125
2	633	5421320	630	5422420	628	5428170	0.130
3	633	5421620	630	5421120	637	5428220	0.130
4	633	5421320	630	5421120	630	5427770	0.122
5	633	5421620	633	5421320	633	5427920	0.125
6	633	5421620	636	5422970	630	5427770	0.122
7	633	5421620	631	5424420	628	5428170	0.130
8	633	5421620	633	5421320	630	5428870	0.142
9	633	5421620	633	5421320	630	5427770	0.122
10	629	6450065	629	5423270	630	5428120	0.142
Pop size	200		200		100		
Num of iter.	250		250		250		%APD=0.128
NFE	50000		50000		50000		

*Table 7 - The best results for 63-Activity project (*Case 2*: daily indirect cost of $3500)*

Run no	Sönmez and Bettemir [10]		Aminbakhsh [14]		This study		%PD
	GASA		DPSO		TLBO		
	Dur. (days)	Cost ($)	Dur. (days)	Cost ($)	Dur. (days)	Cost ($)	
1	629	6181270	616	6177820	621	6180020	0.062
2	630	6177570	626	6177370	621	6179720	0.057
3	633	6184670	621	6176220	621	6181820	0.062
4	631	6183320	621	6178020	621	6182640	0.104
5	618	6180420	629	6177270	622	6179470	0.053
6	629	6180520	621	6177120	625	6180070	0.061
7	629	6179870	621	6176170	621	6179720	0.057
8	621	6180620	618	6177570	618	6182020	0.094
9	629	6177270	618	6177670	621	6182640	0.104
10	630	6182020	618	6177570	623	6182070	0.095
Pop size	200		200		100		
Num of iter.	250		250		250		%APD=0.075
NFE	50000		50000		50000		

Table 8 -Average deviations of 63-activity problem from the optimal solution for the models

Algorithms	Case 1		Case 2	
	Runs	%APD	Runs	%APD
GA, [10]	10	5.86	10	5.16
HA, [10]	10	2.61	10	2.50
DPSO, [15]	10	0.02	10	0.05
NS-TLBO, [24]	10	0.128	10	0.14
This study	10	0.128	10	0.075

Considering Tables 6-8, the results of the partial random initial population based NS-MTLBO for medium networks indicate that the proposed algorithm normally provides the adequate optimal and near-optimal solutions for the TCTP. Convergence histories of the proposed algorithm for O_1-O_4 indices are illustrated in Figs. 4-7, respectively. Thereby, convergence history graphs indicate that the NS-MTLBO algorithm together with the proposed new initial population concept converges to better solutions much faster than the original TLBO. Also, the convergence of the NS-MTLBO algorithm with O_2 index (40% pre-known +60% randomly generated solutions in the initial population) provides the better

solution and a smoothed convergence history (see Fig. 5) for Case 1 and Case 2. The figure illustrates that the implemented generation converges after 150th iteration, which is the optimum value for Case 1. Similarly, it converges the optimum solution after 120th iteration for Case 2.

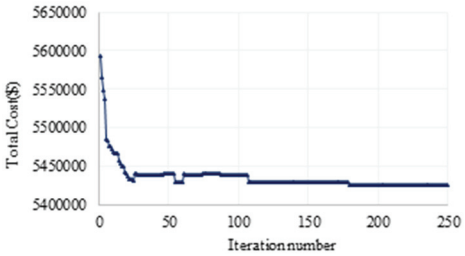

a. Case 1

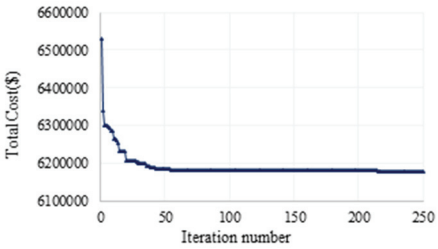

b. Case 2

Fig. 4 - Convergence history of 63-activity TCTP problem with O_1 *index for Case 1 and Case 2*

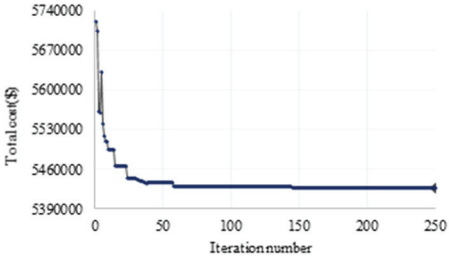

a. Case 1

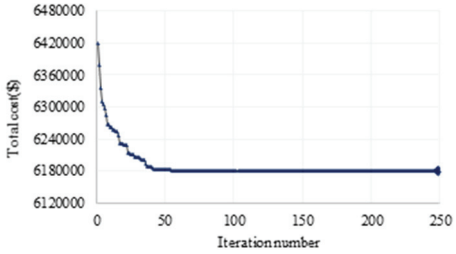

b. Case 2

Fig. 5 - Convergence history of 63-activity TCTP problem with O_2 *index for Case 1 and Case 2*

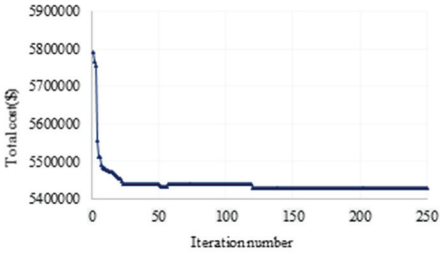

a. Case 1

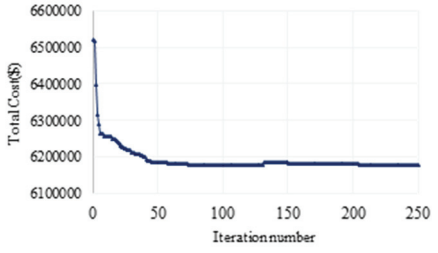

b. Case 2

Fig. 6 - Convergence history of 63-activity TCTP problem with O_3 *index for Case 1 and Case 2*

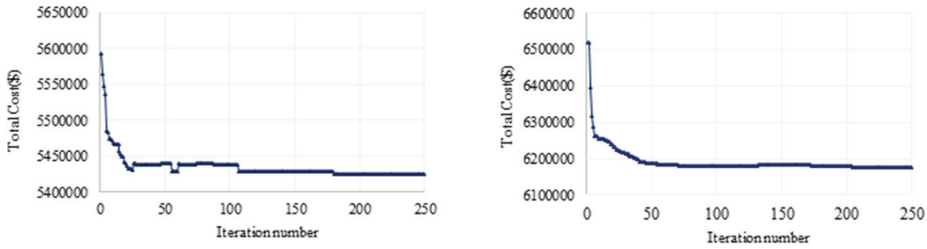

a. Case 1 *b. Case 2*

Fig. 7 - Convergence history of 63-activity TCTP problem with O_4 *index for Case 1 and Case 2*

Large-scale test problem

As it is obvious that the study concentrating on the generation of large-scale complex TCTPs involving more activities and modes, would enable a better understanding of the performance of heuristic and metaheuristic methods for real-world projects. To this end, in this section, to further investigate the performance of the proposed algorithm on a large scale 630-activity project adopted from the literature is examined. The model project was formed by duplicating the 63-activity project nine times [31]. In this project, two overhead costs are considered in two cases: The overhead costs for Case 1 (630a) and Case 2 (630b) are 2300$/day and 3500$/day, respectively. The optimal solutions of 6300 days with $54.211.200 as the cost for 630a and 6210 days with $61.761.700 as the cost for 630b were originally provided by Sönmez and Bettemir [10] using the integer programming.

To solve the current problem, it is found out that the best combination of the partial random initial population (O_2) produces an effective solution for the medium scale problem. Therefore, this suitable combination is adopted to solve the large-scale problem as well. To obtain the best Pareto front solutions, ten consecutive experimental runs are implemented on this project. The best results of 10 runs are demonstrated in Tables 11 and 12 for Case 1 and Case 2 along with corresponding %APD from the optima.

Table 9 - The best results for 630-activity project for Case 1 *(indirect cost=$2300/day)*

This study		%PD	Rank	Crowding distance
NS-MTLBO				
Dur. (days)	Cost ($)			
6387	54775880	0.01	1	0.0640
6447	54682080	0.86	1	0.0498
6480	54684970	0.87	1	0.0486
6417	54687510	0.87	1	0.0434
6458	54695920	0.89	1	0.0416

Table 9 - The best results for 630-activity project for Case 1 *(indirect cost=$2300/day) (continue)*

This study		%PD	Rank	Crowding distance
NS-MTLBO				
Dur. (days)	Cost ($)			
6433	54697060	0.89	1	0.0354
6473	54697450	0.89	1	0.0352
6424	54702050	0.90	2	0.0349
6475	54711350	0.92	1	0.0345
6342	54720110	0.93	1	0.0336
Pop. size	100			
Num. of iterations	250		%APD=0.911	
NFE	50000			

Table 10 - The best results for 630-activity project for Case 2 *(indirect cost=$3500/day)*

This study		%PD	Rank	Crowding distance
NS-MTLBO				
Dur. (days)	Cost ($)			
6204	62591490	1.34	1	0.0857
6127	62650570	1.43	1	0.0834
6114	62680270	1.48	1	0.0786
6094	62691570	1.50	1	0.0742
6060	62696280	1.51	2	0.0316
6043	62697220	1.51	1	0.0315
6137	62702240	1.52	1	0.0312
6030	62704580	1.52	1	0.0301
6159	62711150	1.53	1	0.0300
6130	62723120	1.56	3	0.0294
Pop. size	100			
Num. of iterations	250		%APD=1.49	
NFE	50000			

Comparison of mean values of 10 runs for Case 1 and Case 2 for the previously developed models and the proposed model in this study are presented in Tables 11 and 12, respectively. In addition, Table 13 represents the compared %APD of Case 1 and Case 2 with the previous and basic TLBO algorithms.

Table 11 - Comparison of mean values of 10 runs for Case 1 (: indirect cost =$2300/day)

Results	Bettemir [13]			This study
	NS-GA	NS-ACO	NS-PSO	NS-MTLBO
Mean value	58983147	56703583	54815790	54705438
Pop. size	-	-	-	100
Num. of iteration	-	-	-	250
NFE	250000	250000	250000	50000

Table 12 - Comparison of mean values of 10 runs for Case 2 (: indirect cost =$3500/day)

Results	Bettemir [13]			This study
	NS-GA	NS-ACO	NS-PSO	NS-MTLBO
Mean value	66395840	64574989	63121500	62684849
Pop. size	-	-	-	100
Num. of iteration	-	-	-	250
NFE	250000	250000	250000	50000

Table 13 - Average deviations from the optimal solutions for the cases of 630-activity project

Algorithms	Case 1		Case 2	
	Runs	%APD	Runs	%APD
GA, Bettemir [31]	10	8.83	10	7.50
HA, Sönmez and Bettemir [10]	10	2.41	10	2.47
DPSO, Aminbakhsh [14]	10	0.33	10	0.34
NS-TLBO, Eirgash [24]	10	1.10	10	1.51
This study	10	0.91	10	1.49

Partial random initial population based NS-TLBO algorithm achieved very successful results and outperformed the hybrid genetic algorithm (HA) by Sönmez and Bettemir [10] as well as basic TLBO algorithms for large-scale instances. The acquired %APD values for instances 630a and 630b are 0.91 and 1.49%, respectively. By searching only 50,000 solutions out of 2.38×10^{42} potential solutions, partial random initial population based NS-MTLBO is able to obtain high quality solutions for the large scale problems. The hybrid algorithm of Sönmez and Bettemir [10] is able to achieve %APD values of 2.41 and 2.47% within 50,000 schedules (number of objective function evaluation).

Performance of TLBO has improved due to the partial random initial population-based modification as observed from the results. It can be commented that applied metaheuristic algorithm (TLBO) could not obtain the global optima in any of trials. However, by searching

merely 25,000 solutions out of 1.37×10^{42} potential solutions, proposed algorithm is able to find solutions very close to the optima. The reason for not achieving the global optima can be explained by the complex nature of the problem and premature convergence condition. Therefore, the partial random initial population based NS-MTLBO provides a user-friendly and efficient approach to support the time-cost optimization of medium scale problems. It is worth mentioning that the simplicity of the proposed TLBO algorithm is its most important feature.

6. CONCLUSIONS

Since the previously proposed core NS-MTLBO model was insufficient in solving the large-scale TCTP problems, a new initial population creation approach in NS-MTLBO is developed to further improve the exploration capacity of the core NS-MTLBO model for the TCTPs in this study. If the proposed approach is compared with its former version, the developed model can accelerate the optimization process with a less searching process and enhance the results obtained. However, beside some improvements in the multi-objective optimization process, the proposed model cannot detect the global optima. In contrast, it can identify the satisfactory solutions near-optimum (mostly with less than 7% deviation from the optimal solution) without compromising the quality of the solution. It can be stated that different approaches may be added to the model in order to increase the possibility of catching the global optimum. For further research, some certain recommendations may be done, such as the integration of Levy flight (a random walk) model with the proposed model to systematically surf through the search space to avoid the local minimum. In conclusion, the results obtained from the numerical experiments indicate that the proposed multi-objective model based on NS-MTLBO algorithm including the partial random initial population concept can be preferred as an alternative model in solution of TCTPs.

References

[1] Meyer, W.L., Shaffer, L.R. Extending CPM for Multiform Project Time-Cost Curves. Journal of Construction Division 91(1), 45-68, 1965.

[2] De, P., Dunne, E.J., Ghosh, J.B., Wells, C.E. Complexity of the discrete time-cost trade-off problem for project networks. Operations Research 45(2), 302–306, 1997.

[3] Demeulemeester, E., De Reyck, B., Foubert, B., Herroelen, W., Vanhoucke, M. New computational results on the discrete time/cost trade-off problem in Project networks. Journal of the Operational Research Society 49(11), 1153-1163, 1998.

[4] Yang, H.H., Chen, Y.L. Finding the critical path in an activity network with time-switch constraints. European Journal of Operational Research 120(3), 603-613, 2000.

[5] Vanhoucke, M. New computational results for the discrete time/cost trade-off problem with time-switch constraints. European Journal of Operational Research 165(2), 359-374, 2005.

[6] Feng, C.W., Liu, L., Burns, S.A. Using genetic algorithms to solve construction time-cost trade-off problems. Journal of Computing in Civil Engineering 11(3), 184 –189, 1997.

[7] Siemens N. A Simple CPM Time-Cost Trade off Algorithm. Management Science 17(6), 354–363, 1971.

[8] Vanhoucke, M., Debels, D. The discrete time/cost trade-off problem: extensions and heuristic procedures. Journal of Scheduling 10(5), 311-326, 2007.

[9] Zheng, D., Ng, S., Kumaraswamy, M. applying pareto ranking and niche formation to genetic algorithm-based multiobjective time–cost optimization. Journal of Construction Engineering and Management 131(1), 81–91, 2005.

[10] Sönmez, R., Bettemir, O.H. A hybrid genetic algorithm for the discrete time-cost trade-off problem. Expert Systems with Applications 39(13), 11428-11434, 2012.

[11] Anagnostopoulos, K.P., Kotsikas, L. Experimental evaluation of simulated annealing algorithms for the time-cost trade-off problem. Applied Mathematics and Computation 217(1), 260-270, 2010.

[12] Yang, I.T. Performing complex project crashing analysis with aid of particle swarm optimization algorithm. International Journal of Project Management 25(6), 637-646, 2007.

[13] Zhang, H., Xing, F. Fuzzy-multi-objective particle swarm optimization for time –cost – quality trade-off in construction. Automation in Construction 19(8), 1067-1075. 2010.

[14] Aminbakhsh, S. Hybrid particle swarm optimization algorithm for obtaining Pareto front of discrete time–cost trade-off problem. M.Sc. Thesis, Middle East Technical University, Ankara, Turkey, 2013.

[15] Aminbakhsh, S., Sönmez, R. Applied discrete particle swarm optimization method for the large-scale discrete time–cost trade-off problem. Expert Systems with Applications 51, 177-185, 2016.

[16] Colorni, M., Dorigo, V.M., Trubian, M. Ant system for job-shop scheduling. Journal of Operations Research, Statistics and Computer Science 34, 39–53, 1994.

[17] Ng, S.T., Zhang, Y.S. Optimizing construction time and cost using ant colony optimization approach. Journal of Construction Engineering and Management 134(9), 721-728, 2008.

[18] Xiong, Y., Kuang, Y. Applying an ant colony optimization algorithm-based multiobjective approach for time–cost trade-off. Journal of Construction Engineering and Management 134(2), 153–156, 2008.

[19] Afshar, A., Ziaraty, A., Kaveh, A., Sharifi, F. Nondominated archiving multicolumn ant algorithm in time–cost trade-off optimization. Journal of Construction Engineering and Management 135(7), 668-674, 2009.

[20] Elbeltagi, E., Hegazy, T., Grierson, D. A modified shuffled frog-leaping optimization algorithm: Applications to project management. Structure and Infrastructure Engineering 3(1), 53–60, 2007.

[21] Hafizoğlu, A. B. Discrete time/cost trade-off problem in project scheduling. M.Sc. Thesis, Middle East Technical University, Turkey, 2006.

[22] Abdel-Raheem, M., Khalafallah, A. Using Electimize to solve the time cost trade-off problem in construction engineering. PhD dissertation, University of Central Florida Orlando, USA, 2011.

[23] Narayanan, A.S., Suribabu, C.R. Multiobjective optimization of construction project time cost-quality trade-off using differential evolution algorithm. Journal of Civil Engineering 8(4), 375-392, 2014.

[24] Eirgash, M.A. Pareto-front performance of multiobjective teaching learning based optimization algorithm on time-cost trade-off optimization problems. M.Sc. Thesis, Karadeniz Technical University, Turkey, 2018.

[25] Deb, K., Pratab, A., Agrawal, S., Meyarivan, T. A fast and elitist multiobjective genetic algorithm. NSGA-II. IEEE Transaction on Evolution of Computing 6, 182–197, 2000.

[26] Rao, R.V., Savsani, V.J., Vakharia, D.P. Teaching-learning-based optimization: a novel method for constrained mechanical design optimization problems. Computation Aided Design 43(3), 303-315, 2011.

[27] Rao, R.V., Patel, V. Multi-objective optimization of combined Brayton and inverse Brayton cycles using advanced optimization algorithms. Engineering Optimization 44(8), 965-983, 2011.

[28] Rao, R.V., Savsania, V.J., Balic, J. Teaching-learning-based optimization algorithm for unconstrained and constrained real-parameter optimization problems. Engineering Optimization 44(12), 1447-1462, 2012.

[29] Toğan, V."Design of planar steel frames using teaching-learning based optimization. Engineering Structures 34, 225-232, 2012.

[30] Dede, T., Toğan, V. A teaching learning based optimization for truss structures with frequency constraints. Structural Engineering of Mechanics 53(4), 833-845. 2015.

[31] Bettemir, Ö.H. Optimization of time-cost-resource trade-off problems in project scheduling using meta-heuristic algorithms. PhD dissertation, Middle East Technical University, Turkey, 2009.

Teknik Dergi, 2019 9581-9596, Paper 557

Investigating the Mechanical Behavior of Reclaimed Asphalt Pavement (RAP) Bases in Large Scale Test Box

Ayşegül Güneş SEFEROĞLU[1]
Mehmet Tevfik SEFEROĞLU[2]
Muhammet Vefa AKPINAR[3]

ABSTRACT

The objective of this research was to assess the elastic deformations and permanent strains of reclaimed asphalt pavement (RAP) material as a base layer when it is treated or untreated with pozzolanic cement under cyclic loads. A large-scale cyclic plate loading testing (CPLT) device was developed for studying the mechanical characteristics of pavement base layer. The laboratory test results indicated that when the RAP percentage of the mixtures increased, elastic deformations and permanent strains increased, but the opposite was true when the cement percentage increased. It was concluded that 100% RAP material can be used in base layers with 3% pozzolanic cement. The obtained deformation values and strain rates can be used as reasonable default design input values by pavement designers when using RAP as a substitute for natural aggregate base layers.

Keywords: RAP, CPLT, elastic deformation, permanent strain.

1. INTRODUCTION

To reduce the costs of construction and disposal of used pavement materials, Turkey is increasingly recycling these materials when reconstructing highway pavements. Since most recycled asphalt aggregate (RAP) material is used in hot-mix asphalt pavements, there is a general lack of data pertaining to the mechanical properties for RAP material in other to guide possible future applications, notably pavement unbound base layers. Several authors performed laboratory studies of RAP material, focusing on tests of interest to base layer construction, including proctor compaction experiment, California Bearing Ratio (CBR) and resilient modulus to assess the suitability of RAP as a base layer material [1-8].

Note:
- This paper has been received on April 19, 2018 and accepted for publication by the Editorial Board on December 24, 2019.
- Discussions on this paper will be accepted by January 31, 2020.
- https://dx.doi.org/10.18400/tekderg.416812

1 Gümüşhane University, Dept. of Civil Engineering, Gümüşhane, Turkey - gnskaya61@gmail.com https://orcid.org/0000-0002-1008-6456

2 Karadeniz Technical University, Dept.of Civil Engineering, Trabzon, Turkey - mtseferoglu@gmail.com https://orcid.org/0000-0003-4677-3335

3 Karadeniz Technical University, Dept.of Civil Engineering, Trabzon, Turkey - mvakpinar70@yahoo.com https://orcid.org/0000-0001-7912-8274

The bearing capacity of the base layers strongly depends on the RAP content mixed with the conventional natural aggregate (NA). In general when the percentage of RAP material in mixtures exceeds 20-25%, the required CBR value for the base layer decreases as discussed by several authors [9- 11]. Some researchers reported that the RAP content of the base layer mixtures should be limited to a maximum of 50% by weight [1, 12].

In the literature, there is no study found on the performance of cyclic plate loading test of cement treated and untreated base layers with different RAP percentages. The triaxial load test was used mostly in determining the deformation characteristics. The cyclic plate loading test (CPLT) used by Thakur [13] was performed on 100% RAP pavement base layer reinforced with geocell. The CPLT provides preliminary determination of deformation in the laboratory environment to represent field traffic loads.

Highter et al. [14] reported that larger elastic deformation values would be obtained when the RAP percentage in RAP-NA mixtures is increased.

Pokharel et al. [15] conducted CPLT tests on base layers. In this study, geocell-reinforced granular bases with three types of infill materials (Kansas River (KR) sand, quarry waste (QW), and AB-3 aggregate) were tested and compared with the unreinforced bases under 150 loading cycles. The study experimentally investigated the effect of the geocell reinforcement on the permanent deformation and percentage elastic deformation of the granular bases. The test results showed that the amount of elastic deformation was slightly higher at the beginning of the load cycles but later stabilized to a constant value. Unreinforced QW showed approximately 0.5 mm elastic deformation and unreinforced AB-3 showed about 0.7 mm elastic deformation at the end of the 150th loading cycle.

The resilient response of the granular material is important for the load-carrying capacity of the pavement and the permanent strain response, which characterizes the long-term performance of the pavement [16]. Papp et al. [17] studied the permanent deformation characteristics of recycled concrete aggregate (RCA), RAP and a dense-graded aggregate in base and subbase applications by conducting cyclic triaxial tests and reported that the resilient modulus for RAP in the laboratory testing was higher than that of the conventional materials. However, RAP also had the highest permanent strain after 100,000 repetitions.

Thompson and Smith [6] stated that permanent strains are an important characteristic for determining wearing layer performance. Some researchers have observed that permanent strains increase when RAP percentage increases in RAP-NA mixtures [18-22].

Attia [18], Bennert et al. [19], Garg and Thompson [20] and Kim and Labuz [21] found that the relationship between permanent strains and the number of loading and unloading cycles of 50% RAP and 100% RAP in a linear fashion.

Bennert and Maher [1] indicated that as the RAP percentage in RAP-NA mixtures increases, the cumulative permanent strains obtained at the end of 100,000 loading-unloading cycles increase compared to the 100% NA. Furthermore, the increase in the RAP percentage in the mixture increased the permanent strain rate. The largest strains were obtained at 100% RAP material [23].

In order to allow a higher load distribution capacity in pavements, in comparison to unbound materials, the treatment of the granular materials of road bases/subbases with cement is a good option [24].

2. MATERIALS

2.1. RAP Material

The RAP material used in this study was obtained from main municipal roadway overlay in Trabzon city, Turkey. The RAP material used was not processed after milling only the material over 25 mm sieve was removed. Results of sieve analysis indicated that both the RAP and NA materials were classified as A-1-a type soils according to the AASHTO soil classification system. The filler content (<0.075 mm) of RAP was 3.3%. The plant-mix base layer (PBL) gradation did not allow for more than 10% of the material to pass the 0.075 mm sieve in AASHTO design criteria.

An extraction test following the specifications in AASHTO T-164 [25] showed the asphalt content of 100% RAP was 5.5% by weight. The ASTM D 1557 [26] Modified Proctor test was performed on the RAP material. The maximum dry density (MDD) for RAP was 1.952 t/m^3 at an optimum moisture content (OMC) of 7.2%. Specifications require that the base layer materials have a soaked CBR greater than 120. However, the result of soaked CBR test performed on RAP material according to AASHTO T-193 [27] indicated that it does not meet CBR base layer requirements of 120 alone.

2.2. Natural Aggregate (NA) and Cement

The NA was obtained from a local quarry pit in Trabzon province, Turkey. The NA with loss of weather resistance (with Mg_2SO_4) of 4.56%, abrasion (Los Angeles) of 12.0%, flatness index of 13.0% and water absorption of 1.81% was used in this study. The maximum dry density of the NA was 2.2 t/m^3 at a moisture content of 5.8%. The measured soaked CBR value was 178. 1, 2 and 3% of pozzolanic cement was added to the RAP-NA mixtures in order to increase the CBR up to 120. The pozzolanic cement type was CEM IV 32.5 R.

3. METHOD

The first step of the test program was to determine the untreated 100% RAP content mixture that meets the criteria for grading and soaked CBR for the PBL as specified by the Turkish Department of Transportation (TurkeyDOT) specification. In this specification, the minimum soaked CBR criterion to be provided for PBL is 120, while the maximum amount of mineral filler (<0.075 mm) is limited to 10% [28]. 1, 2 and 3% cement content by dry weight was added to the mixture to meet the requirements.

The second step was to compare the elastic deformations of cement treated and untreated RAP base mixtures to the 100% NA mixes as a reference under cyclic plate loadings.

3.1. Preparation of Mixtures

Sieve analysis, compaction and soaked CBR tests were performed on RAP-NA mixtures that contained 100, 60, 50, 40, 30, 20, 10 and 0% RAP. The CBR testing was performed according to AASHTO T-193 to determine the bearing capacity of NA and RAP mixtures compacted at optimum moisture. For the tests, five replicates were prepared for each mixture. As the

RAP percentage increased the dry density and optimum moisture content decreased. The lowest CBR corresponded to the mix containing 100% RAP. Similar to the behavior of dry density, the CBR values increased, as the percentage of RAP in the aggregate mixture decreased. In maximum untreated mixture with RAP which had the CBR greater than 120 was 20% RAP-80% NA mixture. Results indicated that 20% RAP-80% NA with no cement is a good option when used in the base layer.

Some RAP-NA mixes that did not meet the 120 soaked CBR criteria were tested with different percentages of cement. Three levels of cement content, 1, 2 and 3%, by dry weight were used. The maximum RAP percentages that met the 120 soaked CBR criteria and 100% NA as the control mix were selected for CPLT. Mixtures of aggregate containing 20% RAP-80% NA, 60% RAP-40% NA-3% cement, 100% RAP-3% cement and 100% NA produced CBR greater than 120. Modified Proctor and soaked CBR test results of the mixtures meeting the soaked CBR criteria are given in Table 1.

Table 1 - Modified Proctor and soaked CBR test results of the mixtures

Mixtures (%)			Modified Proctor		Soaked CBR
RAP	NA	Cement	OMC (%)	MDD (t/m^3)	
-	100	-	6.00	2.23	178
20	80	-	5.10	2.15	130
60	40	3	4.82	2.10	147
100	-	3	4.60	2.092	138

3.2. Test Setup

The base layers were prepared with four mixtures separately, with cement treated and untreated blends in maximum RAP content, which meet the min. 120 CBR criterion, and 100% NA as the control mix, then subjected to CPLT. These mixtures are composed of 20% RAP-80% NA, 60% RAP-40% NA-3% cement, 100% RAP-3% cement and 100% NA (Figure 1).

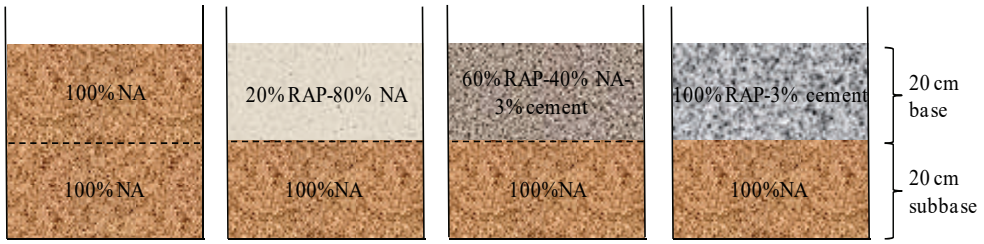

Figure 1 - Prepared base sections

The total compacted thickness of each of the base and subbase layers was 20 cm. The prepared mixtures were placed inside the test box in a lift thickness of 5 cm for four lifts to achieve 98% compaction. The quantity of RAP placed in each lift was calculated by multiplying the volume of that lift by the density of the mixtures. The prepared base layer mixtures were compacted at its optimum moisture content which corresponded to 98% of the maximum dry density. Cement-treated base sections were cured for 7 days in test tank after compaction.

Figure 2 showed the test apparatus used to compact the base and subbase layers. A large-scale (1 m×1 m×0.8 m) steel test tank was constructed for CPLT. The subbase layer of 20 cm thickness consisted of 100% NA. The subbase in the tank compacted to a dry density approximately equal to 98% of the maximum dry density. Compression of the underlying and base layers was accomplished by mounting a steel plate to the loading piston.

(a) *(b)*

Figure 2 - Compaction assessments (a) subbase layer (b) base layer

It was observed that the preliminary work carried out by the loading piston made 10 loading cycles and 98% or more of the compression was carried out by increasing the load to 20 tons capacity per cycle. The test setup consists of 3 different external components, mainly; 3 displacement transducers (LVDTs) placed at different intervals on the surface, 2 strain gauges placed in the base layer and 20 ton force exerting capacity load cell placed on the loading plate. A load cell was used for measuring the load applied; LVDTs and strain gauges are used to measure displacements and strains respectively. All of the cables of the displacement transducers and strain gauges were connected to a data recorder.

A 300 mm in diameter steel circular plate is used to apply cyclic loading on the test sections. The cyclic loads having a peak value of 40 kN and a trough value of 0 kN were applied on the loading plate at a loading wave frequency of 0.77 Hz. The peak value of the load was

selected to simulate the single wheel load of 40 kN, which corresponds to a tire pressure of 550 kPa.

Strain gauges were used to measure the strains that developed at different locations of the base layer during cyclic loading. The strain gauges used in this study had a resistance of 120 ohms, a gauge factor at 24 °C of 1-2 and ±7500 microstrain capacity. Figure 3 showed the strain gauges at the middle of the base layer were placed horizontally 100 mm below the surface. Strain gauges were oriented in the line identical to the width of the test box at distances of 250 and 400 mm from the center (SG-1 and SG-2, respectively).

Figure 3 - Strain gauge placements in the base layer

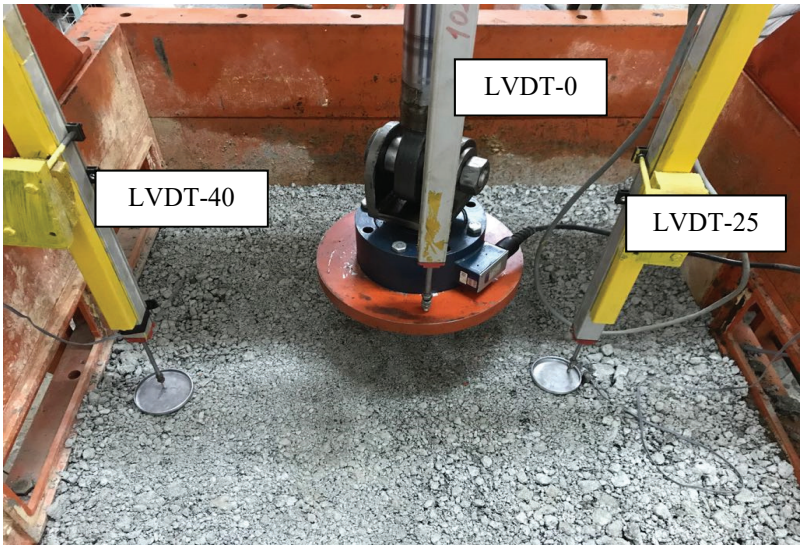

Figure 4 - The configurations of LVDTs

The vertical surface displacements at the plate center and different distances from the center were measured by the linear variable displacement transducers (LVDTs). LVDTs had two displacement ranges: 0 to 50 mm and 0 to 100 mm. One displacement transducers of 100 mm limit were affixed on the loading plate center. Two displacement transducers of 50 mm limit each were affixed at distances of 250 and 400 mm away from the center of the loading plate. The displacement transducers were positioned on the loading plate and base layer surface (Figure 4).

After all the sensors are positioned, the test was performed. Vertical displacements were obtained separately from the base layers prepared from the mixtures over 100 loading cycles. 100% NA was used as the control base material for comparison with the recycled materials at base layer test sections.

4. TEST RESULTS AND DISCUSSION

In this study, according to the data obtained from the LVDT data, sitting deformations are shown positive (+) and swelling deformations are shown negative (-) in graphs. Moreover, the strain was positive under tension and negative under compression.

4.1. Elastic Deformations

The recoverable portion of the deflection during a loading pulse was designated as the elastic deformation. Deformations were measured when the base layer was loaded with the maximum load (40 kN) and unloaded to the minimum load (0 kN). The variation of elastic deformation due to the number of loading cycles was measured by the LVDTs placed at different distances. Figure 5 showed the vertical elastic deformations of 100% NA mixture, at the center of the plate and 250 and 400 mm away from the center of the plate.

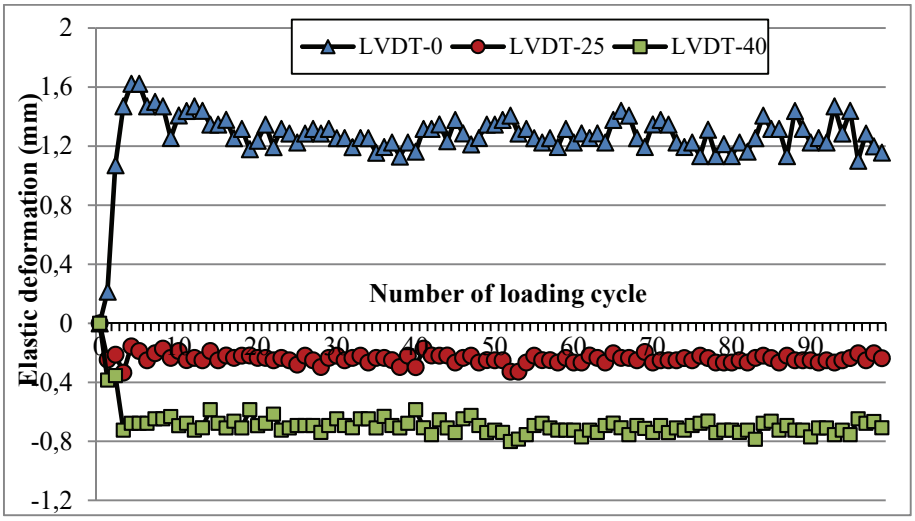

Figure 5 - The elastic deformations of 100% NA mixture versus the number of loading cycles

The surface deformations exhibited a vertical elastic deformation of about 1.4 mm at the center of the plate as a result of 100 loading cycles and the form of settlement. The amount of deformation was approximately 0.2 and 0.7 mm, respectively, compared to the data obtained from the LVDTs at 250 and 400 mm away from the plate center, and the form of swelling. It was shown that the surface elastic deformation was higher at the center and decreased with the distance from the center.

It is shown that the surface elastic deformation (i.e., the rebound during the unloading of each cycle) was higher at the center and decreased at the distances of 250, and 400 mm away from the center. The elastic deformation as shown in Figure 5 increased up to 5 cycles of loading and then decreased slightly to a small rate then stabilized until the end of the test.

The graphics of the elastic deformation of the base layer containing 20% RAP+80% NA mixture are shown in Figure 6.

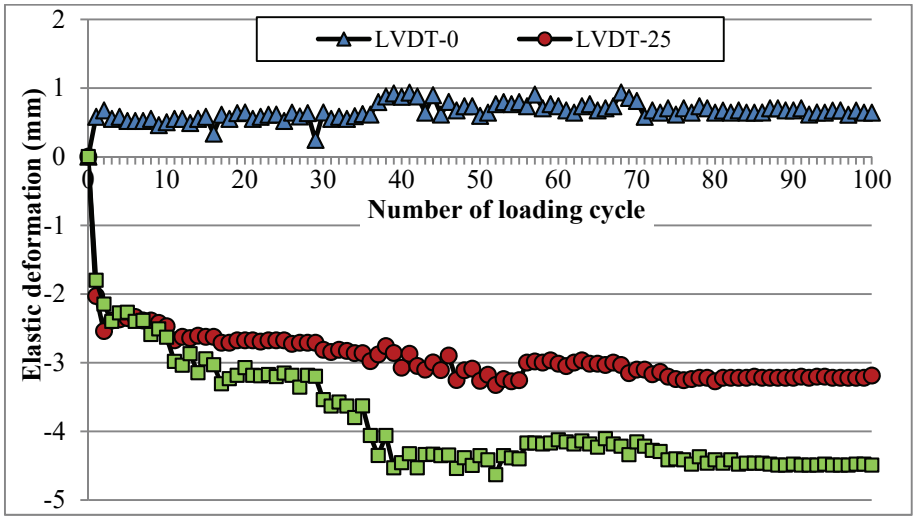

Figure 6 - The elastic deformations of 20% RAP-80% NA mixture versus the number of loading cycles

Figure 6 showed an elastic deformation of about 0.8 mm in the form of settlement under the center of the plate as a result of 100 loading cycles. The amount of elastic deformation was approximately 3.2 and 4.5 mm, respectively, obtained from the LVDTs at 250 and 400 mm away from the plate center. Elastic behavior increased as the distance from the plate increased.

The elastic deformation value obtained under the plate for 20% RAP-80% NA mixture was found to be 2 times lower than the elastic deformation value (1.4 mm) of the base layer conventionally made with 100% NA. This comparison demonstrates that the RAP bases had less elastic responses under loading plate than the NA bases due to the asphalt cement content of the RAP aggregates. However, the elastic deformation at 25 and 40 mm distance from the center of the loading plate was higher than the values obtained from the 100% NA base

section (3.2 and 4.5 mm, respectively). The elastic deformation value obtained from the LVDT-25 was 16 times that of the base layer of 100% NA, while the value at the LVDT-40 was about 6.5 times that of the base of 100% NA. This indicates that the asphalt-containing RAP material trapped under the loading plate with cyclic loading adheres to each other as the number of cycles increase, but the swelling at 250 mm and 400 mm distant points, which are not cramped, are more frequent. That is, the elastic deformation resistance formed at the center of the plate of 100% NA was higher than the 20% RAP blended base section, and this resistance decreases as the distance from the plate center increases. In this context, Highter et al. [14] suggested that the assumption that larger elastic deformation values will be obtained in the case of increased RAP percentage in RAP-NA mixtures is valid for the material out of the plate.

Figure 7 showed the elastic deformations of the base layer made with 60% RAP-40% NA-3% cement mixture.

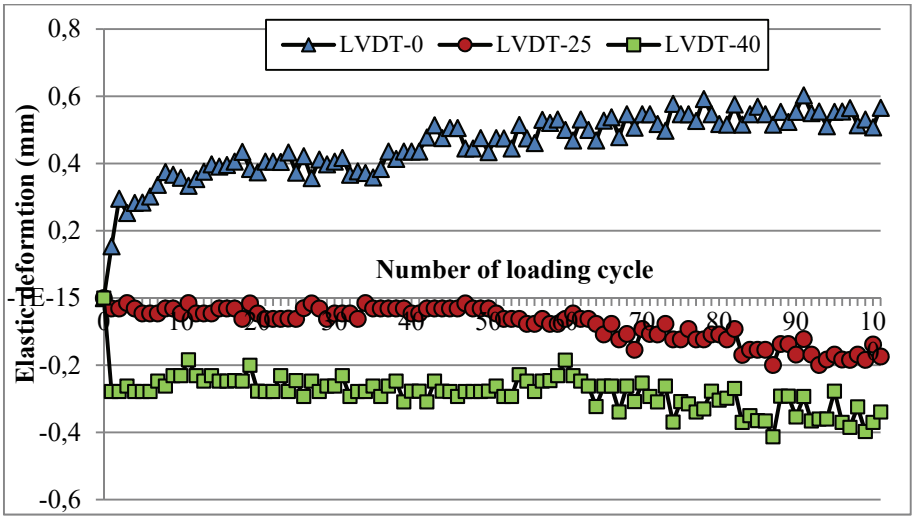

Figure 7 - The elastic deformations of 60% RAP-40% NA-3% cement mixture versus the number of loading cycles

As a result of the 100 loading cycles, an elastic deformation of approximately 0.55 mm in the form of settlement under the center of the plate is observed. According to LVDT-25 and LVDT-40, the amount of elastic deformation was approximately 0.2 mm and 0.3 mm, respectively, and deformation in the form of swelling was also observed. The elastic deformation value obtained under the plate in the 60% RAP-40% NA-3% cement mixture was observed to be 60% less than the elastic deformation value of the base layer made entirely with 100% NA (1.4 mm). The elastic deformation value taken with the LVDT-25 is the same as the value obtained from the section at 100% NA and is determined as 0.2 mm. The measurement taken with the LVDT-40 showed that the elastic deformation is about 0.3 mm, which is about half of the 0.7 mm deformation obtained from the 100% NA base section.

Despite the increased RAP percentage in the mixture, the 60% RAP-40% NA-3% cement mixed base layer showed the same elastic behavior as the 20% RAP-80% NA mixture. The reason why elastic deformation values are close to each other despite the increase of the RAP percentage used is the treatment with cement. Despite a 40% increase in RAP percentage, 3% cement treatment caused the base layer to exhibit similar elastic behavior under cyclic loading.

The graphics of the elastic deformations of the base layer at different locations, made with 100% RAP-3% cement mixture are shown in Figure 8.

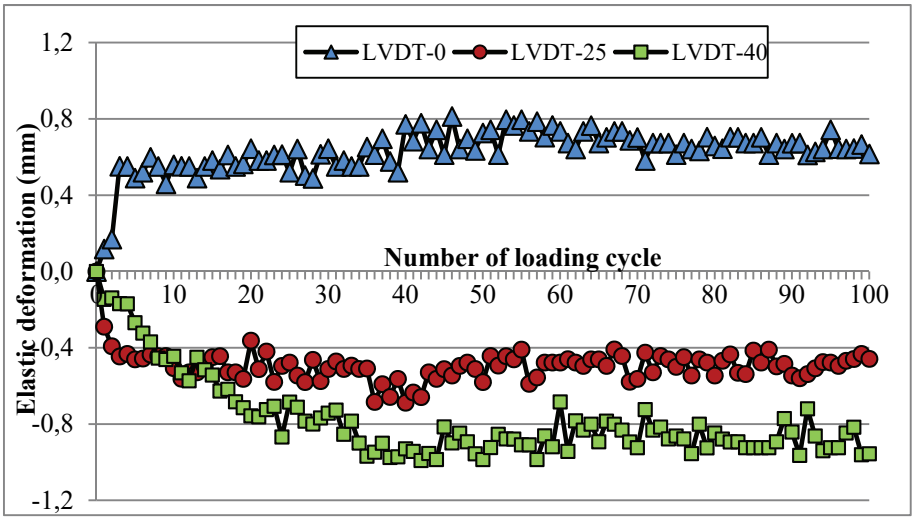

Figure 8 - The elastic deformations of 100% RAP-3% cement mixture versus the number of loading cycles

As a result of the loading cycle of 100, an elastic deformation of about 0.6 mm was observed in the form of settlement with the LVDT-0 for 100% RAP-3% cement mixture. The amount of elastic deformation was about 0.5 mm and 0.9 mm respectively according to the data obtained from LVDT-25 and LVDT-40. It was observed that the elastic deformation value obtained under the plate in the 100% RAP-3% cement mixture was 55% less than the base layer (1.4 mm) made entirely with 100% NA. The elastic deformation value obtained with the LVDT-25 was determined to be 2.5 times greater than the value obtained from the section at 100% NA. The measurement taken with the LVDT-40 showed that the elastic deformation is 0.9 mm, which is 20% greater than the 0.7 mm deformation obtained from the 100% NA base layer. At the end of the 10th cycle, the amount of elastic deformation under the plate center was about 0.6 mm. Thakur [13] obtained elastic deformation values of approximately 2.5 mm under the center of the plate at the end of the 100th cycle as a result of cyclic plate loading test in a base layer of 150 mm thickness prepared with 100% RAP material.

4.2. Permanent Strains

A possible reaction force on the wall of the tank may develop between the material and the steel frame during the loading cycles. For this reason, SG-2 was placed in a horizontal position at a point 400 mm away from the center, near the tank edge. In addition, SG-1 device was placed at a distance of 250 mm from the loading plate center to monitor the changes in distance of the strains. The changes in the loading cycle taking measurements with SG-1 and SG-2 placed 250 and 400 mm away from the center of the plate were investigated for each base layer mixtures. The permanent strains of the base layer due to distance which is prepared with 100% NA are shown in Figure 9.

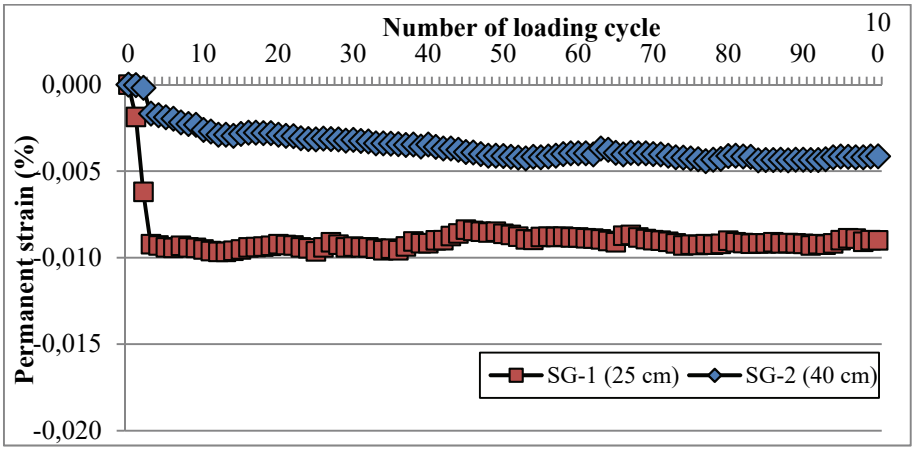

Figure 9 - The measured permanent strain rates of 100% NA mixture versus the number of loading cycles

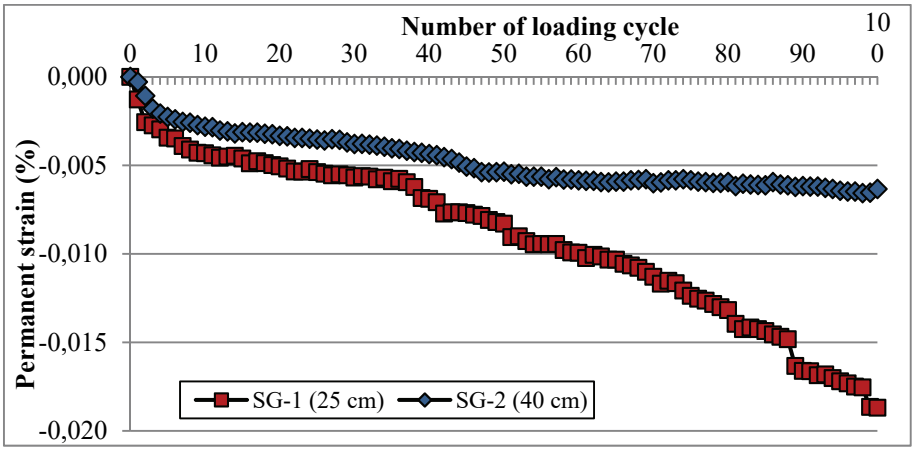

Figure 10 - The measured permanent strain rates of 20% RAP-80% NA mixture versus the number of loading cycles

At the distances of of 250 and 400 mm away from the loading plate center the strains were under tension from the beginning to the end of the test. In the initial loading cycles, a sudden increase in the strains was observed and remained almost the same after 5 loading cycles. A permanent strain rate of about 0.004% was observed in SG-2 (400 mm away from the center of the plate), while a change of about 0.009% in SG-1 (250 mm away) was observed. That is, as one moves away from the center of the plate, the strains decrease. The permanent strain changes of base layer made with 20% RAP-80% NA mixture during the loading cycles of SG-1 and SG-2 are shown in the graphic in Figure 10.

In the initial loading cycles, it is seen that a sudden increase is observed at SG-2, 400 mm away from the center of the plate, and at the SG-1, 250 mm away. At the end of the 100 loading cycles, strain rate of about 0.006% was observed at SG-2, while the strain rate of about 0.018% at SG-1 occurred. The strain changes taken from the SG-1 and SG-2 during the loading cycles of the base layer made with 60% RAP-40% NA-3% cement mixture are shown in Figure 11.

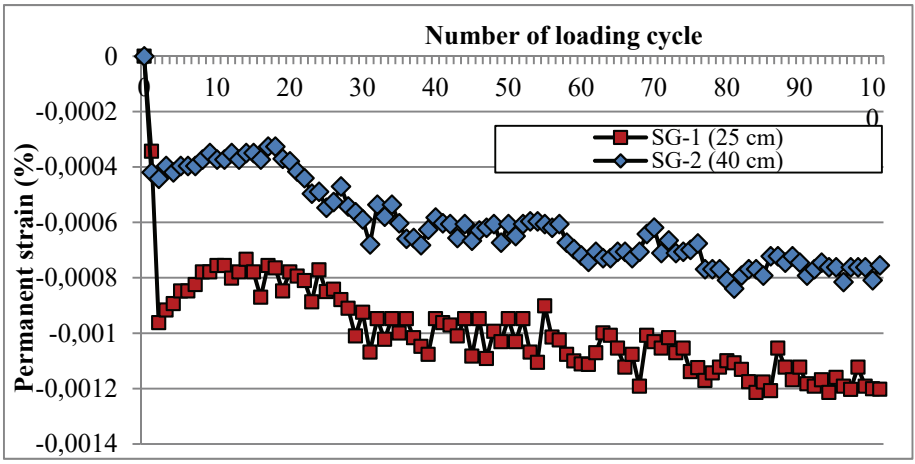

Figure 11 - The measured permanent strain rates of 60% RAP-40% NA-3% cement mixture versus the number of loading cycles

It was determined that initial strains in SG-1 and SG-2 change rapidly, decreased by about 75th cycle, and remained almost constant in the subsequent cycles. The strain rate of about 0.0012% was observed at SG-1, while a change of about 0.0008% at SG-2 occurred. Compared with the base layer made with 100% NA, the strain rates showed a decrease. At the end of the 100 loading cycles, the amount of strain in SG-1 was about 85% lower than that of 100% NA. The strain rate of 100% NA base was 0.009%, while that of 60% RAP-40% NA-3% cement base was 0.0012%. Furthermore, the strain rate obtained at SG-2 for 100% NA base was 0.004% while it decreased by 80% to 0.0008%.

The strain changes caused by the loading cycles, taken from the base layer made with 100% RAP-3% cement mixture and taken with SG-1 and SG-2 devices respectively placed 250 and 400 mm away from the center of the loading plate, are shown in the graph in Figure 12.

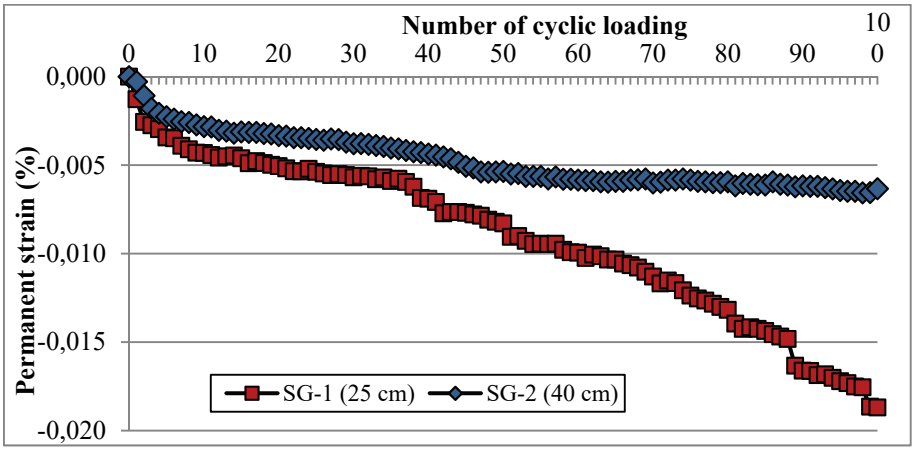

Figure 12 - The measure permanent strain rates of 100% RAP-3% cement mixture versus the number of loading cycles

The largest strains were obtained from 100% RAP-3% cement base layer. At the end of the 100 loading cycles, strains of about 0.018% at SG-1 and about 0.006% at SG-2 for 100% RAP-3% cement mixture were formed. It was observed that the strains obtained from SG-1 continued steadily after about 50 cycles, but in SG-1 increased linearly.

At the end of the 100th cycle, the strains in SG-1 were doubled to 0.018% compared to that of 100% NA mixture. In addition, the strains for 100% NA according to the measurement in SG-2 were 0.004%, it showed a nearly double increase to 0.007% for 100% RAP-3% cement mix. The strain rates obtained from SG-1 and SG-2 for 100% RAP-3% cement mixture were the same as the mixture for 20% RAP-80% NA. Although increasing the RAP percentage in the mixture increases the strains, the strains obtained in the case of increasing the RAP percentage from 20% to 100% are the same in SG-1 and SG-2. It is considered that the reason for the decrease in strain rates is that the cement contained in the 100% RAP-3% cement mixture reduces deformation.

5. CONCLUSIONS

Based on the cyclic plate loading test (CPLT) results presented for the RAP bases, the following conclusions are made:

- As the RAP percentage in the mixtures increases, elastic deformations are increased out of the loading plate but decreased under the plate. The largest elastic deformations for untreated mixtures were obtained at 100% NA mixture under the plate and at 20%RAP-80%NA mixture out of the plate. This is due to the fact that the aged bitumen surrounding the RAP aggregates which adhered the aggregates together due to the compression under the repeated loads.
- Cement treatment reduced the elastic deformations at significant rates. The smallest elastic deformation and strain changes were obtained at 60% RAP-40% NA-3% cement

mixture for all distance. This comparison demonstrates that the cement-treated bases had less elastic responses than the untreated bases due to the binding feature of the cement. The RAP materials with cement treatment can be substituted for unbound aggregate base layers on pavement projects as a reconstruction strategy.

- Unlike cement, the strain rates increased as the RAP percentage in the mixtures increased. The largest strains obtained at 20% RAP-80% NA and 100% RAP-3% cement mixtures. As you moved away from the center of the loading plate, the strains decreased.
- The two most important factors determining road performance were permanent deformation and rutting. But due to poor base, subbase or subgrade conditions, it is difficult to construct roads of good quality. Hence it is important that the design of these layers is well made. Since the deformation of the base layer under traffic loads could adversely affect the coating layer, base layer materials with the least deformations are preferred. However 100% RAP material was too weak and soft as a base layer material therefore, it was blended with natural aggregate and treated with pozzolanic cement to increase the strength and stiffness in this study. Excessive deformations caused by the use of high RAP content significantly reduced with pozzolanic cement treatment. For this reason, the recommended mixture for use in the base layer was 60% RAP-40% NA-3% cement mixture that leads to the lowest deformation and strain rate values.
- This study showed how the RAP material affected the performance of base layers and showed that it was a viable alternative to natural aggregate when treated with pozzolanic cement. The obtained elastic deformation values could be used as reasonable default design input values for pavement designers when the RAP material used as a substitute for natural aggregate base or subbase layer material.

References

[1] Bennert, T., Maher, A., "The Development of a performance specification for granular base and subbase material", Final report no: FHWA-NJ-2005-003, Federal Highway Administration, Washington, 2005.

[2] Chesner, W., Collins, R., MacKay, M., Emery, J., "User guidelines for waste and byproduct materials in pavement construction", Final report no: FHWA-RD-97-148, Federal Highway Administration, Virginia, 1998.

[3] Ooi, P.S.K, "Application of recycled materials in highway projects", Final report no: HWY-L-2005-04, Hawaii Department of Transportation, Highways Division University of Hawaii, Manoa, 2010.

[4] Seferoğlu, A.G., Seferoğlu, M.T., Akpınar, M.V., "Investigation of the effect of recycled asphalt pavement material on permeability and bearing capacity in the base layer", Advances in Civil Engineering, Article ID 2860213, 2018, 1-6, 2018.

[5] Thakur, J.K., Han, J., "Recent development of recycled asphalt pavement (RAP) bases treated for roadway applications", Transportation Infrastructure Geotechnology, 2 (2), 68-86, 2015.

[6] Thompson, M.R., Smith, K.L., "Repeated triaxial characterization of granular bases", Transportation Research Record, 1278, 7-17, 1990.

[7] Wen, H., Warner, J., Edil, T., Wang, G., "Laboratory comparison of crushed aggregate and recycled pavement material with and without high carbon fly ash", Geotechnical and Geological Engineering, 28 (4), 405-411, 2010.

[8] Wu, M.Q., "Evaluation of high percentage recycled asphalt pavement as base course materials", Master Thesis, Washington State University, Washington D.C., 2011.

[9] Copeland, A., "Reclaimed asphalt pavement in asphalt mixtures: State of the practice", Final report no: FHWA-HRT-11-021, Office of Infrastructure Research and Development Federal Highway Administration, Washington D.C., 2011.

[10] Cosentino, P.J., Kalajian, E.H., Bleakley, A.M., Diouf, B.S., Misilo, T.J., Petersen, A.J., Sajjadi, A.M., "Improving the properties of reclaimed asphalt pavement for roadway base applications", Final report no: FL/DOT/BDK81 97702, Florida Department of Transportation, 2012.

[11] McGarrah, E.J., "Evaluation of current practices of reclaimed asphalt pavement/virgin aggregate as base course material", Final report no: WA-RD 713.1, Washington State Department of Transportation, Washington D.C., 2007.

[12] Schaefer, V., Stevens, L., White, D., Ceylan, H., "Design guide for improved quality of roadway subgrades and subbases", Final report no: IHRB Project TR-525, Iowa Highway Research Board, Iowa Department of Transportation, Ames, 2008.

[13] Thakur, J.K., "Experimental study on geocell-reinforced recycled asphalt pavement (RAP) bases under static and cyclic loading", Master Thesis, University of Kansas, Department of Civil, Environment and Architectural Engineering, Kansas, 2011.

[14] Highter, W.H., Clary, J.A., DeGroot, D.J., "Structural numbers for reclaimed asphalt pavement base and subbase course mixes", University of Massachusetts Transportation Center Report, Report no: UMTC-95-2, Department of Civil and Environmental Engineering, University of Massachusetts, Amherst, 1997.

[15] Pokharel, S.K., Han, J., Leshchinsky, D., Parsons, R.L., "Experimental evaluation of geocell-reinforced bases under repeated loading", Int. J. of Pavement Res. and Technol. 11 (2), 114-127, 2018.

[16] Lekarp, F., Isacsson, U., Dawson, A., "State of the art. II: Permanent strain response of unbound aggregates", Journal of Transp. Eng., 126, 76-83, 2000.

[17] Papp, W.J., Maher, M.H., Bennert, T., and Gucunski, N., "Behavior of construction and demolition debris in base and subbase applications", Recycled materials in geotechnical applications, 79, 122-136, 1998.

[18] Attia, M.I.E-S., "Characterization of the structural behavior of reclaimed asphalt pavement as pavement base layer", Ph.D. Thesis, The North Dakota State University, Civil Eng. Department, Fargo, 2010.

[19] Bennert, T., Papp, W.J.Jr., Maher, A., Gucunski, N., "Utilization of construction and demolition debris under traffic-type loading in base and subbase applications", Transp. Res. Rec., 1714, 33-39, 2000.

[20] Garg, N., Thompson, M.R., "Lincoln Avenue reclaimed asphalt pavement base project", Trans. Res. Rec., 1547, 89–95, 1996.

[21] Kim, W., Labuz, J.F., "Resilient modulus and strength of base course with recycled bituminous material", Final report no: MN/RC-2007-05, Minnesota Department of Transportation, 2007.

[22] Wen, H., Wu, M., "Evaluation of high percentage recycled asphalt pavement as base materials", Final report no. TNW2011-15, United States Department of Transportation, 2011.

[23] Yuan, D., Nazarian, S., Hoyos, L.R., Puppala, A.J., "Cement treated RAP mixes for roadway bases", Final report no: FHWA/TX-10/0-6084-1, Federal Highway Administration, Washington D.C., 2010.

[24] Xuan, D.X., Molenaar, A.A.A., Houben L.J.M., "Evaluation of cement treatment of reclaimed construction and demolition waste as road bases", J. of Cleaner Production, 100, 77-83, 2015.

[25] AASHTO: AASHTO T-164-Standard method of test for quantitative extraction of asphalt binder from hot mix asphalt (HMA), Washington D.C., 2014.

[26] ASTM: ASTM D-1557-Standard test methods for laboratory compaction characteristics of soil using modified effort, ASTM International, West Conshohocken, 2000.

[27] AASHTO: AASHTO T-193-Standard method of test for the California bearing ratio, Washington D.C., 2013.

[28] Turkey Department of Transportation Technical Specifications for Highways, Part:402-Base, Turkey Department of Transportation, Highway Technical Specification Manuel, Ankara, 468-470, 2006.

Teknik Dergi, 2019 9597-9620, Paper 558

Evaluation of Statistical Methods for Estimating Missing Daily Streamflow Data

Mustafa Utku YILMAZ[1]
Bihrat ÖNÖZ[2]

ABSTRACT

In this study, it was aimed to investigate the applicability of various statistical estimation methods for the Porsuk River basin, which has sparse streamflow observations. Estimations were performed using regression analysis (REG), the single donor station based drainage area ratio (DAR), the multiple donor stations based drainage area ratio (MDAR), standardization with mean (SM), standardization with mean and standard deviation (SMS), inverse distance weighted (IDW) methods. Two separate studies were conducted for both partially missing data and completely missing data. In order to estimate streamflow statistics for use in SM and SMS methods, logarithmic regression equations were suggested. The promising results obtained from ensemble approaches will provide a significant hydrological contribution to streamflow estimations.

Keywords: Missing data, Porsuk River basin, regression, streamflow estimation.

1. INTRODUCTION

Nowadays, estimation of missing streamflow data for gauged basins (partially missing data) or estimation of streamflow for ungauged basins (completely missing data) is a popular subject that has been researched extensively in hydrological studies because researchers need reliable data to make accurate analyzes [1,2]. In many basin-based studies, there are several reasons for missing data in historical records of meteorological data (precipitation, temperature, evaporation, snow etc.) and hydrological data (streamflow) provided by different institutions. The missing data due to various reasons such as station failures, transportation, and climatic difficulties, human-induced effects etc., creates significant problems in terms of effective water resources planning and management [3]. Especially in developing countries or regions such as Turkey, recorded data of natural events are limited. With these limited values, it is too difficult to reliably determine the hydrological behavior

Note:
- This paper has been received on May 04, 2018 and accepted for publication by the Editorial Board on December 24, 2018.
- Discussions on this paper will be accepted by January 31, 2020.

• https://dx.doi.org/10.18400/tekderg.421091

1 Kirklareli University, Department of Civil Engineering, Kirklareli, Turkey - utkuyilmaz@klu.edu.tr https://orcid.org/0000-0002-5662-9479

2 Istanbul Technical University, Department of Civil Engineering, Istanbul, Turkey - onoz@itu.edu.tr https://orcid.org/0000-0002-4531-2476

of a particular basin. There are significant problems of missing data in most river basins of Turkey. This case is one of the biggest challenges faced by scientists working on streamflow estimation in Turkey [4].

A station for which streamflow data is missing is called the target station and a station used to estimate the missing data is called the donor station. Selection of donor stations that are most likely to be hydrologically similar is the most critical step for a good streamflow estimation because their data will be used to estimate the missing values. The donor station is usually chosen as the nearest station for estimating missing values at the target stations. In other words, the distance is the main selection criterion for donor streamflow station selection. Choosing the nearest streamflow station as the donor streamflow station is preferred in widespread practice, but acceptance of the distance as the primary donor streamflow station selection criterion may not always be correct. Although the distance is currently used as the selection criterion for selecting a donor station, it may be possible to obtain better results by using the most correlated station as the donor station for estimation of target stations [4]. On the other hand, the use of multiple donor stations can provide improved streamflow estimation instead of using a single donor station [1,5].

Many statistical modeling methods require complete and uninterrupted data. In case of missing data, statistical analyses do not provide confidence. Various methods are used to estimate the missing data (partially or completely) using data from the donor station in hydrology sciences. The most common methods for estimating missing data are single and multiple regression analysis [6], interpolation such as kriging and inverse distance weighted (IDW) [7], time series analysis [8, 9], artificial neural networks [10,11]. Flow duration curves, which show the percentage of time that a specific streamflow is equaled or exceeded during a given period, can also be used for estimating missing data [5,12]. Moreover, algorithms such as expectation maximization and nearest neighbors in statistical software packages can be used to estimate missing data [13]. In addition, if there is missing data at the gauging station (partially missing data), the missing data can be replaced easily using the mean imputation method (the mean of the recorded data of the target station). Obviously, this method may not provide good representation [14]. Without depending on only one method, estimating missing data with as many different methods as possible and using the best method compared with others are of great importance.

Drainage area ratio (DAR) method is the most commonly preferred method to estimate streamflow for target stations where streamflow data are not available using data from a single donor station [15,16,17,18]. The multiple donor stations based DAR (MDAR) method was developed by Shu and Ouarda [1]. MDAR produces the streamflow estimations for a target station as the weighted average of the estimations from more donor stations. Their estimation performance was improved by a weighted combination of donor stations [1]. IDW interpolation method, which is a variant of the DAR method, is a widely used method for the estimation of missing data in hydrology [7,19]. In the DAR method, streamflow values are transferred from a single donor station to the target station. However, the IDW method is used for direct streamflow transfer to the target station from multiple donor stations. The estimation performance was improved significantly by expanding the DAR method to consider multiple donor stations [7]. Standardization by the mean streamflow (SM) [20] and maintenance of variance extension method introduced by Hirsch [15], which Farmer and Vogel [20] termed standardization with mean and standard deviation (SMS) are common in

hydrology. These methods are used for estimation of streamflow time series for ungauged basins or gauged basins which have missing data. Regional regression models were developed by Farmer and Vogel [20] to estimate streamflow statistics for use in SM and SMS methods as a function of drainage area and some meteorological parameters. Hirsch [15] showed the suggested method, called the SMS method, has better performance than the DAR, but Farmer and Vogel [20] revealed that both the SM and the SMS methods may not always be superior to the DAR method. Although different methods are used to estimate the missing data, the correlation between the stations should be considered [21]. Thus, a comparison is made between more stations instead of a single station to act as a target station.

In this study, various statistical estimation methods were evaluated for estimating missing daily streamflow data at the selected stations located in the Porsuk River basin. Missing data estimation was applied in two ways as partially missing data and completely missing data (ungauged). First, the missing data at each station was completed with one of the linear and nonlinear regression analysis, DAR, SM and SMS methods (adapted to daily streamflows) according to the performance approach described in the application section. Secondly, DAR, SM, SMS, MDAR and IDW methods were applied to estimate completely missing data of stations. These methods used were preferred to methods such as the artificial intelligence methods because: (1) they do not require much data and (2) they are relatively simple to apply and (3) they are robust and effective methods. There were significant statistical difficulties in both applying and evaluating the methods. One of the biggest challenges of the study was low water potential and a large amount of missing daily data. Another difficulty was that all missing data at the target station could not be completed with the best donor station and another donor station was required.

In order to reduce the uncertainties in individual methods, two of the methods used were weighted according to their relative performance as measured by Nash-Sutcliffe efficiency (NSE) and then combined to obtain the recommended ensemble estimates for each station. The all possible pairwise combinations of the methods are used to employ ensemble approaches for each target station in the study. The performance of these ensemble approaches was compared with individual methods. Statistical parameters (mean and standard deviation) used in the SM and SMS methods were calculated by suggested regression equations based on logarithmic relationships between statistical parameters and drainage area. These regression relationships were obtained for each target station using data from all other stations. A method for estimating missing data should conserve streamflow characteristics such as mean, standard deviation, skewness coefficient. For this purpose, after the missing data for each station are replaced with estimated values, statistical characteristics between long-term completed data and long-term original data were compared. Thus, it was examined whether the statistical structure of the dataset was preserved after the completion process. In addition, it was determined whether there was a difference in the statistical characteristics by comparing the significant percentiles of the flow duration curves of the observed and the estimated dataset.

The objectives of this research are (1) to investigate the use of applied methods for estimating missing daily streamflows for such a difficult basin and (2) to improve the estimation performance of the methods by identifying the most appropriate donor stations and (3) to obtain ensemble approaches that provide more efficient results compared to individual methods.

2. STUDY AREA

Porsuk River basin located in the northwestern part of the Central Anatolia Region of Turkey was selected as the study area (Figure 1). This basin lies between north latitudes of 38°44' to 39°99' and east longitudes of 29°38' to 31°59'. Porsuk River basin is a sub-basin of the Sakarya basin and has a drainage area of about 11000 km². It is one of the most economically important basins. Almost half of the land in the Porsuk River basin is devoted to agricultural activities, and forests and meadows constitute the other half. Residential and industrial areas account for only about 5% of the total basin area. The extensive and intensive agricultural activities are due to the high fertility of the soil. Most of the basin has a typical continental climate, with hot and dry summers and cold and semi-humid winters. Porsuk River with a length of 460 km is one of the longest tributaries of Sakarya River. The river originates at the Murat Mountain and flows in an easterly direction until its confluence with the Sakarya River. Sakarya River with a length of 824 km is the third longest river in Turkey and flows into the Black Sea. The long-term average annual precipitation for the whole basin is approximately 450 mm. Thus, the water potential of the basin is slightly lower than Turkey's long-term (1970-2010) average annual precipitation of 643 mm [22].

Figure 1 - Location map of Porsuk River basin in Turkey

3. DATA

Daily streamflow data used in this study were provided from the State Hydraulic Works (DSI) of Turkey. Some details of the stations and the statistical characteristics of the streamflow data considered in this study are presented in Table 1. Performance of missing data estimation methods was tested for selected streamflow gauging stations in the Porsuk River basin. Observed daily streamflow data were available for 6 stations on the same stream for the 21 years investigated period of 1990-2010. Figure 2 shows the locations of the 6 selected stations. The selected stations are not located downstream of a dam or reservoir. Data of the

stations were missing for at least 2 years and at most 5 years. The years of measurement of the streamflow data for each station are given in Figure 3. Selected 6 stations have highly logarithmic linear relationships between statistical parameters (long-term mean and standard deviation) and their drainage area is as shown in Figure 4. The coefficients of determination (R^2) of each relationship are 0.9667 for mean and 0.9644 for standard deviation, respectively. The nearest and the most correlated stations for each station were identified and provided in Table 2.

Table 1 - Characteristics of the stations and statistics calculated from daily mean streamflow data

Station Number	D12A033	D12A055	D12A063	D12A093	D12A181	E12A003
Drainage Area (km^2)	2432	297	290,7	153,1	3810,5	3938,4
Elevation (m)	951	1062	826	1130	912	855
Observations (days)	7670	7670	7670	7670	7670	7670
Obs. with missing data (%)	9,5	19,0	9,5	23,8	14,3	0,0
Obs. without missing data (%)	90,5	81,0	90,5	76,2	85,7	100,0
Mean (m^3/s)	2,432	0,862	0,594	0,512	5,172	4,666
Std. deviation	4,815	1,734	1,348	1,022	6,323	4,535
Zero (%)	0,00	18,04	0,17	7,97	0,00	0,00

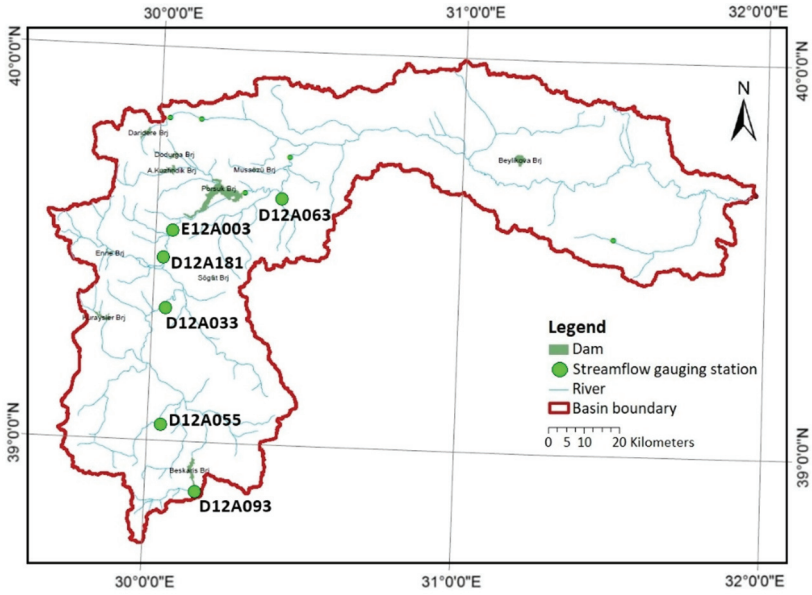

Figure 2 - Locations of the 6 selected streamflow gauging stations used for this study

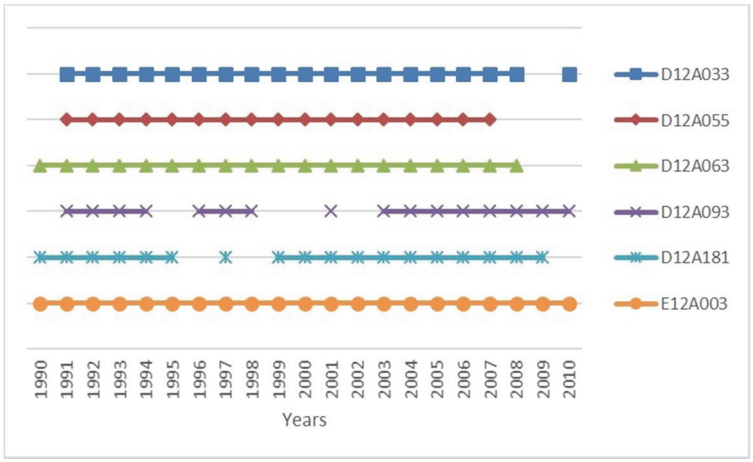

Figure 3 - The years of measurement of the streamflow data for each station

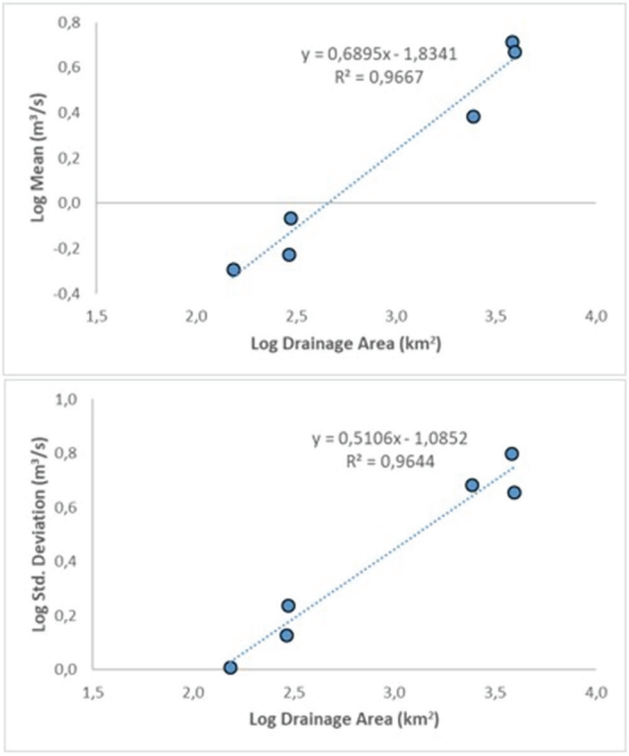

Figure 4 - Logarithmic linear relationship between mean and std. deviation of long-term daily streamflow and drainage area

Table 2 - The nearest and the most correlated stations to each station

	The Nearest		Distance (km)		The Most Correlated		Correlation Coefficent (r)	
Station Number	**1st station**	**2nd station**	**1st station**	**2nd station**	**1st station**	**2nd station**	**1st station**	**2nd station**
D12A033	D12A181	E12A003	13,20	20,58	D12A181	E12A003	0,85	0,83
D12A055	D12A093	D12A033	22,62	34,56	E12A003	D12A181	0,74	0,73
D12A063	E12A003	D12A181	32,27	37,24	D12A055	D12A093	0,62	0,56
D12A093	D12A055	D12A033	22,62	54,30	E12A003	D12A181	0,75	0,73
D12A181	E12A003	D12A033	7,60	13,20	E12A003	D12A033	0,95	0,85
E12A003	D12A181	D12A033	7,60	20,58	D12A181	D12A033	0,95	0,83

4. METHODS

The methods used to estimate the missing data discussed in this study are given below.

a) Regression analysis (REG): Regression analysis is a statistical method that is commonly used to explain relationships among variables. In this study, the linear, exponential and logarithmic regression analysis are applied. The mathematical relationship with the highest R^2 value between the two stations was taken into account to estimate daily streamflow at the target station. The daily streamflow, Q (m^3/s) between target and donor station is represented by

$$Q_{target} = \alpha Q_{donor} + \beta \quad (1)$$

$$Q_{target} = \alpha Q_{donor}^{\beta} \quad (2)$$

$$Q_{target} = \alpha ln Q_{donor} + \beta \quad (3)$$

where α and β are the coefficients of the regression equations. They are calculated using concurrent daily streamflow data at the donor and the target stations.

b) Drainage area ratio (DAR): The applicability of the DAR method is closely related to the hydrological similarity (similar drainage area, climate, and geographical conditions) between two stations. This method assumes that the streamflow per unit area of hydrologically similar basins is equal. That is, for any given days,

$$Q_{target} = \frac{A_{target}}{A_{donor}} Q_{donor} \quad (4)$$

where the ratio of drainage areas for the target and donor station, A_{target}/A_{donor}, is used to transfer streamflow at the donor station, Q_{donor}, to that at the target station, Q_{target}.

DAR method is commonly used when the stations are located on the same stream and the ratio between the drainage areas of the donor station and the target station (A_{target}/A_{donor}) is between 0.5 and 1.5 [23].

c) Standardization with mean (SM): This method takes into account the ratio of streamflow to the mean streamflow. Mathematically,

$$Q_{target} = \frac{\mu_{Q_{target}}}{\mu_{Q_{donor}}} Q_{donor} \quad (5)$$

where Q is the daily streamflow at the subscripted station and μ is the mean of the flows at the subscripted station.

In this study, the SM method applied with annual (SM1) and monthly (SM12) variations. SM1 standardizes the daily time series with the annual mean streamflow, while SM12 standardizes the daily time series with monthly mean streamflow.

d) Standardization with mean and standard deviation (SMS): This method is based on assumption that the standardized streamflows at both a target and a donor station are approximately equal, and can be expressed as:

$$Q_{target} = \mu_{Q_{target}} + \sigma_{Q_{target}} \left(\frac{Q_{donor} - \mu_{Q_{donor}}}{\sigma_{Q_{donor}}} \right) \quad (6)$$

where μ and σ are the mean and standard deviation of the streamflows at the subscripted station.

In this study, the SMS method applied with annual (SMS1) and monthly (SMS12) variations. The distinction between these variations of the SMS method is similar to the distinction between SM1 and SM12.

Two standardization methods (SM and SMS) described above require streamflow statistics (mean and standard deviation) for the target station. Linear regression equations to estimate streamflow statistics (mean and standard deviation) at the target station for use in SM and SMS methods are suggested in this study. Mean and standard deviation of streamflow data should be highly related to drainage area on account of its statistic stationarity. Considering this assumption, suggested equations were derived from logarithmic relationships between statistical parameters and drainage area. After some algebraic manipulations, these base 10 logarithmic equations can be shown as:

$$\theta = 10^{\beta} A^{\alpha} \quad (7)$$

where θ is mean or standard deviation of the streamflows and A is the drainage area, α and β are the slope of the regression line (regression coefficient) and intercept value of regression line (constant), respectively. A single regression equation is required for the annual methods (SM1 and SMS1) whereas a regression equation for each month is required for the monthly methods (SM12 and SMS12).

e) Multiple donor stations based DAR (MDAR): This method produces the streamflow estimations at a target station as the weighted average of the estimations from n donor stations which are calculated as:

$$Q_{target} = \frac{\sum_{i=1}^{n} w_i Q_{d_i}}{\sum_{i=1}^{n} w_i} \quad (8)$$

$$w_i = \frac{\frac{1}{d_i}}{\sum_{i=1}^{n} \frac{1}{d_i}} \quad (9)$$

$$d_i = \sqrt{\left(A_{target} - A_{donor}\right)^2} \quad (10)$$

where Q_{d_i} is the estimation from the donor station i, and w_i is the weight assigned to the donor station i, and d_i is the similarity distance measure between the target station and donor station i, and A is the drainage area at the subscripted station.

f) Inverse distance weighted (IDW): This method is mathematically expressed as:

$$q_{target} = \sum_{i=1}^{n} w_i q_{donor_i} \quad (11)$$

$$w_i = \frac{\frac{1}{d_i{}^p}}{\sum_{i=1}^{n} \frac{1}{d_i{}^p}} \quad (12)$$

$$\sum_{i=1}^{n} w_i = 1 \quad (13)$$

where q is the area normalized streamflow value ($m^3/s/km^2$) at the subscripted station and n is the total number of donor stations considered for the interpolation. The distance between the target and donor station d is calculated individually for each of the n donor stations. d is the distance between two stations, p is power parameter equal to 2 in this study and w is the interpolation weights. The sum of the weights assigned to each donor station is equal to 1. Distance, d, between two stations was calculated using a variation of the Haversine Formula [24]:

$$d = arccos\left(sin(lat_1)\, x\, sin(lat_2) + cos(lat_1)\, x\, cos(lat_2)\, x\, cos(lon_2 - lon_1)\right) x\, r \quad (14)$$

where lat_1 and lon_1 represent latitude and longitude in radians of the station 1, respectively and lat_2 and lon_2 represent the latitude and longitude in radians of the station 2, respectively. The radius of the earth, r, is approximately 6378.1 km.

4.1. Proposed Method (Ensemble Streamflow Estimation)

In the study, the ensemble approaches combining two methods were proposed in order to get more consistent estimation and reduce uncertainties in the individual methods used. These approaches were applied by considering the weighted average of any two individual methods. All possible double combinations of individual method 1 and 2 (i.e. DAR-SM, DAR-SMS, DAR-IDW, MDAR-IDW, IDW-SM, IDW-SMS etc.) were considered. The mathematical expression of estimated streamflow, $\hat{Q}$, using the weighted ensemble approach (adapted from Farmer and Vogel) [20] is given in Equation (15).

$$\hat{Q}_{ensemble} = w\hat{Q}_{method_1} + (1 - w)\hat{Q}_{method_2} \quad (15)$$

where $\hat{Q}$ is the daily streamflow estimated from subscripted method and w is a weight (bounded by 0 and 1) which is based on the relative efficiency of any two methods. The weight was estimated by using the Langmuir equation as the ratio of NSE of any two methods as given in Equation 16 and Equation 17.

$$w = \frac{\varphi}{1+\varphi} \tag{16}$$

$$\varphi = \frac{\left(NSE_{method_2}-1\right)^2}{\left(NSE_{method_1}-1\right)^2} \tag{17}$$

4.2. Construction of Flow Duration Curves

A flow duration curve (FDC) was constructed from the daily streamflow for each station. The FDC was separated into three segments which represent different hydrological conditions: high-flow ($Q_{0.1}$, $Q_{0.5}$, Q_2, Q_5, Q_{10}), middle-flow (Q_{20}, Q_{30}, Q_{40}, Q_{50}, Q_{60}), low-flow (Q_{70}, Q_{80}, Q_{90}, Q_{95}, Q_{99}). Each percentile (streamflow exceedence probabilities) represents a different segment of the FDC.

4.3. Evaluation Criteria

Nash-Sutcliffe efficiency (NSE) [25] and root mean square error (RMSE) were used to evaluate the performance of each method. Their formulations are given as follows:

$$NSE = 1 - \frac{\sum_{i=1}^{n}\left(X_i^{obs}-X_i^{est}\right)^2}{\sum_{i=1}^{n}\left(X_i^{obs}-\overline{X^{obs}}\right)^2} \tag{18}$$

$$RMSE = \sqrt{\frac{\sum_{i=1}^{n}\left(X_i^{obs}-X_i^{est}\right)^2}{n}} \tag{19}$$

where X_i^{obs} is the i-th observed value, X_i^{est} is the i-th estimated value and $\overline{X^{obs}}$ is the mean of all the observed data for a time series of length n. The ideal values NSE and RMSE are 1 and 0, respectively.

In this study, the methods were tested using a jack-knife approach on the original data. In jack-knife (leave-one-out) approach, each station is in turn considered in common period as ungauged (completely missing) for obtaining a streamflow estimation in that station.

5. APPLICATION OF THE METHODS

5.1. Completion of Missing Data (Partially Missing Data)

For this application, data from the most appropriate donor station was needed to complete the missing data of each target station. Each station whose data are available was selected as a donor station of the target station for REG, DAR, SM and SMS methods. Because the

estimated missing data were not compared with the actual data, the estimation performance of methods was evaluated on values before and after the missing data, where observed values are available. Although this evaluation approach does not provide a real estimation performance, it provides a strong emphasis in favour of the estimated values. The most appropriate donor stations of the target station were identified, giving the best NSE and RMSE results according to each method. Then, the missing data at each station was completed with the estimated values obtained from the most appropriate donor stations. In this way, the complete 21-year daily streamflow data were obtained for each station. The linear (Equation 1), exponential (Equation 2) and logarithmic (Equation 3) regression analysis (REG) were applied to express mathematically the relationships between stations. Coefficients of determination, R^2, were calculated to assess the relationship between stations. The mathematical relationship with the highest R^2 value between the two stations was used in the study. As an example, the relationships obtained for one station was given in Figure 5. Prior to logarithmic regression analysis, streamflow data that were zero were replaced with one percent of the minimum observed daily flow from the dataset of each station in order to avoid problems related to log-transforming values of zero. If streamflow data from the most appropriate donor station were also missing, streamflow data from the next most appropriate donor station were used to estimate missing streamflow data at the target station. When the intercept value (constant) was negative in the calculated regression equations, these equations generated some negative streamflow values. These negative values were replaced with zero streamflow.

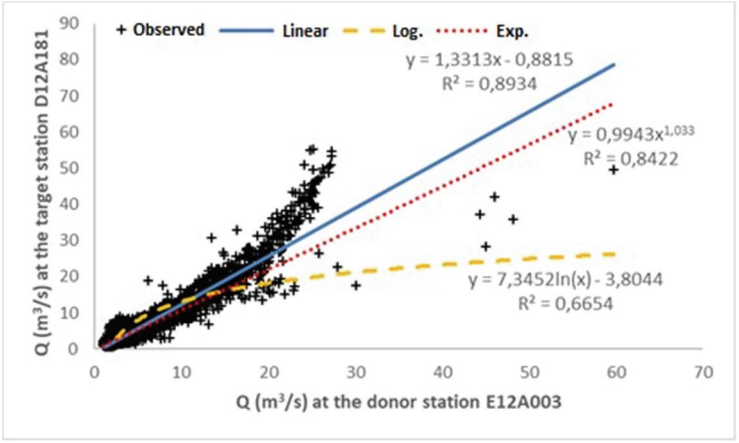

Figure 5 - Investigation of relationships between stations and selection of mathematical equations

5.2. Estimation of Streamflow for Ungauged (Completely Missing Data)

Two separate study periods for ungauged application were conducted, one for simultaneous common years of all stations and the other for 21 years (completed data) of all stations. The daily streamflow data were estimated for assumed completely missing data (ungauged). First, simultaneous common years of all stations were determined in a 11 year period (1991, 1992, 1993, 1994, 1997, 2001, 2003, 2004, 2005, 2006, 2007). Each of the stations was considered

ungauged in turn. In other words, the data record of one of the stations in this study area was kept out from the database and considered as an ungauged station. Each of the other stations in turn was selected as the donor station of the ungauged station for the DAR, SM and SMS methods. All of the other stations (all potential donors) were selected as the donor stations of the ungauged station for the MDAR and IDW methods. Then, the daily streamflow data for the ungauged station were estimated using the data from the donor stations. This process was repeated for all target stations considered. The actual daily streamflow data were used to evaluate the estimation performance of methods. Secondly, the same procedure was repeated using 21 years of data for each station. Ensemble estimations were generated using the best possible results of individual methods for 21 year period. In order to find the combination of two methods that gave the best streamflow estimates of the target stations, the all possible ensemble approaches combining two methods were tried.

In this study, it was necessary to estimate the mean and standard deviation of each target station for use in SM and SMS methods. Therefore, each station in turn was considered as a target station, and logarithmic linear relationships between statistical parameters (mean and standard deviation) and drainage areas were obtained for each target station using data from all other stations. For example, the logarithmic linear regression equations obtained for station D12A063 have 0.972 R^2 value for mean, and 0.9622 R^2 value for standard deviation, respectively (Figure 6a). For station D12A181, R^2 values of each relationship are 0.9654 for mean and 0.9618 for standard deviation, respectively (Figure 6b). The obtained logarithmic equations were converted into algebraic equations (Equation 7) as explained in the SM and SMS methods. The drainage area of the target station was replaced by the A parameter in these equations, and then the long-term mean and standard deviation of the target station were calculated. The equations of the SMS method generated negative values when the difference between streamflow value and mean was larger than the estimated mean value. When the equations generated negative values, the negative values were replaced with zero streamflow.

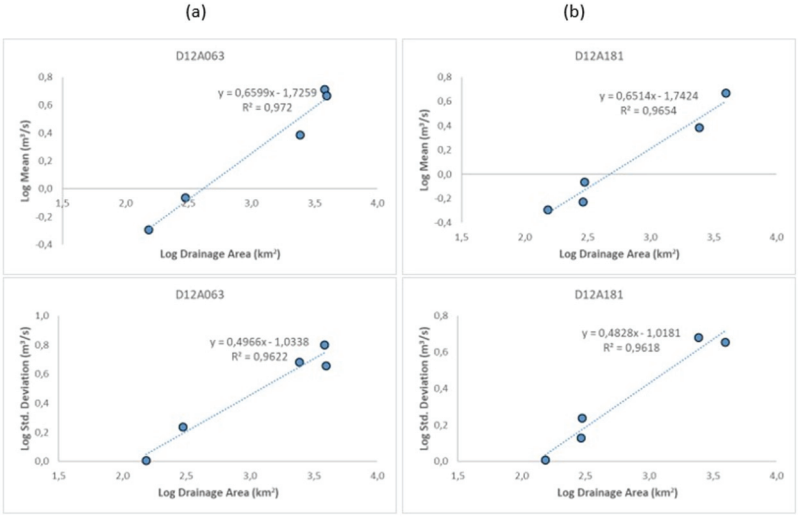

Figure 6 - Logarithmic linear relationships obtained (a) for station D12A063 and (b) for station D12A181

5.3. Estimation of the Flow Duration Curves

The flow duration curves (FDC) of the estimated values giving the best NSE results for each individual method were estimated. The selected 15 percentiles for different hydrological conditions of 11 year and 21 year FDCs of observed and estimated daily streamflow were compared and will be presented in section 6.

6. RESULTS AND DISCUSSION

The results of partially missing (completion of missing data) and completely missing (assumed ungauged) applications were described below, respectively.

In order to determine the missing data completion method, Figure 7 shows the range of the best NSE and RMSE values of each station for each individual methods. Results showed that the REG method for each station gave better NSE and RMSE values than the other methods, according to the evaluation approach of the performance of the methods to complete the missing data. The mean of the NSE values was 0.66 and the mean of the RMSE values was 1.67.

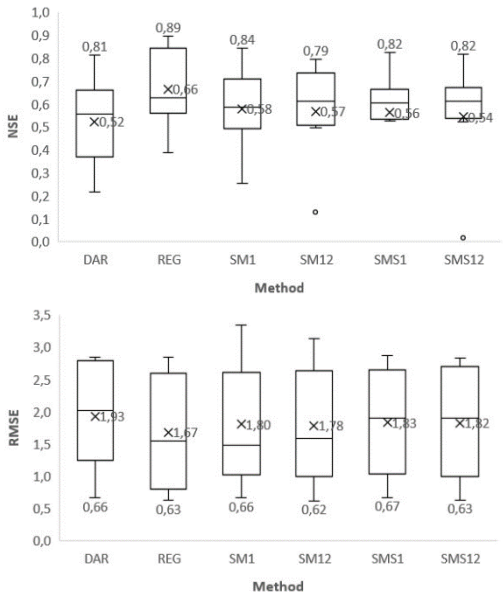

Figure 7 - Performance evaluation of the methods for missing data completion

Also, the REG method gave satisfactory results in terms of estimating missing data in preserving streamflow characteristics (mean, standard deviation, skewness) (Table 3). Unfortunately, there was no station in the study area with the highest correlation to the data of stations D12A063. Thus, missing data at this station were completed using the next most correlated station whose data was available. The results after completion of data indicated

that the obtained estimation was statistically significant and the statistical structure of the data for each station was mostly preserved after the completion process (Table 3).

Table 3 - Long-term statistical parameters for completed data of each station

Target station	Method	Donor station	R^2	Mean	Std
D12A033	REG-Exp	D12A181	0,81	2,413	4,716
D12A055	REG-Linear	E12A003	0,55	0,851	1,646
D12A063	REG-Exp	D12A093	0,33	0,608	1,302
D12A093	REG-Linear	E12A003	0,56	0,568	1,033
D12A181	REG-Linear	E12A003	0,89	5,330	6,333

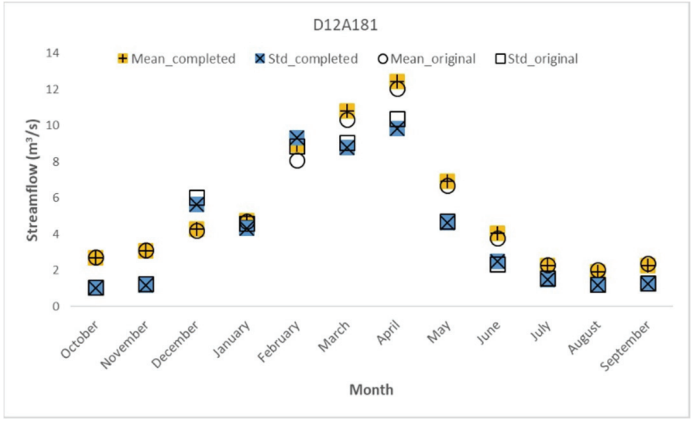

Figure 8 - Comparison of long-term statistical parameters between the completed data and original data of station D12A181

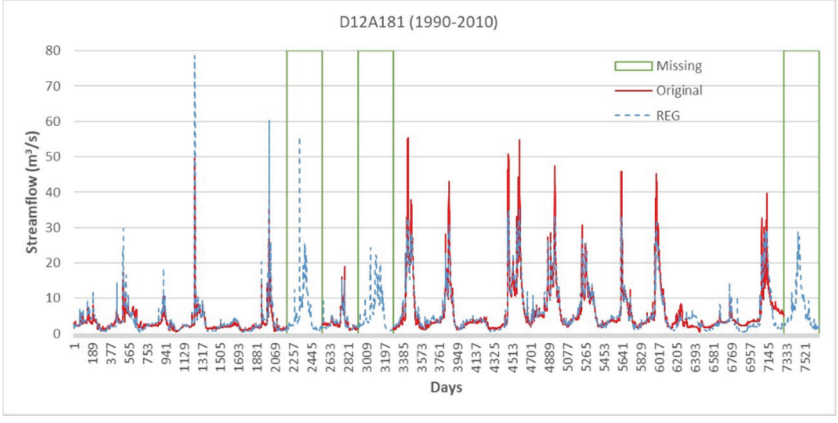

Figure 9 - The observed and estimated daily streamflow data of station D12A181

For example, as shown in Figure 8, when long-term monthly mean and standard deviation between completed data and original data of station D12A181 were compared, it was determined that there were no significant differences. The missing data of the station D12A181 were completed by a mathematical relation depending on correlation and the complete 21-year data of the station were obtained (Figure 9).

Figure 10 contains all estimates obtained for each station using each individual method for 11 year period and for 21 year period. For the 11 year period, the graphical overview for the estimation performance of each model was presented in the box plots (Figure 10a and Figure 10b). The ranges of NSE values resulted using a single donor from DAR, SM1, SM12, SMS1, and SMS12 methods for all stations were; −24.43 (outlier) to 0.82, −1.37 (outlier) to 0.85, −1.44 (outlier) to 0.79, −1.23 (outlier) to 0.81 and −0.83 (outlier) to 0.79, respectively. The ranges of NSE values resulted using all potential donors from MDAR and IDW methods for all stations were; −0.48 to 0.80, and 0.50 to 0.86 (outlier), respectively. The mean NSE values of these seven methods were −2.06, 0.17, 0.24, 0.23, 0.28, 0.36, and 0.59, respectively. For the 21 year period, the graphical overview for the estimation performance of each model was presented in the box plots (Figure 10c and Figure 10d). The ranges of NSE values resulted using a single donor from DAR, SM1, SM12, SMS1, and SMS12 methods for all stations were; −29.51 (outlier) to 0.82, −2.41 (outlier) to 0.87, −0.87 to 0.85, −0.62 to 0.84 and −0.33 to 0.83, respectively. The ranges of NSE values resulted using all potential donors from MDAR and IDW methods for all stations were; −0.14 to 0.82, and 0.27 (outlier) to 0.89 (outlier), respectively. The mean NSE values of these seven methods were −3.16, 0.09, 0.24, 0.28, 0.29, 0.40, and 0.55, respectively.

For both application periods, the DAR method demonstrated the greatest variability, while the IDW method exhibited the least variability. Where the ratio of the drainage areas of the target and donor station were greater than 1.5, almost all NSE values resulted from DAR method were negative. The best NSE results of each station were given in Table 4 for both 11 year period and for 21 year period. According to the results, the methods using multiple donors were superior than the methods using a single donor. For all target stations in the study area, the D12A181 or E12A003 mainstream stations were found to be good donor station options. Estimation performance of the individual methods for the 21 year period at 4 out of 6 stations was better than those for the 11 year period.

Table 4 - The best NSE results of each station

	11 year period			21 year period		
Target Station	**Method**	**Donor Station**	**NSE**	**Method**	**Donor Station**	**NSE**
D12A033	**MDAR**	All potential donors	0,56	**SM12**	D12A181	0,70
D12A055	**SM12**	D12A181	0,64	**SMS12**	E12A003	0,62
D12A063	**IDW**	All potential donors	0,53	**IDW**	All potential donors	0,27
D12A093	**SM12**	D12A181	0,58	**SMS1**	E12A003	0,63
D12A181	**IDW**	All potential donors	0,86	**IDW**	All potential donors	0,89
E12A003	**SM1**	D12A181	0,85	**SM1**	D12A181	0,87

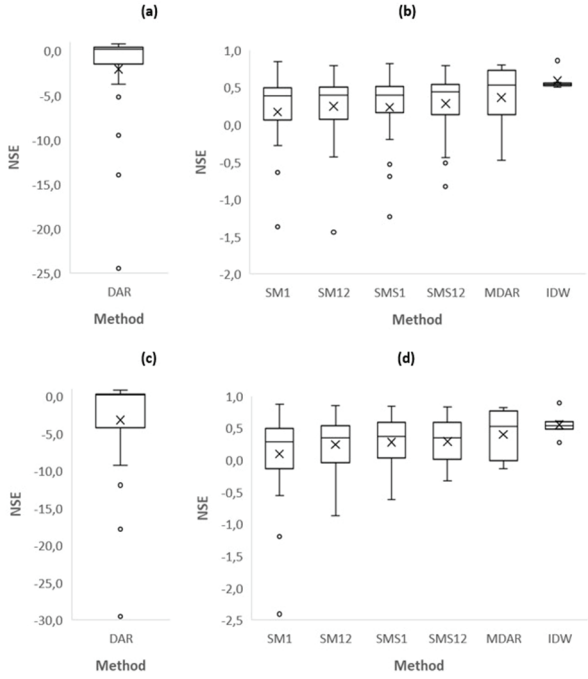

Figure 10 - Statistical summary of NSE performance of the individual methods (a) DAR method for 11 year period, (b) other methods for 11 year period, (c) DAR method for 21 year period, (d) other methods for 21 year period

The performance of the ensemble approaches, which combine two individual methods, showed a slight improvement compared to the best individual methods. NSE values of the best ensemble approaches for each station were given in Table 5. As shown Figure 11 the best ensemble approach for each station was better or almost of equal performance compared to the best individual method for each station.

Table 5 - NSE values of the best ensemble approach for each station

Target station	The best ensemble approach	NSE
D12A033	MDAR-SM12	0,72
D12A055	MDAR-SMS1	0,65
D12A063	DAR-SMS1	0,35
D12A093	IDW-SMS1	0,67
D12A181	IDW-SMS1	0,89
E12A003	IDW-SM1	0,87

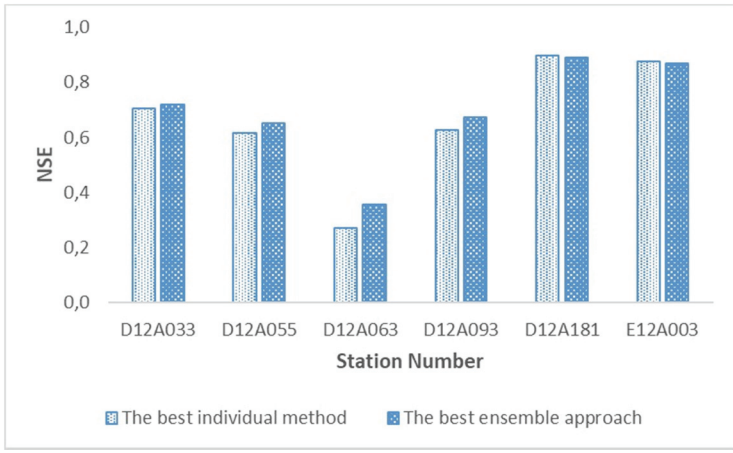

Figure 11 - Comparison of NSE performance between the best individual methods and the best ensemble approaches for each station.

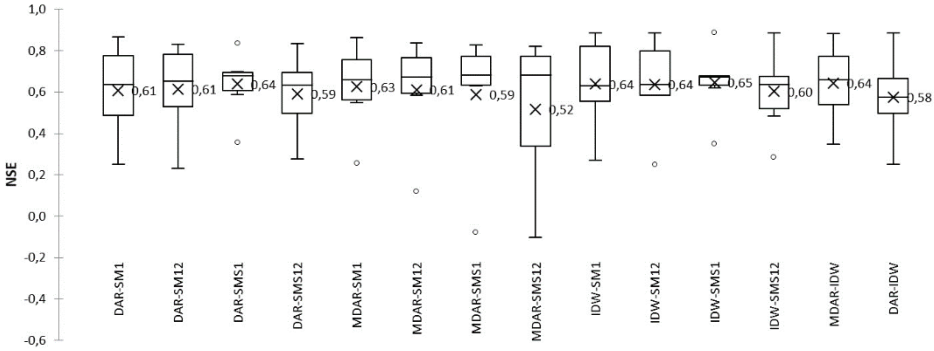

Figure 12 - Comparison of NSE values of all possible ensemble approaches

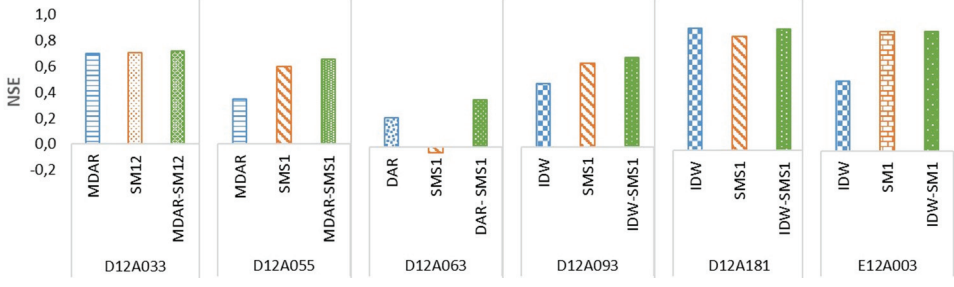

Figure 13 - Comparative performance evaluation of the individual methods and the best ensemble approach which is a combination of these individual methods

The box plots of NSE values for all stations using all possible ensemble approaches were presented in Figure 12. The mean NSE value was slight higher for IDW-SMS1 than the other ensemble approaches. Also, IDW-SMS1 had the least variability. As shown in Figure 13, the ensemble approaches combining two individual methods produced generally better results than individual methods.

The scatter plots between observed and estimated streamflow using DAR, SMS1, IDW methods and the best ensemble approach (IDW-SMS1) for station D12A181 were shown in Figure 14. The estimated streamflow plotted against the observed streamflow show a good match except for observed peak values of streamflow (Figure 14). The estimated values matched the observed values reasonably well, with R^2 of 0.93 for the best ensemble approach (IDW-SMS1) for station D12A181. The Nash-Sutcliffe efficiency (NSE) indicates how well the plot of observed against estimated streamflow data fits the 1:1 line. DAR, SMS1, IDW, and IDW-SMS1 have good method performance with NSE values of 0.82, 0.84, 0.89 and 0.89, respectively.

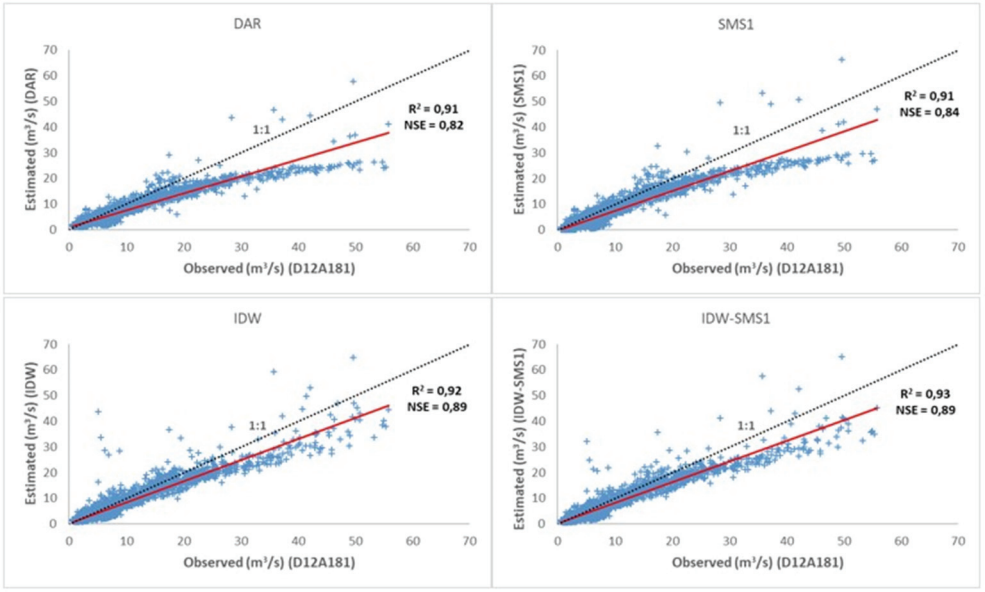

Figure 14 - Comparison between observed and estimated streamflow using DAR, SMS1, IDW method and the best ensemble approach (IDW-SMS1) for station D12A181

Estimation performance evaluation was also conducted for flow duration curves (FDC). Figure 15 illustrated the worst (D12A063) and the best (D12A181) station results for estimated FDC. The NSE values at each hydrological condition (high flow, middle flow, low flow) were calculated. The results indicated that estimated 21-year flow duration curves have better agreement with observed (original) flows than estimated 11-year flow duration curves.

Regional some descriptive statistics as the minimum, mean, maximum, and standard deviation of the estimates given in Table 6 and Table 7 showed a close match between the observed and estimated values. Both for 11 year period and for 21 year period (1990-2010), except for $Q_{0.1}$ and Q_{99}, all of the percentiles of the estimates obtained by the method with the best performance for each station, showed high coefficient of determination (linear relationship between mean observed and mean estimated values).

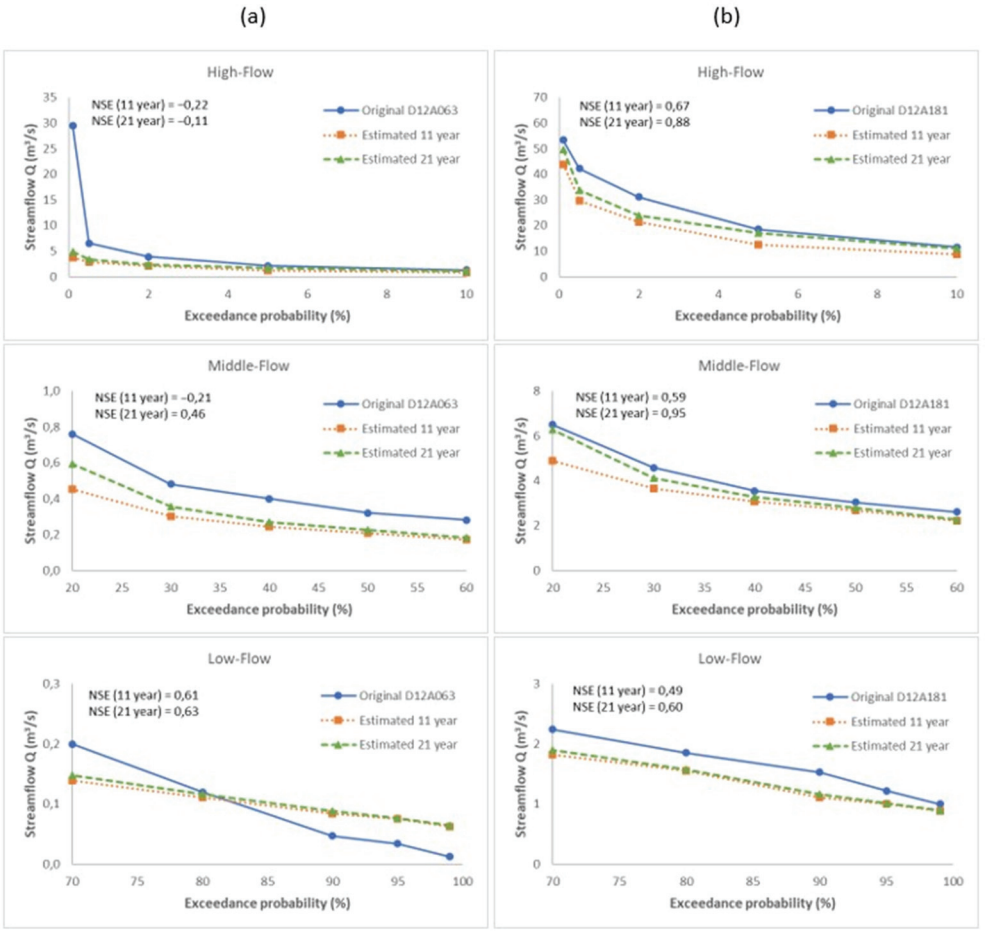

Figure 15 - Comparison of observed and estimated 15 percentiles of different hydrological conditions using the best individual method (a) for station D12A063 (the worst) and (b) for station D12A181 (the best)

Table 6 - Regional results of the estimation of the 15 percentile flows for 11 year period

	Percentile Flow	R^2	Observed				Estimated			
			Min	**Mean**	**Max**	**Std**	**Min**	**Mean**	**Max**	**Std**
High-flow	$Q_{0.1}$	0,57	7,5	30,7	62,7	23,5	3,7	19,9	43,8	17,4
	$Q_{0.5}$	0,81	5,0	17,7	36,7	13,7	2,9	15,2	30,3	12,6
	Q_2	0,89	3,3	12,3	25,4	9,6	2,1	10,7	21,5	9,0
	Q_5	0,99	1,8	6,7	13,9	5,2	1,2	6,1	12,6	5,1
	Q_{10}	0,98	1,0	4,5	9,9	3,9	0,8	4,2	8,7	3,7
Middle-flow	Q_{20}	0,95	0,5	2,5	5,9	2,4	0,5	2,4	4,9	2,1
	Q_{30}	0,93	0,3	1,8	4,2	1,8	0,3	1,8	3,6	1,6
	Q_{40}	0,90	0,2	1,5	3,5	1,6	0,2	1,4	3,1	1,3
	Q_{50}	0,87	0,1	1,2	3,1	1,4	0,2	1,2	2,7	1,2
	Q_{60}	0,84	0,1	1,0	2,6	1,2	0,1	1,0	2,2	1,0
Low-flow	Q_{70}	0,83	0,0	0,9	2,3	1,1	0,1	0,9	1,8	0,9
	Q_{80}	0,81	0,0	0,7	1,9	0,9	0,0	0,7	1,6	0,7
	Q_{90}	0,81	0,0	0,5	1,5	0,7	0,0	0,6	1,3	0,6
	Q_{95}	0,81	0,0	0,5	1,3	0,6	0,0	0,5	1,1	0,5
	Q_{99}	0,77	0,0	0,4	1,1	0,5	0,0	0,4	0,9	0,4

Table 7 - Regional results of the estimation of the 15 percentile flows for 21 year period (1990-2010)

	Percentile Flow	R^2	Observed				Estimated			
			Min	**Mean**	**Max**	**Std**	**Min**	**Mean**	**Max**	**Std**
High-flow	$Q_{0.1}$	0,72	8,2	34,9	56,3	18,5	4,8	25,5	49,7	20,0
	$Q_{0.5}$	0,79	6,3	21,0	42,1	13,9	3,4	18,5	33,7	14,8
	Q_2	0,91	3,8	14,7	29,0	10,0	2,4	13,0	23,8	10,0
	Q_5	0,96	2,0	9,3	19,0	6,9	1,7	8,9	17,2	6,8
	Q_{10}	0,94	1,2	6,0	12,2	4,6	1,1	5,6	11,0	4,4
Middle-flow	Q_{20}	0,87	0,7	3,4	7,1	2,7	0,6	3,1	6,3	2,6
	Q_{30}	0,85	0,5	2,2	4,8	1,9	0,4	2,0	4,1	1,8
	Q_{40}	0,82	0,3	1,7	3,7	1,6	0,2	1,6	3,3	1,5
	Q_{50}	0,82	0,2	1,4	3,2	1,4	0,1	1,3	2,8	1,3
	Q_{60}	0,80	0,1	1,1	2,7	1,2	0,0	1,1	2,3	1,1
Low-flow	Q_{70}	0,78	0,0	0,9	2,3	1,1	0,0	0,9	1,9	0,9
	Q_{80}	0,78	0,0	0,7	2,0	0,9	0,0	0,7	1,6	0,7
	Q_{90}	0,77	0,0	0,5	1,5	0,7	0,0	0,5	1,2	0,6
	Q_{95}	0,80	0,0	0,5	1,3	0,6	0,0	0,5	1,0	0,5
	Q_{99}	0,66	0,0	0,4	1,2	0,5	0,0	0,4	0,9	0,4

7. CONCLUSION AND RECOMMENDATION

In this study, two separate application trials were conducted in case of both partially missing data and completely missing data (ungauged). In partially missing data application, REG, DAR, SM and SMS methods were used to complete the missing data at the target station. With the evaluation approach described in the application section, the most appropriate completing method was selected for each station. Missing data at each target station were

completed with the selected methods. Thus, the complete time series of 21 years was obtained for each station. In completely missing data application (each of the target stations was in turn considered as ungauged), DAR, SM, SMS, MDAR, and IDW methods were used to estimate daily streamflow at the ungauged station. Individual methods were assessed with observed 11 year period and completed data (21 year period). The results showed that the use of multiple donor stations significantly improved the estimates at the target station. The estimates obtained from the IDW method were found generally to be superior to other individual methods. The DAR method had an unacceptable performance with negative NSE values for most estimations in this study area. Ensemble approaches combining two individual methods were proposed in order to obtain more significant estimates in the study. Proposed ensemble approaches are carried out for only 21 year period. All possible ensemble approaches combining individual methods used in the study were tested. Thus, promising estimation results were obtained for each station. In the study, it is not claimed that any method can give always much better results than other methods. However, ensembles approaches combining individual methods can work well and achieve good estimation performance, although they are not always superior to individual methods.

Improving streamflow estimations is critical to a more effective and sustainable management of water resources in ungauged or limited gauged basins. Ensemble streamflow estimations can be used to improve the reliability of hydrological estimations. It is our suggestion that future studies should focus on the issue concerning which can increase the reliability of estimations in ungauged basins. In this study, both estimation of daily streamflows and flow duration curves, which have an important role in the development and operation of water resources, were implemented successfully in the Porsuk basin where the streamflow data are missing and the number of stations with streamflow data in the common long period (at least 10 years) is limited. Finally, successful results obtained in such a poorly gauged basin are expected to contribute to the streamflow estimation literature.

Symbols

A : Drainage area

A_{donor} : Drainage area for the donor station

A_{target} : Drainage area for the target station

d : The distance between two stations

d_i : Similarity distance measured between the target station and donor station i

lat : Latitude in radians of the station

lon : Longitude in radians of the station

n : The total number of donor stations

p : The power parameter

q : The area normalized streamflow value

Q : Daily streamflow

Q_{donor} : Daily streamflow for the donor station

Q_{target} : Daily streamflow for the target station

$\widehat{Q}$: Daily streamflow estimated from the subscripted method

r : The radius of the earth

R^2 : The coefficient of determination

w : Weight

w_i : The weight assigned to the donor station i

X_i^{obs} : The i-th observed value

X_i^{est} : The i-th estimated value

$\overline{X^{obs}}$: The mean of all the observed data for a time series of length n

α : The coefficients of the regression equations

β : The coefficients of the regression equations

θ : The mean or standard deviation of the streamflows

μ : The mean of the streamflow

σ : The standard deviation of the streamflow

φ : The ratio

Acknowledgements

This study was supported by the Research Fund of Istanbul Technical University under the project 'Improvement of Streamflow Estimation in Ungauged Basins' (Project number: 40717). The authors thank the State Hydraulic Works (DSI) of Turkey for providing data.

References

[1] Shu C. & Ouarda T. B. M. J., Improved methods for daily streamflow estimates at ungauged sites. Water Resour. Res., 48, p. W02523, 2012. https://doi.org/10.1029/2011WR011501

[2] Razavi T. & Coulibaly P., An evaluation of regionalization and watershed classification schemes for continuous daily streamflow prediction in ungauged watersheds. Can. Water Resour. J., 42, pp. 2–20, 2017. https://doi.org/10.1080/07011784.2016.1184590

[3] Kalteh A. M. & Hjorth P., Imputation of missing values in precipitation-runoff process database. Hydrology Research, 40 (4), pp. 420-432, 2009. https://doi.org/10.2166/nh.2009.001

[4] Ergen K. & Kentel E., An integrated map correlation method and multiple-source sites drainage-area ratio method for estimating streamflows at ungauged catchments: A case study of the Western Black Sea Region, Turkey. Journal of Environmental Management, 166, 309–320, 2016. https://doi.org/10.1016/j.jenvman.2015.10.036

[5] Hughes D. A. & Smakhtin V., Daily flow time series patching or extension: a spatial interpolation approach based on flow duration curves. Hydrological Sciences Journal, 41: 851–871, 1996. https://doi.org/10.1080/02626669609491555

[6] Tencaliec P., Favre A. C., Prieur C. & Mathevet T., Reconstruction of missing daily streamflow data using dynamic regression models. Water Resour. Res., 51 (2015), pp. 9447-9463, 2015. https://doi.org/10.1002/2015WR017399

[7] Patil S. & Stieglitz M., Controls on hydrologic similarity: role of nearby gauged catchments for prediction at an ungauged catchment. Hydrology and Earth System Sciences 16: 551–562, 2012. https://doi.org/10.5194/hess-16-551-2012

[8] Elshorbagy A. A., Panu U. S. & Simonovic S. P., Group-based estimation of missing hydrological data: I. Approach and general methodology. Hydrological Sciences Journal, 45, 849–866, 2000. https://doi.org/10.1080/02626660009492388

[9] Panu U. S., Khalil M. & Elshorbagy A., Streamflow data infilling techniques based on concepts of groups and neural networks. In: Govindraju, R.S., Rao, A.R. (Eds.). Artificial Neural Networks in Hydrology. Kluwer Academic Publishers, Dordrecht, 235-258, 2000.

[10] Elshorbagy A., Simonovic S. P. & Panu U. S., Estimation of missing streamflow data using principles of chaos theory. Journal of Hydrology, 255, pp. 123-133, 2002. https://doi.org/10.1016/S0022-1694(01)00513-3

[11] Dastorani M.T., Moghadamnia A., Piri J., & Rico-Ramirez M., Application of ANN and ANFIS models for reconstructing missing flow data. Environmental Monitoring and Assessment 166: 421–434, 2010. https://doi.org/10.1007/s10661-009-1012-8

[12] Mohamoud Y. M., Prediction of daily flow duration curves and streamflow for ungauged catchments using regional flow duration curves. Hydrological Sciences, 53 (4), pp. 706-724, 2008. https://doi.org/10.1623/hysj.53.4.706

[13] Giustarini L., Parisot O., Ghoniem M., Hostache R., Trebs I., & Otjacques B., A user-driven case-based reasoning tool for infilling missing values in daily mean river flow records. Environmental Modelling & Software, 82, 308-320, 2016.

[14] Gill M. K., Asefa T., Kaheil Y. & McKee M., Effect of missing data on performance of learning algorithms for hydrologic prediction: Implication to an imputation technique. Water Resour. Res., 43, W07416, 2007.

[15] Hirsch R. M., An evaluation of some record reconstruction techniques. Water Resour. Res., 15, 1781–1790, 1979. https://doi.org/10.1029/WR015i006p01781

[16] Wiche G. J., Benson R. D. & Emerson D. G., Streamflow at selected gaging stations on the James River in North Dakota and South Dakota, 1953–1982, with a section on climatology, Water Resources Investigations Report 89-4039, US Geological Survey, 99 pp, 1989.

[17] Emerson D. G., Vecchia A. V. & Dahl A. L., Evaluation of drainage-area ratio method used to estimate streamflow for the Red River of the North Basin, North Dakota and Minnesota. US Geological Survey Scientific Investigative Report 2005–5017, 13 pp, 2005.

[18] Asquith W. H., Roussel M. C. & Vrabel J., Statewide analysis of the drainage-area ratio method for 34 streamflow percentile ranges in Texas. US Geological Survey Scientific Investigative Report 2006–5286, 34 pp, 2006.

[19] Chen T., Ren L., Yuan F., Yang X., Jiang S., Tang T., Liu Y., Zhao C. & Zhang L., Comparison of spatial interpolation schemes for rainfall data and application in hydrological modeling. Water, 9, 342, 2017. https://doi.org/10.3390/w9050342

[20] Farmer W. H & Vogel R. M., Performance-weighted methods for estimating monthly streamflow at ungauged sites. Journal of Hydrology 477: 240–250, 2013. https://doi.org/10.1016/j.jhydrol.2012.11.032

[21] Burgess T. M. & Webster R., Optimal interpolation and isarithmic mapping of soil properties: I. The semivariogram and punctual kriging. Journal of Soil Science, 31 pp. 315-331, 1980. https://doi.org/10.1111/j.1365-2389.1980.tb02084.x

[22] DSI, Management Plan for Porsuk Watershed, Final Report, State Water Works, Ankara, 2001.

[23] Hortness J. E., Estimating low flow frequency statistics for unregulated streams in Idaho. US Geol. Survey. Sci. Invest. Report 2006-5035, 2006.

[24] Sinnott R. W., Virtues of the Haversine. Sky and Telescope, vol. 68, no. 2, p. 159, 1984.

[25] Nash J. E. & Sutcliffe J. V., River flow forecasting through conceptual models. Part I-A discussion of principles. Journal of Hydrology, 10 (3), 282–290, 1970. https://doi.org/10.1016/0022-1694(70)90255-6

Teknik Dergi, 2019 9621-9645, Paper 559

Numerical Modeling of Interaction of Turbulent Flow with a Buried Circular Cylinder on a Plane Surface

M. Sami AKÖZ[1]
Oğuz ŞİMŞEK[2]
N. Göksu SOYDAN[3]

ABSTRACT

Turbulent flow characteristics around a partially buried horizontal circular cylinder are investigated numerically for the burial ratio of B/D=0.50 (B is burial depth, D is the diameter of the cylinder). The governing equations are numerically solved using ANSYS-Fluent for the flows having the same conditions with the experiments related to measurements of velocity field by Particle Image Velocimetry for Reynolds numbers based on the cylinder diameter, in the ranges of $1000 \leq Re_D \leq 7000$. Standard k-ε, Renormalization-group k-ε, Realizable k-ε, Modified k-ω, Shear Stress Transport k-ω and Reynolds Stress turbulence models are employed. Experimental validations of the numerical results show that Shear Stress Transport k-ω model provides better predictions for the kinematic properties of the turbulent flow than the other turbulence models used herein. Force coefficients also predicted numerically at Reynolds numbers in the ranges of $1000 \leq Re_D \leq 7000$ for the burial ratio, B/D=0, 0.25 and 0.5.

Keywords: Buried cylinder, force coefficients, PIV, turbulence models, turbulent flow.

1. INTRODUCTION

Turbulent flow around bluff bodies, especially cylinders, has been studied extensively because of an important subject encountered in many engineering applications. When a cylindrical structure is installed on an erodible bed such as submarine pipelines, interaction of the turbulent flow with the floor may create erosion that causes problems such as instability of the structure. The horse shoe vortex around the structure and down-flow that results from the downward hydraulic gradient in front of the structure contribute significantly to the scour.

Note:
- This paper has been received on June 08, 2018 and accepted for publication by the Editorial Board on January 28, 2019.
- Discussions on this paper will be accepted by January 31, 2020.
- https://dx.doi.org/10.18400/tekderg.432310

1 Çukurova University, Department of Civil Engineering, Adana, Turkey - msa@cu.edu.tr - https://orcid.org/0000-0003-0282-0574

2 Harran University, Department of Civil Engineering, Şanlıurfa, Turkey - oguzsimsek@harran.edu.tr - https://orcid.org/0000-0001-6324-0229

3 Mersin University, Department of Civil Engineering, Mersin, Turkey - goksusoydang@mersin.edu.tr - https://orcid.org/0000-0001-6469-2649

Following the propagation of the scour along the pipeline, it can lead to bearing failure and self-weight settlement of the pipeline and subsequently the pipeline may be covered by sand and presumably be self-buried [1]. In spite of the fact that the processes of scouring and self-burial of the pipelines are governed by various mechanisms, they depend mostly on the hydrodynamic behavior of the flow around the pipeline. Therefore, a deeper physical understanding of vortical flow structure is very important for stability of the structure. There are a number of experimental studies in the literature for the analysis of the flow characteristics around a cylindrical structure [2, 3, 4, 5, 6, 7, 8, 9]. The primary interests in these and related studies include measurements of the distribution of pressure around a cylinder, analysis of vortex shedding mechanisms and consequently obtaining the Strouhal number, investigation of the wall-proximity effects on the hydrodynamic forces, description of the mechanisms of scour and self-burial process and visualization of the turbulent flow structures around the cylindrical structure.

With the rapid development of computers and computational fluid dynamics (CFD) in recent years, a number of numerical simulations of the turbulent flow interaction with bluff bodies and scour process have been conducted. Olsen and Kjellesvig [10], modeled numerically in three-dimensional flow around a circular cylinder placed vertically in a flume. In the numerical modeling of 3*D* turbulence flow, the governing equations were solved by k-ε turbulence closure model. They found that the calculated maximum scour depth corresponds reasonably well with empirical formulas and other calculated flow characteristics such as the development of the scour hole, the shape of the scour hole and the water surface elevation around the cylinder correspond well with observations from physical model studies. Liang, Cheng and Li [11], developed a vertical two-dimensional numerical model for time dependent local scour below offshore pipelines subject to unidirectional steady flow. They examined the performance of two turbulence models, the standard k-ε model and Smagorinsky sub-grid scale (SGS) model, on modeling time dependent scour processes. From the comparisons of the predicted and measured scour-hole profiles, it is found that the proposed model works well for both clear-water and live-bed scour situations and the k-ε turbulence closure model is more preferable regarding the SGS model in the 2*D* scour model. Zhao and Fernando [12], used an Eulerian two-phase model embedded in FLUENT software to simulate scour around pipelines on a sandy bed. They used k-ε turbulence closure model for the fluid phase in the numerical model. Their simulation results were validated using experimental data by Mao [13]. They reported that the quantitative results on scour depth (time) evolution and the maximum scour depth agree well with the experimental results. Kirkgoz, Oner and Akoz [14], carried out the numerical simulation of 2*D* turbulent flow around a horizontal circular cylinder near a rigid bed with gap ratio $G/D = 0.3$ at Reynolds number based on cylinder diameter $Re_D = 9500$. The governing equations were solved by k-ε, k-ω and Shear Stress Transport (SST) k-ω turbulence closure models. It was reported that the shedding of vortices in the cylinder wake was not predicted by k-ε model and the numerical modeling using either k-ω and SST k-ω turbulence models were reasonably successful. Akoz and Kirkgoz [15], investigated numerically the turbulent flow around a horizontal wall-mounted circular cylinder at Reynolds numbers in the range of $1000 \leq Re_D \leq 7000$. The flow field was solved using k-ε, k-ω and SST turbulence models. By comparing the experimental and numerical results it was found that the velocity field obtained using k-ω and SST turbulence models were generally more accurate than k-ε model. Dixen, Sumer and Fredsoe [16], investigated the flow and scour around a half-buried sphere exposed to a

steady current experimentally and numerically. They compared experimental findings obtained by the hot-film and Laser Doppler Anemometer measurements with the numerical results obtained using k-ω SST turbulence closure model. They reported that the scour depth increases and time scale decreases when the effect of externally-generated turbulence is incorporated in the calculations and the equilibrium maximum scour depth in the live-bed regime can be approximated by $0.5D$ in which D is the sphere diameter. Zhu, Qi, Lin and Yang [17], performed a numerical study on the flow field around a submarine pipe equipped with a spoiler in a rectangular configuration and the variation of seabed surface caused by current-induced scouring beneath the pipe. Euler–Euler two-phase flow model was employed to capture the flow characteristics of sea water and seabed sandy particles based on two-dimensional Reynolds-Averaged Navier–Stokes (RANS) equations using the SST k-ω turbulence model. Their numerical results showed that both flow field around submarine pipe and seabed scouring were sensitive to the relative spoiler height and gap ratio. Increasing the spoiler height or decreasing the gap ratio could accelerate the self-burial process for submarine pipe equipped with a spoiler.

Further studies on the numerical analysis of the flow around the buried cylinders or cylinders over a scoured bed using different turbulence models for different flow conditions would be useful to experimentally validate and enhance the reliability of the CFD simulations for scour and self-burial mechanisms. In this study, the turbulent characteristics of flow around a partially buried horizontal circular cylinder located at the bottom of the channel are investigated numerically for Reynolds numbers in the range of $1000 \leq Re_D \leq 7000$. Firstly, in order to determine the most successful turbulence model, the governing equations are solved numerically by ANSYS-Fluent software using; Standard k-ε (SKE), Renormalization-group k-ε (RNG), Realizable k-ε (RKE), Modified k-ω (MKW), Shear Stress Transport k-ω (SST) and Reynolds Stress Model (RSM) for flow condition of $Re_D = 5000$. Secondly, the numerical results using the most successful turbulence models are compared with PIV measurements by Aköz [9] for Reynolds numbers, in the range of $1000 \leq Re_D \leq 7000$ based on the cylinder diameter. Turbulence characteristics of the flow field and coefficients of forces exerted on the cylinder are also presented for $1000 \leq Re_D \leq 7000$.

2. EXPERIMENTAL SET-UP

The numerical model validation was achieved against the experimental data by Aköz [9] (Fig.1). Experiments were performed in a closed-loop water channel test-section. The channel, made of transparent Plexiglas with 15 mm thickness, is 8.0 m in length, 1.0 m in width and 0.75 m in height. During the experimental study, the height of water (h) was 0.45 m and Reynolds numbers based on the cylinder diameter were Re_D=1000, 3000, 5000 and 7000. The different Reynolds numbers were obtained by changing the flow velocity. A smooth circular cylinder having the burial ratio as B/D=0.50, was mounted horizontally on the channel surface, in which B is burial depth, D is the diameter of the cylinder. The diameter and height of the cylinder were 30 mm and 15 mm respectively for B/D=0.50. The Digital Particle Image Velocimetry (PIV) technique was employed to obtain the instantaneous velocity vector field around the partially buried circular cylinder. The flow field illumination was provided by two Nd: Yag laser sources of a wavelength of 532 nm, each with a maximum energy output of 120 mJ. Dantec Dynamics Processor, which was controling the timing of the data acquisition, was used to synchronize the image taking and laser unit. In each

experiment, 300 instantaneous images at 15 Hz frequency were captured, recorded and stored in order to obtain averaged-velocity vectors and other statistical properties of the flow field. More details for PIV measurements may be found in Aköz [9].

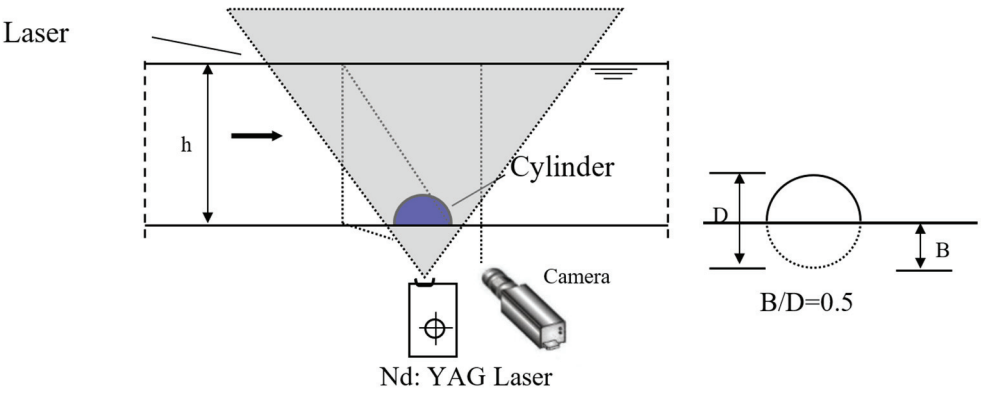

Figure 1 - Experimental setup (Aköz [9])

3. NUMERICAL MODELING

3.1. Governing Equations and Turbulence Closure Models

2-D Reynolds-averaged continuity and Navier-Stokes equations (RANS) are used to theoretically simulate the present open channel flow over a partially buried circular cylinder. For an incompressible, Newtonian fluid flow these equations can be expressed as

$$\frac{\partial \overline{u}_i}{\partial x_i} = 0 \tag{1}$$

$$\rho\left(\frac{\partial \overline{u}_i}{\partial t} + \overline{u}_j \frac{\partial \overline{u}_i}{\partial x_j}\right) = \rho g_i - \frac{\partial \overline{p}}{\partial x_i} + \mu \frac{\partial^2 \overline{u}_i}{\partial x_j^2} + \frac{\partial \tau_{ij}}{\partial x_j} \tag{2}$$

In Eqs. (1) and (2), u_i is the velocity component in x_i-direction, g_i is gravity, p is pressure, μ is dynamic viscosity, ρ is fluid density, t is time, $\tau_{ij}(=-\rho\overline{u_i'u_j'})$ is the turbulence stresses. The turbulence stresses are obtained from the linear constitutive equation formulated by Boussinesq

$$\tau_{ij} = -\rho\overline{u_i'u_j'} = \mu_t\left(\frac{\partial \overline{u}_i}{\partial x_j} + \frac{\partial \overline{u}_j}{\partial x_i}\right) - \frac{2}{3}\rho k \delta_{ij} \tag{3}$$

In Eq. (3) u_i' and u_j' are the horizontal and vertical velocity fluctuation component, respectively, μ_t is turbulent viscosity, k ($=\overline{u_i'u_i'}/2$) is turbulent kinetic energy and δ_{ij} is Kronecker delta. The models used for the turbulent viscosity in Eq. (3) are briefly described in the following. To determine the turbulent viscosity μ_t in Eq. (3), turbulence closure models given below were used.

1. Standard *k-ε* (SKE) [18],

2. Renormalization-group *k-ε* (RNG) [19],

3. Realizable *k-ε* (RKE) [20],

4. Modified k-ω (MKW) [21],

5. Shear Stress Transport *k-ω* (SST) [22],

6. Reynold Stress Model (RSM) [23].

3.2. Solution Domain and Boundary Conditions

The conditions for numerical simulations were made to be the same as those used in the experiment. The computational domain that its height is equal to 15*D,* extends 50*D* downstream and 20*D* upstream, above, and below the cylinder (Fig.2). At the inflow boundary, the vertical distributions of the horizontal velocity components were assumed to be uniform $u=u_0$ and the vertical velocity component as $v=0$. The uniform horizontal velocity components are u=33.3, 100.0, 166.7 and 233.3 mm/s for Re_D=1000, 3000, 5000 and 7000, respectively. All solid walls were defined as the wall boundary condition in which no-slip condition is imposed i.e., $u=0$, $v=0$. On the top boundary of the domain, symmetric conditions are imposed, i.e. normal gradients of velocity are set to zero on the boundary. At the outflow boundary $p=0$ was used.

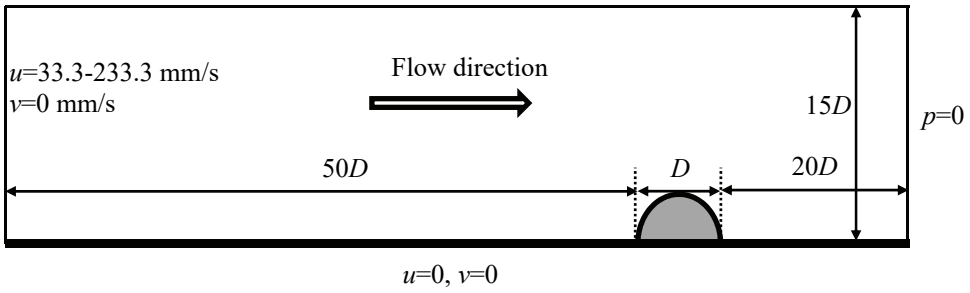

Figure 2 - Geometry and boundary conditions of computational domain

Considering the low turbulence characteristics of the flow at the inflow boundary, the turbulent intensity was accepted to be 0.01. The fluctuating velocity component v' at the

inflow boundary was assumed to have the magnitude of the inlet velocity v times the inlet intensity, and the turbulence length scale was calculated as the hydraulic diameter multiplied by the inlet scale factor. In the numerical modeling the transient analyses were performed. From the experimental measurements the turbulence intensity and the hydraulic diameter were obtained as 1% and 0.2368, respectively under flow condition at Re_D=7000. In the inlet boundary condition of the numerical modeling these parameters were used. The iteration number in the numerical analyses was given as 10 while the time step size was 0.001. The solution time was taken as 60 seconds for all analyses, which is determined by the provisions of the continuity equilibrium.

3.2.1. Near-wall treatment

In this study, two-layer approach was applied for resolving the near wall region. In this approach, the whole domain is subdivided into a fully-turbulent region and a viscosity affected region. In the fully turbulent region, *k-ε, k-ω* models and RSM model are employed. In the viscosity-affected region (the viscous sublayer and the buffer layer), the one equation-model of Wolfshtein [24] is employed with extremely fine grids and no slip conditions (i.e. u=v=0). Two-layer formulation of turbulent viscosity is smoothly blended with high Re-number definition for μ_t from outer region. A similar procedure is applied in order to ensure a smooth transition between the algebraically specified $\varepsilon\,(=k^{3/2}/l_e,$ where l_e is the length scale) in the viscosity affected region and ε obtained from the solution of the transport equation, in the outer region.

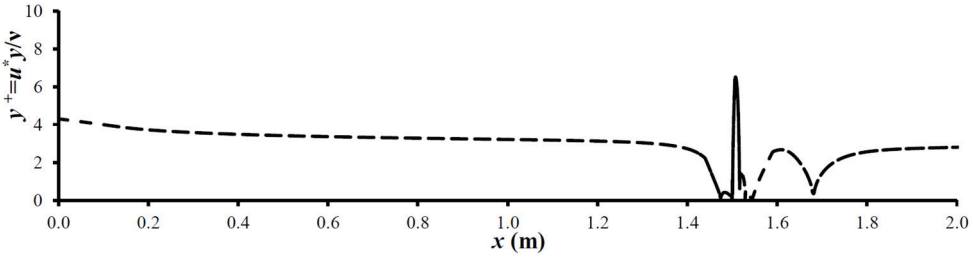

Figure 3 - The variation of $y^+(=v_*y/\nu)$ value along the solid boundary

The size of the wall adjacent cell should be so adjusted that it is embedded in the viscous sublayer where the linear viscous relation takes place between the dimensionless velocity $u^+(=u/v_*)$ and dimensionless distance $y^+(=v_*y/\nu)$, in which y is the distance normal to the wall, $v_*=(\tau_0/\rho)^{1/2}$ is the shear velocity and τ_0 is boundary shear stress. Kirkgoz and Ardiclioglu [25], reported that the experimental data fit the linear velocity distribution in the viscous sublayer if $y^+\leq 10$. This result was used as a criterion to evaluate the adequacy of the near-wall mesh size for the two layers model. The mesh resolution was therefore adjusted to have the first mesh point within the viscous sublayer by keeping the near-wall mesh size normal to the solid bed within the limit of $y^+\leq 10$. Fig.3 shows the variation of $y^+(=v_*y/\nu)$ value along the channel and on the buried cylinder surface obtained by using the SST turbulence model

for the fine mesh under flow condition at Re_D=7000. As shown in the figure, the maximum value of y^+ takes place on the backward shoulder of the buried cylinder and its value is less than 10. It is also seen that the y^+ values in the subcritical and supercritical region are below 2.

3.3 Computational Meshes

3.3.1. Mesh Design

Fig. 4 shows the computational grid used for the numerical solutions. As seen in the figure, solution domain is divided into 10 sub-domains with four-node quadrilateral elements. Considering the characteristics of the flow within the solution domain, relatively compressed meshes were used toward the solid boundaries (i.e. near the cylinder surface and the plane wall) to improve the prediction accuracy for the shear layer region where the velocity gradient is high. Table 1 gives the element numbers of the three mesh systems used for computations. In this study the mesh orthogonal skewness is obtained as 0.399. If the value is between 0.25 and 0.50, cell quality is defined as good. The range for orthogonal quality is 0-1, where a value of 0 is worst and a value of 1 is best [26]. The minimum orthogonal quality is obtained as 0.610 in the present study.

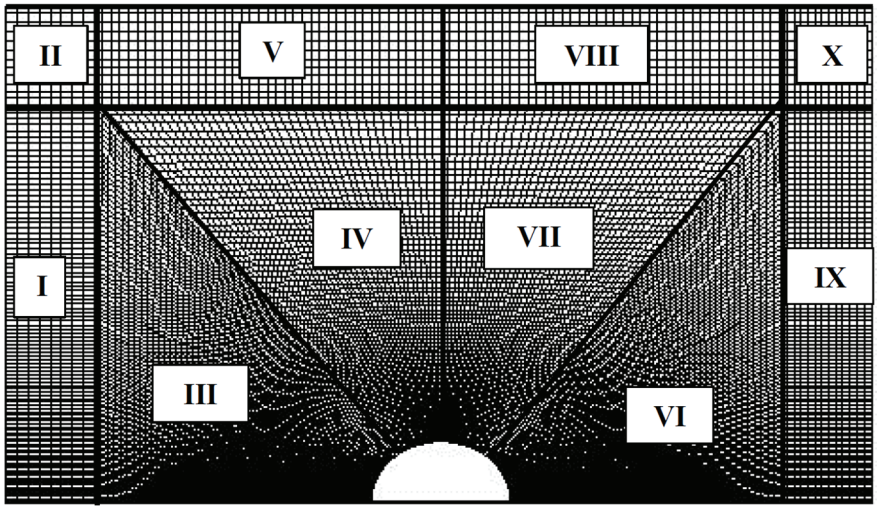

Figure 4 - Sub-domains of computational grid

Table 1 - Element numbers of the three mesh systems used for computations

Sub-domains of three meshes	Mesh 1 (coarse)	Mesh 2 (medium)	Mesh 3 (fine)
I	40x50	60x75	80x100
II	40x40	60x60	80x80

Table 1 - Element numbers of the three mesh systems used for computations (continue)

Sub-domains of three meshes	Mesh 1 (coarse)	Mesh 2 (medium)	Mesh 3 (fine)
III, IV	40x40	60x60	80x80
V	40x50	60x75	80x100
VI	50x75	75x100	100x150
VII	50x5	75x5	100x10
VIII, IX	40x5	60x5	80x10
X	75x5	100x5	150x10
Total number of mesh elements	11,775	24,875	47,100

3.3.2. Estimation of discretization error

A grid convergence index (GCI) was determined for the computed velocities on the three meshes, which is the most common and reliable technique for the quantification the discretization uncertainty of the numerical results [27]. Using the Richardson error estimator to compare the three grids, the fine-grid convergence index is defined as

$$\mathrm{GCI}_{23}^{\mathrm{fine}} = \frac{1.25\left|E_{23}\right|}{r_{23}^{P}-1} \tag{4}$$

where $E_{23}=(u_{s3}-u_{s2})/u_{s3}$ = approximate relative error between the medium and fine meshes, u_{s2} and u_{s3} = medium and fine mesh solutions for velocities obtained with grid spacing d_2 and d_3, respectively, and P = local order of accuracy. For the three-grid solutions, P is obtained by solving the equation

$$P = \frac{1}{\ln r_{23}} \ln \frac{(r_{23}^{P}-1)\,e_{12}}{(r_{12}^{P}-1)\,e_{23}} \tag{5}$$

in which $e_{12}=u_{s1}-u_{s2}$, $e_{23}=u_{s2}-u_{s3}$, and $r_{12}=d_1/d_2$ and $r_{23}=d_2/d_3$ = grid refinement factors between coarse and medium, and medium and fine grid, respectively. For the present comparisons $d_3<d_2<d_1$.

In this study, the profiles of computed velocities u at x=1.45, 1.515 and 1.60 m were used to determine the numerical uncertainties due to discretization. Table 2 shows the discretization uncertainty for the fine-grid solutions using the SST turbulence model. Note that the maximum uncertainty in the chosen velocity profiles on Mesh 3 is 1.959% corresponding to ±0.0129 m/s at x=1.60 and y=0.008 m. As it is seen from Table 2, the numerical uncertainty of discretization in the computed velocities for Mesh 3 remains within 2% which is an excellent indication.

Table 2 - Sample error estimates in velocity profiles at x=1.45, 1.515 and 1.60 m.

***x*=1.45 m**		***x*=1.515 m**		***x*=1.60 m**	
***y* (m)**	GCI_{23}^{fine} for *u* **(%)**	***y* (m)**	GCI_{23}^{fine} for *u* **(%)**	***y* (m)**	GCI_{23}^{fine} for *u* **(%)**
0.000	0.747	0.016	0.928	0.001	1.280
0.002	1.363	0.017	1.166	0.005	0.040
0.004	-1.937	0.019	-1.909	0.008	1.959
0.008	0.671	0.020	0.119	0.010	1.819
0.012	1.849	0.021	0.016	0.012	0.473
0.016	0.190	0.022	0.829	0.014	1.938
0.020	-0.899	0.023	0.998	0.016	1.850
0.024	0.070	0.024	0.070	0.018	0.005
0.028	0.071	0.026	0.376	0.021	1.368
0.032	0.376	0.028	1.095	0.025	0.004
0.036	0.980	0.030	-1.395	0.030	-1.504
0.040	0.102	0.032	-1.783	0.032	-1.391

4. EXPERIMENTAL AND COMPUTATIONAL RESULTS

4.1. Experimental and Computed Velocity Profiles

A quantitative evaluation of the measured and computed velocity comparisons was made by the mean absolute relative error (MARE)

$$MARE = \frac{1}{N}\sum_{n=1}^{N}\left|\frac{\overline{u}_m - \overline{u}_c}{\overline{u}_m}\right| x100 \qquad (6)$$

in which $\overline{u}_m$ and $\overline{u}_c$ are the measured and computed horizontal velocities, respectively and N is the total number of data on the velocity profiles. The results for MARE using Eq. (6) for the horizontal velocity profiles at different channel sections for Re_D=5000 were given in Table 3 for all turbulence closure models used in the present study. The numbers in parentheses in the table indicate the order of success in regard to compliance with the experimental measurements. SKE model shows superior performance in the upstream and upper region of the buried cylinder except for the upstream separation region in front of the cylinder as expected. In the upstream separation region, SST turbulence model performs better than the others. However, the results using the MKW and RSM are very close to those of the SST in this region. SKE, RNG and RKE turbulence models give very poor results in the downstream region of the cylinder especially in the near wake region. SST model shows better agreement at x/D=0.5 in the near wake region. RSM model provides better estimations

of horizontal velocity component far away from the cylinder when compared to the others. On the other hand, in terms of the mean MARE values, the SST turbulence model gives the best predictions which are followed by the MKW and RSM models.

Table 3 - MARE values for the horizontal velocity profiles at different sections for the turbulence models

x/D	SKE	RNG	RKE	MKW	SST	RSM
-1.5	**6.35**(1)	6.50(3)	6.43(2)	10.15(6)	10.01(5)	8.28(4)
-1.0	**9.18**(1)	9.36(3)	9.34(2)	13.63(6)	13.48(5)	10.90(4)
-0.5	29.17(6)	28.45(5)	28.14(4)	23.10(2)	**20.52**(1)	27.11(3)
0.0	**5.02**(1)	5.17(2)	5.21(3)	9.10(6)	8.59(5)	7.48(4)
0.5	236.56(6)	206.65(5)	164.21(4)	51.35(2)	**46.23**(1)	97.45(3)
1.0	95.77(6)	84.62(5)	66.77(4)	39.49(3)	23.53(2)	**19.24**(1)
1.5	82.08(6)	68.93(5)	45.75(4)	42.33(3)	34.47(2)	**25.56**(1)
Mean	66.31(6)	58.53(5)	46.55(4)	27.02(2)	**22.40(1)**	28.00(3)

The graphical comparisons of the horizontal velocity profiles between the experimental data and numerical predictions using the turbulence models for Re_D=5000 were also given in Figure 5. It can be seen clearly that while SST model shows better agreement with the experimental measurements at x/D=-0.5 and x/D = 0.5, SKE model gives superior results to the other models at x/D=0.

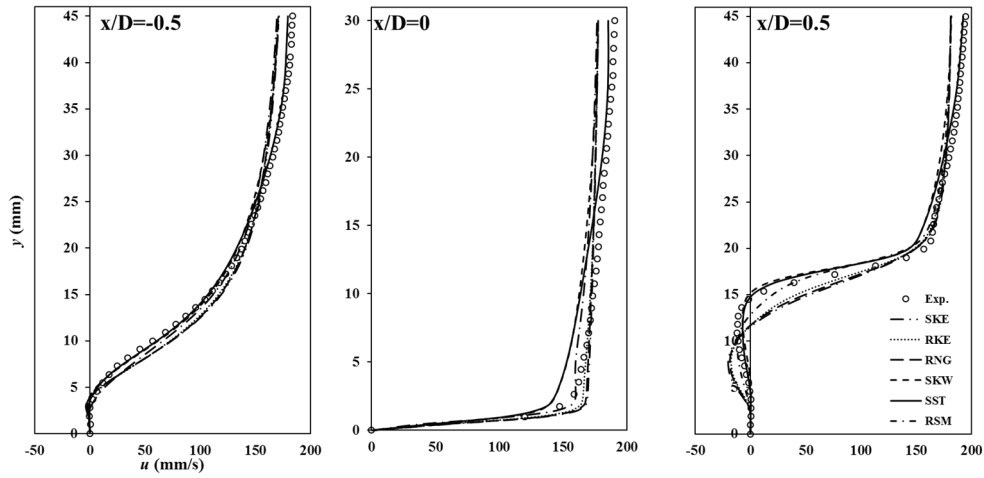

Figure 5 - Comparisons of measured and computed horizontal velocity profiles obtained by the present turbulence models at three different sections for Re_D=5000

Figure 6 shows the measured and predicted horizontal velocity profiles obtained by the most successful turbulence model (SST) regarding the mean MARE values on Mesh 3 at different channel sections for Reynolds numbers in the range of $1000 \leq Re_D \leq 7000$. The agreement appears to be very good between the experimental data and predictions of SST turbulence model. The largest discrepancies of SST predictions take place in the wake region of the cylinder. It is also seen that SST model predicts successfully the upstream and downstream separation region of the buried cylinder.

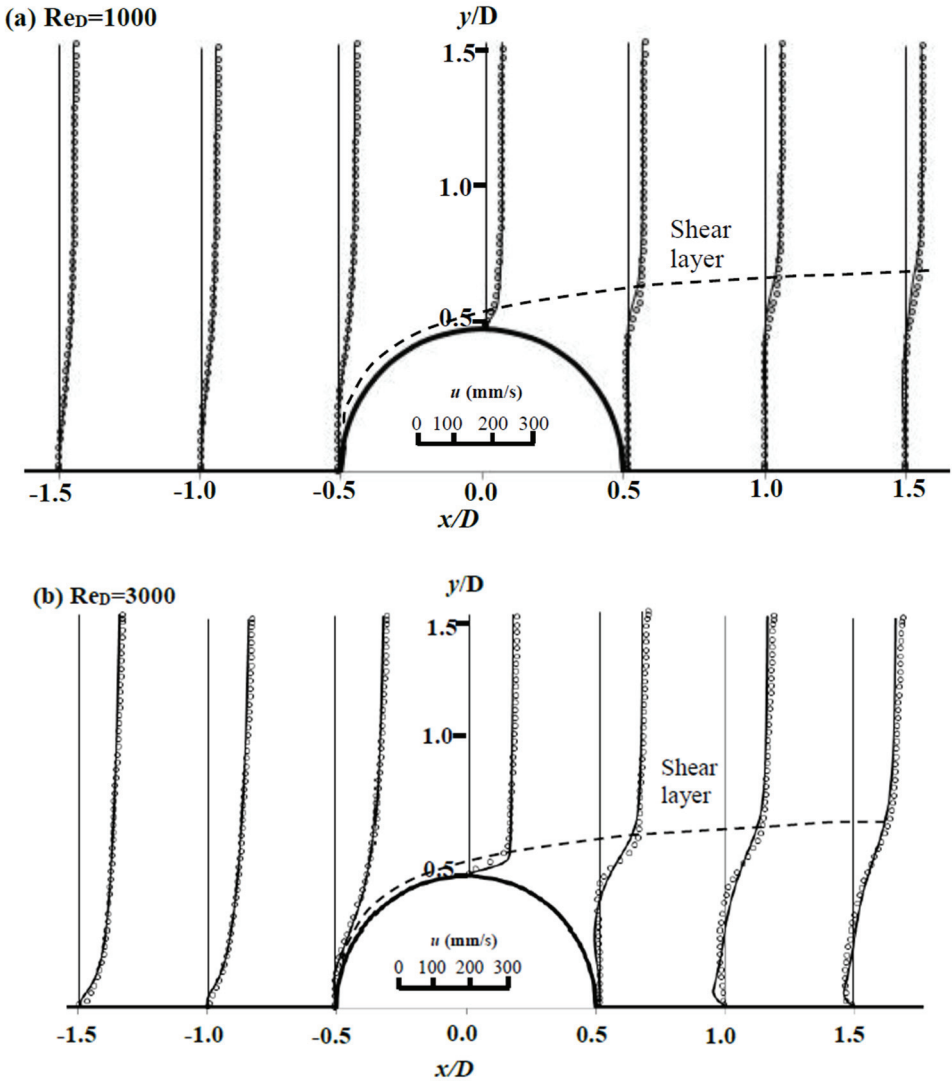

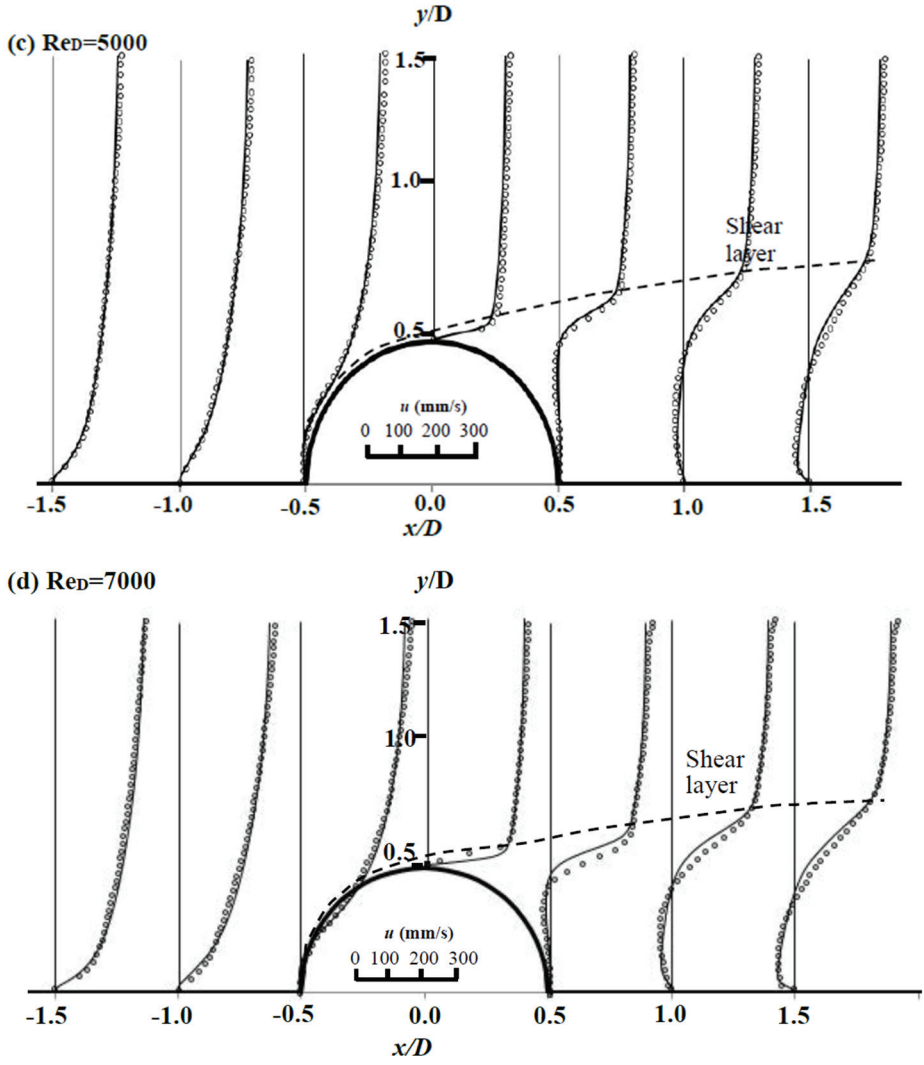

Figure 6 - Measured and computed horizontal velocity profiles using SST model at different channel sections for 1000≤Re_D≤ 7000

4.2 Experimental and numerical streamlines and velocity vectors

Since SKE model is the most unsuccessful turbulence model as compared to the others to predict the velocity data at x/D =-0.5 and x/D=0.5, as seen in Table 3, it should not be expected to provide accurately the separation region upstream and downstream of the cylinder. Therefore, in Figure 7 and 8, the comparisons of the experimental and numerical averaged patterns of corresponding streamline topology and velocity vectors in the upstream and downstream of the buried cylinder obtained using other five turbulence models were

presented for flow condition at Re_D=5000, respectively. It can be seen from the first columns of the figure that the computed length of the separation region in the upstream of the cylinder is overpredicted in the present simulations. However, reasonable predictions for the separation region in the upstream region of the buried cylinder were obtained except for RSM which predicted two reattachment points on the channel floor. RKE, RNG, MKW and SST predict almost identical location of separation point, S_s (approximately 1.5D) upstream of the cylinder. The numerical length of the separation regions upstream of the buried cylinder were predicted to be 1.02D, 0.92D, 0.83D and 0,78D for the RKE, RNG, MKW and SST, respectively. On the other hand, the experimental distance of S_s was determined to be approximately 0.54D. It can be also easily seen from the figures that a focus (F) that corresponds to vortex centers takes place between the separation point and forward face of the cylinder. The size of the vortices in the upstream region obtained using the present turbulence models is larger than the experimental result. The time-averaged distributions of the velocity vectors given in the last columns of the Figure 8 also reveal identical flow structures around the buried cylinder.

There are two separation regions called primary separation region which occurs in the downstream of the cylinder and secondary downstream separation region which is apparent in the near wake of the cylinder [13]. The second column of the Figure 7 shows the predicted time-averaged patterns of streamline in the downstream region of the buried cylinder. As can be seen in the figure, while the experimental length of the secondary downstream separation region was obtained as 0.40D, the numerical lengths of the secondary downstream separation regions were predicted to be 0.24D, 0.22D, 0.83D, 0,49D, and 0.25D for the RKE, RNG, MKW, SST and RSM, respectively. As can be understood from these values, SST model is the most successful turbulence model in predicting the flow structure around the buried cylinder.

Figure 9 shows the experimental and numerical time-averaged patterns of streamline topology obtained using the most successful turbulence model, SST for Reynolds numbers Re_D=1000, 3000, 5000 and 7000. For Re_D=1000, a vortex cluster does not appear in the experimental time-averaged streamline patterns upstream and downstream of the cylinder, while it does not take place only downstream of the cylinder in the numerical time-averaged streamline patterns. A possible reason is that the separation/boundary layer developing over the cylinder is not fully turbulent (transitional) in this case, whereas numerical model cannot sense such regimes due to the inherence of two-equation RANS closure used. As may be seen from the figure, SST model provides slightly longer separation regions in both upstream and downstream of the buried cylinder compared to the measurement ones for $1000 \leq Re_D \leq 7000$. Similar to the experiments, the length of the separation regions decreases with increasing Reynolds number. Also, the vortex in the junction region of the cylinder and channel bed weakens for increasing Reynolds number, as seen in Figure 9. This is because core flow easily penetrates into the wake region in the upstream and downstream of the buried cylinder due to the higher momentum at higher Reynolds number. Table 4 gives the comparison of boundary layer separation angles for B/D=0, B/D=0.25 and B/D=0.5 obtained by using SST turbulence model with the experimental measurements of Akoz [9] for $1000 \leq Re \leq 7000$. It can be said that as the Reynolds number increases for $1000 \leq Re \leq 7000$, boundary layer separation angles using SST turbulence model and PIV decreases. Akoz [9] analyzed the boundary layer separation angles for B/D=0 at Re_D=5000 by using SST turbulence model. The results for Re_D=5000 given in Table 4 are compatible with the values given by Akoz [9].

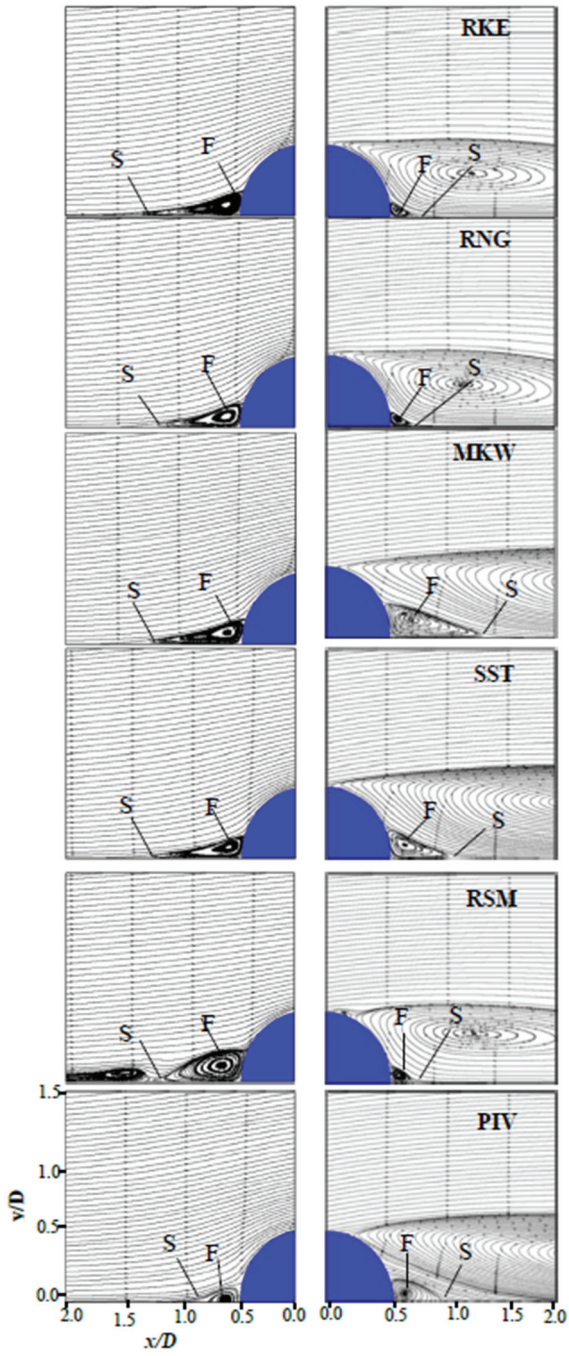

Figure 7 - Experimental and numerical time averaged patterns of streamlines for Re_D=5000

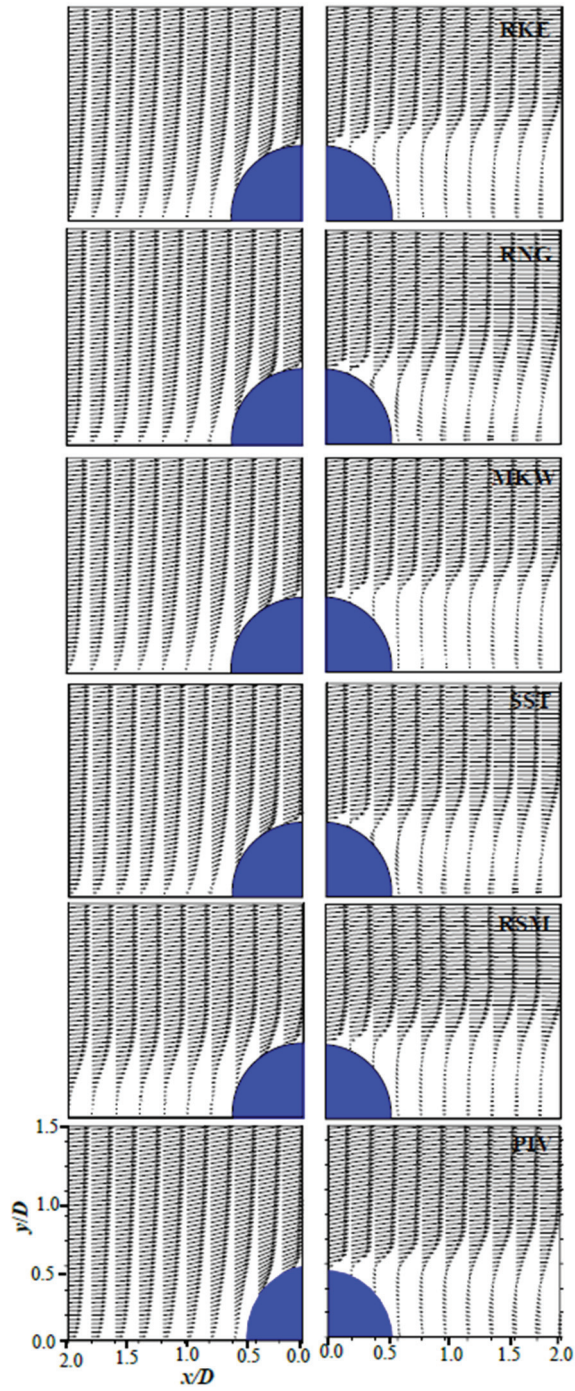

Figure 8 - Experimental and numerical distribution of velocity vectors for Re_D=5000

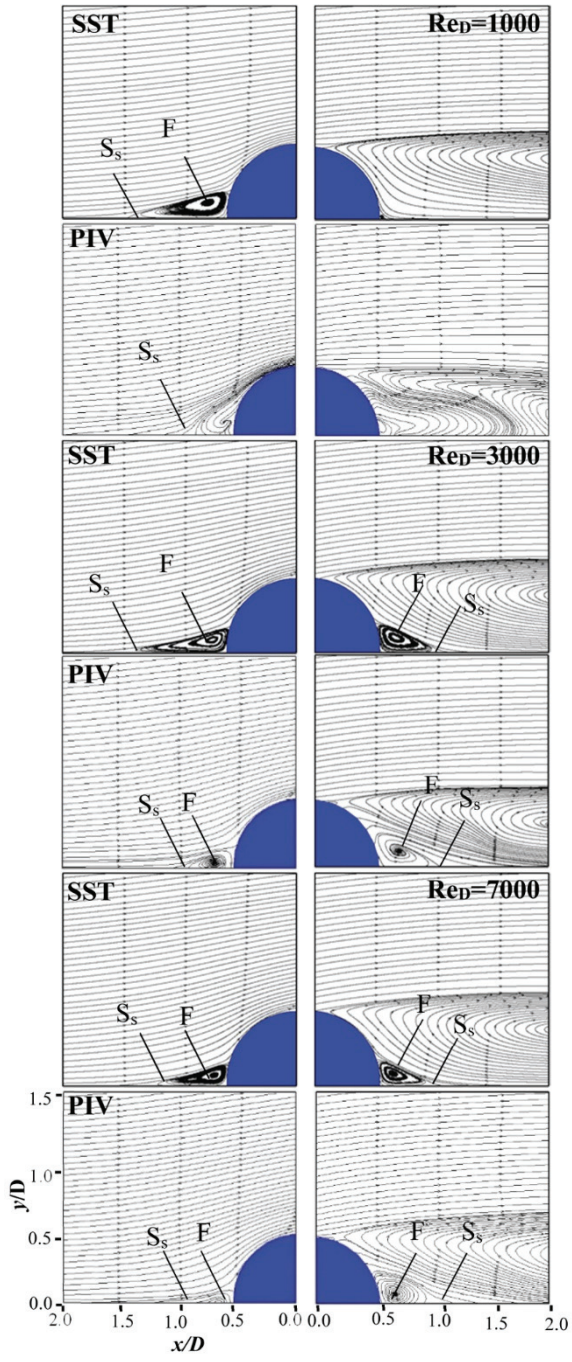

Figure 9 - Experimental and numerical time-averaged streamline patterns for $1000 \leq Re_D \leq 7000$

Table 4 - Experimental and numerical boundary layer separation angles for B/D=0, B/D=0.25 and B/D=0.5

	SST			PIV		
Re_D-B/D	**0**	**0.25**	**0.5**	**0**	**0.25**	**0.5**
1000	120	118	123	104	107	112
3000	112	116	111	98	99	109
5000	106	108	108	98	97	104
7000	103	107	107	98	98	104

4.3. Force Coefficients

Figure 10 depicts the pressure coefficient, C_p distribution on the cylinder for B/D=0, 0.25 and 0.5 at Reynolds numbers in the ranges of $1000 \leq Re_D \leq 7000$. The pressure in the wake region is negative due to the flow separation. The characteristic of the pressure distribution for Re_D=1000 differs slightly from others and its pressure values are very small compared to other Reynolds numbers. Positive and negative C_p values are increasing with the increase of Reynolds number. The maximum values of pressure coefficient take place in the upstream of the cylinder. The point where the pressure passes from the positive to negative is almost the same point on the cylinder surface for all Reynolds numbers except for Re_D=1000, its starting point moves further downstream for Re_D=1000. The minimum values of C_p occur on the front shoulder of the cylinder. Its locations are between $\theta=70^o$ and 90^o for $0 \leq B/D \leq 0.50$ and they move slightly in the backward direction as the buried ratio increases. Table 5 gives the maximum negative values of C_p for B/D=0, B/D=0.25 and B/D=0.5. In addition, as the buried ratio, B/D is increased, the absolute value of pressure coefficient is decreased. This is consistent with the experimental data of pressure distribution around a cylinder for different buried pipe position by Cokgor and Avci [28].

Table 5 - The maximum negative values of Cp for B/D=0, B/D=0.25 and B/D=0.5

B/D-Re_D	**1000**	**3000**	**5000**	**7000**
0	-2.291	-2.417	-2.477	-2.813
0.25	-2.136	-2.363	-3.061	-3.543
0.5	-1.466	-1.692	-1.763	-2.031

The pressure, drag and lift coefficients for the forces acting on the cylinder were calculated. The drag and lift force coefficients, C_d and C_l, are

$$C_d = \frac{F_d}{\frac{1}{2}\rho u_0^2 D} \tag{7}$$

$$C_l = \frac{F_l}{\frac{1}{2}\rho u_0^2 D} \tag{8}$$

where the drag and lift forces, F_d and F_l, per unit length on the cylinder are

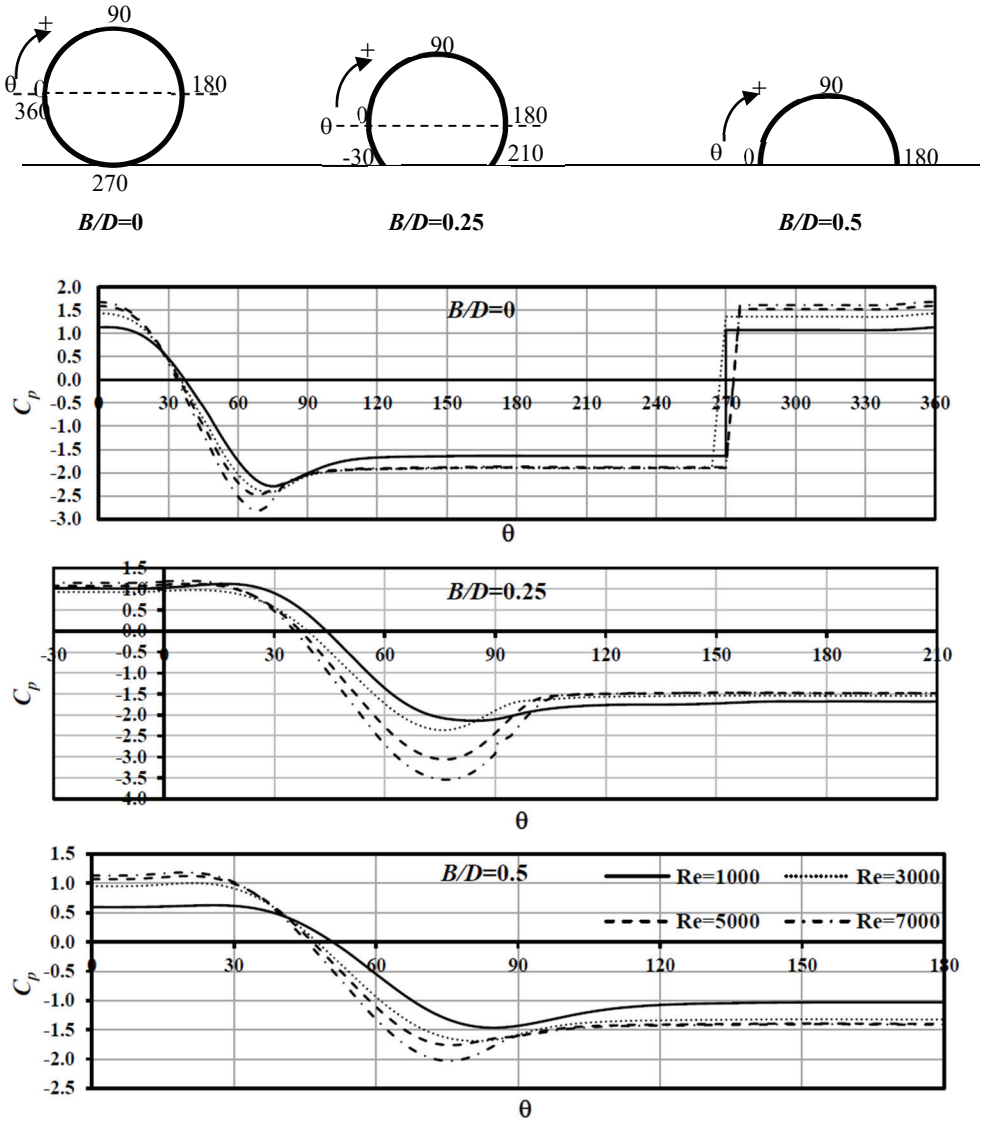

Figure 10 - Pressure coefficient distribution on the cylinder for B/D=0, 0.25, and 0.5 at Reynolds numbers 1000≤Re_D≤7000

Figure 11 shows the computed values of mean drag coefficient ($\overline{C}_d$) and lift coefficient ($\overline{C}_l$), using SST turbulence model for *B/D*=0, 0.25 and 0.5 at Reynolds numbers between Re_D=1000 and 7000. $\overline{C}_d$ values for *B/D*=0 are markedly greater than the values for the burial ratios of *B/D*=0.25 and 0.5. $\overline{C}_d$ tends to decrease with increasing of the Reynolds numbers. In addition, $\overline{C}_d$ decreases as the burial ratio increases. This can also be seen from the Table 6 which shows the $\overline{C}_d$ and $\overline{C}_l$ values for the different Re_D and *B/D* obtained by SST and DES models. The mean lift coefficients decrease with increasing of the Reynolds numbers. As may be also seen from Table 6, $\overline{C}_l$ decreases as the burial ratio increases.

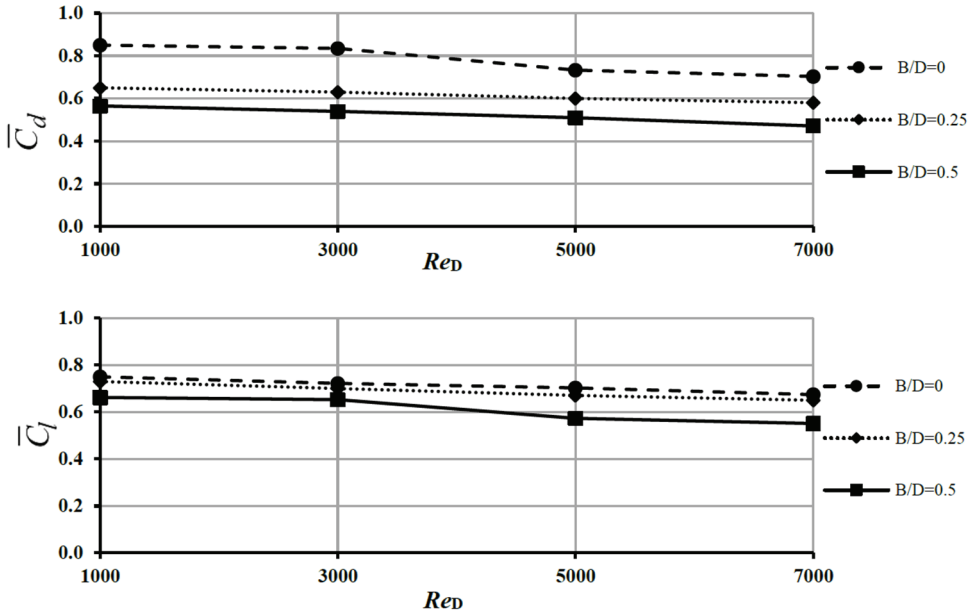

Figure 11 - Calculated mean drag ($\overline{C}_d$) and lift ($\overline{C}_l$) by SST turbulence model for B/D=0, 0.25 and 0.5 at Reynolds numbers in the ranges of 1000≤Re_D≤7000

Table 6 - The values of predicted mean drag and lift coefficients by SST and DES models for B/D=0, 0.25 and 0.5 at Reynolds numbers in the ranges of 1000≤Re_D≤7000

$\overline{C}_d$-RANS				
B/D	**Re_D=1000**	**Re_D=3000**	**Re_D=5000**	**Re_D=7000**
0	0.850	0.835	0.733	0.703
0.25	0.650	0.630	0.600	0.580
0.5	0.565	0.540	0.509	0.471

Table 6 - The values of predicted mean drag and lift coefficients by SST and DES models for B/D=0, 0.25 and 0.5 at Reynolds numbers in the ranges of 1000≤Re_D≤7000 (continue)

$\overline{C}_d$-DES				
B/D	**Re_D=1000**	**Re_D=3000**	**Re_D=5000**	**Re_D=7000**
0	1.080	0.998	0.901	0.888
0.25	0.860	0.782	0.718	0.686
0.5	0.670	0.525	0.461	0.429
$\overline{C}_l$-RANS				
B/D	**Re_D=1000**	**Re_D=3000**	**Re_D=5000**	**Re_D=7000**
0	0.750	0.722	0.703	0.674
0.25	0.730	0.700	0.670	0.650
0.5	0.662	0.652	0.573	0.551
$\overline{C}_l$-DES				
B/D	**Re_D=1000**	**Re_D=3000**	**Re_D=5000**	**Re_D=7000**
0	0.957	0.929	0.899	0.802
0.25	0.860	0.800	0.766	0.740
0.5	0.755	0.740	0.728	0.706

The numerical results of drag and lift coefficients in this study are consistent with the measurements of the earlier researchers. Zdravkovich [29], found that the value of drag coefficient was 0.86 for *B/D*=0 at Re_D=8000. Kalghatgi and Sayer [30] reported that C_d was equal to 0.80 for *B/D*=0 at Re_D=10000. Cokgor and Avci [28] presented graphically the variation of drag and lift coefficient with the burial ratio and they reported that the drag and lift coefficient decreased with increasing burial ratio. The variation of the drag and lift coefficient with the burial ratio obtained from the studies mentioned above and the present numerical model is shown in Figures 12 and 13. The discrepancies from the previous studies in the literature could result from different flow and structure conditions. There are discrepancies in the RANS results, so the numerical analyses were reperformed by using DES (detached eddy simulation) model in two (2D) and three (3D) dimensional and LES models. The results obtained from 3D and 2D DES model are very compatible with each other. That's why the analyses for *B/D*=0, 0.25 and 0.5 at Reynolds numbers between Re_D=1000 and 7000 were carried out in 2D by using DES model. From the comparison of DES results with Cokgor and Avci [28] at Re=8000, it is obtained that the force coefficients are more compatible with each other according the RANS model results. Looking at Figures, it can be seen that numerical mean drag and lift coefficient distributions are very similar to those of experimental measurements.

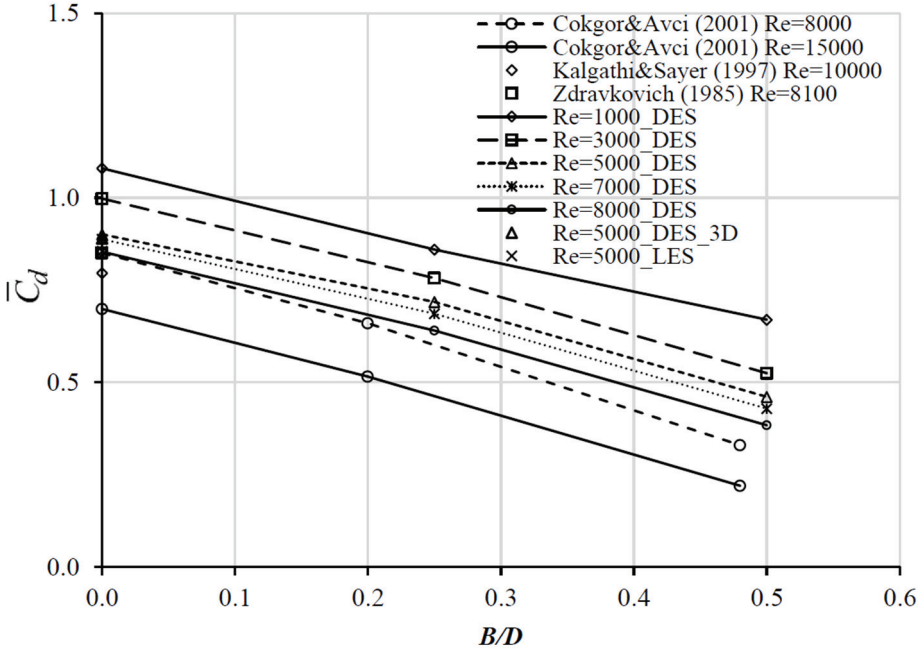

Figure 12 - Drag coefficient vs. burial ratio, B/D, for the different Re_D number

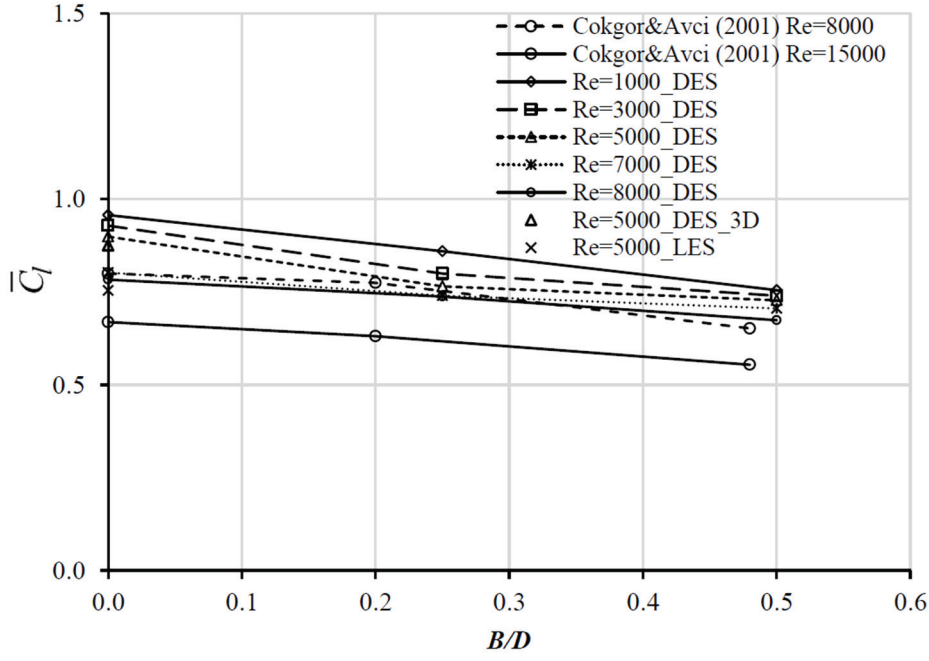

Figure 13 - Lift coefficient vs. burial ratio, B/D, for the different Re_D number

4.4. Experimental and numerical turbulence kinetic energy distributions

Figure 14 shows the comparison of turbulence kinetic energy (TKE), that is the rate at which energy is transferred from the main flow to the turbulent eddies, obtained from PIV and predicted using SST model at Re_D ranging from $1000 \leq Re_D \leq 7000$ for $B/D=0.5$. Maximum and incremental values of the turbulent kinetic energy are given in the figures. The distributions of TKE obtained from PIV and SST turbulence model are similar for all Reynolds numbers. It can be clearly seen that the maximum value of the turbulence kinetic energy is increasing with the increase of Reynolds number for both PIV and SST. A cluster and maximum value of TKE occur along the shedding shear layers.

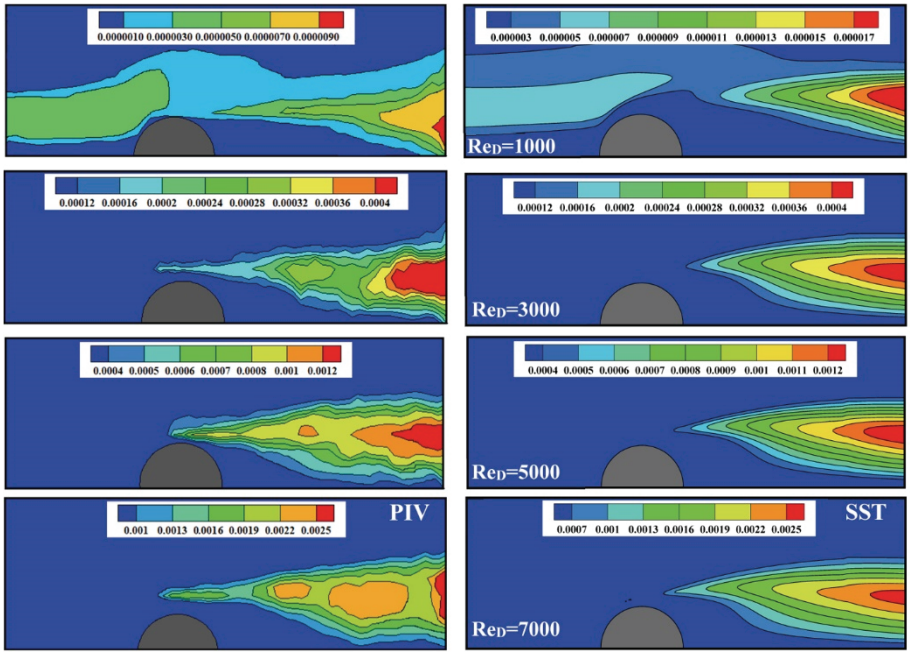

Figure 14 - Experimental and numerical turbulent kinetic energy for B/D=0.5

5. CONCLUSIONS

Analysis of the hydrodynamic behavior of the turbulent flow around a pipeline is important for the understanding of processes of scouring and self-burial of the pipelines governed by various mechanisms. To investigate the characteristics of the complex turbulent flow around the cylinder with different burial ratios at Reynolds number based on the cylinder diameter ranging from $1000 \leq Re_D \leq 7000$, the numerical simulation conducted using the Ansys-Fluent package program based on finite volume method. Standard k-ε, Renormalized Group k-ε, Realizable k-ε, Modified k-ω, Shear Stress Transport k-ω and Reynolds Stress Model turbulence models were employed to close the system of equations. Predicted velocity profiles were compared with those measured in laboratory using Particle Image Velocimetry.

The mean absolute relative error statistics were used as a criterion for the quantitative analysis of numerical results obtained from the turbulence closure models. From the comparisons of the numerical and experimental results, the simulation using SST model were found generally more accurate than other models. The pressure (C_p), mean drag ($\overline{C_d}$) and mean lift ($\overline{C_l}$) coefficients were predicted with SST turbulence model and DES model for the burial ratio B/D=0, 0.25 and 0.5 at Reynolds numbers in the range of $1000 \leq Re_D \leq 7000$ and it was found that the force coefficients from the present computations were consistent with the measurements of the earlier researcher. Drag ($\overline{C_d}$) and lift ($\overline{C_l}$) coefficients decrease as the burial ratio increases. Turbulent kinetic energy obtained from PIV and SST turbulence model was increased with increasing Reynolds number and it concentrated along the shedding shear layers from the cylinder in which high velocity gradients occurred.

References

[1] Sumer, B., and Fredsoe, J., Self-Burial of Pipelines at Span Shoulders, International Journal of Offshore and Polar Engineering, 4, 1, 1994.

[2] Bearman, P., and Zdravkovich, M., Flow Around a Circular Cylinder Near a Plane Boundary, Journal of Fluid Mechanics, 89, 1, 33-47, 1978.

[3] Zdravkovich, M., Aerodynamics of Two Parallel Circular Cylinders of Finite Height at Simulated High Reynolds Numbers, Journal of Wind Engineering and Industrial Aerodynamics, 6, 1-2, 59-71, 1980.

[4] Fredsøe, J., and Hansen, E. A., Lift Forces on Pipelines in Steady Flow, Journal of Waterway, Port, Coastal, and Ocean Engineering, 113, 2, 139-155,1987.

[5] Lei, C., Cheng, L., and Kavanagh, K., Re-Examination of the Effect of a Plane Boundary on Force and Vortex Shedding of a Circular Cylinder, Journal of Wind Engineering and Industrial Aerodynamics, 80, 3, 263-286, 1999.

[6] Price, S., Sumner, D., Smith, J., Leong, K., and Paidoussis, M., Flow Visualization around a Circular Cylinder Near to a Plane Wall, Journal of Fluids And Structures, 16, 2, 175-191, 2002.

[7] Oner, A. A., Kirkgoz, M. S., and Akoz, M. S., Interaction of a Current with a Circular Cylinder near a Rigid Bed, Ocean Engineering, 35, 14, 1492-1504, 2008.

[8] Akoz, M. S., Flow Structures Downstream of the Horizontal Cylinder Laid on a Plane Surface, Proceedings of The Institution of Mechanical Engineers, Part C: Journal of Mechanical Engineering Science, 223, 2, 397-413,2009.

[9] Aköz, M. S., Investigation of Vortical Flow Characteristics around a Partially Buried Circular Cylinder, Ocean Engineering, 52, 35-51, 2012.

[10] Olsen, N. R., and Kjellesvig, H. M., Three-Dimensional Numerical Flow Modeling for Estimation of Maximum Local Scour Depth, Journal of Hydraulic Research, 36, 4, 579-590, 1998.

[11] Liang, D., Cheng, L., and Li, F., Numerical Modeling of Flow and Scour Below a Pipeline in Currents: Part II. Scour Simulation, Coastal Engineering, 52, 1, 43-62, 2005.

[12] Zhao, Z. H., and Fernando, H. J. S., Numerical Simulation of Scour around Pipelines Using an Euler-Euler Coupled Two-Phase Model, Environmental Fluid Mechanics, 7, 2, 121-142, 2007.

[13] Mao, Y., The interaction between a pipeline and an erodible bed, Series Paper Technical University of Denmark, 39, 1987.

[14] Kirkgoz, M. S., Oner, A. A., and Akoz, M. S., Numerical Modeling of Interaction of a Current with a Circular Cylinder Near a Rigid Bed, Advances in Engineering Software, 40, 11, 1191-1199, 2009.

[15] Akoz, M. S., and Kirkgoz, M. S., Numerical and Experimental Analyses of the Flow around a Horizontal Wall-Mounted Circular Cylinder, Transactions of the Canadian Society for Mechanical Engineering, 33, 2, 189-215, 2009.

[16] Dixen, M., Sumer, B. M., and Fredsoe, J., Numerical and Experimental Investigation of Flow and Scour around a Half-Buried Sphere, Coastal Engineering, 73, 84-105, 2013.

[17] Zhu, H., Qi, X., Lin, P., and Yang, Y., Numerical Simulation of Flow around a Submarine Pipe with a Spoiler and Current-Induced Scour Beneath the Pipe, Applied Ocean Research, 41, 87-100, 2013.

[18] Launder, B. E., and Spalding, D. B., Lectures in Mathematical Models of Turbulence, Academic Press, London, 1972.

[19] Yakhot, V., Orszag, S. A., Thangam, S., Gatski, T. B., and Speziale, C. G., Development of Turbulence Models for Shear Flows by a Double Expansion Technique. Physics of Fluids a-Fluid Dynamics, 4, 7, 1510-1520, 1992.

[20] Shih, T. H., Liou, W. W., Shabbir, A., Yang, Z. G., and Zhu, J., A New Kappa-Epsilon Eddy Viscosity Model for High Reynolds-Number Turbulent Flows. Computers & Fluids, 24, 3, 227-238, 1995.

[21] Wilcox, D. C., Turbulence Modeling for CFD, DCW Industries, Inc., California, 1998.

[22] Menter, F. R., 2-Equation Eddy-Viscosity Turbulence Models for Engineering Applications. AIAA Journal, 32, 8, 1598-1605, 1994.

[23] Launder, B. E., Reece, G. J., and Rodi, W., Progress in the Development of a Reynolds-Stress Turbulence Closure, Journal of Fluid Mechanics, 68, 3, 537-566, 1975.

[24] Wolfshtein, M., The Velocity and Temperature Distribution in One-Dimensional Flow with Turbulence Augmentation and Pressure Gradient, International Journal of Heat and Mass Transfer, 12, 3, 301-318, 1969.

[25] Kirkgoz, M. S., and Ardiclioglu, M,. Velocity Profiles of Developing and Developed Open Channel Flow, Journal Hydraulic Engineering-ASCE, 123, 12, 1099-1105, 1997.

[26] Ansys Fluent User Guide, Ansys Inc., 2012.

[27] Roache, P. J., Verification of Codes and Calculations, AIAA Journal, 36, 5, 696-702, 1998.

[28] Cokgor, S., and Avci, I., Hydrodynamic Forces on Partly Buried Tandem, Twin Pipelines in Current, Ocean Engineering, 28, 10, 1349-1360, 2001.

[29] Zdravkovich, M., Flow Induced Oscillations of Two Interfering Circular Cylinders, Journal of Sound and Vibration, 101, 4, 511-521, 1985.

[30] Kalghatgi, S., and Sayer, P., Hydrodynamic Forces on Piggyback Pipeline Configurations, Journal of waterway, port, coastal, and ocean engineering, 123, 1, 16-22, 1997.

Teknik Dergi, 2019 9647-9673, Paper 560

Earthquake Response Analysis of Multiple Towers on a Common Podium: A Representative Case Study

Cem TURA[1]
Kutay ORAKÇAL[2]

ABSTRACT

In this study, a hypothetical tall building structure consisting of two towers and a common podium is analyzed, considering effects of interaction between the towers due to the connected podium floors. Interaction effects on the podium level are included in the analyses using either an upper bound or lower bound approach, by assigning fixed or free end restraints at the continuous boundaries of single tower models, respectively. Responses of the single tower models are then compared with the response obtained for the combined model, which includes both of the towers as well as the common podium and basements. Results obtained using different linear and nonlinear analysis methods indicate that single tower models with fixed end restraints overestimate the internal forces at the podium floors, although to a reasonable extent.

Keywords: Tall building, multiple towers, common podium, nonlinear analysis, performance based design.

1. INTRODUCTION

In projects with multiple towers on a common podium, even when the structural properties of the towers are similar to each other, dynamic response of the towers during real seismic events are likely to vary due to several reasons, including the service loads on the towers, local soil conditions, and spatial variability of the ground motion. Possible out of phase response of individual towers due to this variance in dynamic response may create excessive in-plane stresses at the connected podium level diaphragms. To prevent possible diaphragm failure, design engineers must consider these effects as critical (i.e., non-ductile) design quantities. Furthermore, such interaction between the towers may also influence the response

Note:
- This paper has been received on October 04, 2018 and accepted for publication by the Editorial Board on January 28, 2019.
- Discussions on this paper will be accepted by January 31, 2020.

• https://dx.doi.org/10.18400/tekderg.467371

1 Boğaziçi University, Department of Civil Engineering, İstanbul, Turkey - cem.tura@boun.edu.tr https://orcid.org/0000-0002-5745-6442

2 Boğaziçi University, Department of Civil Engineering, İstanbul, Turkey - kutay.orakcal@boun.edu.tr https://orcid.org/0000-0001-5043-4024

parameters (e.g., interstory drifts, story shear forces, story overturning moments, etc.) associated with the design of each individual tower.

Contrary to linear elastic analysis methods and strength based design used for regular structures, nonlinear response history analysis is required for tall buildings within the performance based design framework. Nevertheless, in real-life practice, due to time restrictions on project schedules, analysis of multiple towers using a combined structural model is typically not employed, and interaction effects between multiple towers are simply neglected, since computational demand for nonlinear response history analyses of multiple-tower models is significantly high. However, diaphragm forces developing in the podium floors of such structures is not an issue that can be disregarded in design.

Multiple towers on common podium buildings were not prevalent up to recent years since such structures were designed using seismic joints, forcing the response of the towers to be independent of each other. Therefore, although there is a scarce amount of relevant research in the literature, analysis of multiple towers on a common base is a subject that is not yet adequately investigated. One of the few studies that focus on multiple towers on common base is conducted by Qi and Chen [1]. Dynamic behavior of two towers connected with a typical podium structure is investigated through a parametric study. Towers and podium levels are modeled linear elastically using a lumped mass and equivalent stiffness approach. A simplified three degree of freedom (DOF) system is analyzed under a "constant" acceleration response spectrum, considering variation in mass and stiffness characteristics. This early study identifies the interaction effects between the towers to the seismic response of each, considering linear elastic forces only. However, this study does not include investigation of diaphragm effects at the connecting podium levels. In a more recent study by Behnamfar et al. [2], the importance of interaction effects between the two structures with various dynamic properties are addressed. A formulation is developed for simple multi degree of freedom systems to examine the severity of interaction forces on each structure. Linear springs are suggested for analysis using separate models for each tower. However, these linear springs are intended to represent only the kinematic interaction between the towers and neglect kinetic interaction caused by inertial effects. In addition, defining stiffness values for these springs may be tedious in real projects with complex structural configurations, especially projects that contain more than two towers on a single podium. Furthermore, in high rise structures, kinetic (i.e., inertial) interaction caused by out-of-phase vibration of the towers can be more predominant compared to kinematic interaction. Although this study provides notable amount of information for structures where inertial interaction is not expected to significantly affect the structural response, it is not adequate for reliable seismic response analysis of structures with high rise towers and connecting podiums.

The dynamic interaction between the towers and its effect on the dynamic response of the overall structure and the diaphragm effects on the podium levels is an issue that is explicitly warned against in design guidelines [3, 4, 5]; however, extremely limited literature is available on the subject. There is a clear need for additional analytical studies on this topic, which focus on the nonlinear response of real-life structural systems. As well, considering computational limitations, there is also a need for development of more practical approaches to be used for analysis and design of such structures.

Therefore, in this study, a practical approach is sought to evaluate the seismic response of structures incorporating multiple towers on a single podium, with emphasis on assessment of diaphragm effects at the podium levels. The main motivation is to assess whether critical response quantities for the towers and the podium floors can be approximately obtained within less computation time, by analyzing the towers separately with different assumptions for the end restraints, instead of using a combined model for analysis of the multiple tower structure.

Within the scope of this work, linear and nonlinear models of a hypothetical structure with two towers on a common podium are generated. The structure is analyzed using single-tower and combined double-tower models. The combined double model incorporates the entire structure including the towers, as well as the connecting podium and basement levels. The single models consist of a single individual tower, together with the corresponding half of the podium and basement floors, with different kinematic boundary conditions defined at the interface.

2. METHODOLOGY

2.1. Building Properties

The hypothetical reinforced concrete structure investigated in this study consists of two towers with 44 stories above and five stories below ground level. With 3.2 m typical height for each story, total height of the structure is 156.8 m and clear heights of the towers are 140.8 m. An identical structural system for both towers consist of a core wall system connected with coupling beams, T-shaped walls, outrigger beams (connecting core walls to perimeter walls), and perimeter frames along all four edges. The two towers are connected to each other by four podium floors above ground level, as well as five basement floors surrounded by perimeter walls (Figure 1). Architectural properties of the building are assumed such that the basement floors are utilized as parking garages, podium floors are utilized as commercial zones, and towers are utilized as residential buildings. Based on strength based design of the structure compliant with Turkish Building Earthquake Code 2018 (TBEC2018) [6], cross-sectional dimensions of the structural members are obtained as presented in Table 1.

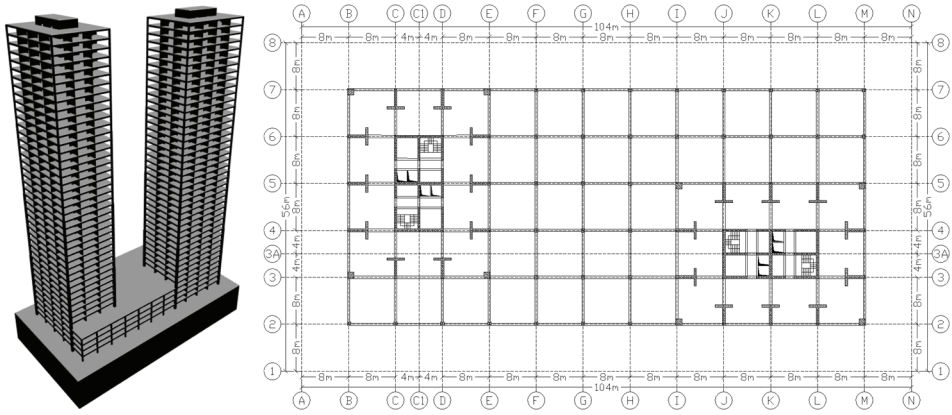

Figure 1 - 3D view of the structure and typical plan view for connected podium floors.

Table 1 - Cross-sectional dimensions of the structural members.

	-16.00m +00.00m	+00.00m +12.80m	+12.80m +35.20m	+35.20m +67.20m	+67.20m +102.4m	+102.4m +137.6m
Core Wall Web (restrained at both ends)	500mm				400mm	
Core Wall Flange (restrained at one end)	400mm				300mm	
T-Wall Web	500mm				400mm	
T-Wall Flange	400mm				300mm	
Basement Perimeter Walls	400mm	N/A				
Tower Columns	1200/1200mm	1100/1100mm	900/900mm	800/800mm	700/700mm	600/600mm
Podium Columns	800/800mm	600/600mm	N/A			
Coupling Beams	400/750mm				300/750mm	
Outrigger Beams	500/700mm				400/700mm	
Perimeter Frame Beams	400/600mm					
Podium Beams	400/600mm		N/A			
Slab	200mm					

2.2. Interaction Behavior

Interaction effects between the two towers can be classified into kinematic interaction and kinetic (inertial) interaction. Kinematic interaction is the effect of a tower to nearby towers due to its lateral stiffness properties. This type of interaction can be modeled using linear springs with constant stiffness. Second type of interaction is inertial interaction, which is related to the relative (in-phase, out-of-phase, or in-between) vibration of the towers due to their respective inertial properties. This type of interaction cannot be simply modeled using linear springs with stiffness values obtained from static analysis, since stiffness of thesprings would change depending on relative displacements (deformed shape) of the towers at the podium levels.

The scope of this analytical study comprises evaluating the aforementioned dynamic interaction effects on the seismic response of a representative multiple-tower structure, in terms of the in-plane axial and shear forces developing in the podium and basement level diaphragms, as well as the seismic response demands of the individual towers, using a combined structural model of the multi-tower system and employing both linear and nonlinear modeling and analysis methods. Analysis results obtained using the combined model are also compared to simplified upper bound and lower bound modeling and analysis approaches, where the lower bound approach simply neglects the interaction between the towers and the upper bound approach can be interpreted to represent the interaction to the full extent. Prior to conducting analyses using a double (combined two-tower) model, single (one-tower) models are generated, by cutting the double model along the centerline of the podium structure between the two towers (Figure 2). For the case when the response of two towers completely out of phase, fixed supports are assigned to the joints where double model is cut. With this approach, the single models are analyzed assuming that there is an identical tower with completely symmetric response on other side of the cutting plane. On the other hand, for the case when response of two towers are completely in phase, no horizontal restraint (roller supports) are assigned to the joints where the double model is cut. Using this approach, the single models are analyzed assuming that there is an identical adjacent tower, with an identical response on other side of the cutting plane. Depending on these extreme assumptions, linear and nonlinear analysis results obtained using single fixed and single free models for both towers are compared with analysis results of the combined double tower model.

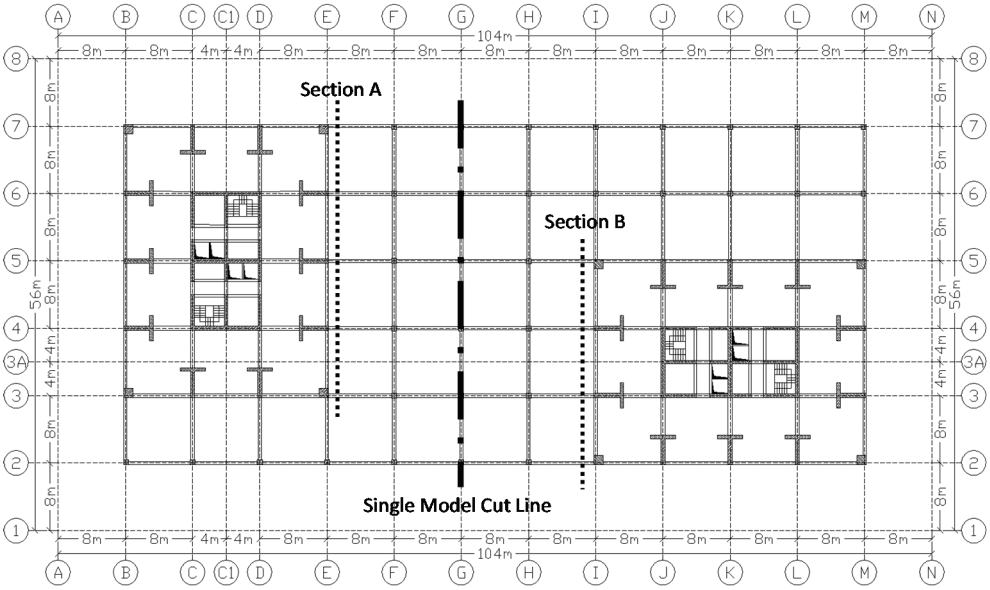

Figure 2 - Section cut and single model cut line locations.

2.3. Linear Elastic Modeling

Linear elastic models of the structure are generated using CSI ETABS [7] software for linear analyses. For linear modeling, concrete elastic modulus is defined as defined in Requirements for Design and Construction of Reinforced Concrete Structures (TS500) [8]. In design of this structure, C50 concrete class and B420C reinforcing steel grade are used, with characteristic compressive strength of f_{ck}=50 MPa and yield strength f_{yk}=420MPa, respectively. Effective rigidity of structural members, masses and damping characteristics are defined according to TBEC2018. Modeling assumptions used are compliant with the criteria in TBEC2018. Loads corresponding to different architectural utilization properties are defined according to Design Loads for Buildings (TS 498) [9]. Natural vibration periods and corresponding modal mass participation ratios of the structure obtained using free vibration analysis are provided in Table 2 for the model configurations generated. Based on free vibration analysis of the double model, fundamental mode shapes of the towers are also presented in Figure 3. To satisfy the total mass participation of 95% in each direction requirement defined in TBEC2018, first 120 modes of the structure are included in analyses.

Table 2 - Fundamental vibration periods and corresponding mass participation ratios of the towers for single fixed, double, and single free models.

		Tower A			Tower B		
		Fixed	Double	Free	Fixed	Double	Free
X Direction	Period	4.88s	5.20s	5.44s	3.96s	4.08s	4.29s
	Mass Participation	43.7%	31.6%	48.6%	42.7%	14.9%	47.1%
Y Direction	Period	4.08s	4.29s	4.33s	5.12s	5.41s	5.48s
	Mass Participation	46.7%	21.5%	50.5%	43.5%	25.9%	46.8%

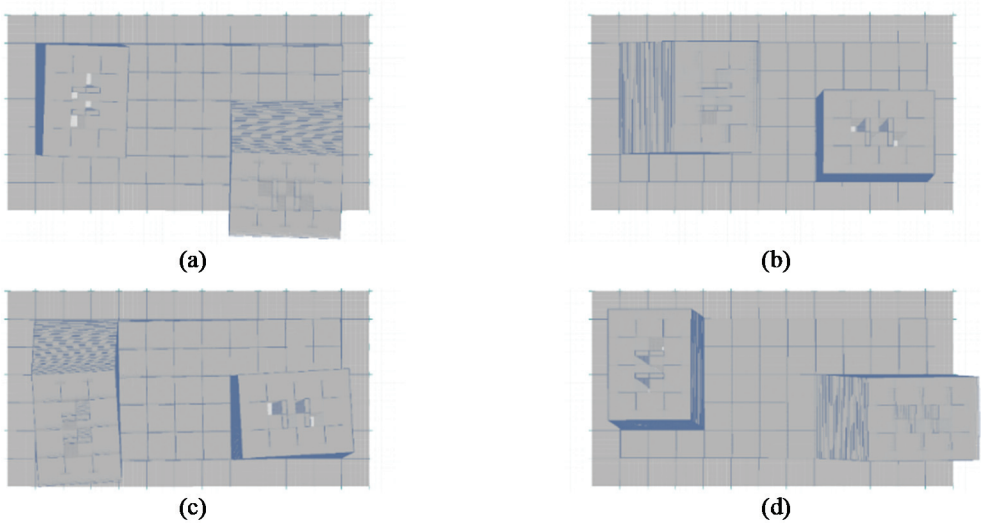

Figure 3 - Mode shapes for fundamental periods (a) TBY, (b), TAX, (c) TAY, (d) TBX.

2.4. Nonlinear Modeling

Nonlinear models of the structure (Figure 4) are generated using the commonly-used software Perform3D [10]. Methods, assumptions, and criteria used in modeling and analysis of the structure are compliant with specifications in TBEC2018, and recommendations in LATBSDC2015 [4] and ASCE41-13 [11]. Based on the state-of-the-art design codes and guidelines, nonlinear flexural behavior of beams and columns are modeled using the so-called lumped plasticity (plastic hinge) approach (Figure 5), utilizing ASCE41-13 backbone relationships, whereas nonlinear flexural behavior of the structural walls is modeled using the distributed plasticity (fiber modeling) approach (Figure 6). Floor slabs at the podium levels and the basement walls, which are expected to remain linear elastic under seismic effects, are included in the nonlinear model using linear elastic material properties. Floor slabs of the tower structures are not included in the model, and their in-plane stiffness is idealized using a rigid diaphragm constraint in the model. For nonlinear modeling, the expected compressive strength of concrete is defined as $f_{ce} = 65$ MPa and the expected yield strength of reinforcing steel is defined as $f_{sye} = 504$ MPa, according to TBEC2018 and LATBSDC2015 specifications.

Majority of the hysteretic energy dissipation sources in the structure are considered in nonlinear analysis, by explicit modeling of the hysteretic behavior of the aforementioned structural members. Equivalent viscous damping characteristics of the structure (2.5% viscous damping ratio specified in TBEC2018 for tall buildings is introduced in the model as 2.4% modal damping and 0.1% Rayleigh damping ratios, also for damping out higher vibration modes as suggested by Powell [12].

2.5. Analysis Methods

To evaluate the seismic response of the structure, various analysis methods that are commonly used in practice are adopted. These methods are linear modal time history analysis (LMTHA), response spectrum analysis (RSA) and nonlinear response history analysis (NLRHA).

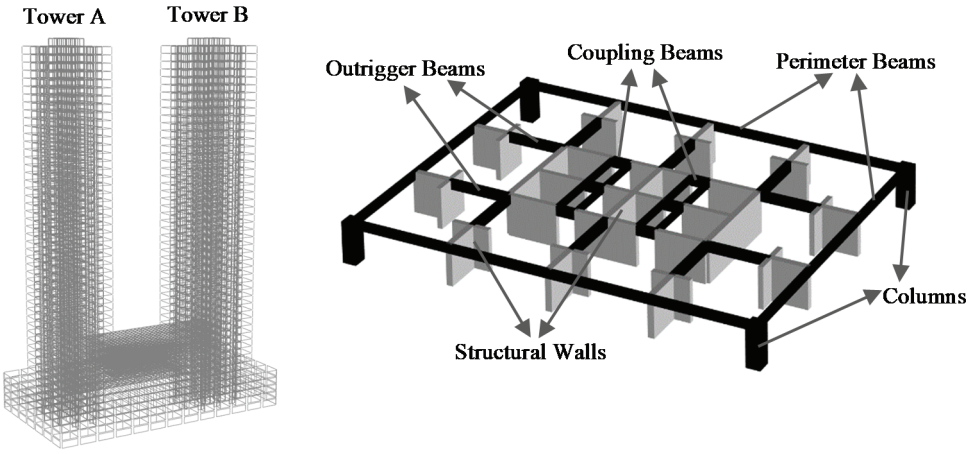

Figure 4 – Nonlinear double-tower model geometry and nonlinear structural elements.

2.6. Seismic Hazard Definition and Ground Motion Selection

The structure is analyzed under the DD1 and DD2 level earthquakes defined in TBEC2018, where DD1 (maximum credible earthquake) and DD2 (design level earthquake) levels corresponds to earthquake scenarios with probabilities of exceedance of 2% (2475 years recurrence period) and 10% (475 years recurrence period) in 50 years, respectively. Spectrum parameters at a hypothetical project site coordinates (40˚58'39.1"N, 28˚48'52.1"E) required to define the target spectrum are obtained from the Turkish Earthquake Hazard Map (TEHM) website [13] released by the Disaster and Emergency Management Presidency. Considering hazard levels at the site, distance between project site and closest active fault, as well as local soil conditions, design spectral acceleration coefficients are defined and design spectra are generated as shown in Figure 7 according to TBEC2018.

Ground motions are selected from the NGAWest2 Ground Motion Database [14] by matching the SRSS resultant acceleration spectra of the ground motion components with a target spectrum that is defined as 1.3 times the design spectrum defined in TBEC2018 (Figure 8) for the DD1 and DD2 level earthquakes. Details on ground motion selection and scaling, as well as detailed information on modeling and analysis of the investigated structure are presented by Tura [15].

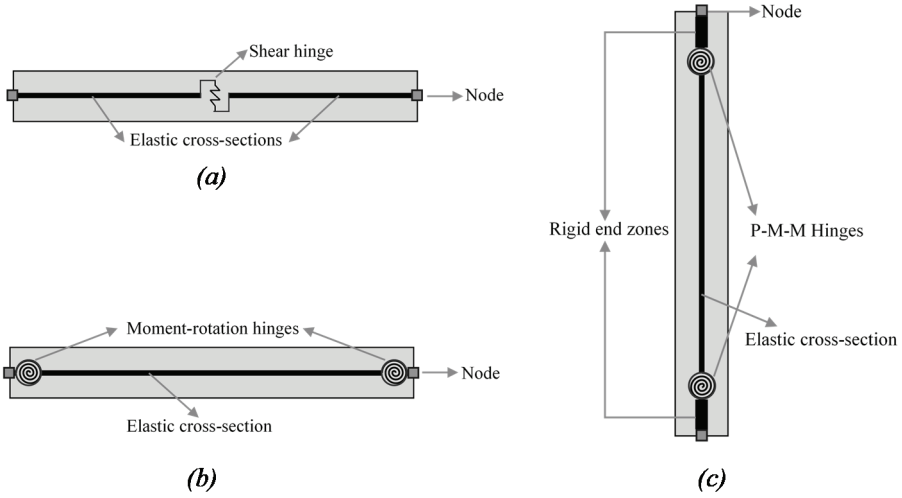

Figure 5 - Modeling of frame elements with lumped plasticity approach in Perform 3D; (a) coupling beams (b) outrigger and perimeter beams (c) columns.

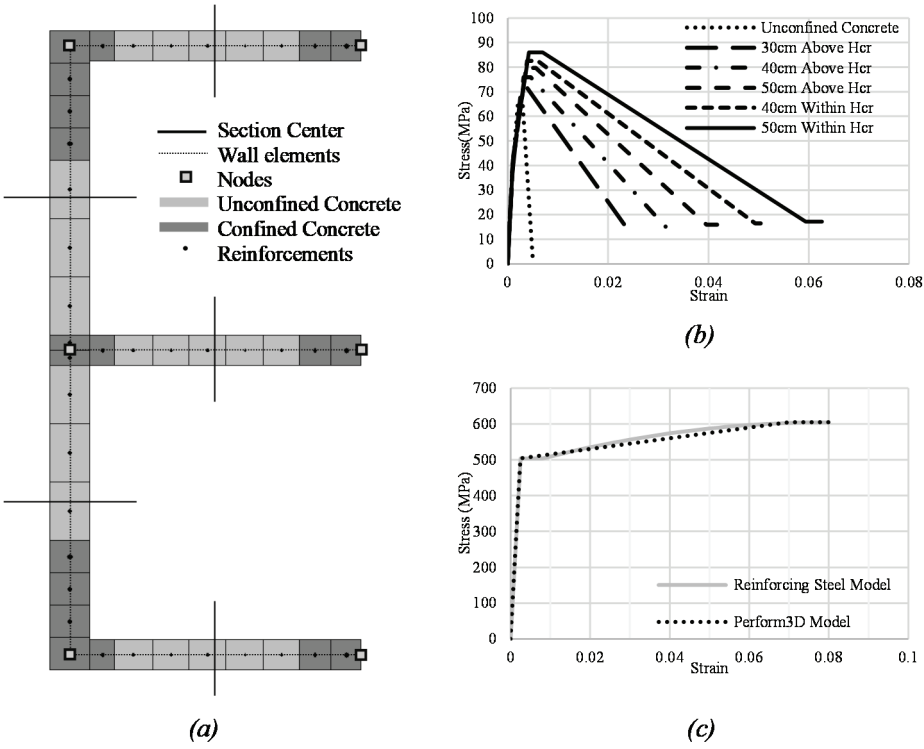

Figure 6 - Modeling of structural walls with distributed plasticity (fiber modeling) approach in Perform 3D; (a) cross-sectional view (b) unconfined and confined concrete stress-strain relationships (c) reinforcement stress-strain relationship.

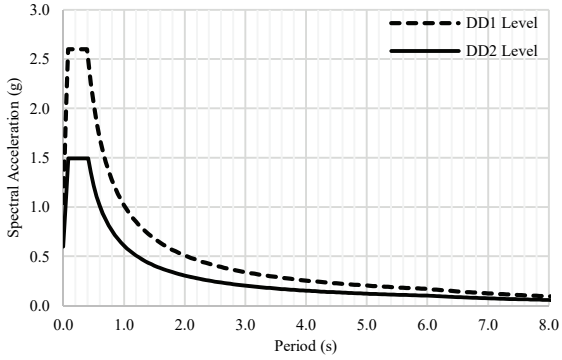

Figure 7 - Design spectra for DD1 and DD2 level earthquakes.

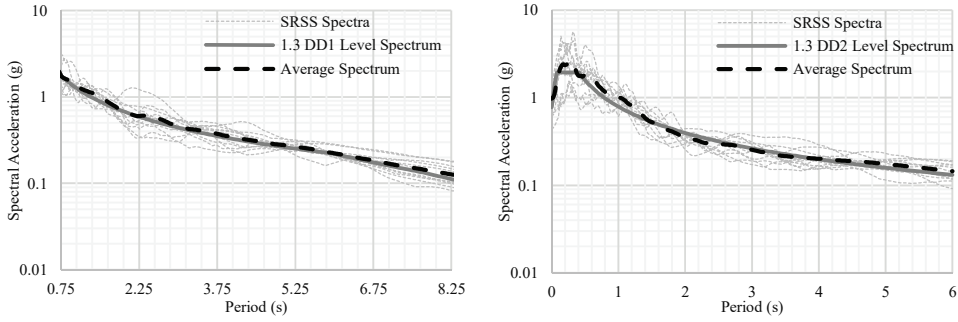

(a) *(b)*

Figure 8 - SRSS acceleration spectra of selected ground motions for earthquake levels; (a) DD1 (b) DD2.

3. ANALYSIS RESULTS

In linear analyses, design spectrum of DD2 level (design level, i.e., 10% probability of exceedance in 50 years) seismicity (Figure 7) is used for RSA and 11 pairs of ground motion records selected for the target spectrum of DD2 level seismicity (Figure 8) are used for LMTHA. Furthermore, seismic demand is defined for linear analyses using a structural system behavior factor R = 6 for structural systems where all seismic demand is resisted by uncoupled structural walls according to TBEC2018. On the other hand, 11 pairs of ground motion records selected for the design spectrum corresponding to DD1 level (maximum credible, i.e., 2% probability of exceedance in 50 years) seismicity are used for NLRHA. In all response history analyses, total of 22 analyses are conducted, first by applying 11 ground motion record pairs, and secondly by reapplying the records at 90 degree rotated state. In all analyses, in-plane (diaphragm) tensile forces in X direction and in-plane (diaphragm) shear forces are obtained at section cuts defined adjacent to the tower edges (Figure 2). During evaluation of analysis results of linear analysis, earthquake effects are magnified using the over-strength factor D = 2.5, as is specified in TBEC2018.

3.1. Response Spectrum Analysis (RSA) Results

In plane distribution of resultant tensile forces (per unit slab length) in the floor diaphragm at +12.80 m elevation is presented in Figure 9 for RSA using the double-tower model. From the figure, stress concentration between the two towers due to interaction at the podium floors can be observed clearly. Resultant tensile force magnitudes in slab elements reach up to 600 kN/m at locations where stiff structural walls and floor slab are connected. In addition, due to beam action in the podium diaphragm, stress concentrations at upper and lower edges of the critical zone are noted. From a design perspective, when resultant tensile forces are compared with limit 330 kN/m corresponding to design tensile strength of concrete, it is clear that concrete cracks under tension and additional diaphragm reinforcement is required for code-compliant behavior.

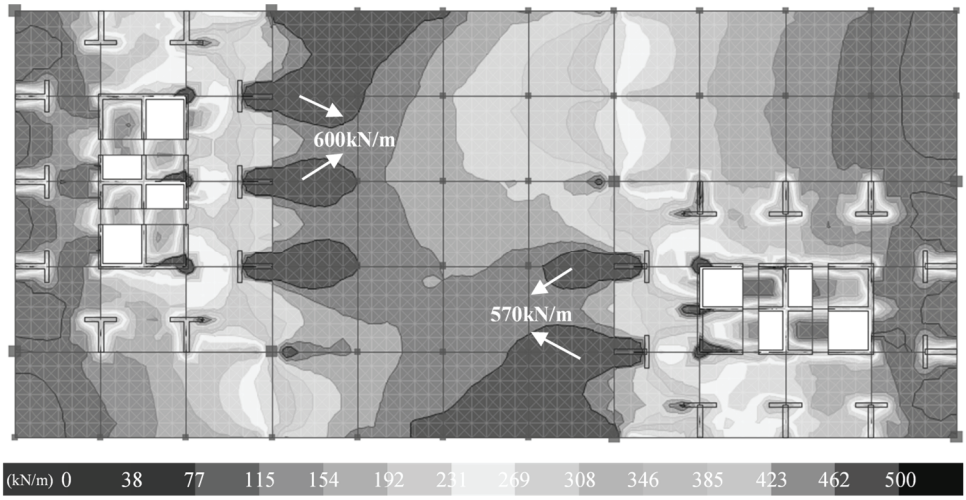

Figure 9 - Diaphragm tensile force distribution (in X direction) per unit length of slab at +12.80 m elevation of double model obtained from RSA.

Resultant tensile forces obtained from RSA of the double and single models, developing in the connected podium diaphragms are presented in Figure 10. As it is expected, interaction effects are much more critical at the uppermost diaphragm level compared to those at lower stories. When the resultant tensile forces at the section cuts are evaluated, it is clear that single models with fixed end restraints overestimate the in-plane axial forces at the connected podium slabs. According to section cut results obtained from RSA of the double model, average tensile stresses (averaged over the entire slab cross section) are calculated as 2.68 MPa for Section A and 2.75 MPa for Section B of the diaphragm, at +12.80 m elevation. In addition, axial loads on beams range between 800 kN and 1000 kN, with a total of 4420 kN at Section A and 3540 kN for Section B. Considering this distribution, additional diaphragm reinforcement can be designed as ϕ16/300 mm (1340 mm^2/m) additional top and bottom reinforcement in slabs and 8ϕ20 (2512 mm^2) skin (i.e., longitudinal web) reinforcement in beams at Section A, and ϕ16/300 mm (1340 mm^2/m) additional top and bottom reinforcement in slabs and 8ϕ20 (2512 mm^2) skin reinforcement in beams at Section B. Furthermore, when average stresses at lower podium levels are evaluated (1.36 MPa for Section A, 1.41 MPa for

Section B), it is noted that concrete at these levels does not crack under axial tension; therefore, no additional reinforcement in the slab or the beams is required.

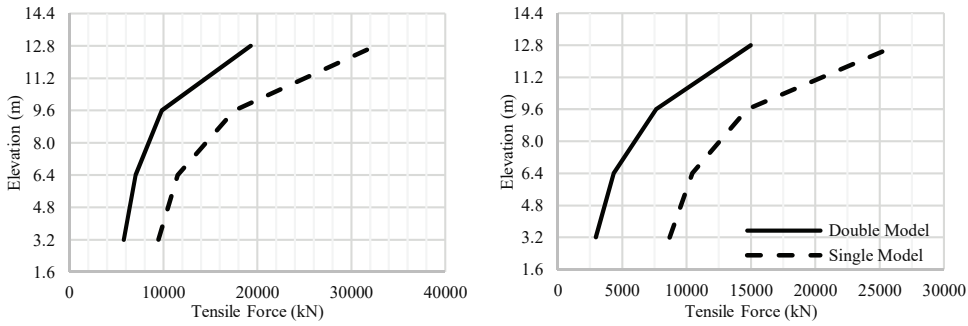

(a) *(b)*

Figure 10 - Resultant tensile forces (in X direction) obtained from RSA at (a) Section A, (b) Section B.

On the other hand, if the single-fixed model analysis results are used in design, additional slab and beam reinforcement amounts calculated using the double model increase up to ϕ16/200 mm (2010 mm^2/m) and 8ϕ26 (4248 mm^2) at Section A, and ϕ16/175 mm (2297 mm^2/m) and 8ϕ26 (4248 mm^2) at Section B. Furthermore, according to the single-fixed model results, the diaphragm at +09.60 m elevation also cracks and it can be designed for ϕ12/200 mm (1130 mm^2/m) additional reinforcement in the slabs and 6ϕ22 (2280 mm^2) skin (longitudinal web) reinforcement in beams at Section A, and ϕ12/175 mm (1291 mm^2/m) additional reinforcement in the slabs and 8ϕ20 (2512 mm^2) skin reinforcement in the beams at Section B.

In-plane distribution of the resultant shear forces (per unit slab length) developing in the podium floor diaphragm at +12.80 m elevation is presented in Figure 11, based on RSA results using the double model. Resultant shear forces in the slab elements vary between 200 kN/m and 250 kN/m in the regions between the two towers. Comparing these magnitudes with a resultant shear force capacity 214 kN/m (corresponding to the concrete shear strength of 1.07 MPa), it is observed that diaphragm shear forces are as not critical as tensile forces for this structure. Furthermore, resultant shear forces in the connected diaphragms are presented in Figure 12 for RSA using double and single-fixed models. Similar to the tensile force distributions, total shear forces are highest at the uppermost connecting diaphragm, with magnitudes of 7046 kN at Section A and 5542 kN at Section B, and reduce throughout the lower stories down to 3785 kN for Section A and 2778 kN for Section B. Besides, resultant shear forces obtained using double and single-fixed models differ significantly, similarly to tensile force resultants. Therefore, if analysis results using the single-fixed model are used in design, average shear stress values increase up to 2.27 MPa for Section A and 2.41 MPa for Section B. Accordingly, the required amount of additional slab reinforcement for design increases up to 658 mm^2/m for Section A and 734 mm^2/m for Section B. Based on these demands, additional slab reinforcement can be designed as ϕ12/350 mm (646 mm^2/m) top and bottom bars at Section A, and ϕ12/300 mm (753 mm^2/m) top and bottom bars at Section B. Furthermore, according to section cut results of the fixed model under RSA,

average shear stresses in the diaphragm at +09.60 m elevation are calculated as 1.29 MPa at Section A and 1.35 MPa at Section B. Since these average stress levels are very close to the concrete design shear strength of 1.07 MPa, the required amount of additional reinforcement can also considered to be negligible for design purposes.

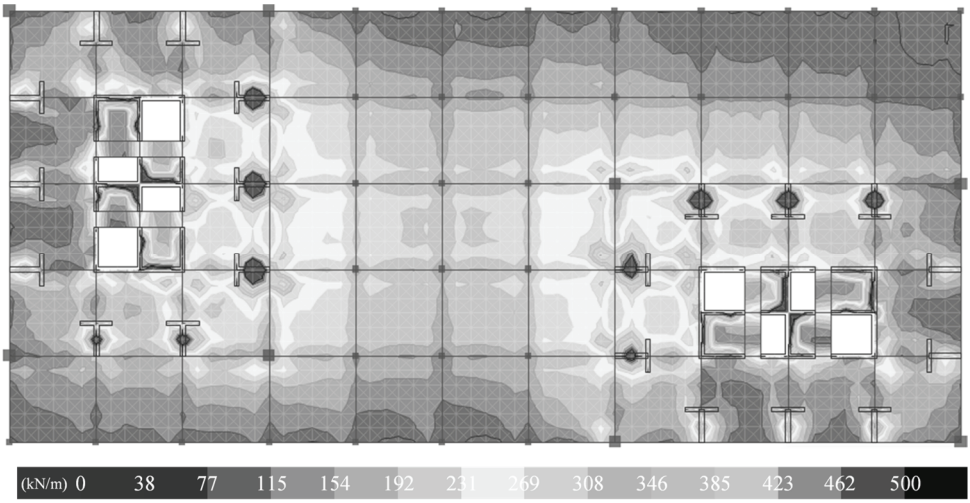

Figure 11 - Diaphragm shear force distribution per unit length of slab at +12.80 m elevation of double model obtained from RSA.

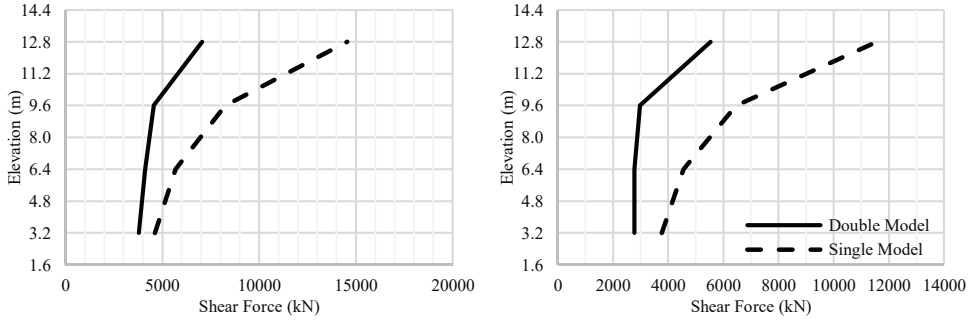

(a) *(b)*

Figure 12 - Resultant diaphragm shear forces obtained from RSA at (a) Section A, (b) Section B.

3.2. Linear Modal Time History Analysis (LMTHA) Results

Distribution of resultant tensile forces in the floor diaphragm at +12.80 m elevation is presented in Figure 13 for LMTHA of the double model under the DD2 level earthquake. When LMTHA and RSA distributions are compared, it is observed that LMTHA gives

similar resultant tensile force magnitudes and distributions compared to RSA results. The only difference noted is marginally smaller magnitudes at critical regions of the diaphragm.

Resultant tensile forces in the connected podium floors, obtained from LMTHA of the structure using the double and single-fixed models, is presented in Figure 14 For consistency with RSA results, mean of 22 analysis results are presented in the table and figure. Similar to RSA, analysis results of the single-fixed model overestimate the double model results. Based on the average of 22 analyses, maximum resultant tensile force values obtained in the first connecting diaphragm are 18024 kN at Section A and 14322 kN at Section B. These resultants corresponds to average tensile stresses of 2.50 MPa at Section A and 2.63 MPa at Section B. Since these stress levels are close to results of RSA, an identical reinforcement design is applicable to resist the diaphragm forces.

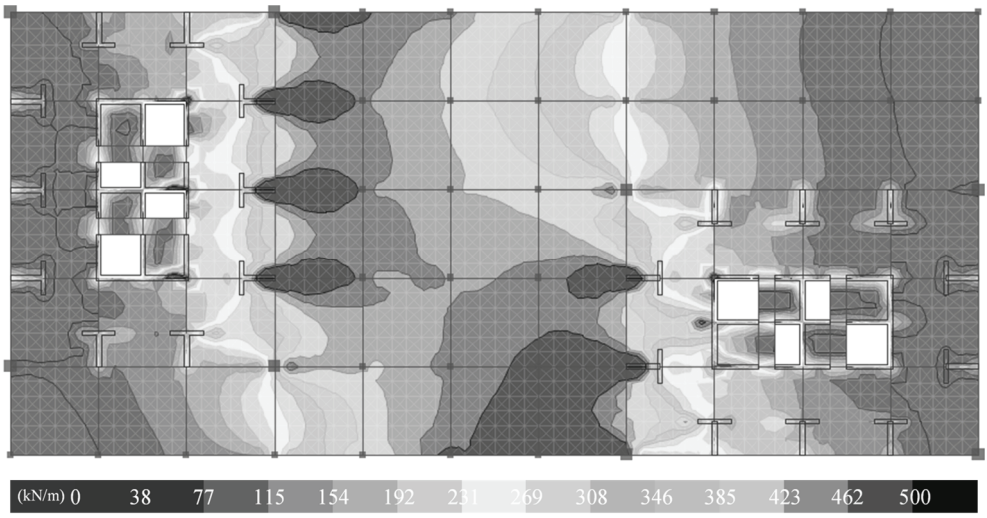

Figure 13 - Diaphragm tensile force distribution (in X direction) per unit length of slab at +12.80 m elevation of double model obtained from LMTHA.

In-plane distribution of resultant shear forces in the floor diaphragm at +12.80 m elevation is presented in Figure 15 for LMTHA using the double model. Similar to tensile forces, distribution of resultant shear forces are also similar to RSA results. As was the case in RSA, resultant shear forces (per unit length) in the slabs vary between 200 kN/m and 250 kN/m in the region between the two towers.

Resultant shear forces along the connected podium floors are presented in Figure 16 for LMTHA using single-fixed and double models. Similar to RSA, analysis results obtained using the single- fixed model overestimate the double model results. According to average of 22 analyses, maximum resultant shear forces (per unit slab length) developing in the topmost connecting diaphragm are 5359 kN at Section A and 4324 kN at Section B. These resultants correspond to average shear stresses of 0.84 MPa at Section A and 0.90 MPa at Section B. Since these shear stress levels do not exceed the concrete design shear strength of 1.07 MPa, no additional diaphragm shear reinforcement is required.

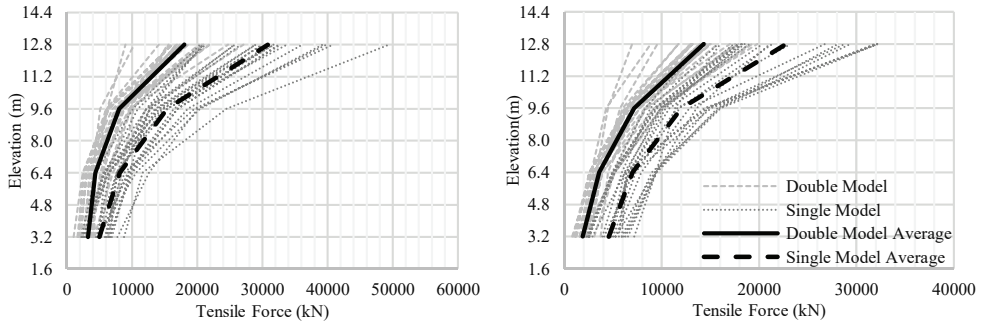

(a) *(b)*

Figure 14 - Resultant tensile forces (in X direction) obtained from LMTHA at (a) Section A, (b) Section B.

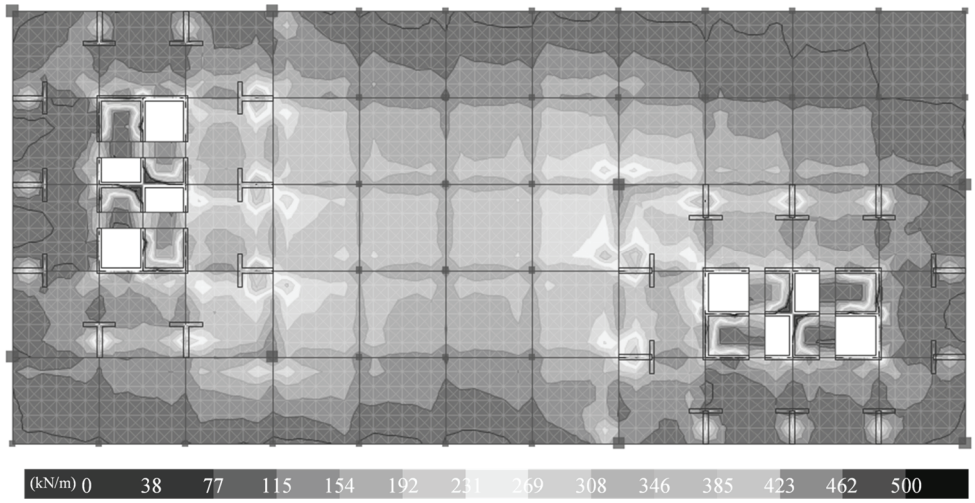

Figure 15 - Diaphragm shear force distribution per unit length of slab at +12.80 m elevation of double model obtained from LMTHA.

On the other hand, if single-fixed model analysis results are used in design, average shear stresses increase up to 2.27 MPa at Section A and 2.18 MPa at Section B. Since these stresses exceed the design shear strength of concrete 1.07 MPa, the required amount of additional slab reinforcement increases up to 658 mm^2/m at Section A and 608 mm^2/m at Section B at this level. According to these amounts, additional slab reinforcement can be designed as ϕ12/350 mm (646 mm^2/m) top and bottom bars at Section A, and ϕ12/350 mm (646 mm^2/m) top and bottom bars at Section B. In addition, according to section cut results of the fixed model under LMTHA, average shear stresses in the diaphragm of +09.60 m elevation are calculated as 1.34 MPa at Section A and 1.29 MPa at Section B. Since these stress levels are very close to the concrete design shear strength of 1.07 MPa, the required amount of additional slab reinforcement is negligible in design.

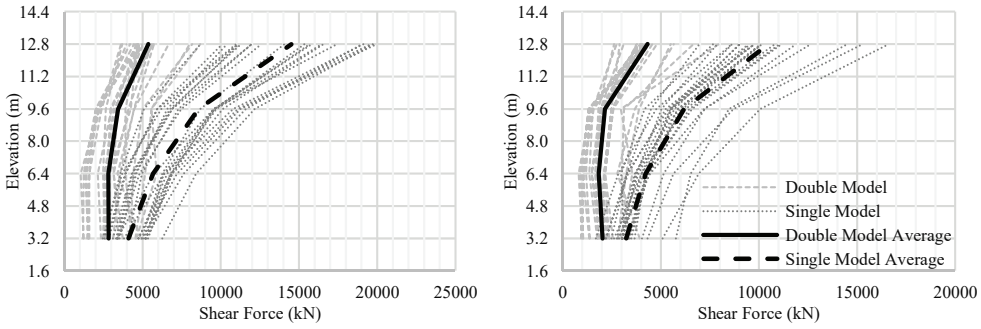

Figure 16 - Resultant diaphragm shear forces obtained from LMTHA at (a) Section A, (b) Section B.

In the following figures, comparison of resultant tensile and shear forces obtained from RSA and LMTHA of the single-fixed and double models, throughout the connected podium floors are presented. According to Figure 17, LMTHA consistently gives smaller tensile force values with respect to RSA. Resultant tensile forces at critical sections are very close to each other at the topmost connecting diaphragm, except for the single model results obtained for Tower B. Furthermore, differences in results of the two analysis methods are more significant at lower diaphragm levels. Similarly, according to Figure 18, diaphragm shear force resultants obtained by LMTHA are generally smaller than RSA results. The only exception is the fixed model results for the section cut at +09.60 m elevation of Tower A. At this section, the result of LMTHA is barely higher than the RSA result.

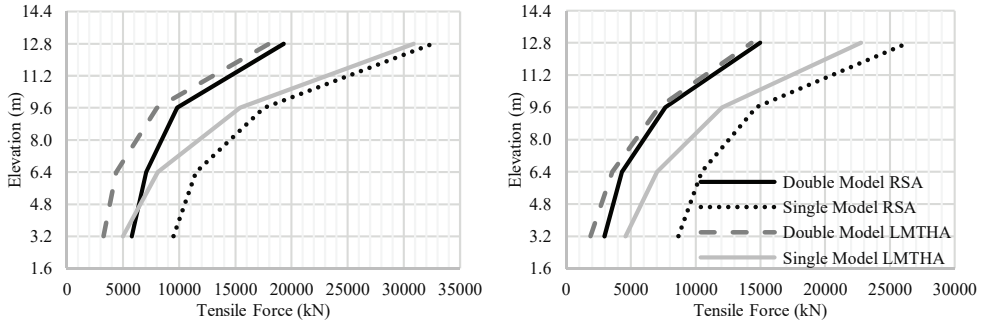

Figure 17 - Comparison of resultant diaphragm tensile forces (in X direction) obtained from LMTHA and RSA at (a) Section A, (b) Section B.

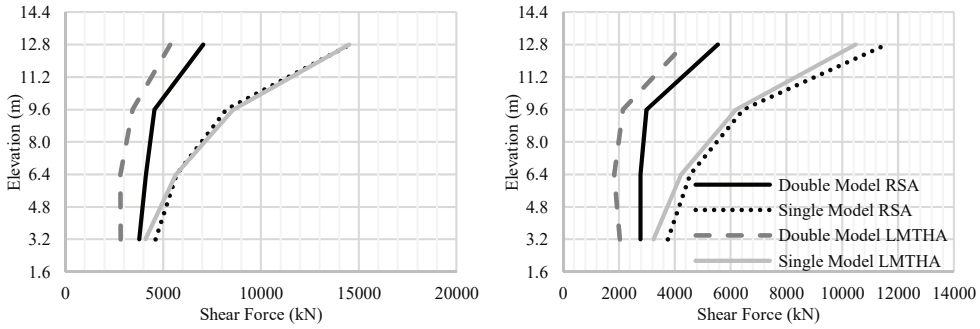

Figure 18 - Comparison of resultant diaphragm shear forces obtained from LMTHA and RSA at (a) Section A, (b) Section B.

3.3. Nonlinear Response History Analysis (NLRHA) Results

In this section, the diaphragm forces at the connecting podium levels are evaluated using a performance-based design approach, using NLRHA of the structure under the DD1 level earthquake (maximum credible earthquake, 2% probability of exceedance in 50 years), again using both double and single-fixed tower models. In the evaluation, diaphragm forces in the podium-level slabs and beams are considered as critical (i.e., non-ductile) response quantities and are assessed using a strength-based approach. Required amounts of diaphragm reinforcement obtained from NLRHA results to reach sufficient diaphragm strength are compared with reinforcement amounts obtained using linear analysis results under the design-level earthquake. Furthermore, seismic performance predictions obtained for Tower A using the double tower model under DD1 level ground motions are compared with predictions obtained using a single tower model, with both free and fixed end restraints at the connecting podium levels.

3.3.1. Podium Diaphragm Force Resultants

In order to facilitate convergence and reduce analysis time to a manageable level, podium diaphragms are modeled using shell elements with a relatively larger size in the nonlinear model of the structure. Although local distribution of the diaphragm forces is not captured since the diaphragms are more crudely-meshed, reliable values for diaphragm force resultants can still be obtained from the analyses. Because NLRHA of the double model required weeks of analysis time, analysis under different ground motion records were run in parallel, using separate models running on separate computers. For illustrative purposes, distribution of the diaphragm tension force (per unit length) developing in the topmost podium floor is illustrated in Figure 19, for a representative ground motion record referred to as RSN1762 [14] (used with a scaling factor of 3.326 in the analysis), which produces similar diaphragm force resultant magnitudes compared with the average of all 22 analyses. Differently from linear analysis results, due to the crude meshing, local stress concentrations in the slab at the structural wall connections are not recognizable. However, the overall distribution of the diaphragm tension forces is clearly shown in the figure. Tensile force concentrations between the two towers as well as at top and bottom edges of the connecting podium can be identified, similarly to the results of linear analysis.

Diaphragm tensile force resultants developing in the connected podium floors are presented in Figure 20, for the average of 22 NLRHA cases (corresponding to 22 ground motions). Compared to results of RSA and NLRHA, force resultant distribution along the podium floor elevations follows a similar pattern. However, there is 18% increase at Section A and 31% increase at Section B, in the total tensile force resultants at the floor with +12.80 m elevation, compared to RSA. This percent difference reaches upto 48% increase at Section A and 35% increase at Section B, when analysis results using the single-fixed models are considered.

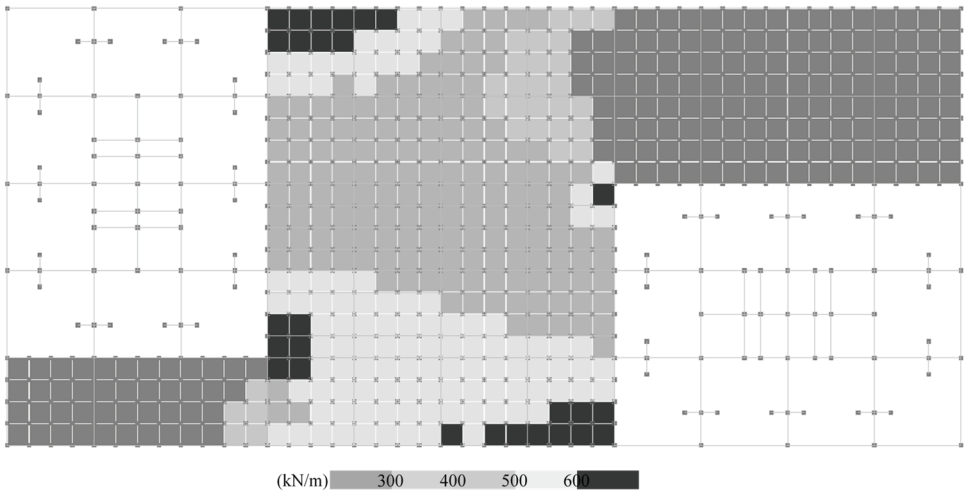

Figure 19 - Diaphragm tensile force distribution (in X direction) per unit length of slab at +12.80 m elevation of double model obtained from NLRHA under record RSN1762 [14].

Considering mean analysis results obtained using the double model, average tensile stresses developing at the topmost podium diaphragm are calculated as 3.17 MPa at Section A and 3.60 MPa at Section B. Comparing these stress levels with the expected tensile strength of concrete 2.82 MPa, it is deduced that concrete cracks in tension and additional reinforcement is required in these regions, similar to linear analysis results. Using the expected yield strength of reinforcement, total amounts of required slab reinforcement are calculated as 45339 mm^2 at Section A and 38813 mm^2 at Section B.

Furthermore, contribution of beams to the total tensile force resultant is obtained as 6762 kN at Section A and 5243 kN at Section B. Note that, percentages corresponding to contribution of beams to the total diaphragm tension force are 30% for Section A and 27% for Section B, whereas they were obtained as 23% for Section A and 24% for Section B from RSA. Taking into account all the information mentioned above, the required additional reinforcement can be designed as ϕ14/300 mm (1027 mm^2/m) top and bottom bars in the slabs and 9ϕ20 (2826 mm^2) skin (i.e., longitudinal web) reinforcement in the beams at Section A, and ϕ14/250 mm (1232 mm^2/m) top and bottom bars in slabs and 7ϕ22 (2660 mm^2) skin reinforcement in the beams at Section B. Average tensile stress levels at lower podium floors, which are 1.79 MPa at Section A and 1.88 MPa at Section B, are lower than the expected tensile strength of concrete. Therefore, no additional reinforcement is required to resist diaphragm tension at lower podium floors.

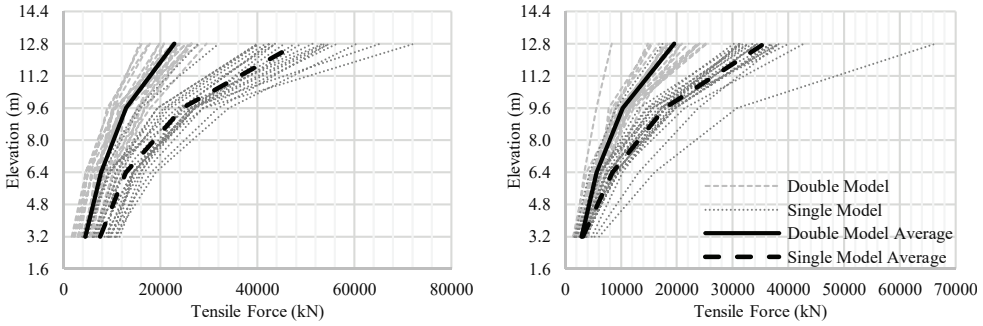

Figure 20 - Resultant tensile forces (in X direction) obtained from NLRHA at (a) Section A, (b) Section B.

On the other hand, when fixed model results are taken into account, average tensile stresses developing in the slabs at the topmost podium floor increase to 6.70 MPa at Section A and 6.82 MPa at Section B. According to these stresses, the required additional reinforcement can be designed as ϕ18/250 mm (2032 mm^2/m) top and bottom bars in slabs, and 8ϕ30 (5656 mm^2) skin reinforcement in beams at Section A, and ϕ20/300 mm (2093 mm^2/m) top and bottom bars in slabs and 8ϕ28 (4928 mm^2) skin reinforcement in beams at Section B. Additionally, average tensile stress levels at the podium floor of +09.60 m elevation increases to 3.41 MPa at Section A and 3.29 MPa at Section B. Therefore, concrete at this floor also cracks and additional tension reinforcement is required. Required additional reinforcement at this elevation can be designed as ϕ14/300 mm (1027 mm^2/m) top and bottom bars in slabs and 8ϕ22 (3040 mm^2) skin (i.e., longitudinal web) reinforcement in beams at Section A, and ϕ14/300 mm (1027 mm^2/m) top and bottom bars in slabs and 8ϕ20 (2512 mm^2) skin reinforcement in beams at Section B.

In plane distribution of diaphragm shear forces (per unit length) in the podium floor slab at +12.80 m elevation is presented in Figure 21 for NLRHA of the double model under the RSN1762_0 [14] ground motion record (scaled with a factor of 3.326). Similarly to diaphragm tensile forces, despite crude meshing, diaphragm shear effects are clearly reflected in the analysis results. The in-plane shear force distribution is similar to linear analysis results.

Resultant diaphragm shear forces along the connected podium floors are presented in Figure 22, as average of the 22 analysis cases used in NLRHA. Comparing results of RSA (Figure 12, under DD2 level earthquake) and NLRHA (Figure 22, under DD1 level earthquake), the distribution along the floors follows similar patterns in the single-fixed models, and slightly different patterns in the double models. In terms of magnitudes, there is a 91% increase at Section A and an 87% increase at Section B in the total diaphragm shear force acting on the podium floor with +12.80 m elevation in the double model, compared to RSA. This percent increase changes to 109% increase at Section A and 81% increase at Section B, when RSA and NLRHA results using fixed models are considered.

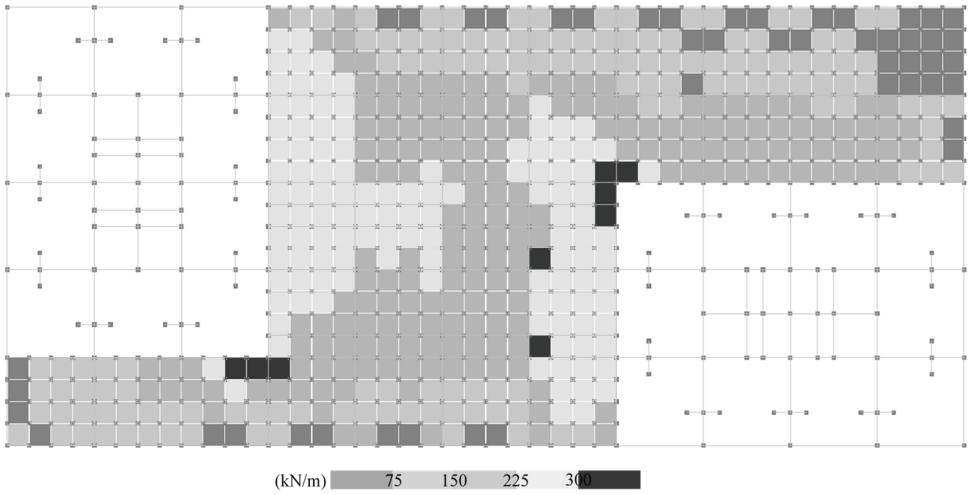

Figure 21 - Diaphragm shear force distribution per unit length of slab at +12.80 m elevation of double model obtained from NLRHA under RSN1762 [14] record.

Considering mean response quantities of double model, average diaphragm shear stress values at the topmost podium floor are calculated as 2.10 MPa at Section A and 2.16 MPa at Section B. Since these stress levels are very close to the concrete design shear strength 1.83 MPa, the required amounts of additional diaphragm shear reinforcement are negligible amounts for design purposes. Furthermore, analysis results show that the contribution of beams to diaphragm shear forces is negligible, as is typical.

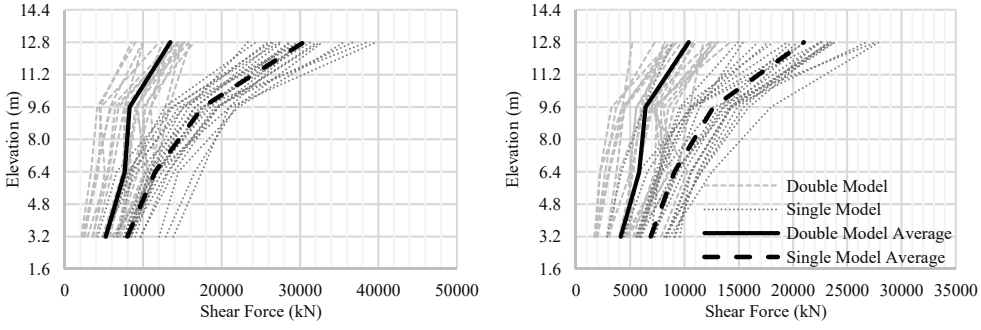

(a) *(b)*

Figure 22 - Resultant shear forces obtained from NLRHA (a) Section A, (b) Section B.

On the other hand, if single-fixed model analysis results are considered in design, average diaphragm shear stress values at the topmost podium floor increase to 4.76 MPa at Section A and 4.37 MPa at Section B. Therefore, required amount of additional slab reinforcement increases up to 1163 mm^2/m at Section A and 1008 mm^2/m at Section B, at this elevation.

Corresponding reinforcement can be designed as ϕ14/250 mm (1232 mm^2/m) additional top and bottom reinforcement at Section A and ϕ14/300 mm (1027 mm^2/m) additional reinforcement at Section B. Again, diaphragm shear forces in the beams are negligible.

Additionally, based on section cut results from NLRHA of the fixed models, average diaphragm shear stresses at the floor with +09.60 m elevation are calculated as 2.75 MPa at Section A and 2.64 MPa at Section B. Considering these stress levels, the floor slab at this elevation can be designed using ϕ10/400 mm (393 mm^2/m) additional top and bottom bars at Section A and ϕ10/500 mm (314 mm^2/m) additional bars at Section B.

Finally, comparisons of diaphragm reinforcement required at critical sections, obtained using RSA (under DD2 level earthquake considering the code-prescribed load reduction factor and overstrength coefficient) and NLRHA (under DD1 level earthquake), are presented in Table 3 for Section A and Table 4 for Section B. According to the results listed in the tables, the amount of reinforcement required for design against diaphragm effects, obtained from RSA and NLRHA of the double model, are very close to each other. On the other hand, when fixed models are used for the analysis, the required amount diaphragm reinforcement obtained from NLRHA is moderately larger than that obtained using RSA.

It is also interesting to observe that the amount of diaphragm reinforcement obtained from NLRHA of the double model under the DD1 level earthquake, which is the most robust and reliable analysis approach, is less than the reinforcement amount obtained from RSA of the single fixed model under the DD2 level earthquake, which is the simplest analysis approach that can be used for diaphragm design. This happens mostly because the fixed model overestimates the diaphragm effects in the connecting podium floors, as previously discussed in detail, and also because the design based on NLRHA uses expected material strengths, rather than reduced design strength values for the materials. Overall, this is a comforting result, since it implies that diaphragm design of connecting podium floors based on simple RSA of a fixed single tower model under the design level earthquake can potentially satisfy the required performance criteria of the double tower structure under the maximum considered earthquake level

Table 3- Comparison of additional (diaphragm) reinforcement at Section A based on RSA (under DD2 level earthquake) and NLRHA (under DD1 level earthquake) results.

Section A			RSA (DD2 level EQ.)		NLRHA (DD1 level EQ.)	
			+12.80 m	+09.60 m	+12.80 m	+09.60 m
Double Model	Tension	Beams	2512 mm^2	0	2826 mm^2	0
		Slab	1340 mm^2/m	0	1027 mm^2/m	0
	Shear	Slab	0	0	0	0
Single-Fixed Model	Tension	Beams	4248 mm^2	2280 mm^2	5656 mm^2	3040 mm^2
		Slab	2010 mm^2/m	1130 mm^2/m	2032 mm^2/m	1027 mm^2/m
	Shear	Slab	646 mm^2/m	0	1232 mm^2/m	393 mm^2/m

Table 4 - Comparison of additional (diaphragm) reinforcement at Section B based on RSA (under DD2 level earthquake) and NLRHA (under DD1 level earthquake) results.

Section B			RSA (DD2 level EQ.)		NLRHA (DD1 level EQ.)	
			+12.80 m	+09.60 m	+12.80 m	+09.60 m
Double Model	Tension	Beams	2512 mm^2	0	2660 mm^2	0
		Slab	1340 mm^2/m	0	1232 mm^2/m	0
	Shear	Slab	0	0	0	0
Single-Fixed Model	Tension	Beams	4248 mm^2	2512 mm^2	4928 mm^2	2512 mm^2
		Slab	2297 mm^2/m	1291 mm^2/m	2533 mm^2/m	1027 mm^2/m
	Shear	Slab	753 mm^2/m	0	1027 mm^2/m	314 mm^2/m

3.3.2. Comparison of Single and Double Model Responses for Tower A

In this section, average analysis results obtained for important response quantities related to performance-based design of one of the two towers (Tower A), obtained using the double, single-fixed, and single-free models are compared (Figure 23). Comparisons of interstory drift ratios, beam plastic rotations, wall shear forces, and wall boundary longitudinal strains are presented in Figure 24 to Figure 28. As shown in the figures, it is observed that response quantities obtained using double tower model are typically underestimated by the single-fixed model (i.e., the single-tower model with fixed end restraints at the connecting podium levels), whereas the results of the single free model (i.e., the single-tower model with free end restraints) are much closer to those of the double-tower model. Overall, comparison with NLRHA results obtained using the double tower model show that the single-free model provides reliable results that are reasonably representative of the results of the comprehensive double-tower model, for important response quantities associated with the seismic design and performance of the individual tower structure.

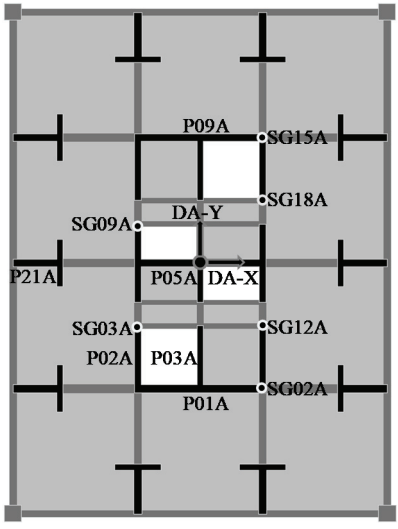

Figure 23 - NLRHA interstory drift ratio, structural wall shear force and strain control nodes for Tower A.

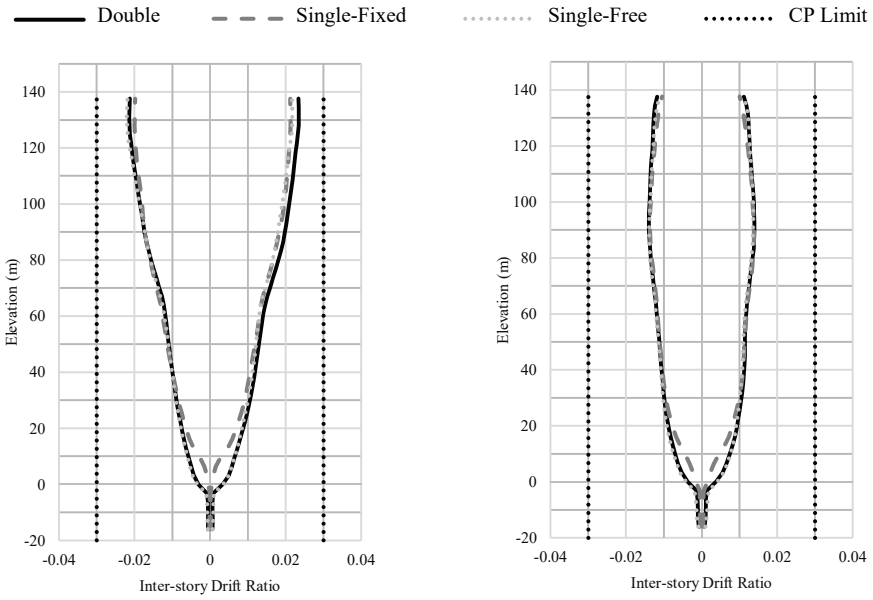

Figure 24 - Comparison of NLRHA interstory drift ratio distributions for double, single-fixed and single-free models of Tower A at (a) DA-X, (b) DA-Y.

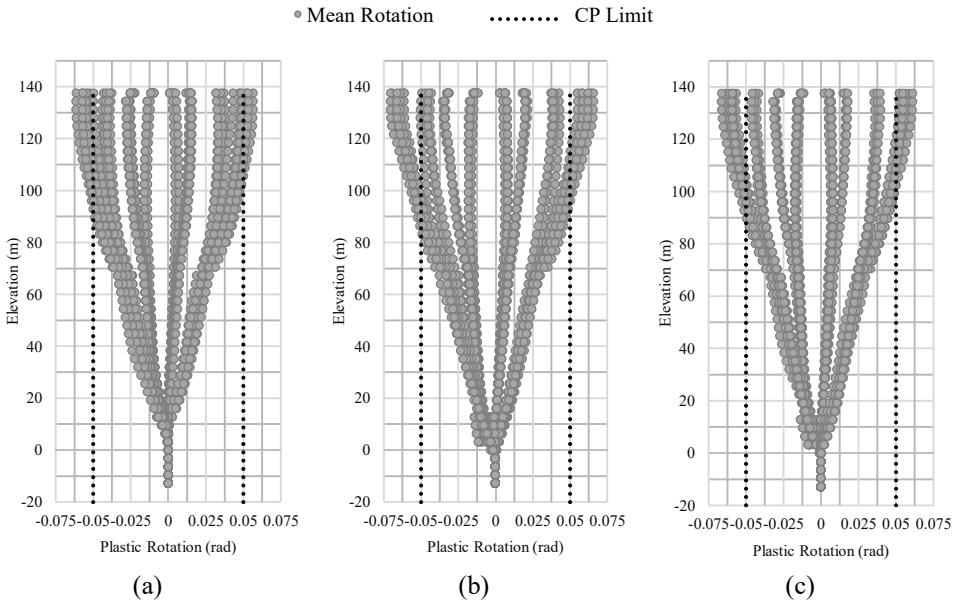

Figure 25 - Comparison of NLRHA outrigger and perimeter beams plastic rotations for (a) single-fixed, (b) single-free, (c) double models of Tower A.

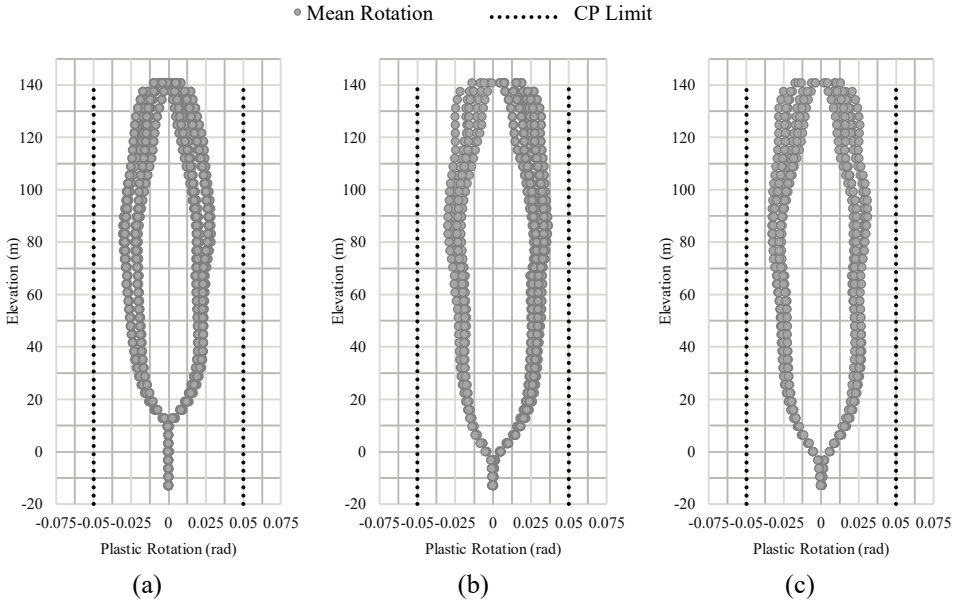

Figure 26 - Comparison of NLRHA coupling beam plastic rotations for (a)single- fixed, (b) single-free, (c) double models of Tower A.

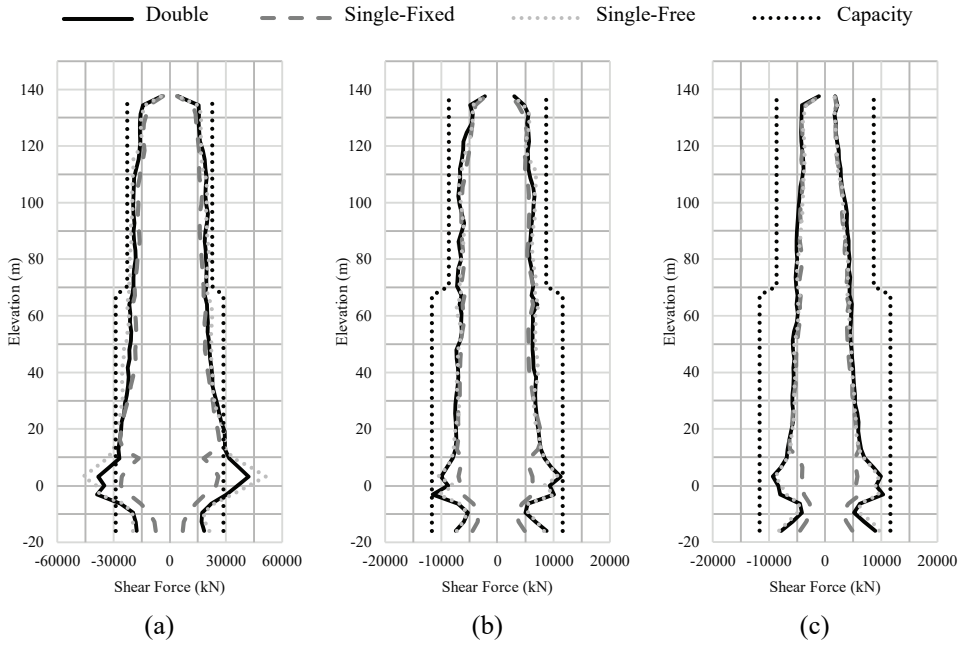

Figure 27 - Comparison of NLRHA structural wall shear force distributions for double, single-fixed and single- free models of Tower A at (a) P01A, (b) P02A, (c) P03A.

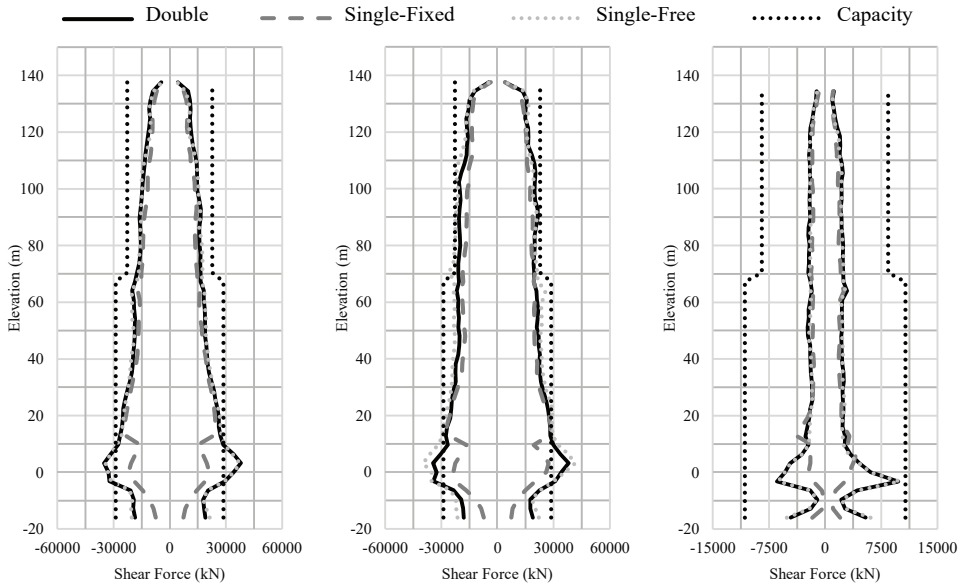

Figure 27 (continued) - Comparison of NLRHA structural wall shear force distributions for double, single-fixed and single- free models of Tower A at (d) P05A, (e) P09A, (f) P21A.

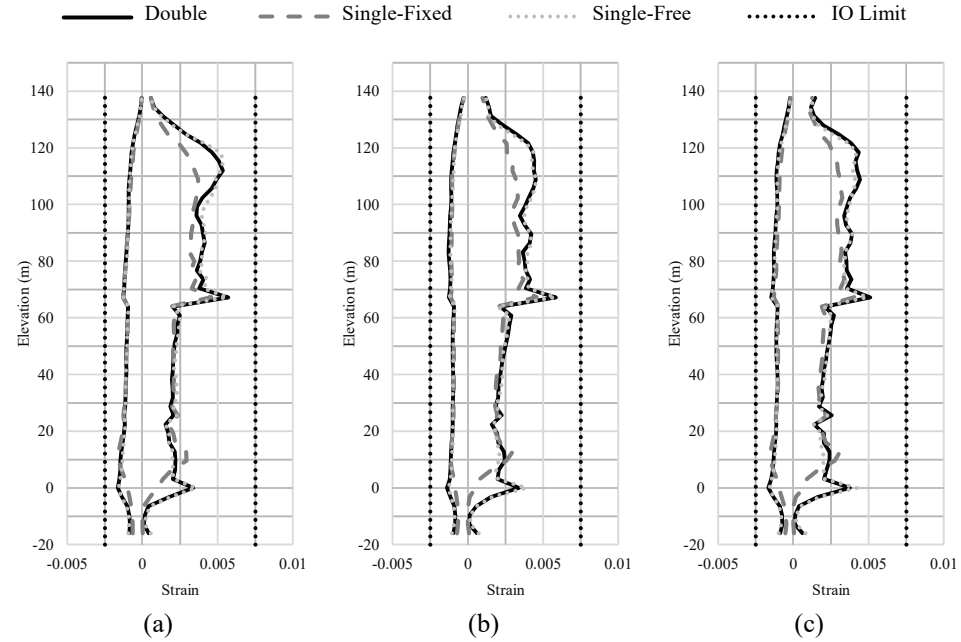

Figure 28 - Comparison of NLRHA strain distributions of structural walls for double, single-fixed and single- free models of Tower A at (a) SG02A, (b) SG03A, (c) SG09A.

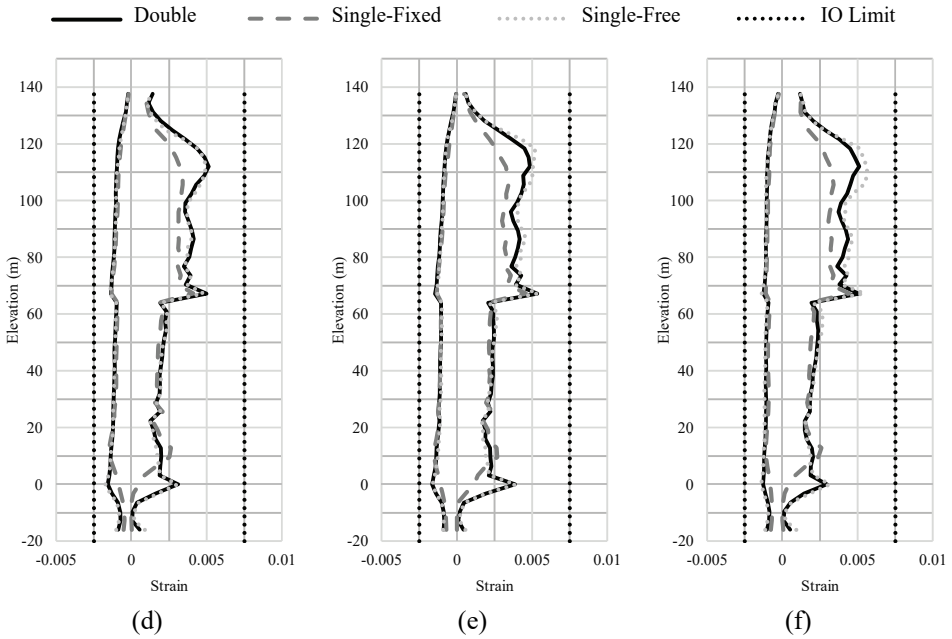

Figure 28 (continued) - Comparison of NLRHA strain distributions of structural walls for double, single-fixed and single- free models of Tower A at (d) SG12A, (e) SG15A, (f) SG18A.

4. CONCLUSIONS

Under the light of the analysis results obtained using different modeling approaches and analysis methods used in this study, the following conclusions can be drawn:

- When results of linear elastic analysis methods (RSA and LMTHA) conducted under the design level (DD2) earthquake effects using double (combined double tower) and single-fixed (single tower with fixed end restraints) model results are compared, it is observed that RSA provides diaphragm tensile force resultants that are only approximately 10% larger than LMTHA at the connected podium levels. The difference between results of the two analysis methods increase to 25% only for diaphragm shear forces obtained using the double model, yet these diaphragm shear forces are relatively small in magnitude.
- When linear elastic analysis results using the double and single-fixed models are compared, it is observed that the single-fixed model can provide diaphragm tension forces that are up to 75% higher that the double model results, independently from the analysis method used (RSA or LMTHA). However, this percent difference increases to more than 100%, when diaphragm shear forces are considered, also because the diaphragm shear force magnitudes are small.
- When results of NLRHA obtained using double and single-fixed models are compared, it is observed that the single-fixed model can provide diaphragm force resultants that are almost twice those calculated using the double model.

- NLRHA of the double model of the structure under the DD1 level (maximum credible) earthquake gives approximately 20-30% higher diaphragm tensile forces compared to RSA of the double model under the DD2 level (design level) earthquake. On the other hand, in case of diaphragm shear forces, NLRHA results obtained using the double model are almost twice those obtained from RSA at critical sections. Although NLRHA gives higher diaphragm forces, the total amount of required diaphragm reinforcement for tension is 5% to 15% less than RSA, since expected material strengths are used for design based on NLRHA results. Additionally, diaphragm shear forces obtained in both analyses do not exceed concrete shear strength limits, not necessitating any diaphragm shear reinforcement.
- Differently from the double model, when the single-fixed model is used in the analysis, NLRHA can produce 50% higher diaphragm tensile forces as compared to RSA. On the other hand, diaphragm shear forces from NLRHA are approximately twice those obtained by RSA, as observed in the double model. When required reinforcement amounts against diaphragm tension are compared, NLRHA results using the single-fixed model require approximately 10% larger amount of reinforcement, as compared to RHA of the single-fixed model.
- Interestingly, the amount of diaphragm reinforcement obtained from NLRHA of the double model under the DD1 level (maximum credible) earthquake, which is the most robust and reliable analysis approach, is less than the reinforcement amount obtained from RSA of the single-fixed model under the DD2 level (design level), which is the simplest analysis approach that can be used for diaphragm design. This happens mostly because the fixed model overestimates the diaphragm effects in the connecting podium floors, and also because the performance-based design based on NLRHA uses expected material strengths, rather than reduced design strength values for the materials.
- NLRHA results show that the single-free (single tower with free end restraints) model provides results for critical response quantities associated with the seismic performance of the individual tower structures (interstory drifts, wall strains, wall shear forces, beam plastic rotations, etc.) that are reasonably close to analysis results obtained using the double model.
- Generally, taking into consideration of analysis duration and modeling complexity, it is recommended to use single-tower models with free end restraints for design of the individual towers, and single-tower models with fixed end restraints for design of the podium slabs for in-plane axial load and shear forces, whenever comprehensive analyses using a combined multiple-tower model is not possible.

Notations

LMTHA Linear modal time history analysis

NLRHA Nonlinear response history analysis

RSA Response spectrum analysis

References

[1] Qi Xiaoxuan, Chen Shuang, 1996, "Dynamic Behavior and Seismic Design of Structural Systems Having Multiple High-rise Towers on a Common Podium,Paper No. 1101", Sociedat Mexicana De Ingenieria Sismica, Eleventh World Conference on Earthquake Engineering, Acapulco, Mexico, June'23-28, 1996, California.

[2] Behnamfar F., Dorafshan S., Taheri A., Hashemi B. H., 2015, "A Method for Rapid Estimation of Dynamic Coupling and Spectral Responses of Connected Adjacent Structures", The Structural Design of Tall and Special Buildings, Vol. 25, pp: 605-625.

[3] Applied Technology Council, 2010, Modeling and Acceptance Criteria for Seismic Design and Analysis of Tall Buildings, ATC72-1, Pacific Earthquake Engineering Research Center, California.

[4] Los Angeles Tall Buildings Structural Design Council, 2015, An Alternative Procedure for Seismic Analysis and Design of Tall Buildings Located in the Los Angeles Region, Los Angeles Tall Buildings Structural Design Council, California.

[5] Pacific Earthquake Engineering Research Center, 2010, Guidelines for Performance-based Seismic Design of Tall Buildings, Report PEER-2010/05, Pacific Earthquake Engineering Research Center, University of California.

[6] Turkish Building Earthquake Code, 2018, Specifications for Design of Buildings under Earthquake Action, Disaster and Emergency Management Presidency, Ankara.

[7] ETABS Ultimate v16.1.0, 2017, Extended 3D Analysis of Building Structures, Computers and Structures, Inc., California, USA.

[8] Turkish Standards Institute, 2000, Requirements for Design and Construction of Reinforced Concrete Structures, TS500, Turkish Standards Institute, Ankara Turkey.

[9] Turkish Standards Institute, 1997, Design Loads for Buildings, TS498, Turkish Standards Institute, Ankara.

[10] Computer and Structures, Inc., 2011, Perform 3D V6.0.0: Nonlinear Analysis and Performance Assessment for 3D Structures, California, USA.

[11] ASCE/SEI Seismic Rehabilitation Committee, 2014, Seismic Evaluation and Retrofit of Existing Buildings, ASCE/SEI41-13, American Society of Civil Engineers, Reston, VA.

[12] Powell, G. H., 2010, Modeling for Structural Analysis, Behavior and Basics, Computers and Structures Inc. Berkeley, California.

[13] Disaster and Emergency Management Presidency, 2017, Turkish Earthquake Hazard Map https://tdth.afad.gov.tr/, accessed June 2017.

[14] Pacific Earthquake Engineering Research Center, 2013, Next Generation Attenuation-West2, http://ngawest2.berkeley.edu/, accessed at June 2017.

[15] Tura C., Earthquake Response Analysis of Multiple Towers on a Common Podium, M.S. Thesis, Boğaziçi University, 2017.

TECHNICAL NOTE

Teknik Dergi, 2019 9675-9682, Paper 561, ***Technical Note***

Effects of Straits on Hydro-Thermal Performance of Small Bays

Ahmet Metin GER[1]

ABSTRACT

The heated surface jet discharged into a bay which is connected to a larger body of water through a strait may experience bifurcation in the bay and stratification in the strait. The combined effects of bifurcation and stratification may lead to a substantially greater rise in temperature than the rise expected in case of unrestricted receiving body of water. In this study, the behavior of heated effluents discharged into bays with a restricted access to a large body of water is scrutinized experimentally by the help of a scaled physical model. Dimensional analysis leads to a new dimensionless parameter A_r, area restriction parameter, on which the difference between the excess temperatures at the inlet of the strait for restricted and free receiving mediums, $\Delta(\Delta T/\Delta T_0)$ is shown to be strongly dependent.

Keywords: Heated effluents, surface jets, excess heat.

1. INTRODUCTION

Thermal Power Plants are still in use to provide energy to satisfy the ever-increasing energy demand. Being the most convenient and cheapest method, cooling water from the condensers in the form of heated effluent is discharged to the nearest body of water. The excess heat thus introduced may cause irreversible changes in the immediate vicinity of the discharge. If the receiving medium is a bay with a geometrically restricted access to a larger body of water in the form of a strait, the heat to be build up in the small bay may be prohibitively high. This will not only reduce the performance of the power plant but also damage the aquatic environment permanently.

A heated effluent discharged at the surface into a body of water is called a surface buoyant jet. The temperature difference between the effluent and the receiving ambient results in a density disparity, which causes the buoyant forces to affect the behavior significantly.

Several attempts have been made to describe and predict the behavior of heated surface effluents. Some studies focused on the cooling ponds for which the receiving volume is

Note:
- This paper has been received on October 05, 2018 and accepted for publication by the Editorial Board on January 28, 2019.
- Discussions on this paper will be accepted by January 31, 2020.
- https://dx.doi.org/10.18400/tekderg.467567

1 Kadir Has University, Faculty of Engineering and Natural Sciences, İstanbul, Turkey - ger.metin@gmail.com - https://orcid.org/0000-0002-3422-485X

limited in size and used also as the source of cooling water (1,2,3,4,5). The majority of the work, however, focused on the behavior of heated surface effluents into an infinitely large body of water. Policastro and Tokar (6) summarized and compared the models available. Among the available mathematical simulations, the model of Stolzenbach and Harleman (7) is selected as the benchmark for this study.

The three-dimensional model developed by Stolzenbach and Harleman (7) simulates the heated surface effluent from a rectangular channel into an infinitely large, non-stratified body of water. The model can be used to predict the behavior of the heated effluent to the extent that not only the centerline temperature variations but also the spatial extent of the heat contamination can be assessed.

When the heated effluent is discharged into a small bay with a restricted access to a larger body of water, the behavior of the jet is greatly influenced by the geometrical characteristics of the bay and the strait. The strait being the only connection between the bay and the large body of water may cause the heated surface jet to be divided into two parts; one leaving the bay through the strait and the other circulating in the bay. Furthermore, the buoyancy effects may cause a layered flow in the strait.

Thus, combined effects of bifurcation and stratification may lead to a substantially greater rise in temperature than the rise expected in case of infinitely large receiving medium as demonstrated by Nalbantoğlu (8) and Ger (9). The data used in this work is the data originally collected by Nalbantoğlu (8) in a similar attempt made to study the behavior of heated effluents discharged in a bay with a restricted outlet to a larger body of water.

2. THE EXPERIMENTAL SETUP AND THE EXPERIMENTS

The idealized model of the experimental set up is as depicted in Figure 1. In this figure, all geometric variables of interest in the process are also identified.

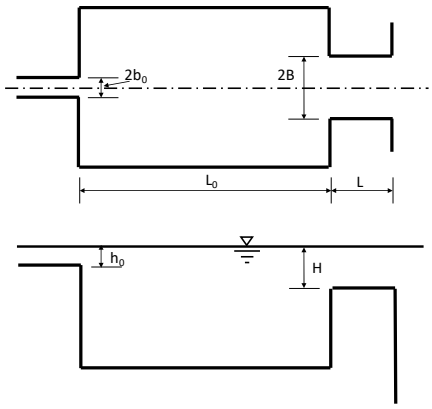

Figure 1 - Schematic representation of the idealized model

ΔT, temperature difference between the heated effluent and the receiving ambience, at the entrance to the strait was chosen as the independent variable representing the effect of the strait on the behavior of the heated effluent issued into the restricted bay. The variables that may contribute to the behavior of the effluent are listed in Table 1.

Table 1 - The list of contributing variables

CONTRIBUTOR	CHARACTERISTICS
OUTLET	b_0: half width of the outlet channel h_0: depth of flow in the outlet channel
SMALL BAY AND THE STRAIT	L_0: length of the small bay B: half width of the strait H: depth of flow in the strait L: length of the strait
EFFLUENT, RECEIVING AMBIENCE, AIR, and OTHERS	ΔT_0: temperature difference between the heated effluent and the receiving ambience $\Delta\rho_0$: density difference between the heated effluent and the receiving ambience u_0: velocity of the effluent at the outlet ρ_w: ambient density ν_w: kinematic viscosity of the receiving ambience c_w: specific heat of water α_w: thermal diffusivity ΔT_a: temperature difference between the air and the receiving ambience K_e: Surface heat exchange coefficient ΔT: temperature difference between the heated effluent and the receiving ambience at the entrance of the strait g: the gravitational acceleration

The following functional form, thus, can be formed.

$$\Delta T = f_1(b_0, h_0, L_0, B, H, L, \Delta T_0, \Delta\rho_0, u_0, \rho_w, \nu_w, \alpha_w, c_w, \Delta T_a, K_e, g) \quad (1)$$

Employing Buckingham's π Theorem one obtains

$$\frac{\Delta T}{\Delta T_0} = f_2\left(Fr_d, Fr, Re, Pr, \frac{K_e}{\rho_0 c_w u_0}, \frac{\Delta T_a}{\Delta T_0}, \frac{L}{L_0}, \frac{h_0}{b_0}, \frac{H}{B}, \frac{(h_0 b_0)^{1/2}}{L_0}, \frac{h_0 b_0}{HB}, \frac{h_0}{B}\right) \quad (2)$$

where Fr_d is the Densimetric Froude Number at the outlet defined as $Fr_d=u_0/(\Delta\rho_0 g h_0/\rho_w)$; Fr is the Froude Number at the outlet defined as $Fr=u_0/(gh_0)^{1/2}$; and Re is the Reynolds Number at the outlet defined as $Re=u_0(h_0b_0)^{1/2}/\nu_w$; Pr is the Prandtl Number in the bay defined as $Pr=\nu_w/\alpha_w$.

The effects of Fr, Re, and Pr may be neglected (29). Furthermore, since u_0 and ΔT_a are kept constant and $L_0>>h_0$ throughout the experiments, the effects of $K_e/\rho_0 c_w u_0$, $\Delta T_a/\Delta T_0$, h_0/b_0, H/B, and h_0/B will be insignificant and may also be disregarded. Therefore, Equation 3 reduces to

$$\frac{\Delta T}{\Delta T_0} = f_3\left(Fr_d, \frac{L}{L_0}, \frac{(h_0b_0)^{1/2}}{L_0}, \frac{h_0b_0}{HB}\right) \tag{3}$$

At this step, in order to emphasize the presence of the strait a new parameter is introduced; the ratio of the nominal cross-sectional area of the effluent at the location of the inlet in the absence of the strait to the cross-sectional area of the strait. The representative depth h_{max} and half width y_c are reported to be

$$h_{max} \propto (h_0b_0)^{1/2}Fr_d \tag{4}$$

and

$$y_c \propto L_0\, Fr_d^{-1/4} \tag{5}$$

as given by Harleman (10) and Jen et. Al. (11). Thus, the new parameter, area restriction parameter A_r is defined as

$$A_r = \frac{(h_0b_0)^{1/2}L_0Fr_d^{3/4}}{HB} \tag{6}$$

coupling equations 3 and 6 and considering that A_r is a combination of Fr_d, $(h_0b_0)^{1/2}/L_0$ and h_0b_0/HB; equation 3 becomes

$$\frac{\Delta T}{\Delta T_0} = f_4\left(A_r, \frac{L}{L_0}, \frac{L_0}{(h_0b_0)^{1/2}}\right) \tag{7}$$

Once the functional relationship, of Equation 7, that can be used in investigating the effect of restriction imposed by a strait on the behavior of a heated effluent was established, an experimental setup was designed to facilitate the observation of the aforementioned effects of the strait on the behavior of the heated effluent.

The experiments were carried out using several different combinations of geometric variables. The characteristics of the experiments run are listed in Table 2. In this Table, T_0, T_w, and T are temperatures measured at the outlet, at the small bay, and at the inlet of the strait, so that $\Delta T_0=T_0-T_w$ and $\Delta T=T-T_w$. In Table 2, the respective values of the variables appearing in Eqn. 7 are also included.

Table 2 - Observed and reduced values of the variables involved

Code no	H cm	B cm	T_O ^0C	T_w ^0C	h_0 cm	b_0 cm	u_o m/s	L_0 cm	L cm	T ^0C	Ar	$L_0/(h_0b_0)^{1/2}$	L/L_0	$\Delta T/\Delta T_0$
101	1.9	24.7	36.5	15.3	2.0	0.5	0.2	40.0	10.0	25.5	3.327	40.000	0.250	0.481
102	6.9	2.2	36.8	15.0	2.0	0.5	0.2	40.0	10.0	28.3	10.178	40.000	0.250	0.610
103	6.9	7.2	36.6	15.0	2.0	0.5	0.2	40.0	10.0	23.0	3.125	40.000	0.250	0.370
104	14.4	2.2	37.0	15.0	2.0	0.5	0.2	40.0	10.0	26.8	4.853	40.000	0.250	0.536
105	14.4	7.2	37.1	15.0	2.0	0.5	0.2	40.0	10.0	22.1	1.479	40.000	0.250	0.321
106	24.4	7.2	34.0	15.0	2.0	0.5	0.2	40.0	10.0	21.4	0.946	40.000	0.250	0.337
201	1.9	7.2	30.7	10.5	2.0	0.5	0.2	30.0	20.0	24.6	9.526	30.000	0.667	0.698
202	1.9	24.7	28.5	10.5	2.0	0.5	0.2	30.0	20.0	20.3	2.963	30.000	0.667	0.544
203	6.9	2.2	29.6	10.4	2.0	0.5	0.2	30.0	20.0	22.0	8.852	30.000	0.667	0.604
204	6.9	7.2	29.1	10.5	2.0	0.5	0.2	30.0	20.0	19.5	2.748	30.000	0.667	0.484
205	14.4	2.2	29.3	9.7	2.0	0.5	0.2	30.0	20.0	19.7	4.250	30.000	0.667	0.510
206	14.4	7.2	30.8	9.0	2.0	0.5	0.2	30.0	20.0	18.6	1.238	30.000	0.667	0.440
207	24.4	2.2	29.5	10.5	2.0	0.5	0.2	30.0	20.0	18.8	2.513	30.000	0.667	0.437
208	24.4	7.2	29.1	10.5	2.0	0.5	0.2	30.0	20.0	18.0	0.777	30.000	0.667	0.403
301	1.9	7.2	29.5	11.0	2.0	1.0	0.2	40.0	10.0	24.8	18.691	28.284	0.250	0.746
302	1.9	24.7	29.3	11.5	2.0	1.0	0.2	40.0	10.0	22.0	5.512	28.284	0.250	0.590
303	6.9	2.2	31.2	11.5	2.0	1.0	0.2	40.0	10.0	25.9	16.116	28.284	0.250	0.731
304	6.9	7.2	30.8	11.5	2.0	1.0	0.2	40.0	10.0	22.0	4.981	28.284	0.250	0.544
305	6.9	24.7	31.3	10.5	2.0	1.0	0.2	40.0	10.0	19.2	1.418	28.284	0.250	0.418
306	14.4	2.2	30.0	11.2	2.0	1.0	0.2	40.0	10.0	23.2	7.969	28.284	0.250	0.638
307	14.4	7.2	30.8	10.0	2.0	1.0	0.2	40.0	10.0	19.7	2.353	28.284	0.250	0.466
308	14.4	24.7	30.3	10.6	2.0	1.0	0.2	40.0	10.0	18.9	0.699	28.284	0.250	0.421
309	24.4	2.2	29.7	10.7	2.0	1.0	0.2	40.0	10.0	22.9	4.720	28.284	0.250	0.642
310	24.4	7.2	30.0	10.3	2.0	1.0	0.2	40.0	10.0	19.6	1.424	28.284	0.250	0.472
311	24.4	24.7	30.6	9.6	2.0	1.0	0.2	40.0	10.0	17.3	0.406	28.284	0.250	0.367
401	1.9	7.2	30.5	10.0	2.0	1.0	0.2	30.0	20.0	26.4	13.487	21.213	0.667	0.800
402	1.9	24.7	29.2	11.2	2.0	1.0	0.2	30.0	20.0	23.1	4.133	21.213	0.667	0.661
403	6.9	2.2	31.7	10.4	2.0	1.0	0.2	30.0	20.0	26.9	11.802	21.213	0.667	0.775
404	6.9	7.2	29.7	10.5	2.0	1.0	0.2	30.0	20.0	23.0	3.818	21.213	0.667	0.651
405	6.9	24.7	31.3	11.0	2.0	1.0	0.2	30.0	20.0	20.6	1.068	21.213	0.667	0.473
406	14.4	2.2	30.0	10.0	2.0	1.0	0.2	30.0	20.0	23.7	5.907	21.213	0.667	0.685
407	14.4	7.2	30.8	10.8	2.0	1.0	0.2	30.0	20.0	21.4	1.778	21.213	0.667	0.530
408	14.4	24.7	30.3	11.4	2.0	1.0	0.2	30.0	20.0	20.8	0.529	21.213	0.667	0.497
409	24.4	2.2	29.7	10.7	2.0	1.0	0.2	30.0	20.0	22.1	3.540	21.213	0.667	0.600
410	24.4	7.2	30.0	10.3	2.0	1.0	0.2	30.0	20.0	20.0	1.068	21.213	0.667	0.492

3. EXPERIMENTAL FINDINGS AND CONCLUSIVE REMARKS

The recorded variation of dimensionless excess temperature difference, $\Delta T/\Delta T_0$, at the inlet of the strait, with the area restriction parameter, A_r, is depicted in Figure 2. In this figure, dimensionless excess temperature differences, $(\Delta T/\Delta T_0)_{free}$, in the case of unrestricted receiving body of water at the respective locations as predicted by Stolzenbach-Harleman (S-H) are also included for the facilitation of comparison.

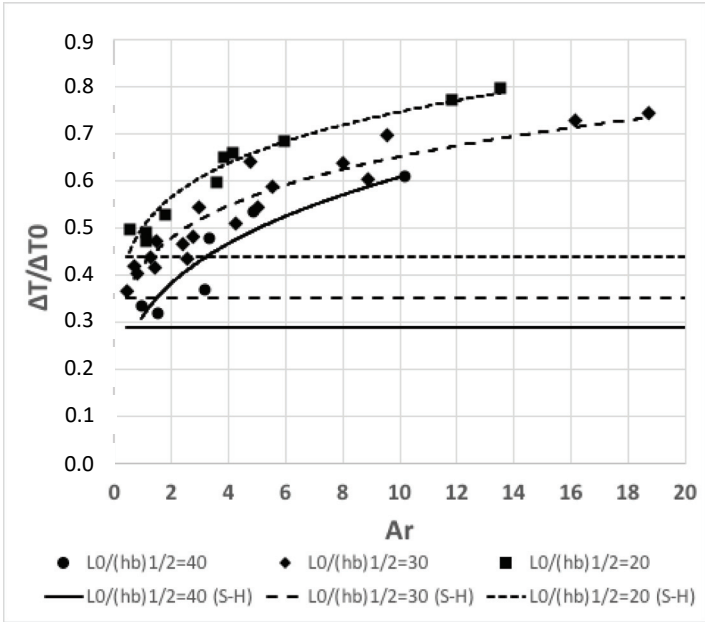

Figure 2 - Variation of heat built up at the inlet of the strait

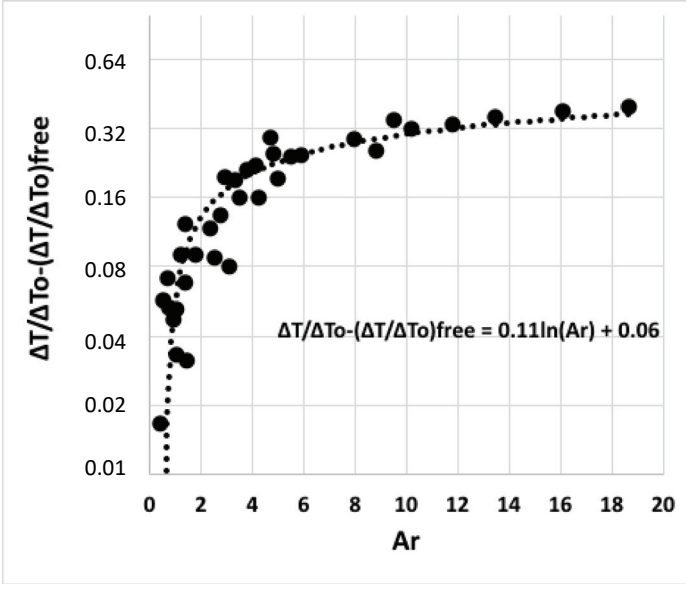

Figure 3 - Variation of difference between the excess temperatures at respective locations for restricted and free receiving mediums

Investigation of the data reveals that the difference between the excess temperatures at the inlet of the strait for restricted and free receiving mediums, $\Delta(\Delta T/\Delta T_0)$, defined as $\Delta(\Delta T/\Delta T_0) = \Delta T/\Delta T_{o.}-(\Delta T/\Delta T_o)_{free}$, is strongly dependent on A_r, such that

$$\Delta(\Delta T/\Delta T_0) = \Delta T/\Delta T_{o.}-(\Delta T/\Delta T_o)_{free} =0{,}11 \ln(A_r) + 0.06 \quad (8)$$

as depicted in Figure 3.

The experimental findings strongly suggest that the excess temperature rise, $\Delta(\Delta T/\Delta T_0)$, at the entrence of the restricting strait can be predicted once the A_r, the restriction parameter, is known.

Acknowledgement:

The author heartily acknowledges the effort of Mr. A. E. Nalbantoğlu who gathered the data used in this study. Thanks are also extended to Middle East Technical University which provided facilities for the experiments.

Symbols

A_r : Area restriction parameter

B : Half width of the strait

b_0 : half with of the outlet channel

c_w : specific heat of water

Fr : Froude Number at the outlet

Fr_d : Densimetric Froude Number

G : the gravitational acceleration

H : depth of flow in the strait

h_0 : depth of flow in the outlet channel

L : length of the strait

L_0 : length of the small bay

K_e : Surface heat exchange coefficient

Re : Reynolds Number at the outlet

Pr : Prandtl Number in the bay

u_0 : velocity of the effluent at the outlet

α_w : thermal diffusivity

ΔT : temperature difference between the heated effluent and the receiving ambience at the entrance of the strait

ΔT_a : temperature difference between the air and the receiving ambience

ΔT_0 : temperature difference between the heated effluent and the receiving ambience

$\Delta \rho_0$: density difference between the heated effluent and the receiving ambience

ρ_w : ambient density

ν_w : kinematic viscosity of the receiving ambience

References

[1] Ryan, P. J., and Harleman, D. R. F., An Analytical and Experimental Study of Transient Cooling Pond Behaviour, R. M. Parsons Lab. for Water Resources and Hydrodynamics, Dept. of Civil Engineering, MIT, USA, Technical Report No. 161, 1973

[2] Adams, E. E., Stolzenbach, K. D., and Harleman, D. R. F., Near and Far Field Analysis of Buoyant Surface Jets, R. M. Parsons Lab. for Water Resources and Hydrodynamics, Dept. of Civil Engineering, MIT, USA, Technical Report No. 205, 1975

[3] Stefan, H., Dilution of Buoyant Two-Dimensional Surface Discharges, J. of Hydraulic Division, ASCE, Vol. 98, HY1, 71-86, 1970

[4] Stefan, H., Heated Dicharge from a Flume into a Tank, J. of Hydraulic Division, ASCE, Vol. 98, SA6, 1416-1432, 1970

[5] Turner, J. S., Buoyancy Effects in Fluids, Cambridge Univ. Press, 1973

[6] Policastro, A. J. and Tokar, J. V., Heated Effluent Dispersion in Lakes: State of the Art of Analytical Modelling Part 1: Critique of Model Formulation, Report No: ANL/ES-11, Aragone National Lab., 1972

[7] Stolzenbach, K. D. and Harleman, D. R. F., An Analytical and Experimental Investigation of Surface Discharges of Heated Water, R. M. Parsons Lab. for Water Resources and Hydrodynamics, Dept. of Civil Engineering, MIT, USA, Technical Report No. 135, 1971

[8] Nalbantoğlu, A. E., Hydro-Thermal Performance of Small Bays, Unpublished M.S. Thesis, Civil Engineering Dept., METU, May 1980

[9] Ger, A. M., Effects of Straits on the Behaviour of Heated Surface Jets, 20th Midwestern Mechanics Conf., Proc. 14b, West Lafeyette, Indiana, 1987

[10] Harleman, D. R. F., Thermal Stratification Due to Heated Discharges, International Symposium on Stratified Flows, Novosibirsk, 1972

[11] Jen, J. A., Wiegel, R. L., and Mobarek, I., Surface Discharge of Horizontal Warm Water Jets, Proceedings, ASCE, Power Division, 1966

TEKNİK DERGİ MANUSCRIPT DRAFTING RULES

1. The whole manuscript (text, charts, equations, drawings etc.) should be arranged in Word and submitted in ready to print format. The article should be typed on A4 (210 x 297 mm) size paper using 10 pt (main title 15 pt) Times New Roman font, single spacing. Margins should be 40 mm on the left and right sides and 52.5 mm at the top and bottom of the page.
2. Including drawings and tables, articles should not exceed 25 pages, technical notes 6 pages.
3. Your contributed manuscript must be sent over the DergiPark system. (http://dergipark.gov.tr/tekderg)
4. The text must be written in a clear and understandable language, conform to the grammar rules. Third singular person and passive tense must be used, and no inverted sentences should be contained.
5. Title must be short (10 words maximum) and clear, and reflect the content of the paper.
6. Sections should be arranged as: (i) abstract and keywords, (ii) title, abstract and keywords in the other language, (iii) main text, (iv) symbols, (v) acknowledgements (if required) and (vi) references.
7. Both abstracts should briefly describe the object, scope, method and conclusions of the work and should not exceed 100 words. If necessary, abstracts may be re-written without consulting the author. At least three keywords must be given. Titles, abstracts and keywords must be fitted in the first page leaving ten line space at the bottom of the first page and the main text must start in the second page.
8. Section and sub-section titles must be numbered complying with the standard TS1212.
9. Symbols must conform to the international rules; each symbol must be defined where it appears first, additionally, a list of symbols must be given in alphabetic order (first Latin, then Greek alphabets) at the end of the text (before References).
10. Equations must be numbered and these numbers must be shown in brackets at the end of the line.
11. Tables, drawings and photographs must be placed inside the text, each one should have a number and title and titles should be written above the tables and below the drawings and photographs.
12. Only SI units must be used in the manuscripts.
13. Quotes must be given in inverted commas and the source must be indicated with a reference number.
14. Acknowledgement must be short and mention the people/ institutions contributed or assisted the study.
15. References must be numbered (in brackets) in the text referring to the reference list arranged in the order of appearance in the text. References must include the following information:

    If the reference is an article: Author's surname, his/her initials, other authors, full title of the article, name of the journal, volume, issue, starting and ending pages, year of publication.

    Example : Naghdi, P. M., Kalnins, A., On Vibrations of Elastic Spherical Shells. J. Appl. Mech., 29, 65-72, 1962.

    If the reference is a book: Author's surname, his/her initials, other authors, title of the book, volume number, editor if available, place of publication, year of publication.

    Example : Kraus. H., Thin Elastic Shells, New York. Wiley, 1967.

    If the reference is a conference paper: Author's surname, his/her initials, other authors, title of the paper, title of the conference, location and year.

    If the source is a thesis: Author's surname, his/her initials, thesis title, level, university, year.

    If the source is a report: Author's surname, his/her initials, other authors, title of the report, type, number, institution it is submitted to, publication place, year.
16. Discussions to an article published in Teknik Dergi should not exceed two pages, must briefly express the addressed points, must criticize the content, not the author and must be written in a polite language. Authors' closing remarks must also follow the above rules.
17. A separate note should accompany the manuscript. The note should include, (i) authors' names, business and home addresses and phone numbers, (ii) brief resumes of the authors and (iii) a statement "I declare in honesty that this article is the product of a genuinely original study and that a similar version of the article has not been previously published anywhere else" signed by all authors.
18. Copyright has to be transferred to UCTEA Turkish Chamber of Civil Engineers. The standard copyright form signed by the authorised author should therefore be submitted together with the manuscript.

CONTENTS

ISSN: 1300-3453